Synchrotron X-ray Studies of Atmospheric Pitting Corrosion of Stainless Steel

by

Na Mi

A thesis submitted to the University of Birmingham

for the degree of Doctor of Philosophy

School of Metallurgy and Materials
University of Birmingham
August 2013

Abstract

Atmospheric pitting corrosion of stainless steel was studied to determine pit growth mechanisms and kinetics. Inkjet printing of chloride was used to investigate the growth of atmospheric corrosion pits. It has been shown that the pit size increases with increasing chloride deposition density, as well as increases with increasing deposit diameter.

Atmospheric pit growth was characterised in situ and in real time with synchrotron X-ray micro-tomography. Most pits were found to have open mouths and shallow depths. Growth of a deep pit was also observed in a pre-existing defect. Pit growth in depth does not appear to be under diffusion control.

Electrochemical kinetics of the metal dissolution reaction including the Tafel slope as well as the critical metal ion concentration for pit propagation were studied with 1D artificial pits in high chloride concentration solutions relevant to atmospheric conditions. The diffusion-limited current density and ratio of the critical metal ion concentration for pit propagation to the saturation concentration were found to decrease with increasing chloride concentration. However, there is no significant effect of the chloride concentration on the Tafel slope. The pitting potential and repassivation potential were measured on abraded wires and were found to decrease with increasing chloride concentration.

Salt layer formation has been observed on 1D artificial pits in 1 M and 6 M solutions with synchrotron XRD. The dominant phase of the salt layer was found to be $FeCl_2 \cdot 4H_2O$. The formation of $FeCl_2 \cdot 2H_2O$ was also observed, predominantly at higher applied potentials.

This work can be used to provide a basis for developing a model to predict pitting corrosion of stainless steel under atmospheric corrosion conditions, for example in the case of storage of stainless steel intermediate nuclear waste containers.

Acknowledgments

I do appreciated many people give me help and support during my postgraduate study.

Firstly, I would like to express my sincere gratitude to my supervisor Dr Alison J. Davenport, who not only supports my academic study with her wide scientific culture and expertise, but also improves my personal effectiveness with her encouragement and enthusiasm. I do appreciated for her patient guidance and kind help in the past six years.

Many thanks also to my co-supervisor Prof Trevor Rayment. I do appreciated his bright suggestions and innovative ideas which broadens my views during my study. It is also an enjoyable experience to work with him because of his kindness and sense of humour.

I greatly acknowledge all the help and supports from people at Diamond Light Source, especially to Dr Christina Reinhard and Dr Robert Atwood at I12 beamline, Dr Fred Mosselmans and Dr Tina Geraki at I18 beamline, Dr Paul Quinn at I 14 beamline, Dr Steve Collins and Dr Gareth Nisbet at I16 beamline.

I would like to thank Dr Donal Krouse, Dr Nick Laycock at Industrial Research Limited, Dr Christiano Padovani at Nuclear Decommissioning Authority for their precious support.

I wish to thank Prof Robert Kelly at University of Virginia and his co-workers for interesting discussions on atmospheric pitting corrosion, which is a delightful experience to work with them.

I could never thank enough to Dr Stephen Kukureka at University of Birmingham, who gives great support, kind help and patient guidance to many international students and make us become familiar with a new environment.

I would like to thank Dr Majid Ghahari for his solid expertise in the pitting corrosion which is impressive beneficial to the progress of my research. I would also like to thank Dr Mehdi Monir, Dr Joshua Hammons, Dr Mahrez Amri who shared their valuable experiences of synchrotron experiments and supported my work.

Thanks to all my colleagues here: Gavin, Ali, Andy, Weichen, Liya, Fei, Steven, Haval, Georgina, Kathrine... I have enjoyed my study here with them, which makes the experience of working in the corrosion group at Birmingham has been especially precious for me.

I also hope to thank people who helped me during my study and my life abroad. I am sorry that I could not list all the names, but my appreciation is always there.

Finally, I would like to thank my family for their support, patience and love, which encourages me to be optimistic and enthusiastic of my study...

Dedicated to my two grandfathers in heaven

Mr Zhende Mi and Mr Tairen Wan

List of symbols

Symbol	Definition
A	Cross-section area
$A_{electrode}$	Electrode cross-section area
b_a	Anodic Tafel slope
C_b	Metal ion concentration at the pit bottom
C_{crit}	Critical metal ion concentration for pit propagation
C_m	Metal ion concentration at the pit mouth
C_{sat}	Saturated metal ion concentration
D	Diffusion coefficient
E	Electrode potential
E_{app}	Applied potential
E_{corr}	Open circuit corrosion potential
E_{pit}	Pitting potential
E_{rep}	Repassivation potential
F	Faraday's constant
i	Current density
i_a	Anodic current density
i^*	Current density of critical metal ion concentration for pit propagation
i_{corr}	Open circuit corrosion current density
i_{lim}	Diffusion-limited current density
i_{sat}	Current density of saturated metal ion concentration
ix	Pit stability product of 1D artificial pit
I	Current
IR	Product of current and resistance/potential drop
l_{salt}	Salt layer thickness
m	Mass of the substance liberated at an electrode
M_w	Molecular weight
n	Number of electrons produced in metal dissolution
Q	Transferred charge
R	Gas constant
R_{bulk}	Bulk solution resistance
R_{salt}	Salt layer resistance
R_{total}	Total cell resistance
$R_{saltfree}$	Pit solution resistance and approach resistance in the salt free state
RH	Relative humidity
r	Pit radius
T	Temperature
t	Time
x	Pit depth
ρ	Pit solution resistivity
η	Salt layer porosity

Contents

1 Introduction

Stainless steel is a corrosion resistant alloy which is widely used in many applications. However, it can be susceptible to atmospheric pitting corrosion. Under atmospheric conditions, aerosols containing salts such as NaCl and $MgCl_2$ can deposit on the metal surface. The salt particles can deliquesce and form salt droplets when the relative humidity (RH) increases, and when the chloride concentration in the droplet exceeds about 6 M, atmospheric pitting corrosion of stainless steel can take place [1].

This is a particular concern for the storage of intermediate level radioactive waste (ILW) in stainless steel containers in the UK [2-4]. They are planned to be stored above the ground for a period of a century during which time they will be exposed to atmospheric conditions. Thus it is essential to understand the mechanism of atmospheric pitting corrosion of stainless steel in order to determine the chloride deposition levels and relative humidity for safe storage of ILW.

The mechanism of pitting corrosion of stainless steel is well understood from previous studies [5, 6]. However, most of the previous work has been carried out under full immersion conditions [7], and relatively little has been carried out under atmospheric conditions.

In order to study the atmospheric pitting corrosion using lab based measurements, it is necessary to control the deposition of salt layer, and for this purpose, deposition techniques such as using a fine tube or a pipette to deposit salt droplets, or placing salt particles on metal surfaces are commonly used. In this project, it is shown that inkjet printing can be used to produce well-defined deposition patterns than those produced with droplets or particle deposition.

The evolution of the morphology of atmospheric corrosion pits has not been extensively studied owing to the difficulty of characterising pits in-situ under droplets. X-rays can penetrate liquid and metal, and are therefore a suitable probe. Synchrotron X-ray micro-tomography can be carried out with far shorter data acquisition times than lab-based measurements, and is particularly suitable for in-situ visualisation of corrosion behaviour.

Since real pits have complex geometry, one dimensional artificial pit methods have long been used to study the electrochemical kinetics of metal dissolution inside pits. In the present work, pit growth kinetics, including the Tafel slope, as well as the critical pit solution chemistry required for pit growth are obtained using 1D artificial pit electrodes, with particular emphasis on the highly concentrated chloride solutions since the environment is close to the real atmospheric conditions. For example, 6 M chloride concentration $MgCl_2$ solution corresponds to about 65% RH.

When the amount of dissolving metal ions in an artificial pit exceeds the saturation point, a salt layer can be formed at the dissolving interface. The salt layer is difficult to characterise since it is not static and can only be observed during the corrosion process. Synchrotron X-ray diffraction is a suitable method for investigating the structure and chemistry of the salt layer on 1D artificial pits in-situ and in real time: in this work, the formation of salt layers in concentrated solutions is investigated for the same reason as described above.

In the present study, an inkjet printing technique has been developed to study the effect of deposition levels, deposition areas and relative humidity on atmospheric pitting corrosion. The evolution of pit growth and electrolyte layer have been measured by synchrotron X-ray micro-tomography as well as estimation of pit growth kinetics. 1D artificial pits have been used to study the electrochemical characteristics in high chloride concentration solutions. The salt layer formation in high chloride concentration solution has been characterised by Synchrotron XRD.

2 Literature review

2.1 Stainless steel

Stainless steels are iron-chromium alloys that can form a passive chromium oxide film on the metal surface to resist corrosion [8-10]. There are four different types of stainless steel: austenitic, ferritic, martensitic, and duplex stainless steels. Austenitic stainless steel has a single austenitic phase, and it has been widely used in industry. The 300 series austenitic stainless steel has a typical composition of "18%Cr-8%Ni" [8-10].

Stainless steel 304 and 316 are the most common austenitic stainless steels. The difference of the chemical composition between Type 304 and Type 316 stainless steels is the presence of molybdenum. Commercial stainless steel 316 normally has 2%-3% molybdenum, which can improve its resistance to pitting corrosion.

2.2 Pitting corrosion of stainless steel

2.2.1 Introduction

Stainless steel is widely used as it has good corrosion resistance owing to the formation of a thin passive chromium oxide film on the surface that is resistant to dissolution and which reforms if the surface is damaged. However, stainless steel is susceptible to localised corrosion such as pitting corrosion and crevice corrosion when it is exposed to a corrosive environment, especially one containing chloride ions [8, 11].

Pitting corrosion is the most common form of localised corrosion. It normally initiates at a secondary phase, such as a MnS inclusion or an oxide particle, which dissolves to form a small pit. Metal dissolves to form metal ions (Equation 2-1), and metal ions can react with water to produce acidity inside the pit (Equation 2-2). The lower pH inside the pit destabilises the passive film and hinders repassivation [5]. In order to maintain charge balance, anions (typically chloride ions) diffuse into the pit. The pit is the net anode. During the metal dissolution process, electrons can transfer through the metal and react with oxygen dissolved in the electrolyte by the oxygen reduction reaction (Equation 2-3). Oxygen is depleted within the pit. The exterior surface where the oxygen reduction reaction takes place is the net cathode. The schematic diagram of the mechanism of pitting corrosion is shown in Figure 2-1.

$$Me \rightarrow Me^{n+} + ne^{-} \qquad \text{Equation 2-1}$$

$$Me^{n+} + H_2O \rightarrow MeOH^{(n-1)+} + H^{+} \qquad \text{Equation 2-2}$$

$$O_2 + 4e^{-} + 2H_2O \rightarrow 4OH^{-} \qquad \text{Equation 2-3}$$

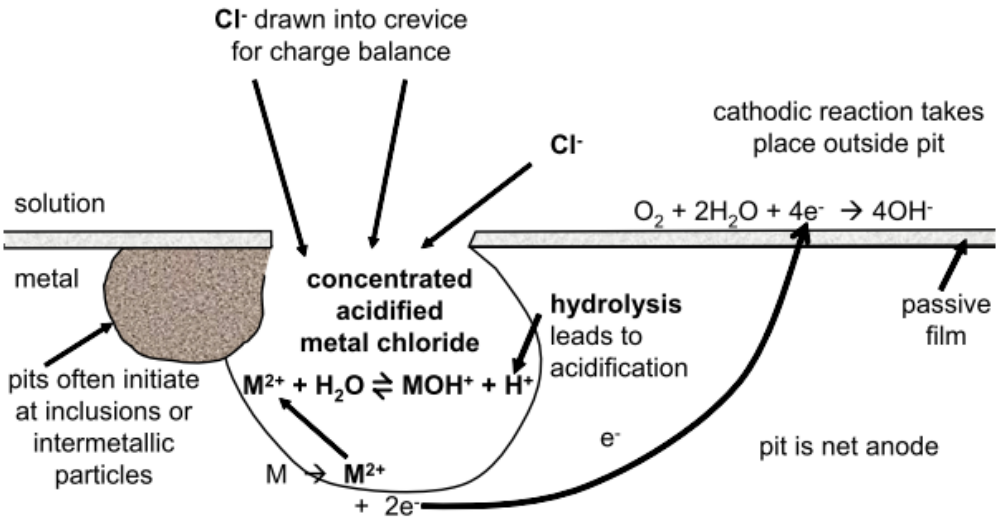

Figure 2-1 A schematic diagram of the mechanism of pitting corrosion [12].

Pitting corrosion is usually described by three stages: pit initiation, metastable pit growth and pit propagation (stable pit growth). The three stages are discussed in more detail in the following sections.

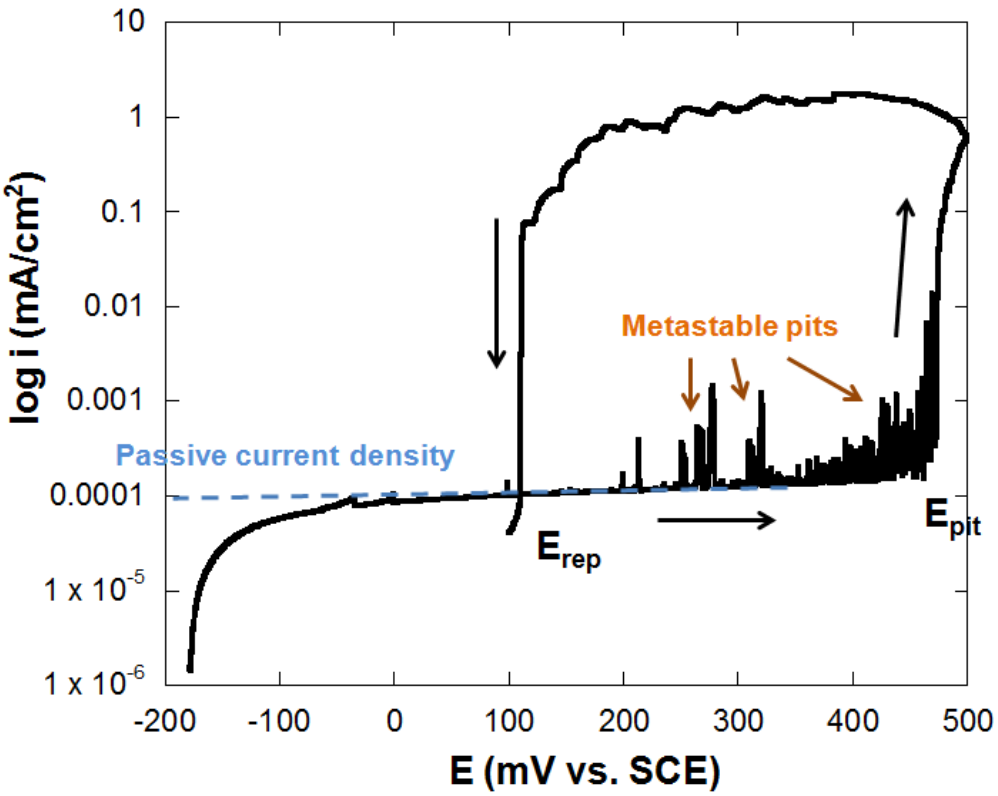

Figure 2-2 A schematic diagram of the polarisation curve of stainless steel in a neutral chloride solution. The pitting potential (E_{pit}), repassivation potential (E_{rep}), meta-stable pit growth and the passive current density are shown in the diagram.

The susceptibility of stainless steel to pitting corrosion can be determined by a polarisation curve as shown in Figure 2-2 [13]. The arrows show the direction of change of applied potential. The flat plateau of current density in Figure 2-2, which is independent of potential, is the passive current density. When the potential further increases, there is a local breakdown of the passive film leading to a sudden increase in current density at the pitting potential (E_{pit}), where a stable pit starts to propagate. When the potential is swept downwards, the current density decreases steeply at the repassivation potential (E_{rep}). The repassivation potential indicates that the pit has stopped propagating and has repassivated.

The basic mechanism of pitting corrosion is fairly well understood in conditions where stainless steel is fully immersed in the solution. However, there has been recent interest in atmospheric pitting corrosion of stainless steel [1, 14-19].

2.2.2 Pit initiation

Pit initiation has been widely studied. Frankel [5] has reviewed previous work in which it has been proposed that pit initiation is a result of passive film breakdown. Three main mechanisms have been proposed, as shown in Figure 2-3: (a) penetration mechanism, (b) adsorption mechanism, and (c) film breaking mechanism.

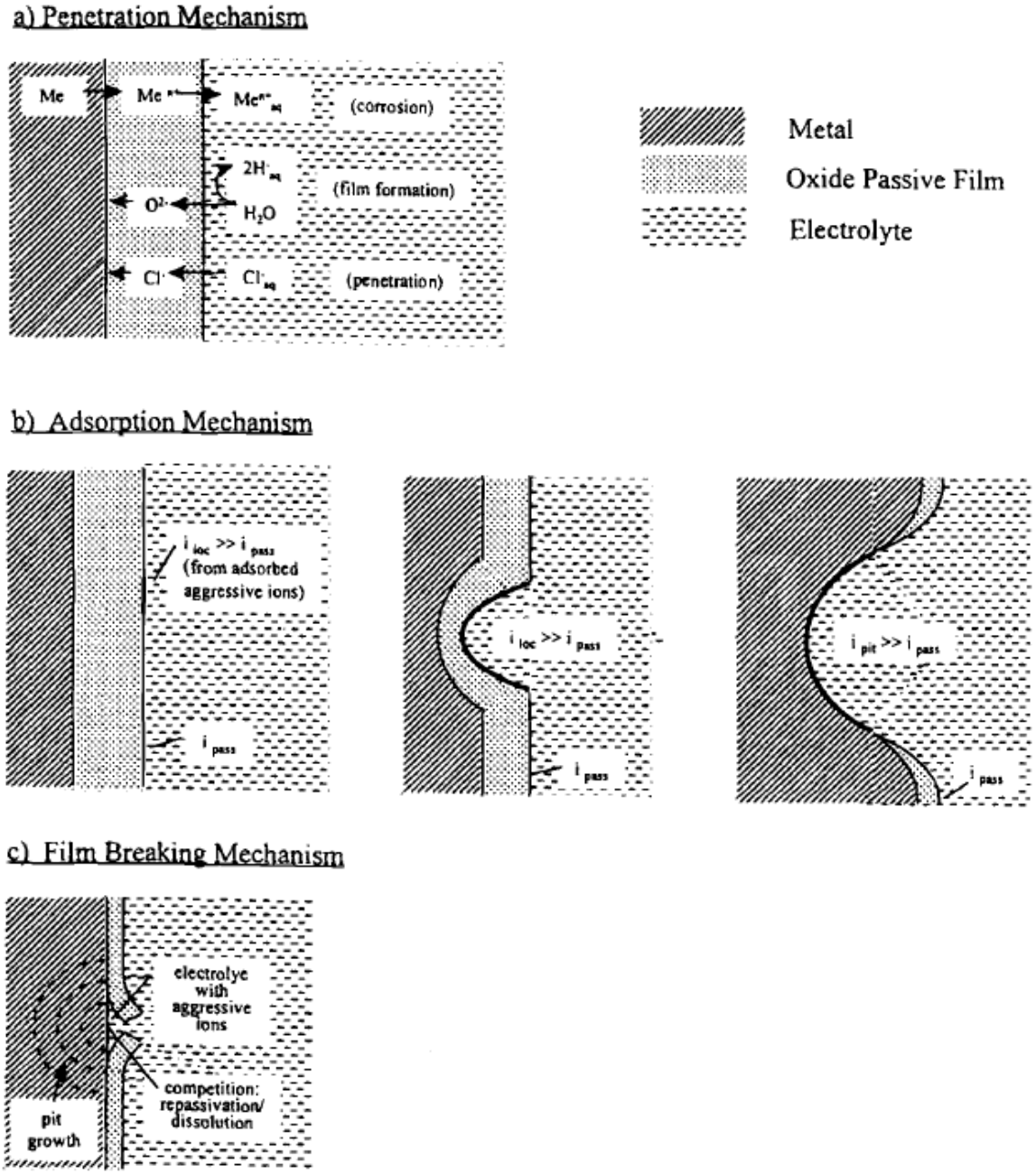

Figure 2-3 Schematic diagrams representing pit initiation by (a) penetration, (b) adsorption and thinning, and (c) film breaking [5].

However, pits in stainless steel mostly initiate at inclusions or secondary phase particles, rather than by film breakdown, and manganese sulphide (MnS) inclusions are reported to be the most important site for the pit initiation process [20-27]. It is generally agreed that the sulphide inclusions can lead to local disturbances in the passive oxide film since MnS is not stable in neutral environments containing chloride [21].

Different reactions have been proposed for the dissolution of MnS. Eklund [21] has applied a program developed by Ingri et al. [28] and calculated the Pourbaix diagram for MnS in chloride solution, suggesting that MnS dissolution proceeds as follows: MnS dissolves in the neutral chloride solution and forms Mn^{2+}, SO_4^{2-} ions and protons (Equation 2-4). The lower pH leads to the reaction shown in Equation 2-5. The H_2S can then be reduced to form sulphur and more H^+ ions (Equation 2-6) leading to sustained dissolution of MnS [20, 21].

$$MnS + 4H_2O = Mn^{2+} + SO_4^{2-} + 8H^+ + 8e^- \qquad \text{Equation 2-4}$$

$$MnS + 2H^+ = Mn^{2+} + H_2S \qquad \text{Equation 2-5}$$

$$H_2S = S + 2H^+ + 2e^- \qquad \text{Equation 2-6}$$

The formation of sulphur has also been demonstrated by Castle and Ke using Auger spectroscopy to study the dissolution of MnS inclusions [26]. It has also been reported that the S layer can decrease the strength of metal-metal bonds and increase the rate of the dissolution process [29] .

Webb and Alkire [23-25] proposed that MnS inclusions can dissolve and produce protons and thiosulphate ions as shown in Equation 2-7. The decreasing pH can further enhance the dissolution of stainless steel.

$$2MnS + 3H_2O = 2Mn^{2+} + S_2O_3^{2-} + 6H^+ + 8e^- \qquad \text{Equation 2-7}$$

Tsutsumi et al. [1] studied pitting corrosion of stainless steel under atmospheric corrosion conditions; and they proposed a similar mechanism to Webb and Alkire shown in Figure 2-4.

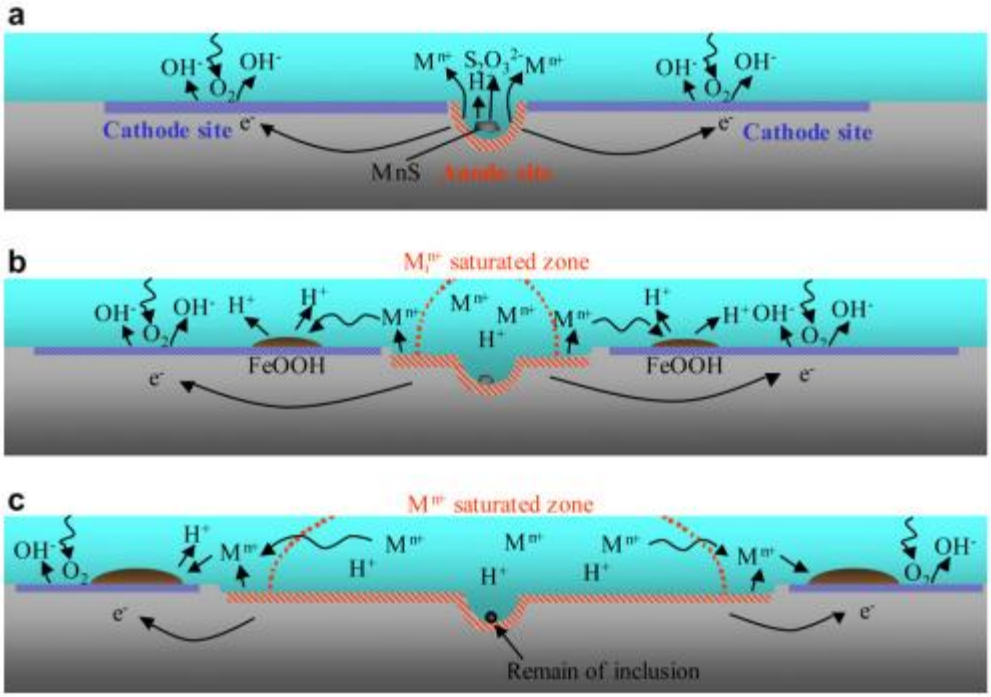

Figure 2-4 A schematic diagram of pit initiation and propagation at an MnS inclusion proposed by Tsutsumi et al. [1].

2.2.3 Pit propagation

It is generally agreed that pits can propagate when the potential of the metal surface is higher than the repassivation potential [30-32].

Pickering and Frankenthal studied the pitting corrosion of stainless steel with electrochemical methods and characterisation of pit morphologies [33, 34]. They developed a one-dimensional model of pit growth that involves metal dissolution and the potential drop in the pit cavity. Galvele [32] proposed a similar one-dimensional pitting corrosion model combining calculations of metal dissolution, metal ion hydrolysis and metal ion transportation by diffusion as shown in Figure 2-5.

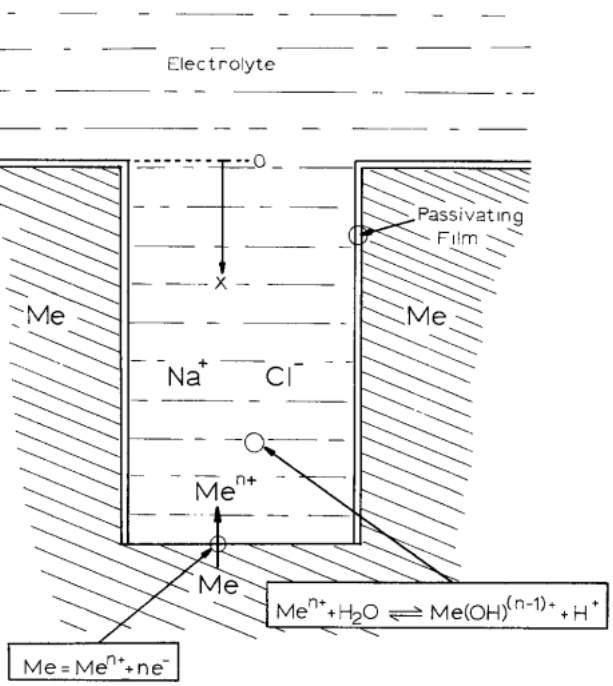

Figure 2-5 A schematic diagram of pit geometry of Galvele's model [32] for pit propagation. The pit is one dimensional since the dissolving surface is the pit bottom, and the walls of the pit are passive.

In Figure 2-5, it can be seen that the walls of the one dimensional pit are assumed to be passive, and the dissolving surface is the pit bottom, which dissolves according to Equation 2-8. The metal ions react with the water in the pit cavity and undergo a hydrolysis reaction (Equation 2-9). To consider that the hydrolysis reaction might lead to a pH difference with the bulk solution, the two equations can be rewritten as below:

$$Me = Me^{n+} + ne^{-} \qquad \text{Equation 2-8}$$

$$Me^{n+} + H_2O = Me(OH)^{(n-1)+} + H^{+} \qquad \text{Equation 2-9}$$

$$2Me^{n+} + H_2O + OH^{-} = 2Me(OH)^{(n-1)+} + H^{+} \qquad \text{Equation 2-10}$$

Then the concentrations of species such as Me^{n+}, $Me(OH)^{(n-1)+}$ and H^{+} shown in Equation 2-10 can be solved by five equations based on the balance of fluxes of metal ion species, balance of net fluxes of species containing O atoms and H atoms, the equilibrium of the hydrolysis reaction and the equilibrium of the ionic product of water.

Galvele proposed a critical value of *ix* for stable pit growth, where the *i* is the current density and the *x* is the pit depth. The value of *ix* has been termed the 'pit stability product' in subsequent literature [30, 35]. After solving the five equations, the concentration of Me^{n+}, $Me(OH)^{(n-1)+}$, H^+ can be plotted with respect to the *ix* product as shown in Figure 2-6. It is possible to calculate the *ix* product from this plot with any sufficient concentration of Me^{n+}. It can be seen that in Figure 2-6 Galvele assumed that a relatively low metal ion concentration was required to sustain the required current density compared with the more recent findings which have shown that molar concentrations of metal ions are required for pit propagation [30, 36, 37].

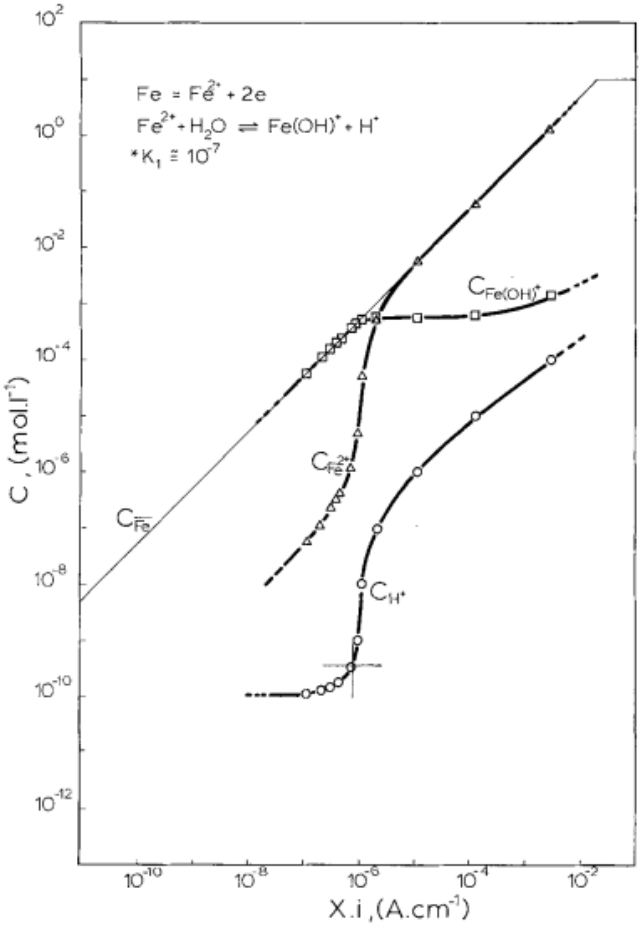

Figure 2-6 A plot of the concentration of Fe^{2+}, $Fe(OH)^+$, and H^+ as a function of the *i·x* product in a unidirectional pit [32].

Galvele's model was published in 1976 and his subsequent papers [32, 38] also demonstrate the dependence of pitting potential on the pH and anion concentration. One of his key statements concerns the dependence of pitting potential on chloride concentration in NaCl

solution as shown in Equation 2-11, where C_{NaCl} is the concentration of the bulk NaCl solution.

$$E_{pit} = A - B\log C_{NaCl} \qquad \text{Equation 2-11}$$

Galvele reported that the dependence of the pitting potential on the chloride concentration *B* is mainly due to the *IR* drop in the pit, which is about 59 mV/decade based on three assumptions that have been summarised by Newman [30]: the pit solution chemistry at the bottom of the pit should be the same at the pitting potential; the chloride is a non-reacting species; and compared with the *IR* drop of the pit solution, the *IR* drop in the solution outside the pit is negligible. Laycock et al. have questioned these assumptions for more concentrated chloride bulk solutions [39]. In the following studies, *B* has been derived from experimental results. Newman et al. found that *B* is about 60 mV for iron and about 90 mV for stainless steel 302 [40]. Laycock and Newman reported B is 93 mV/decade of stainless steel 302 for 120 grit surface finishes, and 100 mV for 1200 grit surface finishes [31].

Galvele's work on the pit stability product has further influenced Pistorius and Burstein's work [35]. They reported that the growth of metastable pits is associated with the pit stability product as discussed below.

2.2.4 Metastable pits

Metastable pits initiate and grow below the pitting potential, but they cannot propagate for an indefinite period and therefore repassivate fairly soon [31, 35, 41]. It is found that to sustain the acidic and aggressive pit solution for stable pit growth, a pit cover is essential, acting as a diffusion barrier to sustain the pit solution [35, 42, 43] or a resistive layer to control the growth [41]. Frankel and his co-workers suggested that the cover works as a resistive layer providing a high ohmic drop. If the cover ruptures forming an open pit mouth, a metastable pit would repassivate unless a salt film is formed at the pit surface so that the pit growth is stabilised [41]. Burstein and his co-workers reported when the pit growth is stable, then the cover is no longer required and can collapse to form an open pit, because the pit depth can supply a sufficient diffusion barrier [35, 42, 43].

Pistorius and Burstein [35] used a similar approach based on Frankel et al.'s work [41] to measure the current density of metastable pit growth when the potential is below the pitting potential. They integrated the current transients and assumed the pit has a hemispherical

geometry, and hence were able to establish the current transient as a function of pit radius. They reported that the pit stability product is between 0.3 A/m and 0.6 A/m, which is close to Frankel's finding of 0.4 A/m [41] and Williams' finding of 0.6 A/m [44]. Pistorius and Burstein indicated that the pit growth can be stabilised when the pit stability product exceeds 0.3 A/m, and the perforated cover is no longer needed.

2.2.5 Solution chemistry of pits in stainless steel and salt layer

The pit solution chemistry of stainless steel has been studied by various researchers. Hoar found that the pit solution is acidified [45]. Mankowski and Szklarska-Smialowska [46], and Wilde and Williams [47] measured the pH of pit solutions. Wilde and Williams reported that a low pH is developed in pit cavity which is associated with high ferrous ion concentration [47]. Mankowski and Szklarska-Smialowska reported that the pH can be below zero depending on the chloride concentration within the pit [46]. Suzuki et al. [48] extracted the pit solution and measured the solution species by atomic absorption spectroscopy. They have found the dissolved species are Fe^{2+}, Cr^{3+}, Ni^{2+}, which have been confirmed by other researchers [49-51].

Isaacs et al. [52] have applied in-situ X-ray fluorescence to measure the concentration of species in a pit. They reported that the total metal ion concentration at the bottom of a pit is about 5 M, comprising 3.5 M Fe, 1.1 M Cr and 0.5 M Ni. The pit solution contains more than 11 M chloride ions. This calculation has not taken into account the solubility of metal chlorides or the formation of metal chloride complexes. Sridhar and Dunn [53] and Brossia et al. [54] used Raman spectroscopy to study the pit solution chemistry. They showed that the Cr-Cl complexes existed in the pit/crevice solution of stainless steel. Davenport et al. [55] studied the oxidation state of Mo in pit solutions in in-situ 1D pits using X-ray spectroscopy. Monir [56] found that the chloro-complexes of Fe and Cr, Fe and Cr hexa-aquo ions, and Ni hexa-aquo ions were present within the pit solution by in-situ X-ray spectroscopy. He reported that chloro-complexes of Fe and Cr are found close to the metal dissolving interface due to the high chloride concentration, and that Fe and Cr hexa-aquo ions are found at the pit mouth. The Ni hexa-aquo ion is found throughout the pit solution.

2.3 One dimensional artificial pit

Real pits have a complex geometry. Artificial pits can provide one dimensional geometry which allows examination of the electrochemistry of pits including the effect of resistance and

diffusion [57-59]. The most commonly used artificial pit electrode is also called a 'lead-in-pencil' electrode [31, 32]. Such a 1D artificial pit electrode consists of a piece of metal wire or metal foil mounted in insulating epoxy resin as shown in Figure 2-7. When metal dissolves, it forms a uniform one dimensional cavity that can be used to simulate the dissolution kinetics in a real pit. The possibility of forming multiple pits is avoided as the pit active surface can be monitored and controlled. The 1D artificial pit has also been extensively used to study the mass transport, pit solution chemistry and salt film formation within pits [31, 36, 59-63].

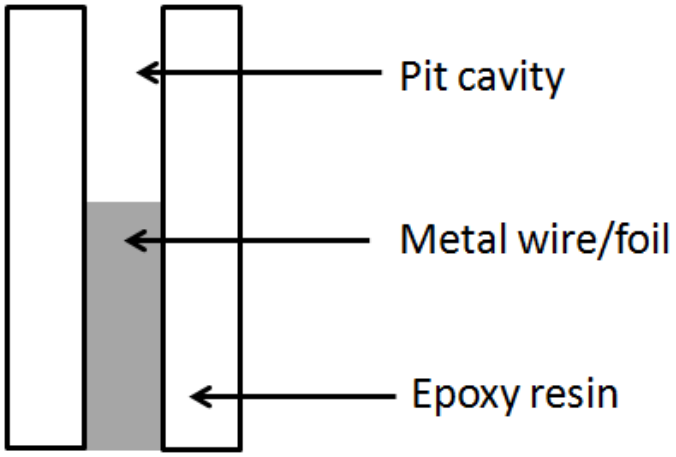

Figure 2-7 A schematic diagram of 1D artificial pit.

2.3.1 Salt film

As described in Section 2.2.4, Frankel et al. reported that a metastable pit can repassivate unless a salt film is formed at the pit surface so that the pit growth is stabilised [41]. The film is not static and is only observed during the corrosion process. Hoar et al. [64] reported that the film dissolves as fast as it forms. A range of papers have been published on investigations of the structure, composition and mechanism of the salt film.

2.3.1.1 Structure

Vetter and Strehblow [65] reported the formation of a salt film at the bottom of a pit, and stated that the film is not porous. Isaacs [66] used an artificial pit electrode to study the pitting corrosion of stainless steel in chloride solutions, and showed that a resistive layer existed at the electrode interface. He also reported this layer is about 10 nm thick and has a resistivity of approximately 10^8 Ω·cm. Beck has supported the assumption that the salt film is a halide barrier layer, but also suggested there might be a hydrated outer layer that allows water to

pass through [67, 68]. Danielson has investigated the formation of salt film of Ni in 0.5 M HCl by stepped potential and impedance methods, and claimed that the salt film contains a small number of pores [69]. Landolt and his co-workers [70-72] have suggested a model of duplex salt film formation on Ni [70], iron [72] and Fe-Cr alloys [71] based on AC impedance measurements. In Landolt and his co-workers' model, the salt film has a duplex structure as shown in Figure 2-8, which includes an inner compact anhydrous layer with high field conduction, and an outer porous hydrated layer with low field conduction.

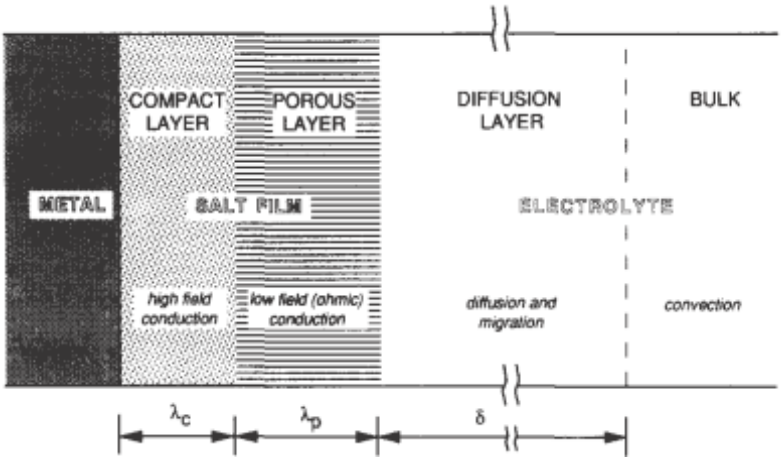

Figure 2-8 A schematic diagram of duplex salt film according to Landolt and his co-workers' model. The salt film includes an inner compact layer with high field conduction and an outer porous layer with low field conduction [71].

2.3.1.2 Composition

As described above, Isaacs et al. [52] used in-situ X-ray fluorescence to analyse the concentration of metal ions in stainless steel artificial pits. They reported that the salt film on stainless steel 1D artificial pit contains a very high amount of iron and small amounts of nickel and chromium. However, the fluorescence technique cannot directly detect the presence of the salt film. In order to obtain the species information of both the precipitated salt film and the dissolved metal ions, Sridhar and Dunn [53] used Raman spectroscopy to characterise the salt film on Ni 1D artificial pits. They detected a $NiCl_2 \cdot 6H_2O$ salt film in the artificial pit and the salt film data could be distinguished from the dissolved metal ion species. Recently, Rayment et al. [73] used in-situ synchrotron X-ray diffraction to characterise the salt film structure on Ni, iron and stainless steel 316 1D artificial pits in 1 M HCl. They found that $NiCl_2 \cdot 6H_2O$ is the dominant phase in the salt film on Ni and $FeCl_2 \cdot 4H_2O$ is the dominant phase on both iron and stainless steel 316.

2.3.1.3 Self -regulating mechanism

Novakovski and Sorokina [74] reported that the dissolution rate of metal decreases linearly with the reciprocal of the pit depth, which indicated that the pit current density is self-regulated by diffusion or migration factors. An assumption was made that precipitation of salt film present on the bottom of the pit can be self-regulated. When a potential is greater than the potential of the salt film crystallisation supported by migration and diffusion, the film can grow thicker automatically to consume the excess potential drop, and maintain the current at the steady state value.

Isaacs [66] used the 1D artificial pit electrode to show that there is a resistive layer formed on the electrode interface which self regulates its thickness when the applied potential is changed. Isaacs reported that the current is independent of potential due to the presence of the layer, and indicated that the transport rate of the metal ions from across this layer to pit solution is equivalent to the diffusion rate of metal ions from the layer.

A further study was carried out by Tester and Isaacs [61] to investigate diffusion effects in simulated pitting corrosion. The equation for the anodic current density at the steady state is given by the Nernst-Einstein equation as shown in Equation 2-12, assuming that convection is negligible:

$$\frac{i}{nF} = -D\left[\frac{\partial C}{\partial x} + C\frac{nF}{RT}D\frac{\partial \Phi}{\partial x}\right] \qquad \text{Equation 2-12}$$

where i is the anodic current density, n is the number of electrons produced in metal dissolution, F is the Faraday constant (96500 C/mol), R is the gas constant, T is the temperature, Φ is the potential drop in solution, and x is the pit depth. If only the diffusion part in the equation is considered and the potential drop in solution is ignored, the equation can be simplified to Equation 2-13 for a diffusion-limited current density (i_{lim}).

$$i_{\lim} = \frac{nFD\Delta C}{x} \qquad \text{Equation 2-13}$$

2.3.2 Current-voltage characteristics of artificial pits

Cyclic voltammetry is one of the most common measurements made on artificial pit electrodes. Figure 2-9 shows a schematic diagram of the current-voltage curve which is characteristic of artificial pits. It starts from the salt free region A and B. The current increases with the potential and is under the activation/ohmic drop control. The metal dissolution rate increases as the current increases. From the region B to C, the production rate of metal ions exceeds the diffusion rate of metal ions to escape the pit cavity. Therefore, supersaturation of the metal ions occurs at the dissolving interface and a salt film precipitates at the metal dissolution interface [31]. The salt film is highly resistive [66, 74], which leads a sudden drop of current as shown in the D region in Figure 2-9. The drop of current causes the thickness of the salt film to decrease, but since the potential then increases, the salt film thickens and the current reaches a steady state in region E, where there is a diffusion-limited current (I_{lim}). The diffusion-limited current is independent of potential, and is under mass-transport control.

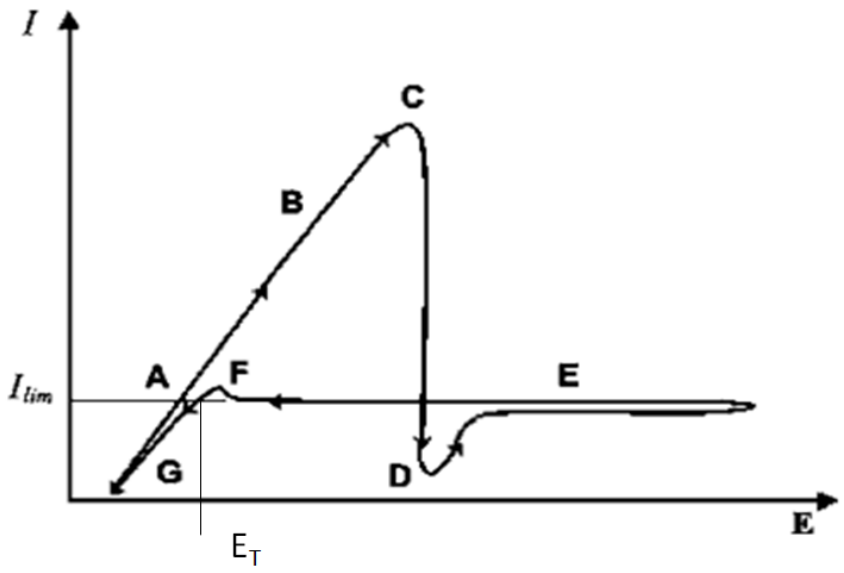

Figure 2-9 Current-voltage characteristics of artificial pits [58].

On the reverse potential sweep, the salt film thins with decreasing potential. In the region F, the salt film is fully dissolved. The transition potential (E_T) is defined as the potential in the salt-film free region at which the electrode is the diffusion-limited current is passing [31]. In the salt film free region G, the dissolution process is again activation/ohmic drop controlled.

2.3.3 Critical pit solution concentration

Gaudet et al. [36] have used the 1D artificial pit method to study the pitting corrosion on stainless steel 304 and high nickel alloy 600 with coupling of the rates of mass transfer and electrochemical reaction. They generated plots of current density vs. surface metal ion concentration as shown in Figure 2-10. In Figure 2-10 (a), the line GA represents the diffusion-limited current density based on Fick's first law. GHIB and GB' represent two theoretical plots of current density vs. surface concentration at different applied potentials. When the potential decreases, the diffusion-limited current density A can drop to either B or B' depending on the applied potential. The curve GHIB represents the rate of surface reaction when the applied potential is relatively high, and the curve GB' represents the low potential condition.

When the potential is relatively low, Figure 2-10 (a) shows that the surface reaction rate of line B'G is lower than the rate of diffusion GA, thus the current density would drop to zero and the metal would repassivate. When the potential is high enough, there are crossing points (G, H and I) of the line GHIB with the linear diffusion flux line, which represent points at which the dissolution rate equals the diffusion rate. These points are predicted to be steady states.

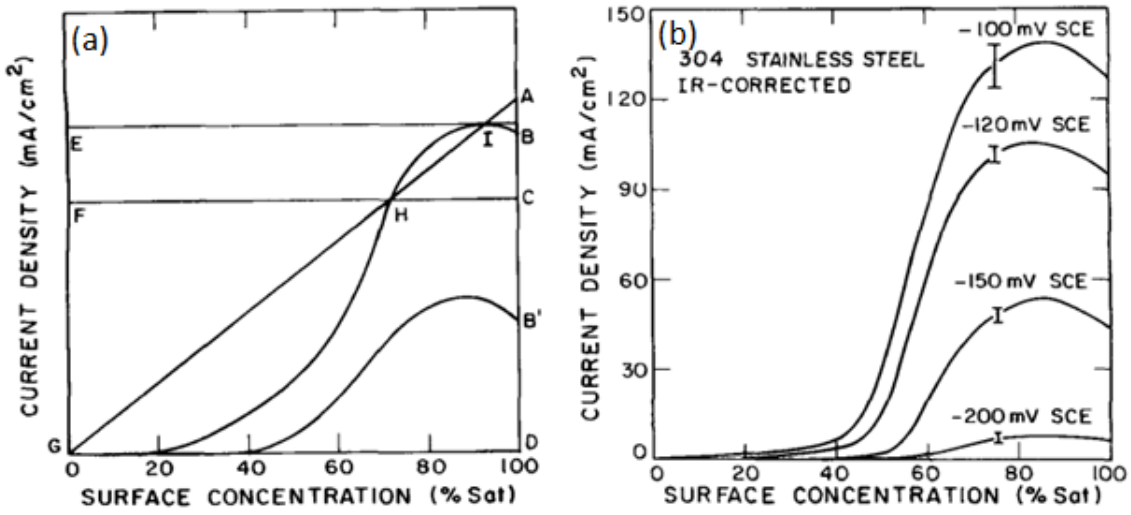

Figure 2-10 (a) theoretical prediction of current density vs. surface concentration of multiple states presented by letters A-H as described in the text (b) reaction rates vs. surface concentration at different applied potentials on stainless steel 1D artificial pits [36].

Figure 2-10 (b) shows the experimental results of the surface reaction rates obtained at different applied potentials with IR correction. Gaudet et al. [36] reported that a pit can only propagate when the surface concentration is higher than a critical metal ion concentration (C_{crit}) which is about 60%-70% of the saturation (C_{sat}). A pit will repassivate if the surface concentration is lower than the C_{crit}. Hakkarainen [75, 76] reported that C_{crit} needs to above 80% of the C_{sat} to maintain the metal dissolution on stainless steel 304 and 316.

Similar studies on measuring the critical metal ion concentration were carried out by Steinsmo and Isaacs for Fe-Cr alloys [59]. They found that C_{crit} increases with increasing Cr content. For example, the critical metal ion concentration is about 10% of saturation on Fe-11.6Cr, which is much lower than 32 and 36% of saturation on Fe-17.4Cr and Fe-24.3Cr. Enerhaug et al. reported 30% of saturation of the surface concentration is needed for pit growth on martensitic stainless steel [63]. Ernst and Newman investigated the behaviour of stainless steel 316 in high chloride concentration NaCl and $CaCl_2$ solution [77]. The ratio of C_{crit} to C_{sat} was observed to decrease steeply when the chloride concentration increases, as shown in Figure 2-11. The ratio C_{crit}/C_{sat} can drop to about 10% in solutions with more than 6 M $CaCl_2$ solution. Laycock et al. have assumed that there might be a similar change on stainless steel 304, and possibly a more steep decrease [39].

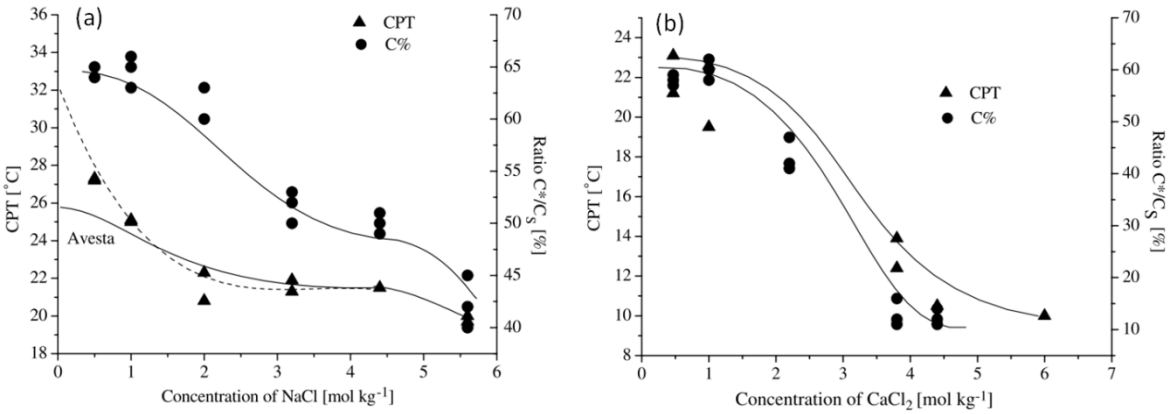

Figure 2-11 Dependence of the critical pitting temperature (CPT) and the C^*/C_s ratio on the bulk concentrations of NaCl and $CaCl_2$ on stainless steel 316L. C^* is the critical metal ion concentration and C_s is the saturated metal ion concentration, the C^*/C_s values are measured at 30 °C [77].

2.3.4 Tafel slope

The dissolution kinetics of 1D pit growth can be described by Equation 2-14 [37] in which the applied potential (E_{app}) is a sum of the activation potential and ohmic drop.

$$E_{app} = E_{corr} + b_a \log\left(\frac{i_a}{i_{corr}}\right) + \phi_s + \phi_{sf} \qquad \text{Equation 2-14}$$

where E_{corr} and i_{corr} are the open-circuit corrosion potential and current density, i_a is the anodic current density, b_a is the anodic Tafel slope, ϕ_s is solution resistance and ϕ_{sf} is the salt film resistance. The E_{corr} and i_{corr} are assumed to be constant, thus the Tafel slope b_a can be obtained by plotting the *IR* corrected potential vs. the anodic current density.

Newman and Isaacs [62] measured the anodic dissolution kinetics under conditions near-saturation at the pit interface. The Tafel slope was obtained by plotting the log current density vs. *IR*-corrected potential. They reported that the Tafel slope of Fe-19Cr-10Ni alloy is about 60 mV/decade when the potential is higher than -300 mV, and is about 75 mV/decade when the potential is lower than -300 mV as shown in Figure 2-12. It is possible that when the potential decreases, the interface chemistry changes which leads to a change in the dissolution kinetics.

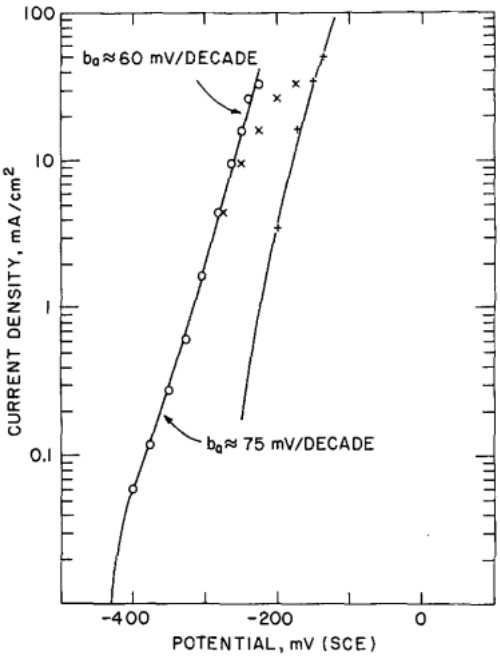

Figure 2-12 Anodic dissolution kinetics measured by plotting log current density vs. *IR*-corrected potential on Fe-19Cr-10Ni alloy [62].

Gaudet et al. [36] measured the Tafel slope with 1D artificial pit electrode, and reported a value of 54 mV/decade. The Tafel slope was measured at the supersaturation condition at the pit interface by plotting the *IR*-corrected potential and current density.

Gaudet et al.'s method was used in Steinsmo and Isaacs's work [78], and Enerhaug et al.'s work [63]. The Tafel slope measured by Steinsmo and Isaacs is about 108 mV/decade on Fe-Cr alloys, which is much higher than the Tafel slope measured for alloys containing Ni content [78]. Enerhaug et al. reported the Tafel slope of 57 mV/decade for martensitic stainless steel [63].

Laycock and Newman [31] also used a 1D artificial pit electrode and obtained the anodic dissolution kinetics by plotting the *IR*-corrected transition potential (E_T) vs. diffusion-limited current density as shown in Figure 2-13. They reported the average Tafel slope (b_a) of 110 mV/decade for stainless steel 302 in 1 M NaCl solution, which is much higher than the values shown above. It has been noticed that the *IR*-corrected transition potential used in their work was only the potential drop out of the pit, but the potential drop within the pit cavity can also have an effect.

Table 2-1 shows the Tafel slope measured in the previous works described above. It can be seen that different methods of measuring the Tafel slope might use different interface chemistry which in turn might lead to very different results.

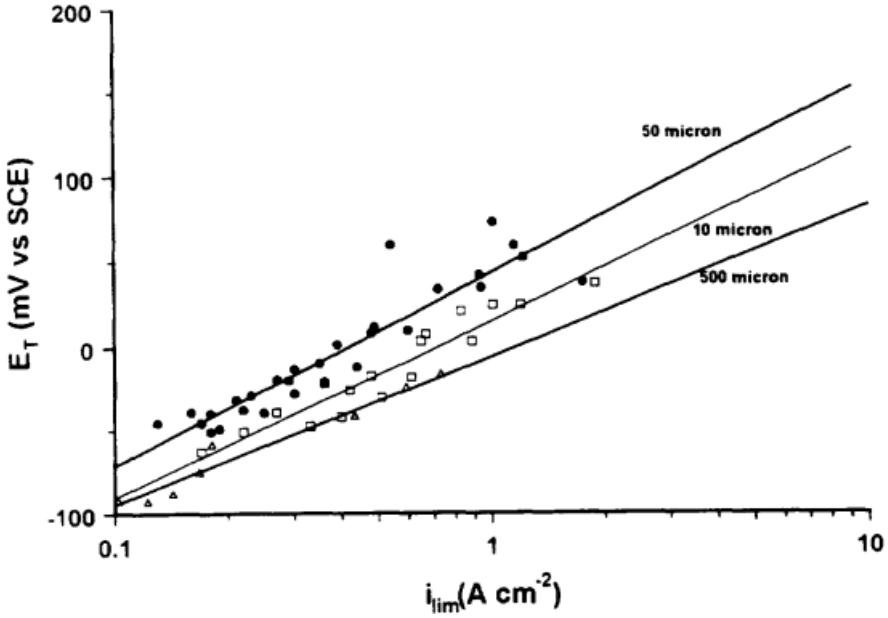

Figure 2-13 Anodic dissolution kinetics measured by plotting *IR*-corrected transition potential (E_T) vs. diffusion limited current density (i_{lim}) for 10, 50 and 500 μm diameter artificial pits of stainless steel 302 in 1 M NaCl solution. The transition potential excludes the potential drop outside the pit from the experimental results [31].

Table 2-1 Tafel slope measured in literature.

Author	Tafel slope (mV/decade)	Materials	Interface chemistry	Reference
Newman and Isaacs	about 60	Fe-19Cr-10Ni alloy	Near satuaration	[62]
Gaudet et al.	54	Stainless steel 304	Supersaturation	[36]
Steinsmo and Isaacs	108	Fe-Cr alloy	Supersaturation	[59]
Enerhaug et al.	57	Matensitic stainless steel	Supersaturation	[63]
Laycock and Newman	110	Stainless steel 302	Saturation	[31]

2.4 Atmospheric pitting corrosion of stainless steel

Pitting corrosion of stainless steel has generally been studied in bulk solutions under full immersion conditions. However, in many practical real applications, for example, on external surfaces of pipework or architectural applications, corrosion takes place under atmospheric conditions with a limited volume of electrolyte. This is a particular concern for the stainless steel containers for intermediate radioactive waste storage since they are planned to be stored above the ground and will be exposed in atmospheric conditions [2, 7, 79].

Under atmospheric conditions, aerosols (e.g. NaCl, $MgCl_2$ etc.) can deposit on a surface. When the relative humidity (RH) increases, these aerosol particles can deliquesce and form salt droplets or thin electrolyte layers. The concentration of the salt droplets or thin electrolyte layers is controlled by the ambient relative humidity via the equilibrium between the gaseous phase and the liquid phase. Figure 2-14 shows a plot of the relative humidity in equilibrium with a range of magnesium chloride concentrations at 300 K [1]. Stainless steels are corrosion resistant alloys, but are susceptible to atmospheric pitting corrosion, when the chloride concentration of the deliquesced droplet exceeds about 6 M, which is equivalent to about 65% RH [1, 80].

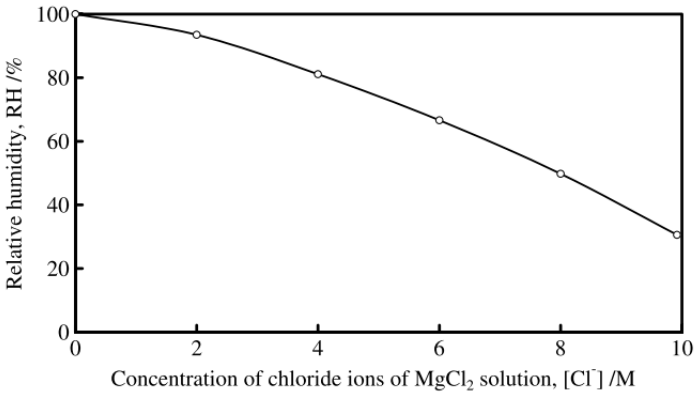

Figure 2-14 Relative humidity of gas phase in equilibrium with a range of chloride concentrations of $MgCl_2$ solutions at 300 K [1].

It is well known that atmospheric aerosols are composed of a variety of salts such as NaCl, $MgCl_2 \cdot 6H_2O$, KCl, $CaCl_2 \cdot 6H_2O$, and $NaNO_3$. The deliquescence point of NaCl is 75% RH, $MgCl_2 \cdot 6H_2O$ is 33% RH, KCl is 84% RH, $CaCl_2 \cdot 6H_2O$ is 29% RH, and $NaNO_3$ is 74% RH at 25 °C [81].

Compared with the extensive literature on the pitting corrosion of stainless steel under full immersion conditions, there is relatively little published work on the pitting corrosion of stainless steel under atmospheric conditions [7].

2.4.1 Deposition of salts for lab-based atmospheric corrosion experiments

In order to study atmospheric pitting corrosion, outdoor exposure experiments and indoor lab exposure experiments have been carried out. For the outdoor exposure experiments, samples are placed at specific positions and exposed to marine environments for a period of time [82]. Airborne salinity can accumulate on the sample surfaces, which leads to atmospheric pitting corrosion. Indoor lab exposure measurements are more common in the literature, since it is possible to deposit controlled quantities of wet salinity on metal surfaces for analysis [83-86].

2.4.1.1 Deposition of salt droplet or particles

There are a range of salt deposition methods for lab exposure measurements. The two most common methods are deposition of salt particles [83, 84, 87-91] and deposition of droplets of salt solution on the sample surface [1, 14, 16, 92, 93].

Clusters of deliquescent salt particles can be deposited on samples by a variety of methods: a probe can be used to select salt particles with a certain range of size then placed them on sample surfaces [83]; The sample may be placed in a mist of salt solution produced by an ultrasonic humidifier [90]; Salt may be dissolved in ethanol and placed as drops on the sample surface which are then dried out to form clusters of salt particles [87-89]. In all of these methods, the sample is subsequently placed in a humid environment to deliquesce the salt crystals, forming droplets.

Direct deposition of droplets of aqueous salt solution has usually involved the use of a fine tube or pipette to transfer a controlled volume and known concentration of salt solution to a metal surface [1, 14, 16, 18, 92, 93]. Some empirical relationships between the droplet volume and diameter have been determined from experiments [1, 16], or from theoretical estimation [18].

However, with all these methods it is difficult to produce well-defined and reproducible patterns on metal surfaces. In the present work, it is shown that inkjet printing can be used to

produce well-defined salt deposits on metal surfaces, allowing systematic study of the effects of salt density on atmospheric corrosion.

2.4.1.2 Inkjet printing technique and its application on corrosion

In the last few years, inkjet technology has been developed to print functional materials, and become a useful tool for a range of fabrication process [94-96], including printing polymers [96, 97], sol-gel materials [98] and nano-particles [99, 100].

In a recent preliminary study, Schindelholz and Kelly have demonstrated the feasibility of using inkjet printing to deposit salt layers on metal surfaces [17] as shown in Figure 2-15. NaCl particles were loaded with density ranged from 10 to 180 μgcm^{-2}, and shown to produce multimodal size distribution. The inkjet printing technique has not previously been used to deposit salt patterns on a metal surface in order to observe the atmospheric pitting corrosion behaviour.

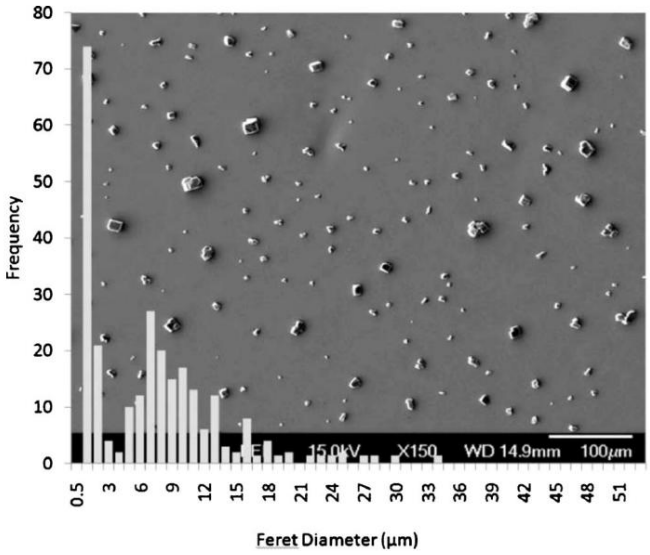

Figure 2-15 A histogram of measured particle sizes for the 1 M, 40% opacity prints overlaid on an SEM image of a typical particle field resulting from these prints [17].

2.4.2 Electrochemical measurements

As described above, one of the differences between atmospheric corrosion and full immersion corrosion is the volume of electrolyte. It is more difficult to use the electrochemical methods to study atmospheric pitting corrosion in a limited volume of electrolyte layer.

Tsuru, Nishikata and their co-workers [101-104] developed a range of electrochemical approaches to study atmospheric pitting corrosion. For example, they used a three-electrode electrochemical cell to measure corrosion rates by electrochemical impedance spectroscopy with humidity control [101, 103].They also developed a method which can combine the AC impedance method and corrosion potential measurements to monitor the corrosion potentials and corrosion rates at the same time.

Frankel et al. [105] used a Kelvin Probe potentiostat method developed by Stratmann and his co-workers [106, 107] to study the atmospheric pitting corrosion. They found that there is a sharp drop of open circuit potential which indicates the pit initiation.

2.4.3 Lab exposure measurements

There have been many studies published of atmospheric pitting corrosion produced by depositing an amount of salt on sample surfaces and then observing the pitting corrosion characteristic after a certain time of laboratory exposure with controlled parameters.

Tsutsumi et al. [1] deposited a range of salt droplets on stainless steel 304 surfaces and left the samples in controlled relative humidity for a certain time. The pit morphology and the composition distribution of the sample surface were analysed afterwards by SEM/EPMA. Figure 2-16 shows one typical pit and its depth profile. At least one small hole about 10-30 μm was always found in the centre of the corroded area, and was indicated as the vestige of an MnS inclusion. There was always a ring outside the corroded area where rust was deposited. Hastuty et al. [16] used a similar method to study the atmospheric pitting corrosion characteristics of stainless steel 430.

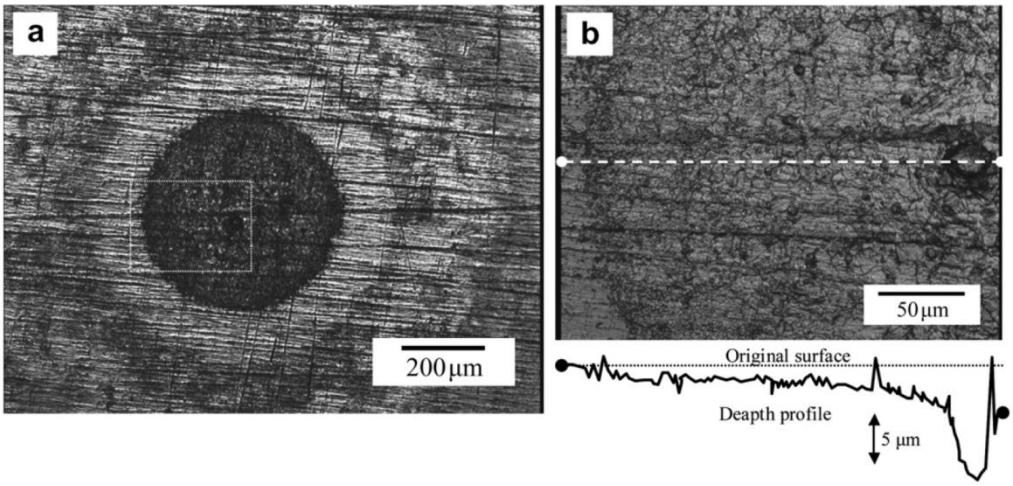

Figure 2-16 Laser-microphotograph and depth profile of pitting corrosion under a $MgCl_2$ droplet at 35% RH. The diameter of the droplet is 12 mm and the thickness is 1.9 µm [1].

Maier and Frankel [18] measured the potential drop of the sample and the thickness of droplets by Scanning Kelvin Probe. They used SEM and a profilometer to measure the pit morphology and pit depth profile as shown in Figure 2-17. The morphology of the pits was observed to be a dished shape after a certain time. Maier and Frankel also observed an ear-shaped region on the pit as shown in Figure 2-18. They assumed this region was the only active region of the pit when the anodic current demand exceeds the maximum cathodic current.

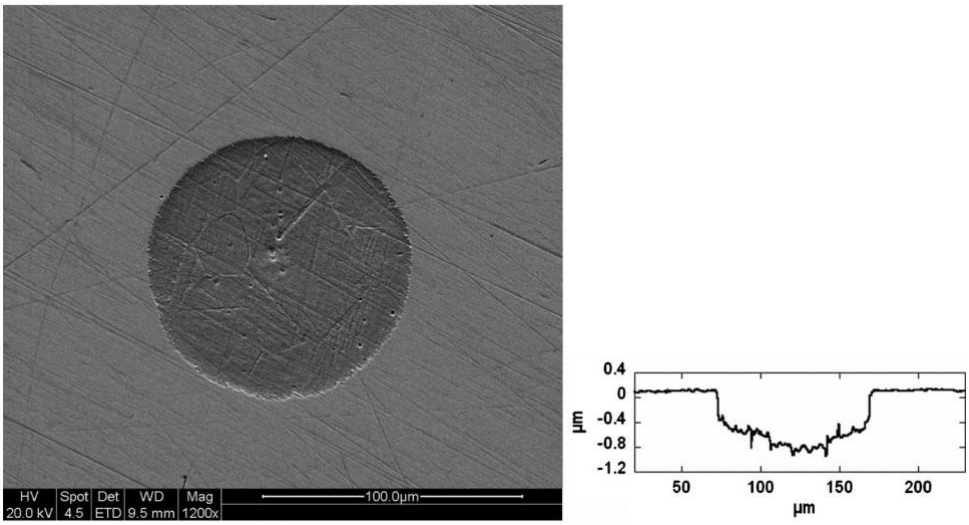

Figure 2-17 SEM image and corresponding profilometer depth profile of pit growing for 38.7 minutes [18].

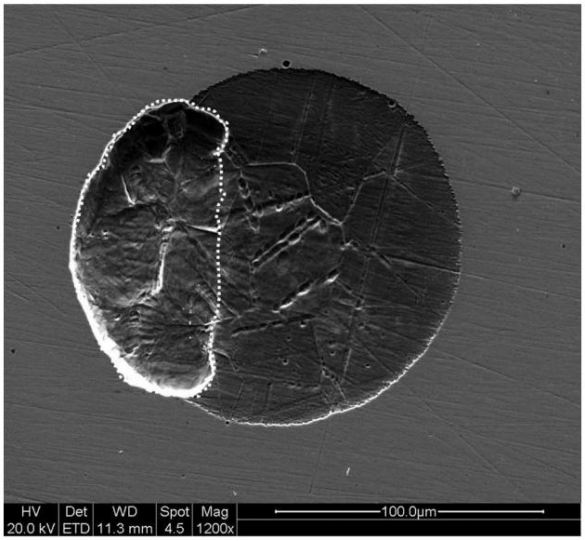

Figure 2-18 The SEM image of a pit exposed in atmospheric conditions. The white dashed line is defined as active pit area according to Maier and Frankel [18].

Maier and Frankel [18] also used the volumes of the pits and active pit surface area measured by profilometer to calculate the average current density of pit. Initially the whole pit surface area was assumed to be active, but if an earing-effect took place as described above, the active area was only considered to be the pit. They reported the current density was stabilised at about 0.6 mA/cm^2 after exposure for a certain time, which is much lower than the current density measured on pits in immersed conditions with electrochemical control.

The studies of atmospheric pitting corrosion described above were not carried out in-situ and were not able to characterise the evolution of pit growth with time.

2.4.4 Effects of exposure conditions

Exposure conditions such as chloride deposition levels and relative humidity can affect the atmospheric pitting corrosion of stainless steel. Matsumi et al. [80] reported that there is a critical chloride concentration of 6 M below which a pit cannot initiate. They used an electrochemical method to monitor the corrosion potential under an electrolyte layer and reported that a pit can initiate in chloride solution above 6 M on stainless steel 304 at 298 K. Tsutsumi et al. [108] exposed stainless steel samples in rural atmospheres and reported that pitting corrosion process only took place when the relative humidity is between 35% to 75% on 304 stainless steel. In subsequent work by Tsutsumi et al. [1], they measured the probability of occurrence of pitting corrosion under droplets in lab, and reported there is a

critical relative humidity for pitting corrosion to take place, which is between 55% (corresponding to about 8.4 M chloride solution) and 75% (corresponding to about 4.9 M chloride solution) for stainless steel 304 at 300 K.

Tsutsumi et al. [1] also reported that the probability of occurrence of pitting corrosion increases with increasing droplet diameter, which is attributed to a larger cathodic area. Maier and Frankel [18] showed that the initiation time for pitting corrosion is shorter under small droplets than under large droplets in 33-34% relative humidity, which was attributed to a faster evaporation rate leading to an increase in the chloride concentration of the droplet.

2.4.5 Kelly's model of atmospheric pitting corrosion

Kelly and his co-workers [109-112] developed a model to predict the maximum pit size on stainless steel in atmospheric conditions under a thin electrolyte layer. The model was developed by combining two factors: the minimum anodic current required for pit stability and the maximum cathodic current. Figure 2-19 shows an example of how the model is used to predict the maximum pit size. The straight line represents the required anodic current (I_{LC}), and the curved line represents the maximum cathodic current ($I_{c,max}$). The pit is only stable when the maximum cathodic current is higher than the minimum required anodic current to supply enough current for pit growth. Otherwise the pit will repassivate. The crossing point of the I_{LC} and $I_{c,max}$ on pit diameter represents the maximum pit size [110].

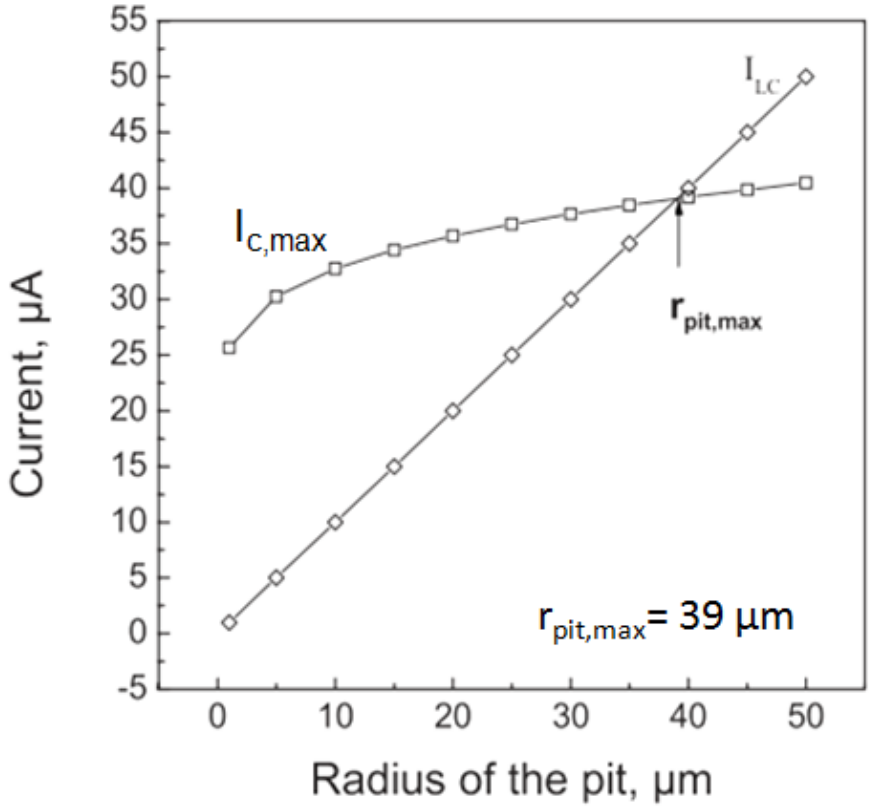

Figure 2-19 The effect of the radius of the pit on the combination of the anodic current demand and the maximum cathode capacity. The effect of the radius of pit on the anodic current demand I_{LC} is 1 A/m. The curved line represents the effect of the radius of pit on the maximum cathode capacity, $I_{c,max}$, which is calculated from the model. The RH is 98% and the deposited NaCl density is 100 μg/cm^2. The intersection of the two curves determines the maximum pit size, which is 39 μm in this condition [110].

The minimum anodic current demand (I_{LC}) used in Kelly's model was based on pit stability product. As described in Section 2.2.3 and Section 2.2.4, *ix* is the pit stability product for a one dimensional pit. Williams et al. [113] developed a pit stability product (I_{pit}/r_{pit}) for a hemispherical pit, and reported that hemispherical pit growth is stable when the pit stability product I_{pit}/r_{pit} exceeds about 2.5 Am^{-1}. In Kelly's model, I_{pit}/r_{pit} is used as the dependence of I_{LC} on pit size, and the value of I_{pit}/r_{pit} that is 6.5 times the *ix* value of 1D stability product (the value of $2\pi ix$) [110].

The maximum cathodic current capacity $I_{c,max}$ can be written as shown below:

$$\ln I_{c,\max} = \frac{r\pi\kappa(RH,T)\Delta E_{\max}}{I_{c,\max}} \frac{DD[1+m_{salt}(RH,T)MW_{salt}]}{m_{salt}(RH,T)\rho(RH,T)MW_{salt}} + \ln[\frac{\pi r_a^2 \int_{E_{corr}}^{E_{rp}} (i_c - i_p)dE}{\Delta E_{\max}}]$$

The first term relates the ohmic resistance in the solution layer. This will depend on its conductivity, which will be controlled by relative humidity, and its thickness, which is dependent on chloride deposition density and relative humidity.

The second term is the cathodic kinetics driven by the overpotential, which is the potential difference between the corrosion potential (E_{corr}) and the repassivation potential (E_{rp}), since the repassivation potential (E_{rp}) is assumed to be the potential of pit mouth. E_{rp} used in the model is -0.4 V (SCE) for 304 stainless steel, and -0.25 V (SCE) E_{rp} for 316 stainless steel [109, 110, 114].

2.5 Synchrotron X-ray radiation techniques

2.5.1 Introduction

Synchrotron radiation is an extremely intense source of X-rays. Figure 2-20 shows a schematic diagram of the third generation synchrotron radiation facility. It consists of an electron gun, linac, booster ring, storage ring and a range of beamlines. When the radiation facility operates, electrons are generated by an electron gun and are injected through the linac into the booster ring and then the storage ring. In the storage ring, there are bending magnets, focusing magnets and insertion devices. X-ray radiation is emitted whenever the electrons change direction in a magnetic field. The beamlines are all approximately tangential to the storage ring, and monochromatic X-rays can be produced which are focused on the sample by suitable optics [115-117].

Pitting corrosion is a dynamic process and it is always associated with the wet environment, which is difficult to study in-situ. The traditional characterisation methods such as SEM and lab-based XRD normally require a vacuum environment. Pits can be characterised after the corrosion process, but cannot be characterised with time dependence by the traditional methods. Synchrotron radiation can supply intense X-rays to detect and characterise corrosion processes in situ and in real time since a vacuum environment is not required. There have been a number of previous studies in which synchrotron X-rays have been used to study corrosion, e.g. [52, 73, 118-121].

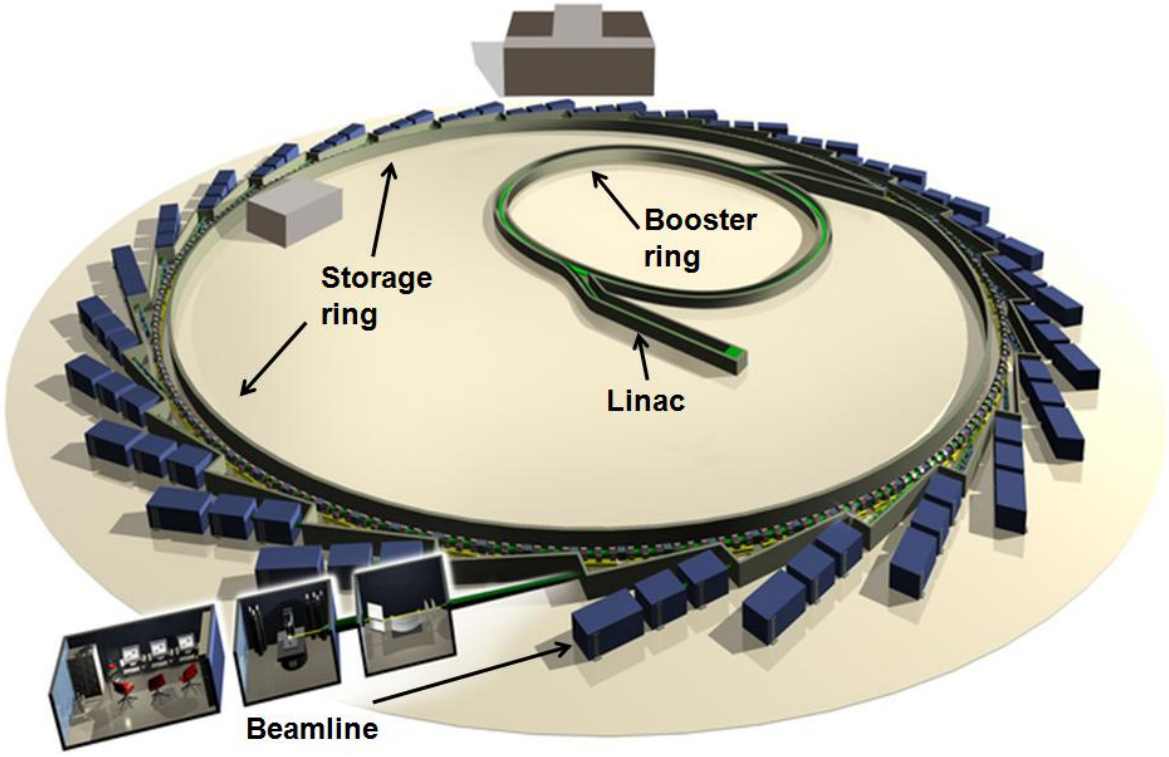

Figure 2-20 A schematic diagram of a synchrotron radiation facility (Courtesy of Diamond Light Source) [122].

2.5.2 Synchrotron X-ray tomography

2.5.2.1 Principle of X-ray tomography

X-ray tomography is a non-destructive method that can provide three dimensional information of the interior microstructure of materials [123-126]. The basis of X-ray tomography is X-ray radiography. The X-ray beam can pass through a sample and be attenuated. A well known equation is shown as Equation 2-15, where I_o is the intensity of the original X-ray beam, and I is the attenuated beam intensity after it passes through a thickness of x of the material. μ is the absorption coefficient of the material.

$$I / I_o = \exp(-\mu x) \qquad \text{Equation 2-15}$$

The transmitted beam attenuated by the sample can be recorded by a suitable imaging detector. The visible image is a two dimensional projection (or radiograph) of the material. If the sample is rotated between 0° and 180°, and a range of the projections is recorded, then a filtered back-projection algorithm can then be used to reconstruct these projections to create a

three dimensional view of the sample [123-126]. Figure 2-21 shows a schematic diagram of the setup of X-ray tomography.

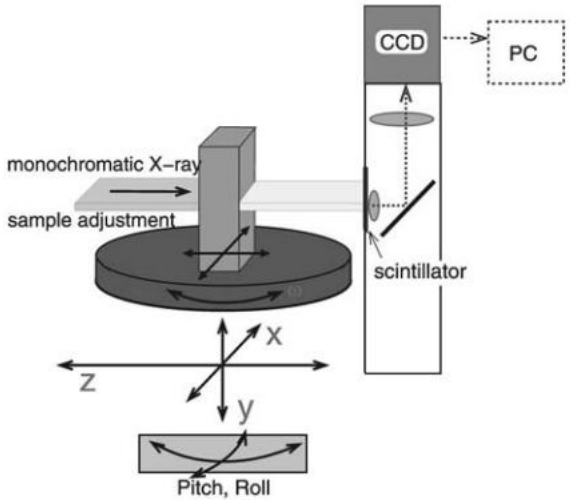

Figure 2-21 A schematic diagram of the setup for X-ray tomography [126].

The spatial resolution is a measure of how closely a feature can be located with a reference feature, in some literature it has been defined as the smallest separation of two distinguished points. The X-ray tomography spatial resolution can approach the level of micrometers.

2.5.2.2 Synchrotron X-ray tomography

There are two sources for X-ray tomography experiments: a laboratory micro-focus X-ray tube or a synchrotron X-ray radiation facility. A recent review shows that X-ray tube tomography can routinely achieve spatial resolutions to submicron level [125]. However, a relatively long collection time is required due to the lower intensity, which makes in-situ time dependent measurements less practical [124, 126].

A synchrotron radiation facility can supply a very high flux X-ray beam that is many orders of magnitude brighter and more intense than a micro-focus X-ray tube. The synchrotron radiation also allows the production of either a monochromatic beam or a white beam. The resolution of the synchrotron X-ray tomography can be to submicron level [123-126]. Synchrotron X-ray requires a relatively short acquisition time for experiments, which can benefit in-situ experiments of material characterisation since the scan time may be far less than the time required to change the micro structure of the material.

2.5.2.3 Synchrotron X-ray tomography in corrosion research

X-rays can penetrate water and metal with different attenuation. As X-ray tomography does not require a vacuum environment and can characterise the microstructure non-destructively, X-ray tomography is suitable for visualisation of corrosion behaviour in real time. Synchrotron X-ray tomography requires a less acquisition time, which is more suitable for characterisation of the in-situ corrosion process as the corrosion rate can be fairly fast.

X-ray tomography has been applied to study the corrosion process on aluminium, magnesium and stainless steel alloys [118-121, 127-129]. For example, Marrow et al. have investigated the intergranular stress corrosion cracking in austenitic stainless steel by X-ray tomography [127]. Ghahari et al. have applied a capillary cell on a stainless steel pin with electrochemical control and visualised pitting corrosion of stainless steel by synchrotron X-ray micro-tomography [118]. Knight et al. have placed a droplet on the top of an aluminium pin and have applied synchrotron micro-tomography technique to visualise the intergranular corrosion of aluminium alloys [121].

2.5.3 Synchrotron X-ray diffraction in corrosion research

X-ray diffraction (XRD) is a tool to characterise the fine structure of matter, which is based on the interference of the scattered X-rays. As described in Section 2.3.1, the salt layer in corrosion pits is not static, but continuously precipitates and dissolves during the corrosion process. Thus it is essential to characterise the salt film with solution present during corrosion. Since X-rays can penetrate liquid, Isaacs et al. used a synchrotron XRF technique to characterise the composition of the salt film on a stainless steel 1D pit. However, this work can only supply a qualitative hypothesis of the structure and composition of the salt layer.

Rayment et al. [73] used synchrotron X-ray diffraction to characterise the composition of salt films on dissolving surfaces in iron, stainless steel and nickel artificial pits. Recently, Ko et al. [130] used this technique to characterise siderite ($FeCO_3$) precipitation on carbon steel during a carbon dioxide corrosion process. Dowsett et al. [131] have observed in-situ copper corrosion and characterised copper corrosion products via a synchrotron XRD method.

2.6 Summary

Stainless steel is known as a corrosion resistant material, but is susceptible to atmospheric pitting corrosion in environments containing chloride. The mechanism of pitting corrosion of stainless steel under full immersion conditions is relatively well understood but far less has been published on pitting corrosion of stainless steel under atmospheric conditions. Since the relative humidity determines the chloride concentration of the solution, which can lead to highly concentrated salt solutions, it is essential to study electrochemical kinetics corresponding to the atmospheric conditions, particularly in the higher chloride concentration solutions.

In the current work, synchrotron micro-tomography is used to supply intense X-rays to produce high resolution images of the evolution of corrosion pits and the electrolyte layer in-situ and in real time. Synchrotron XRD is used to characterise salt films on stainless steel artificial pits in relatively high chloride solutions. Electrochemical measurements are used to determine the current-voltage characteristics, critical pit solution chemistry, and the Tafel slope in solutions of various chloride concentrations. Inkjet printing technique is demonstrated to be a feasible method to deposit salt patterns on 304 stainless steel foils to observe atmospheric corrosion.

3 Experimental method

3.1 Materials

Stainless steel 304 and 316L were obtained from commercial suppliers, Goodfellows Cambridge Ltd., UK, and Advent Research Materials, UK. The details of materials applied in the experiments are listed in Table 3-1.

Table 3-1 Alloys used in experiments (compositions were supplied by the vendors).

	form	Supplier	Thickness /Diameter	Processing	Composition	Experiments
Stainless steel 304	foil	Goodfellow	50 µm	Cold-worked	Cr 17-20%, Mn <2%, Ni 8-11%, C <800 ppm, Fe balance	1D artificial electrode for Synchrotron XRD measurements
		Goodfellow	100 µm	Annealed	Cr 17-20%, Mn <2%, Ni 8-11%, C <800 ppm, Fe balance	Inkjet printing deposition measurements
	wire	Advent Research Materials	250 µm	Annealed	Cr 17-20%, Mn <2%, Ni 8-11%, C <300 ppm, Fe balance	1D artificial pit for electrochemical measurements
	rod	Goodfellow	2 mm	Cold-worked	Cr 17-20%, Mn <2%, Ni 8-11%, C <800 ppm, Fe balance	Synchrotron micro-tomography measurements
Stainless steel 316L	foil	Advent Research Materials	50 µm	Annealed	Cr 16-18%, Ni 10-14%, Mo 2-3%, S<300 ppm, P<450 ppm, C<300 ppm, Si<1%, Mn<2%, Fe balance	1D artificial electrode for synchrotron XRD measurements

3.2 Sample preparation

3.2.1 Wire artificial pit electrodes and electrochemical cells

The wire artificial pit electrodes were made from stainless steel 304 wires (250 µm diameter) mounted in epoxy resin; a schematic diagram of the wire artificial pit electrode is shown in Figure 3-1. The stainless steel wire was degreased with methanol and soldered to an electrical wire for connection. The wire was then placed within an acrylic tube, 6 mm outside diameter and 4 mm inside diameter. EpoFix resin (supplied by Struers) was injected into the tube and cured for at least 24 hours. The connection at the bottom of the wire was covered with Teflon tape and Alradite epoxy to avoid contact with electrolyte. The resin is transparent, thus it is possible to visualise the 1D pit from a horizontal microscope coupled to a CCD camera. In the experiments, only the top surface of the electrode was exposed to electrolyte. The electrochemical cell for measurements with wire artificial electrodes is shown in Figure 3-2, which contains a SCE reference electrode, a platinum wire auxiliary electrode, and about 120 ml of test solution.

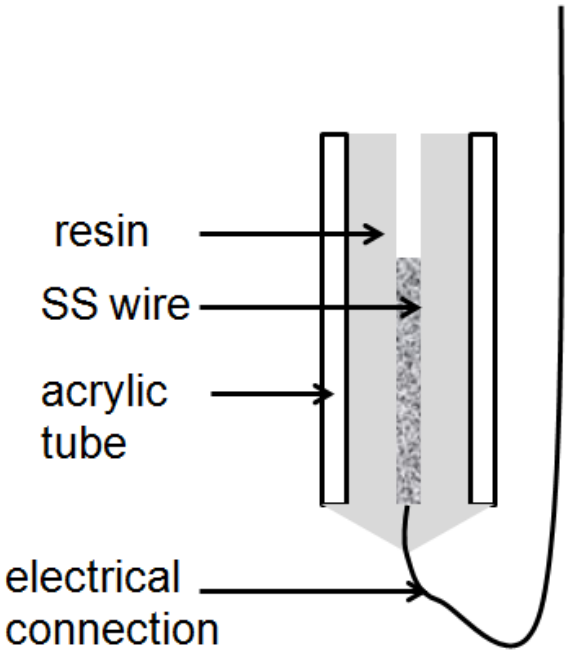

Figure 3-1 A schematic diagram of a wire artificial pit electrode.

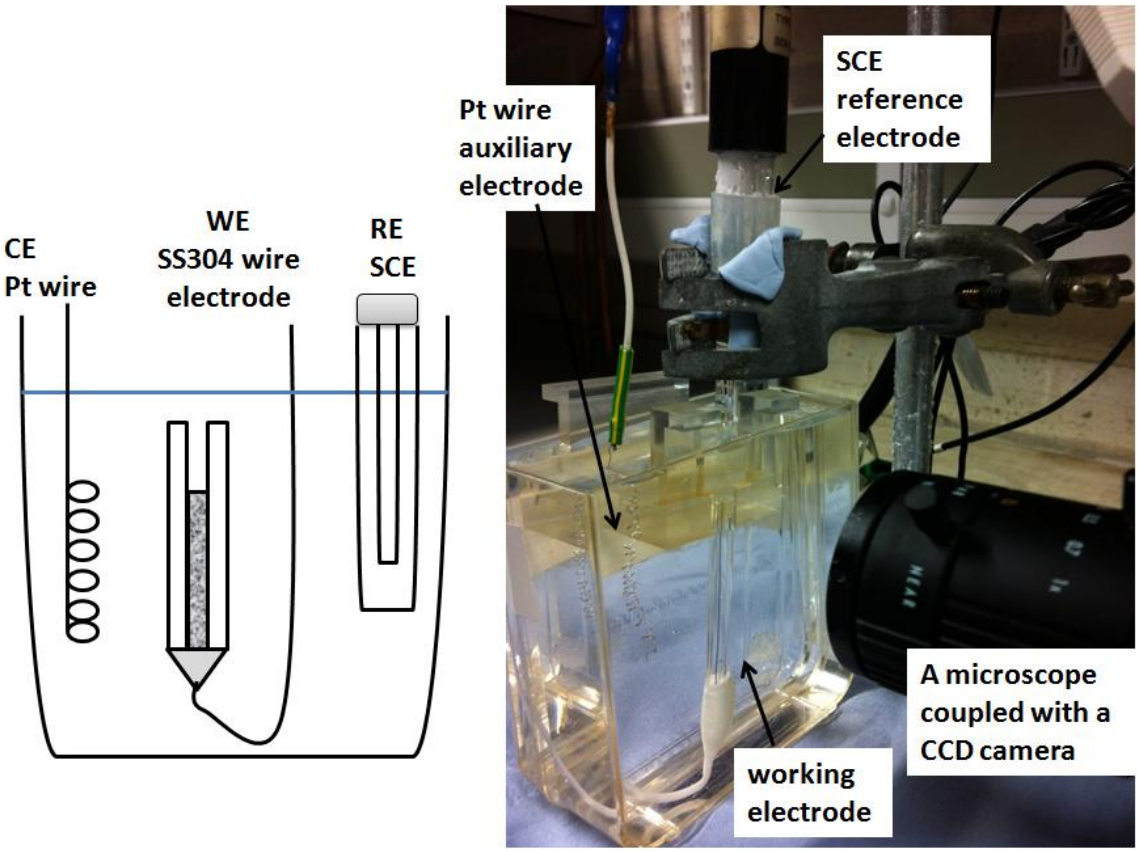

Figure 3-2 A schematic diagram and the experimental setup for a wire artificial pit in an electrochemical cell.

3.2.2 Abraded wire electrodes and electrochemical cells

The abraded wire electrodes are made from stainless steel 304 wires (250 μm). The wires were abraded along their length to either 120 or 4000 grit by SiC paper, and then rinsed with de-ionised water, and were immediately immersed in the solution of the electrochemical cell. The electrode was bent to form a 'J' shape so that the cut end of the electrode was exposed above the waterline. The electrode was immersed to a depth in the cell solution and the surface area immersed in the solution was controlled at 0.5 cm^2. A mark of tape was made on the sample which was placed about 5 mm above the waterline to indicate the position and avoid to be immersed in solution and cause crevice corrosion.

Figure 3-3 shows a schematic diagram and a photograph of the experimental setup of the electrochemical cell for abraded wire electrochemical experiments. The cell contains a SCE reference electrode, a platinum wire auxiliary electrode, and about 200 ml of test solution. The test solution was de-aerated with argon for 20 minutes before the electrode was placed into the cell. Once the electrode had been immersed into the cell solution, the flow of argon

gas into the test solution was switched off and the flow of argon gas above the test solution was switched on to protect the solution and minimise interference by oxygen. Although the flow of argon gas was intended to minimise the dissolved oxygen in the solution, the level of oxygen in the solution was not controlled in the experiments. However, for pitting potential and repassivation potential measurements, the dissolved oxygen level in the solution does not affect the results. In each experiment, a freshly prepared electrode was used which was discarded following use.

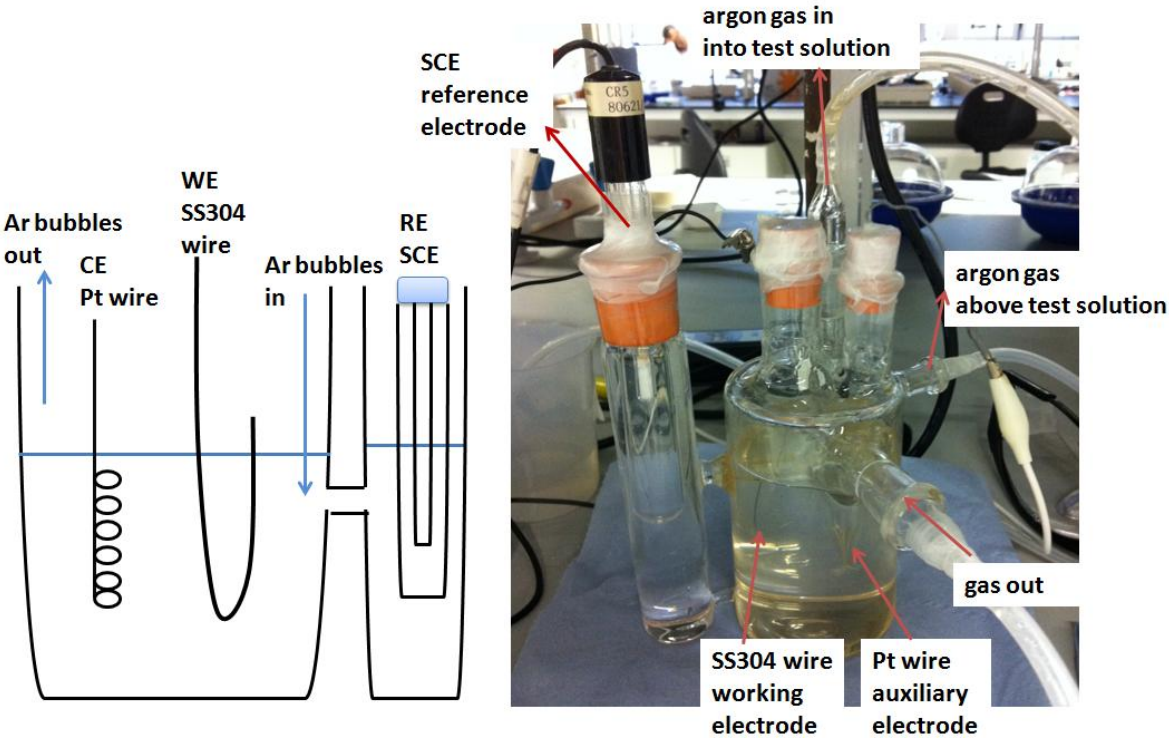

Figure 3-3 The schematic diagram and the experimental setup of abraded wire electrochemical cell.

3.2.3 Foil artificial pit electrodes and electrochemical cells

Foil artificial pit electrodes were made from 3 mm wide, 2.5 cm long strips of 50 µm thickness stainless steel 304 and 316L foils sandwiched with Araldite resin and Kapton tape (RS Components). The Kapton tape was sealed to the end of a PVC plastic tube to form the electrochemical cell as shown in Figure 3-4. The electrochemical cell contains an Ag/AgCl reference electrode, a platinum wire auxiliary electrode, and approximately 20 ml of test solution.

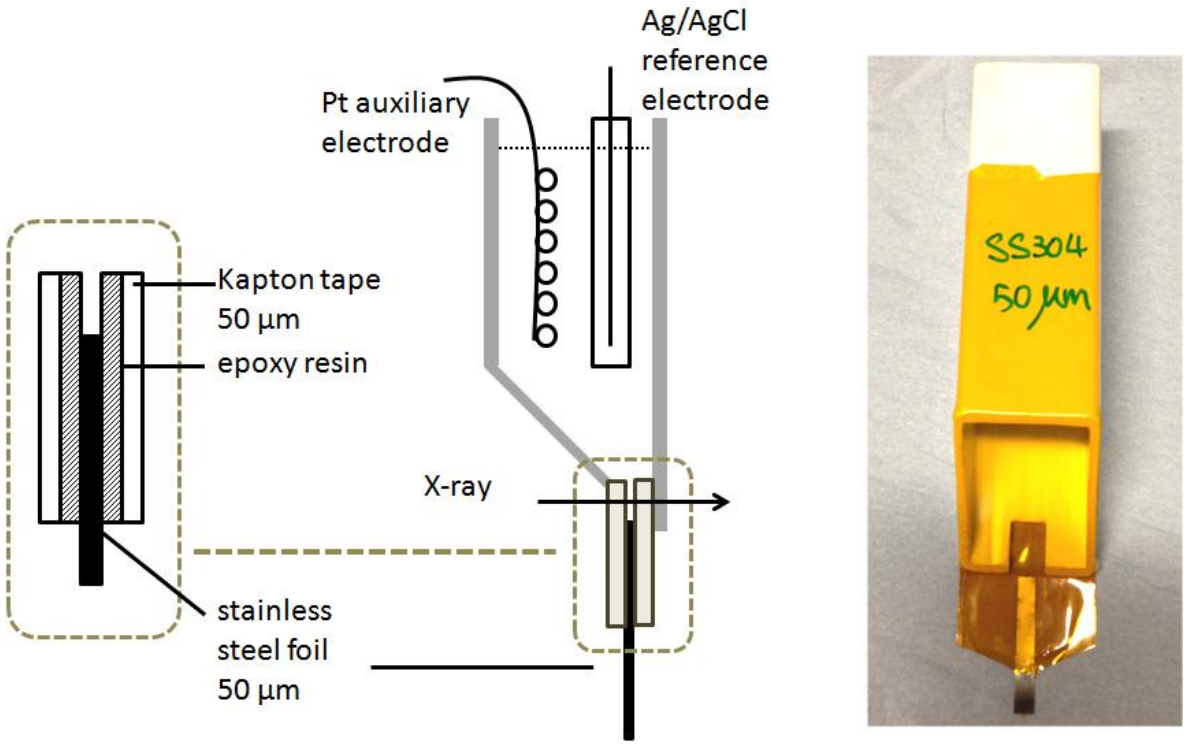

Figure 3-4 The schematic diagram and the experimental setup of a foil artificial pit electrode electrochemical cell.

3.2.4 Stainless steel foils for inkjet printing

Stainless steel 304 foils (100 µm thick) of dimension 3 cm x 6 cm were used as the specimen. The foil surfaces were hand ground with SiC papers up to 800 grit and cleaned with de-ionised water and ethanol immediately before salt deposition.

3.2.5 Stainless steel pins and cell for X-ray tomography

Samples of stainless steel 304, length 25 mm and 2 mm diameter were machined from stainless steel rod 2 mm in diameter (Goodfellow). The top surface was perpendicular to the rolling direction, and was ground with SiC papers up to 800 grit and cleaned with de-ionised water. The sample was immediately deposited with salt solution after being cleaned.

3.3 Test solutions

Aerosols are composed of a variety of salts, however, it is difficult to study the atmospheric pitting corrosion in a mixed salt solution and apply the experimental results to pitting corrosion prediction models. For initial studies, it is more practical to study the atmospheric

pitting corrosion with a single salt that has a relatively low deliquescence point. As presented in Section 2.4, the deliquescence point of $MgCl_2 \cdot 6H_2O$ is 33% RH [81]. $MgCl_2$ solutions were used in the experiments. Solutions were prepared from analytical grade magnesium chloride hexahydrate (Sigma-Aldrich and Fisher Scientific), and de-ionised water (Millipore 18 MΩ·cm).

3.4 Electrochemical procedures

3.4.1 Electrochemical sequences of wire artificial pits

The electrochemical sequences of wire artificial pits were carried out by Ivium CompactStat. All the wire artificial pit electrodes were dissolved to at least 500 μm at an applied potential of 600 mV (SCE) in $MgCl_2$ solutions. The depth of the pit was calculated from the charge passed by use of Faraday's law. The depth of the pit was also measured using the optical microscope coupled with a CCD camera. The depth measured by both methods agreed to within about 8%. Once the electrode had dissolved to 500 μm deep, the potential was gradually swept downwards to a lower potential and was swept upwards to 600 mV (SCE). The lower potential limit was chosen such that the current density decreased to about 80% of the limiting current density. The sweep rates ranged from 2 mV/s to 10 mV/s. Cyclic voltammetry was used to obtain current-voltage characteristics of artificial pits. After each potential scan, the electrode was further dissolved by 200-300 μm at 600 mV (SCE), and examined by cyclic voltammetry. For each electrode, cyclic voltammetry was carried out for at least three cycles to obtain current-voltage characteristics at different pit depths. The final measurement of each experiment involved passivation of the electrode. The procedure for this involved setting the potential to 600 mV (SCE) for 10 minutes, then stepping the potential to 200 mV (SCE) for 10 minutes to thin the salt layer. The resistance will drop at the same time as the salt layer becomes thinner. The potential then was swept at a slow rate of 0.2 mV/s to -300 mV (SCE) to passivate the electrode. The slow backscan of potential method was developed by Ernst and Newman [132] to define the C_{crit} and C_{sat}. During the electrochemical measurements, resistance was measured concurrently with impedance method at a fixed frequency of 100 kHz and 5 mV amplitude.

3.4.2 Cyclic voltammetry experiments on abraded wires

After being immersed in the $MgCl_2$ solution, the open circuit potential (OCP) of the abraded wire electrodes was measured for 15 minutes. When the potential had stabilised, cyclic

voltammetry commenced. The electrode was polarised from -100 mV or -200 mV (vs. OCP) to a possible upper limit of 1000 mV (vs. OCP) at a scan rate of 0.2 mVs^{-1}. When the current density reached 1 $mAcm^{-2}$, then the scan was automatically reversed. The pitting potential (E_{pit}) was defined as the potential at which the current density was 0.1 $mAcm^{-2}$. The potential then was swept downwards until the current density was below 10^{-4} $mAcm^{-2}$. The repassivation potential (E_{rp}) was defined to be the potential at which the current density was 10^{-3} $mAcm^{-2}$.

3.4.3 Electrochemical procedure on foil artificial pits

The foil artificial pit electrodes were used for all synchrotron XRD experiments. Pits were grown to at least 1.5 mm deep prior to the XRD experiments at an applied potential of 0.6 V (Ag/AgCl). This was carried out in a laboratory adjacent to the beamline. The foil electrodes were uniformly dissolved and were covered with a salt film. The cell was then moved to the experimental hutch for XRD experiments. Experiments on the beamline used an Ivium potentiostat. XRD data was collected at a series of fixed potentials.

3.5 Inkjet printing experiments

A Canon Pixma MP610 inkjet printer was used in the salt deposition experiments, since the coloured ink in its cartridges can be washed out and exchanged with salt solutions. In the current work, a yellow ink cartridge was cleaned and dried before injection of the salt solution through a small hole drilled into the cartridge. The concentration of the salt solution for printing was selected to be nearly saturated $MgCl_2$ solution. Another yellow colour cartridge was prepared containing de-ionised water for cleaning the print head after deposition.

The deposition patterns were designed in Microscoft PowerPoint, which allows the salt deposition density to be controlled by changing the colour intensity in the software. The salt deposition printing was performed in CD printing mode, which is designed to print an image on the surface of a CD. Stainless steel foil samples (thinner than the height of a CD) were placed on the printer tray designated for CD printing. In all of the current work, a small gap was maintained between the stainless steel foils and the top of the CD tray to reduce the risk of smearing by the printhead. In order to deposit higher salt densities, the patterns were printed multiple times on the same sample ("overprinting"). Figure 3-5 shows the result of setting a colour intensity 20%, 50% and 100% for a single print pass, and overprinting 100% colour intensity for 2, 5 and 10 times. The printing environment was 21±2 °C, 43±3% RH.

When carrying out multiple over-printing, smearing of the previous salt layer was sometimes observed. To minimize this effect, a hair dryer was used with cold air to dry the salt layer between successive deposition cycles.

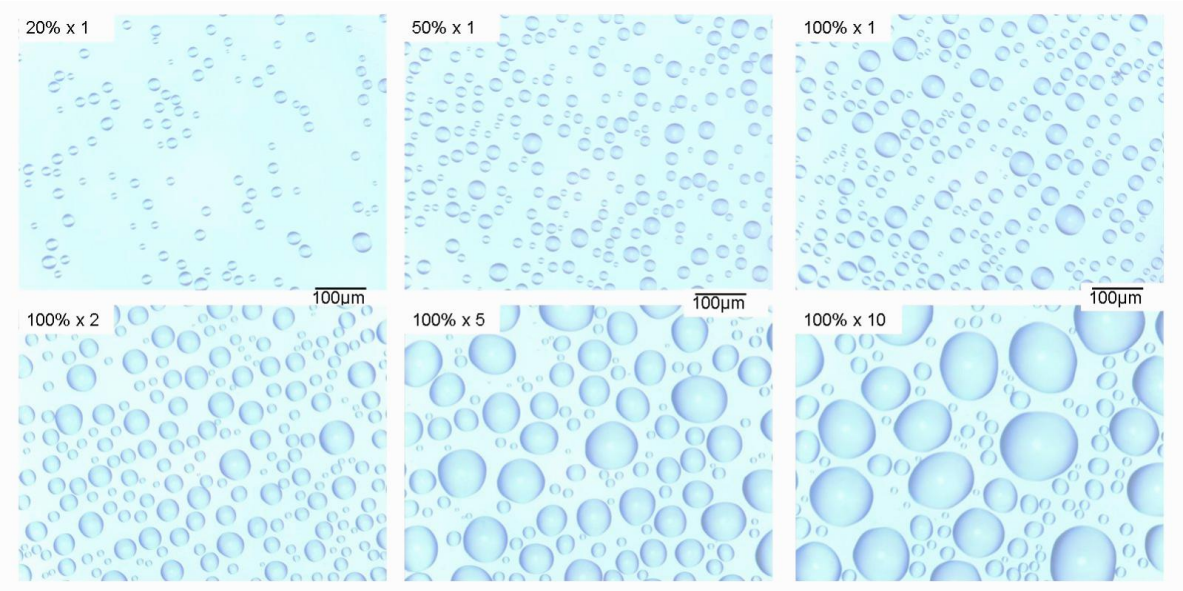

Figure 3-5 The salt deposition of 20%, 50% and 100% colour intensity for a single pass, and 100% colour intensity for 2, 5 and 10 times overprinting on a CD.

In the current work, a single printing pass with 100% colour intensity was found to give a chloride ion density of 35±5 µg/cm^2. The density of printing was measured in three ways: determination of the mass gain (40 µg/cm^2), measuring the chloride concentration washed off the stainless steel surface using a Dionex ICS2000 anion analysis machine, (29 µg/cm^2), and measuring the Mg^{2+} concentration washed off the stainless steel surface by EDTA titration (30 µg/cm^2). A weighing method was used to confirm that there was a linear relationship between the "colour intensity" used in PowerPoint and the density of the deposited salt. Figure 3-6 shows that there was a linear relationship for 20%, 50%, 100% printing densities for a single printing pass.

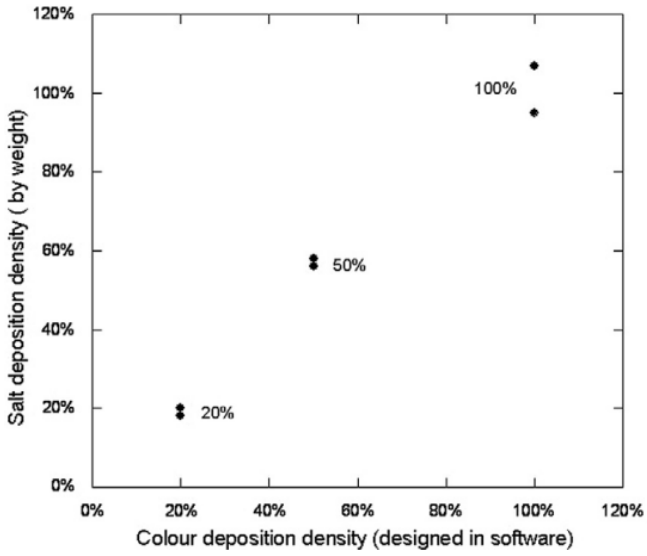

Figure 3-6 The relationship between the salt density deposited by printing a single uniform layer on a stainless steel foil (determined by mass gain) compared with the colour density selected for the printing area in PowerPoint.

The chloride levels selected for studies of corrosion were from 7±1 μg/cm^2 to 350±50 μg/cm^2, which are consistent with those found for atmospheric exposure at Waratah Bay and Flinders Navy Base marine sites, Victoria, Australia, as reported by Cole et al. (10 to 12.3 μgcm^{-2}day^{-1}) [84]. The levels are also in the same range as Tsuru's experimental work on deposited droplets (around 180 μg/cm^2) [1] and values selected for Chen and Kelly's model (10 and 100 μg/cm^2) [109].

Following salt deposition, the stainless steel foils were placed in a humid environment (~90% RH) for one hour to deliquesce the salt deposits. The deliquescence point for $MgCl_2$ at 30 °C is 32% RH and at 20°C is 34% RH [133]. The initial period of high RH was designed to form a salt droplet on the metal surface. The samples were then placed in a desiccator with controlled relative humidity (45±1% RH or 55±1% RH). The humidity was controlled by the equilibrium with $MgCl_2$ solution of known concentration in shallow dishes in a desiccator [1]. The desiccator was placed in a chamber with controlled temperature (300±1 K) for 24 hours. A temperature and humidity sensor was placed in the desiccator to measure the humidity and temperature during exposure. After exposure, macro, optical and SEM images were taken to record corrosion behaviour.

A mechanical syringe pump (Aladdin Programmable Syringe Pump) was used to produce dilute droplets of 50 mM $MgCl_2$) with a similar diameter to the printed area, as a comparison

with the effect of the printed salt droplet. A specific volume (1.6 µl) of liquid was delivered by the syringe pump, forming a droplet of ~2 mm in diameter. The syringe droplets were placed on a 304 stainless steel foil. The foil was exposed at 300 K, 45% RH for 24 hours.

3.6 Synchrotron micro-tomography experiments

Figure 3-7 shows a schematic diagram of the experimental cell designed for tomography studies of atmospheric pitting corrosion. A droplet of volume about 1.8 µl of $MgCl_2$ solution was deposited on the top surface of a metal pin via a micro-pipette. The volume and solution concentration were calculated to provide a chloride deposition density in the range of 0 to 4000 µg/cm^2. The metal pins were placed into sealed x-ray transparent sample cells in which a constant relative humidity was maintained by use of an appropriate saturated salt. The sample cell comprised a short collar of silicone tubing at the base of the pin over which was placed a longer tube of 4 mm internal diameter. A piece of filter paper impregnated with saturated Mg_2Cl_2 solution (about 4.2 M) was placed at the top of the outer tube which maintained a constant relative humidity (RH) at 45%. The presence of an air gap between the side of the metal pin and the vessel wall prevented crevice corrosion. The whole cell was wrapped with parafilm® as an extra seal.

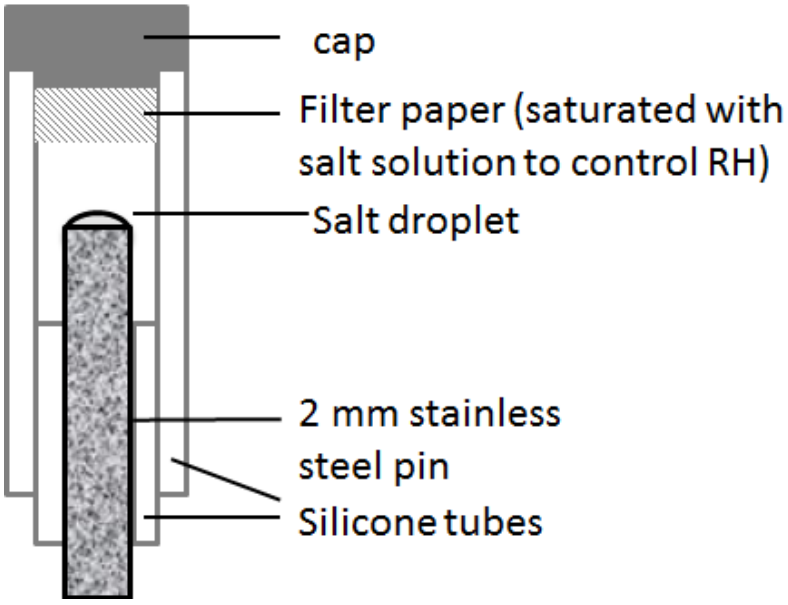

Figure 3-7 A schematic diagram of experimental setup of micro-tomography

X-ray micro-tomography experiments were carried out at I12, the Joint Engineering, Environmental and Processing (JEEP) beamline at Diamond Light Source using 70 keV

X-rays. The field of view was 7.2 x 4.8 mm, and the pixel size was about 1.8 μm. The exposure time was typically 1 s per projection and 1800 projections were collected over a 180° rotation were taken for each tomographic dataset. The total scan time was 40-45 minutes. The projections were re-constructed using filtered backprojection at I12. Fiji and Avizo software packages were used for data analysis. Avizo was used for 3D image visualisation and image segmentation. Fiji was used for 2D image visualisation.

3.7 Synchrotron X-ray diffraction experiments

The XRD measurements were carried out in-situ with electrochemical control at Diamond Light Source on Beamline I18. The beam size is about 2.5 μm (v) x 15 μm (h) with the energy of 12 keV (1.0332 Å). Attenuation filters were used to reduce the incoming beam intensity to avoid beam damage. A CCD area detector with resolution 26 μm x 26 μm was used for data collection.

The electrochemical cell was placed on a translation stage to collect the diffraction patterns at different positions. Figure 3-8 shows a schematic diagram of the positions of the incident X-ray passing through the electrochemical cell. Before collecting the diffraction data, the sample stage was moved to where the incident X-ray beam located in the pit solution region and then raised in 2 μm increments through the salt film so that the final measurement was through the metal foil. The sequence of XRD scans is shown with the blue arrow in Figure 3-8. Each single frame diffraction pattern was collected for 10 s exposure time. Scans through the salt film were carried out five times on the same sample by moving the sample stage horizontally by 0.1 mm each time. The diffraction data collected in various relative horizontal positions can test whether the salt film is uniform across the electrode and also avoid the beam damage. All the diffraction data were analysed by XRDua and FullProf software.

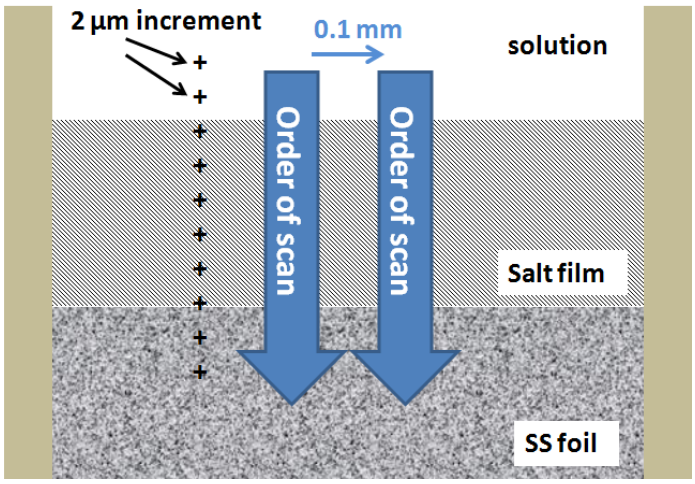

Figure 3-8 A schematic diagram of the positions of the incident X-ray passing through the electrochemical cell. XRD scans start from the pit solution above the salt film and the order of XRD scans is shown via the blue arrow in the figure. Diffraction patterns were collected in 2 µm increments until the beam was located fully in the metal foil. (The cell was moving upwards during the experiment so that the initial measurements were in the solution.)

3.8 Characterisation

3.8.1 SEM

SEM JEOL 6060 and Philips XL30 were used to characterise the materials and pit morphology.

3.8.2 Confocal microscopy

Olympus LEXT OLS3100 confocal laser scanning microscope was used to measure the pit depth profile and obtain a 3D pit morphology. Samples were stainless steel pins used in synchrotron mico-tomography measurements after exposure. The samples were ultrasonically cleaned in de-ionised water for three minutes to remove corrosion products.

4 Inkjet printing deposition technique for investigation of atmospheric pitting corrosion of stainless steel[1]

4.1 Introduction

As described in Section 2.4.1, the controlled deposition of salt layers is an important first step in studies of atmospheric pitting corrosion of stainless steel, since the size and concentration of salt deposits can influence the rate of corrosion. The two traditional methods of salt deposition on a sample surface involve either transferring a volume of salt solution by a micro-pipette [1, 16, 18, 92, 93] or deposition of clusters of deliquescent salt particles [87, 90, 134, 135]. It is difficult to produce well-defined and reproducible patterns on metal surfaces. In the present work, it is shown that inkjet printing can be used to produce well-defined salt deposits on metal surfaces, allowing a systematic study of the effects of salt density on atmospheric corrosion. In this study the deposition of $MgCl_2$ has been selected because it is a particularly corrosive constituent of marine aerosols owing to its ease of deliquescence.

4.2 Results

Two salt inkjet printing salt deposition patterns were designed to investigate the effect of salt deposit diameter on pit size, and the effect of salt deposition density on pit size. The patterns were designed using PowerPoint as described in Section 3.5.

4.2.1 Effect of salt deposit diameter on pit size

The salt deposition pattern shown in Figure 4-1 was designed to illustrate the effect of salt deposit diameter on pit growth for deposits of the same salt density.

[1] The contents of this chapter are based on the paper by Mi, N., M. Ghahari, T. Rayment, and A.J. Davenport, Use of inkjet printing to deposit magnesium chloride salt patterns for investigation of atmospheric corrosion of 304 stainless steel. Corrosion Science, 2011. **53**(10): p. 3114-3121. According to Elsevier's policy, the contents of published journal articles can be included in a thesis. *http://www.elsevier.com/authors/author-rights-and-responsibilities*

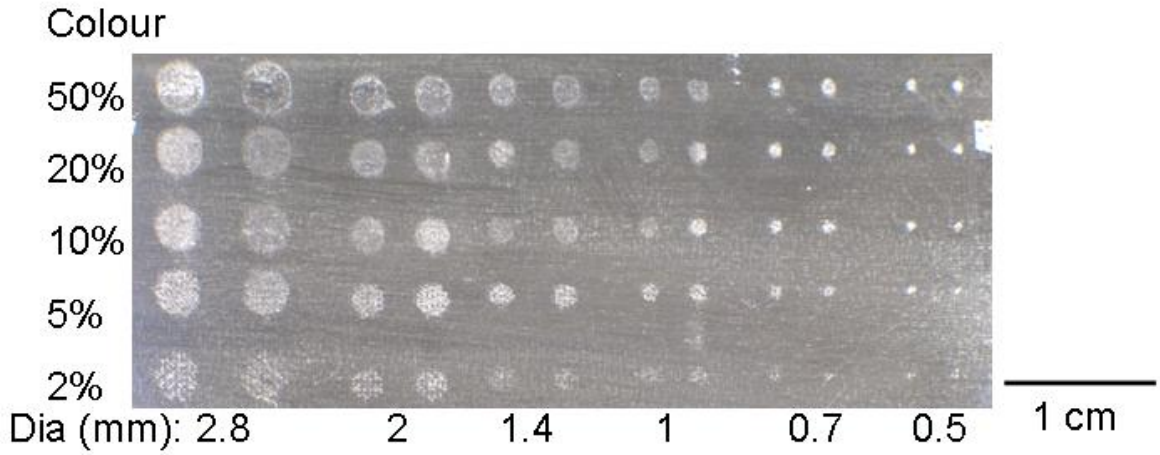

Figure 4-1 $MgCl_2$ deposition pattern with various colour intensities and circle diameters overprinted 10 times on a 304 foil (10x overprinting with 100% intensity corresponds to a chloride deposition density of 350±50 µg/cm^2).

In each row, circles have the same salt deposition density but the diameters range from 0.5 mm to 2.8 mm. The whole pattern was over-printed 10 times, so that the chloride ion deposition densities range from 175±25 µg/cm^2 (10x 50%) to 7±1 µg/cm^2 (10x 2%). Figure 4-2 shows the optical and SEM images of a foil printed with the pattern of salt shown in Figure 4-1 following exposure at 45% RH for 24 hours. In the optical microscope images, the droplets are still present and they appear to have a 'membrane' over the pits. In the SEM images, the 'membrane' has been flushed away with deionised water so that the pits can be observed.

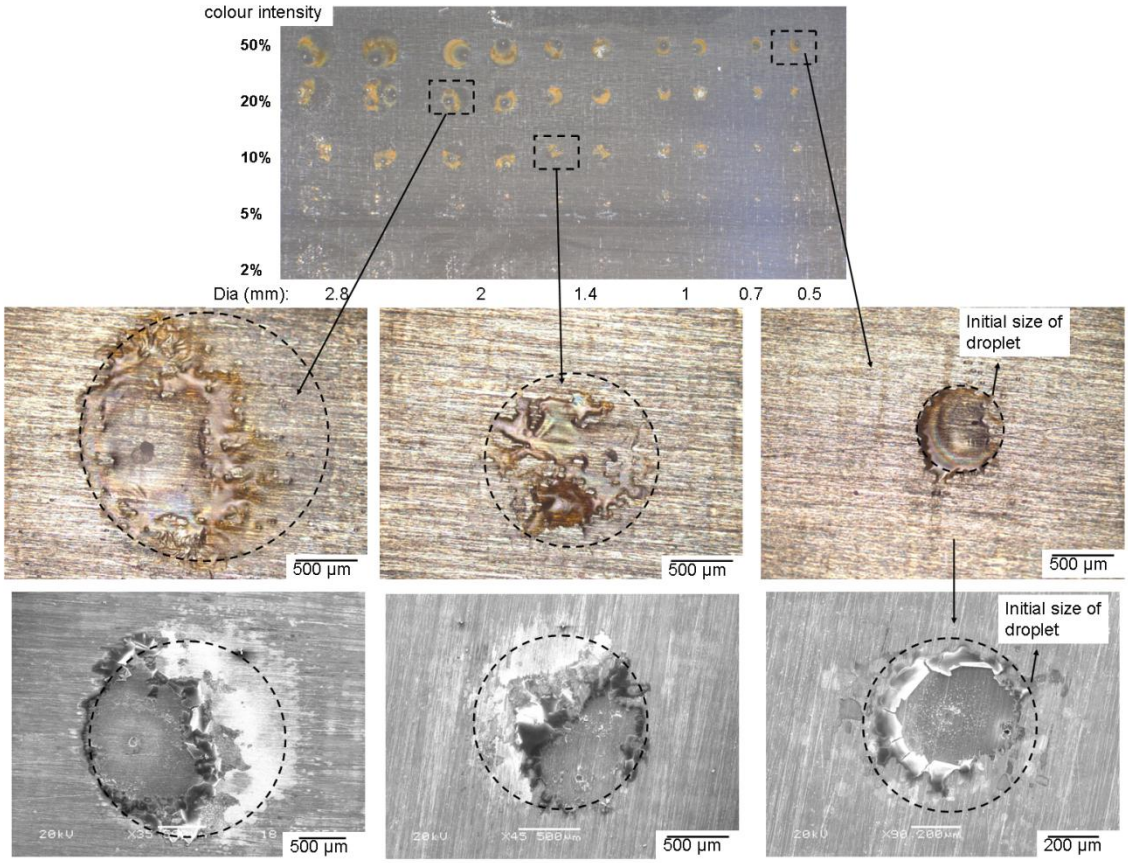

Figure 4-2 A 304 stainless steel foil deposited with $MgCl_2$ in the pattern shown in Figure 4-1 following exposure at 45% RH and 300 K for 24 hours (after 1 hour at ~90% RH): in the optical and SEM images (upper and lower images, respectively). The initial printed area is shown with a broken circle.

The optical microscope images in Figure 4-2 show that the corrosion products are generally confined to the original printed deposit following 24 hours of exposure. Corrosion products and a single pit could be observed in some of the circles. None of the circles showed multiple pits. In this case a "pit" refers to a clearly-defined cavity that is at least 5 µm in size: some poorly-defined spots were observed that may have been smaller pits or small inclusions in the stainless steel. Circles in the same row (fixed deposition density) tend to show similar corrosion behaviour. For example, in the row of 50% salt deposition density, droplets with a relatively continuous layer of electrolyte were formed and a pit could be observed within the droplet. In contrast, in the row of 10% intensity, droplets appeared to have discontinuous electrolyte layers: some of them showed rust and a very small pit, whereas others did not contain a well-defined pit. Figure 4-3 gives a summary of the results shown in Figure 4-1 and

another foil with the same pattern exposed to the same humidity, together with results for two foils with the same pattern exposed to 55% RH. It is evident that the pitting behaviour at 55% RH is similar to that at 45% RH, with slightly fewer pits for smaller amount of salt deposits.

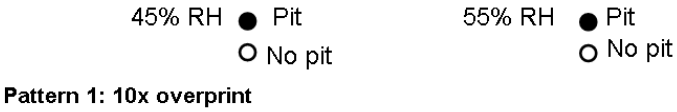

Pattern 1: 10x overprint

Diameter/ Colour intensity	2.8 mm		2 mm		1.4 mm		1 mm		0.7 mm		0.5 mm	
	45% RH	55% RH	45% RH	55% RH	45% RH	55% RH	45% RH	55% RH	45% RH	55% RH	45% RH	55% RH
50%	●● ●●	●● ●●	●● ●●	●● ●●	●● ●●	●● ●●	●● ●●	●● ●●	●● ●●	●● ●●	●● ●●	●● ●●
20%	●● ●●	●● ●●	●● ●●	●● ●●	●● ●●	●● ●●	●● ●●	●● ●●	●● ●●	●● ●●	●● ●●	●● ●●
10%	●● ●○	●● ○○	●● ●○	●● ●○	●● ●○	●● ●○	●● ●○	●● ●○	●● ●○	●● ○○	●● ○○	●● ●○
5%	●○ ○○	●○ ○○	●● ○○	●○ ○○	●● ○○	●○ ○○	●● ○○	●○ ○○	●○ ○○	●○ ○○	●○ ○○	○○ ○○
2%	○○ ○○	○○ ○○	○○ ○○	○○ ○○	○○ ○○	○○ ○○	○○ ○○	○○ ○○	○○ ○○	○○ ○○	○○ ○○	○○ ○○

Figure 4-3 A summary of the results shown in Figure 4-2 for a 304 stainless steel foil deposited with $MgCl_2$ in the pattern shown in Figure 4-1 following exposure at 45 %RH or 55% RH and 300 K for 24 hours (after 1 hour at ~90% RH). For each condition, two foils were tested and on each foil there are two deposited salt circles for each condition. The dots in a horizontal line in the figure represent two deposited salt circles in the same foil.

Figure 4-4 shows SEM images of pits from circles in the top row (50% intensity) of Figure 4-2 with various diameters. The pit diameter as a function of the original salt droplet diameter is shown in Figure 4-5. For the same chloride deposition density per unit area, the resulting pit diameter increases with the size of the original salt droplet.

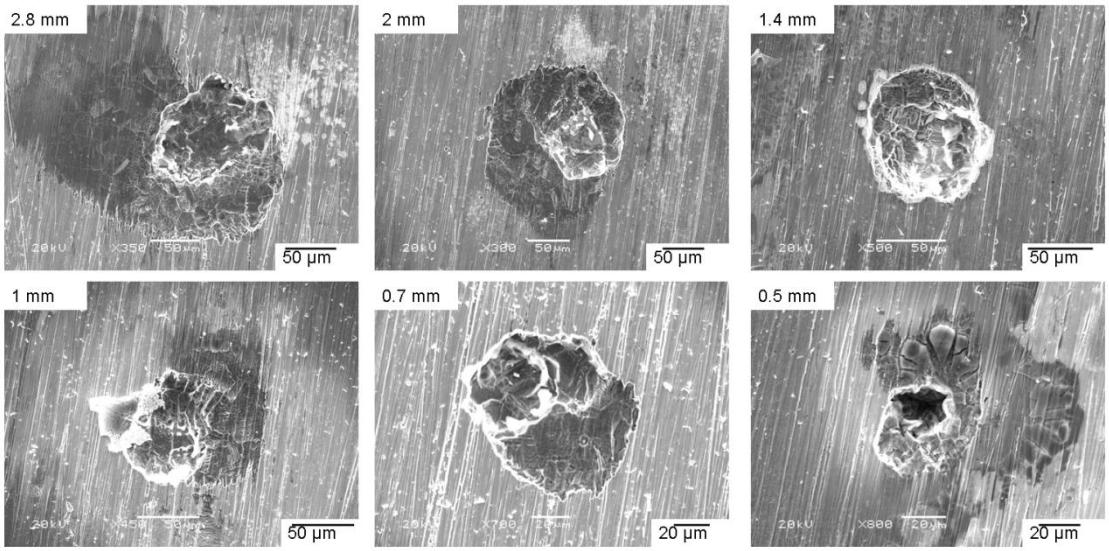

Figure 4-4 SEM images of pits which were formed following deposition of circles of $MgCl_2$ electrolyte layer at 10 x 50% colour intensity (chloride deposition density of 175±25 µg/cm^2), and following exposure 45% RH and 300 K for 24 hours (after 1 hour at ~90% RH). The diameter of the circle is shown as an inset in each image.

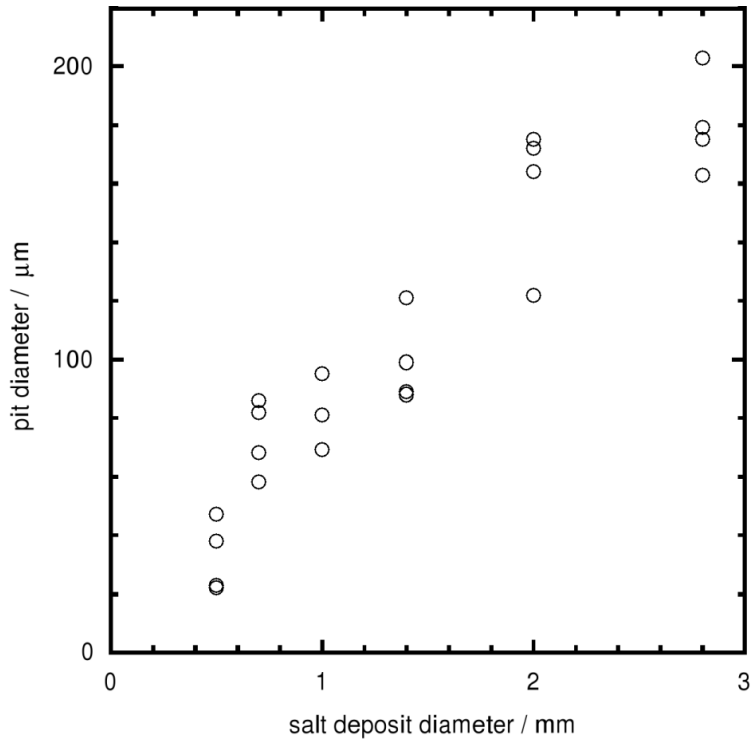

Figure 4-5 The pit diameter plotted as a function of the original droplet diameter for pits which were formed in circles of 10x 50% colour intensity (chloride deposition density of 175±25 µg/cm^2) with diameters ranging from 0.5 mm to 2.8 mm on the foil shown in Figure 4-2 following exposure at 45% RH and 300 K for 24 hours (after 1 hour at ~90% RH).

4.2.2 Effect of salt deposition density on pit size

The second deposition pattern (Figure 4-6) was designed to investigate the effect of changing the salt deposition density for a fixed salt deposit diameter (1.4 mm). It was also used to confirm that the same salt density gave the same pitting behaviour regardless of deposition method (i.e. 5x overprinting of 20% intensity gives similar behaviour to 2x overprinting of 50% intensity). After an initial hydration at ~90% RH for 1 hour at 300 K, the samples were exposed to 45% RH for 24 hours at 300 K. The results are shown in Figure 4-7 and Figure 4-8.

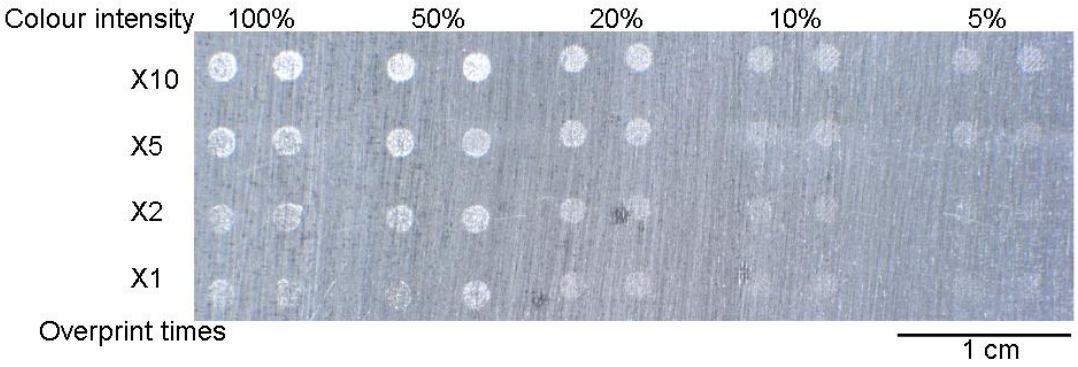

Figure 4-6 $MgCl_2$ deposition pattern of 1.4 mm diameter circles with various overprinting times and colour intensities on 304 foil (10x overprinting with 100% intensity corresponds to a chloride deposition density of 350±50 μg/cm^2).

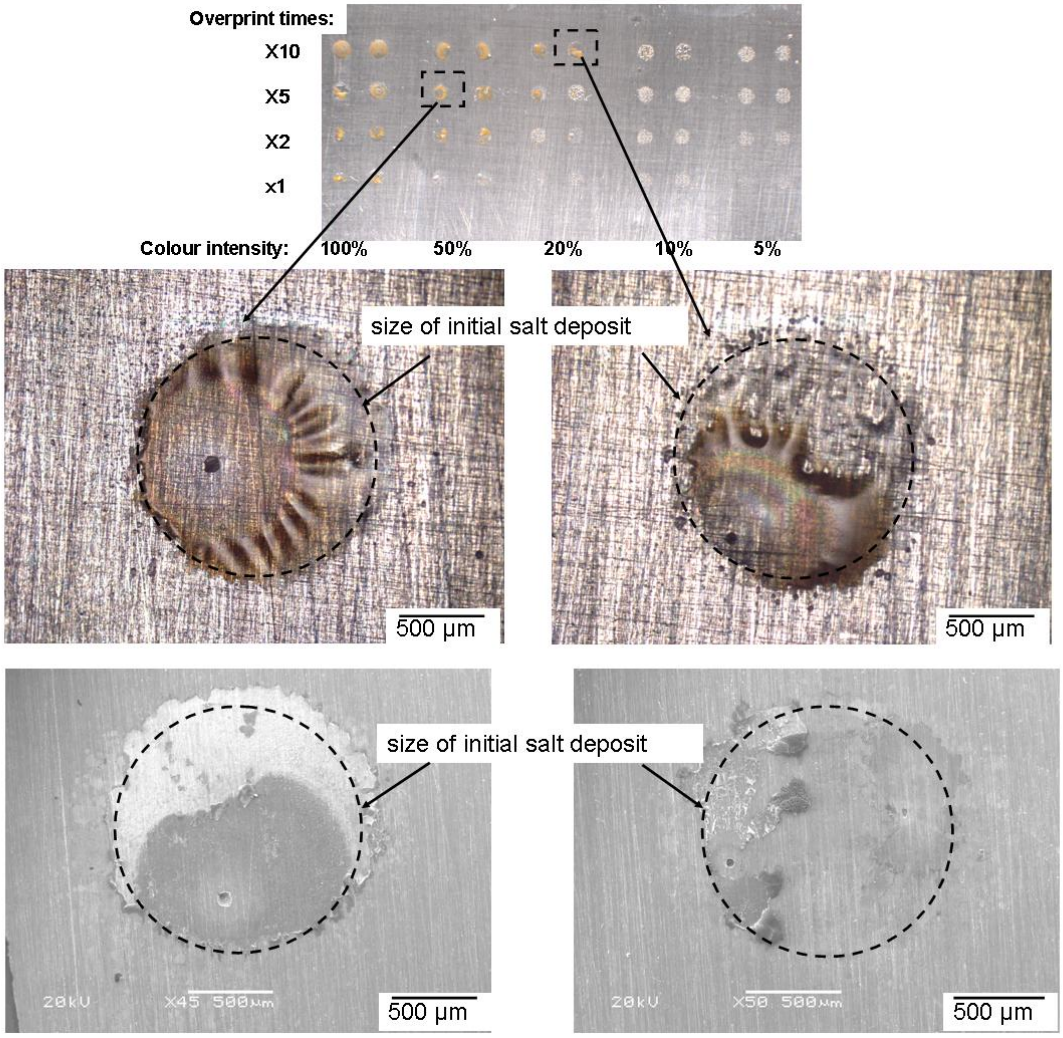

Figure 4-7 A 304 stainless steel foil deposited with $MgCl_2$ in the pattern shown in Figure 4-6 following exposure at 45% RH and 300 K for 24 hours (after 1 hour at ~90% RH). Optical and SEM images show the appearance of droplets and pits found under the droplets. The broken circles show the initial salt printed area.

Circles with a sufficient salt deposition density form droplets which have a membraneous film and a pit underneath, as shown in Figure 4-7. Generally, one pit is formed in each continuous droplet. In some printed circles, there is a limited expansion (~3-6% of the initial printed diameter) after exposure to the controlled relative humidity environment. It was also observed that micro-droplets less than 5 µm in diameter formed around the primary droplet on some occasions. Where there is insufficient salt, relatively discontinuous droplets are formed even after initial hydration at 90% RH, as illustrated in Figure 4-8. Some droplets formed a small pit with rust while some did not.

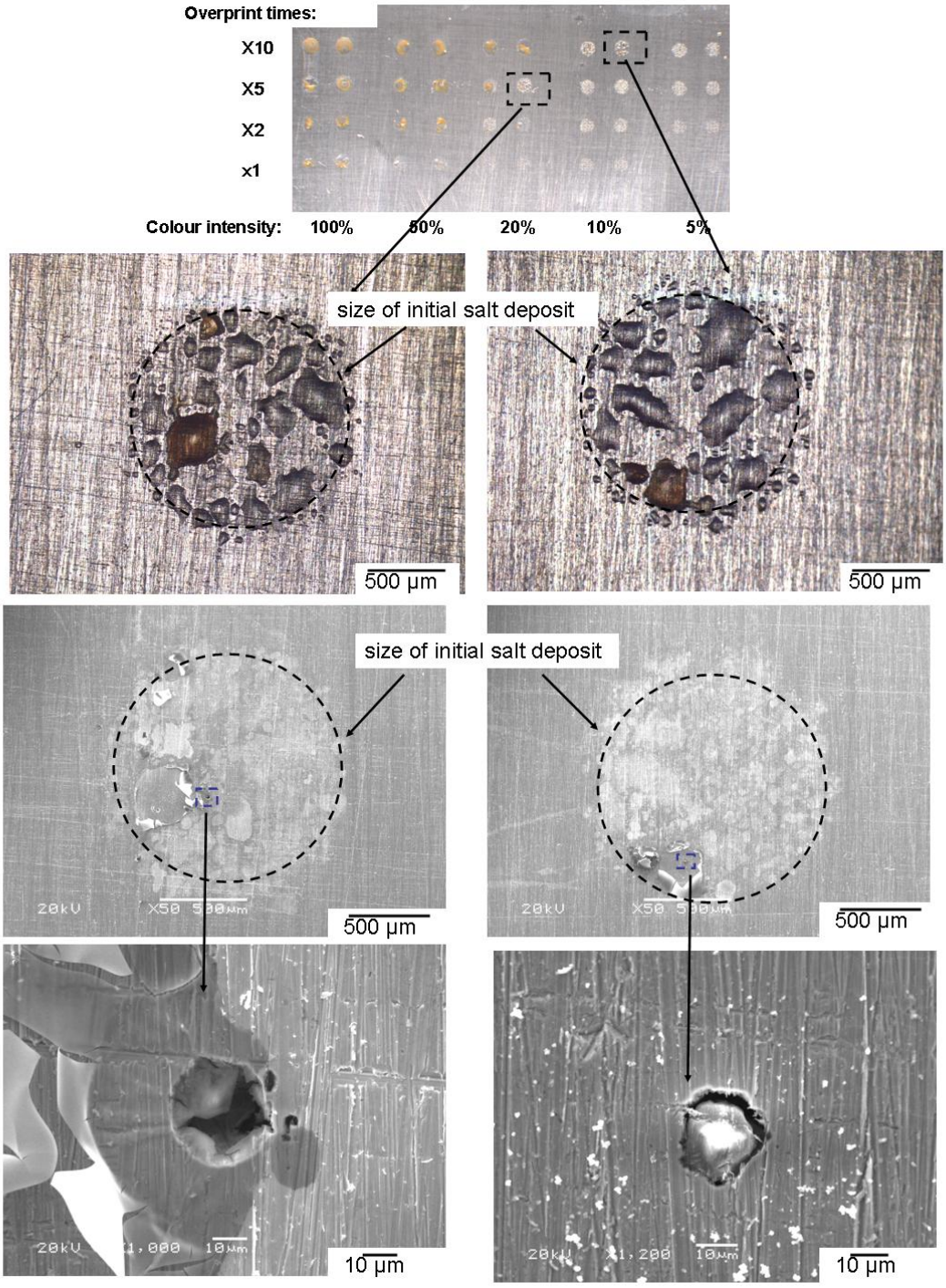

Figure 4-8 A 304 stainless steel foil deposited with $MgCl_2$ in the pattern shown in Figure 4-6 following exposure at 45% RH and 300 K for 24 hours (after 1 hour at ~90% RH). Optical and SEM images show the appearance of droplets and pits found under the droplets. The broken circles show the initial salt printed area.

A summary of the corrosion behaviour under salt deposits printed in the pattern shown in Figure 4-6 is given in Figure 4-9. It can be seen that after 24 hours of exposure, similar corrosion behaviour was observed when the total amount of salt was same: for example, circles of 50% salt overprinted 10 times had a similar corrosion behaviour with the circle of 100% salt printed 5 times and circles of 20% salt printed 5 times had a similar corrosion behaviour to the circles of 100% salt printed once. The results for 45 and 55% RH are similar, with slightly fewer pits at 55% RH.

45% RH ● Pit ○ No pit 55% RH ● Pit ○ No pit

Pattern 2 : initial printing area 1.4 mm diameter

Colour intensity/ Overprint times	100%		50%		20%		10%		5%		1%	
	45% RH	55% RH	45% RH	55% RH	45% RH	55% RH	45% RH	55% RH	45% RH	55% RH	45% RH	55% RH
10x	●● ●●	●● ●●	●● ●●	●● ●●	●● ●●	●● ●●	●● ○○	●○ ○○	●○ ○○	○○ ○○	●○ ○○	○○ ○○
5x	●● ●●	●● ●●	●● ●●	●● ●●	●● ○○	●○ ○○	○○ ○○	○○ ○○	○○ ○○	○○ ○○	○○ ○○	○○ ○○
2x	●● ●●	●● ●●	●● ○○	●○ ○○	●○ ○○	○○ ○○	○○ ○○	○○ ○○	○○ ○○	○○ ○○	○○ ○○	○○ ○○
1x	●○ ○○	●○ ○○	○○ ○○	○○ ○○	○○ ○○	○○ ○○	○○ ○○	○○ ○○	○○ ○○	○○ ○○	○○ ○○	○○ ○○

Figure 4-9 Summary of the results shown in Figure 4-7 and Figure 4-8 for a 304 stainless steel foil deposited with $MgCl_2$ in the pattern shown in Figure 4-6 following exposure at 45% RH or 55% RH and 300 K for 24 hours (after 1 hour at ~90% RH). The dots in a horizontal line in the figure represent two deposited salt circles in the same foil.

Figure 4-10 shows the relationship between pit diameter and initial salt deposition density. It can be seen that at a fixed area of salt deposition, the pit diameter increased with increasing amount of salt per unit area.

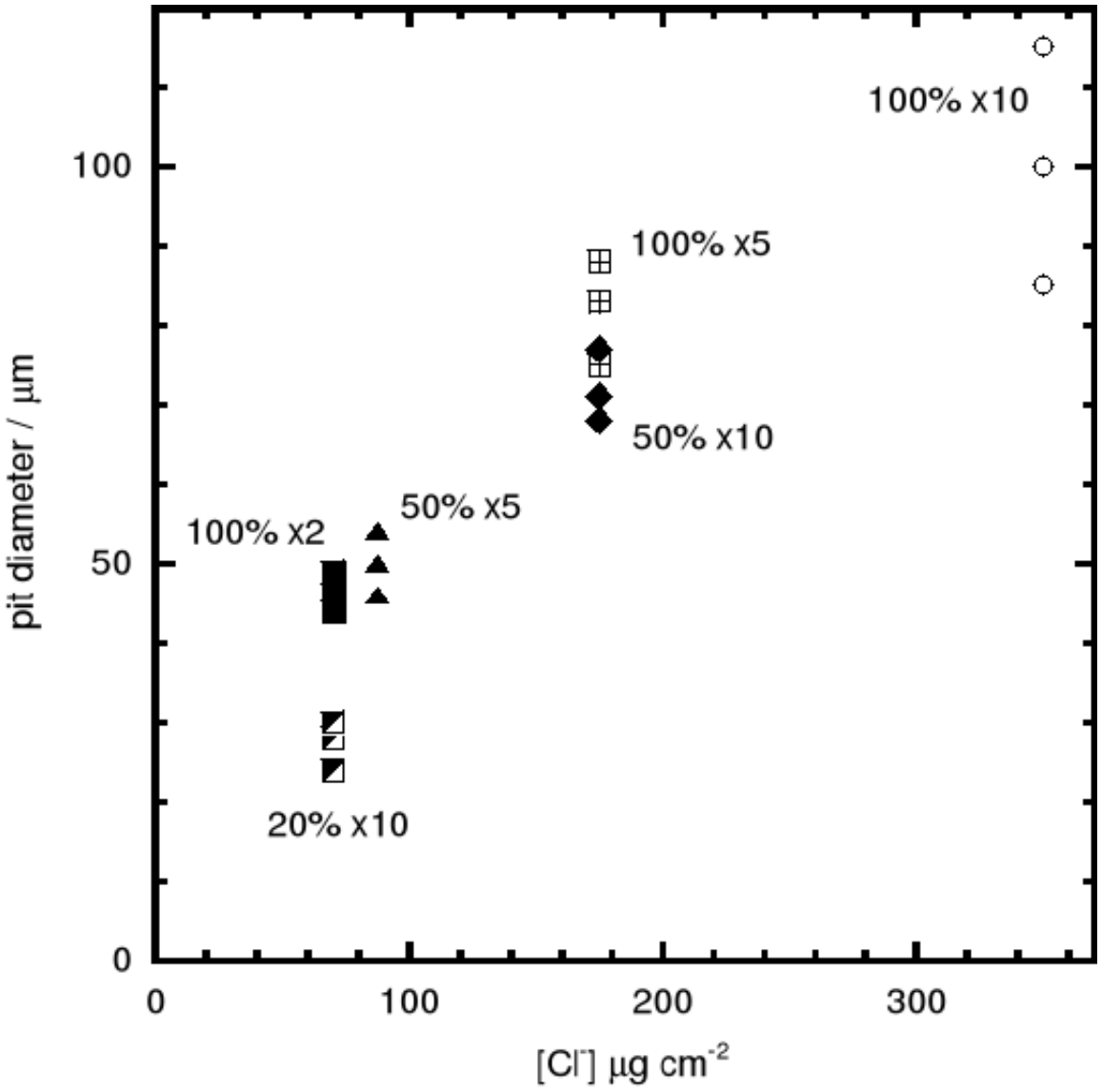

Figure 4-10 The pit diameter as a function of the printing variables (colour intensity and overprint times) for pits formed in 1.4 mm diameter $MgCl_2$ deposits (10x 100% colour intensity corresponds to a chloride deposition density of 350±50 µg/cm^2) on 304 stainless steel foil as shown in Figure 4-7 and Figure 4-8 following exposure at 45% RH and 300 K for 24 hours (after 1 hour at ~90% RH).

4.2.3 Effect of salt deposition method on pitting behaviour

The corrosion behaviour under dilute droplets of 50 mM $MgCl_2$ applied using a syringe pump was compared with that under droplets formed by deliquescence of printed $MgCl_2$ clusters deposited with the inkjet printer. A specific volume (1.6 µl) of liquid was delivered with the syringe pump, forming a droplet of ~2 mm diameter, although the exact area was not very reproducible. From the equation, $X_d = 1.7V_0^{0.35}$ [1], the chloride deposition density is estimated to be ~180 µg/cm^2. These droplets were compared with inkjet printing droplets formed by 10 times overprinting and 50% colour intensity (chloride deposition density is 175±25 µg/cm^2). Four routes of salt deposition were compared: (a) a droplet directly deposited with the syringe; (b) syringe droplet dried before exposure; (c) inkjet deposition with initial deliquescence at high humidity to form a continuous droplet before exposure (the method used for the results shown above); and (d) and (e) inkjet deposition without the initial deliquescence step. All samples were exposed for 24 hours in 45% RH, and pictures were taken to record the corrosion behaviour (Figure 4-11). Figure 4-11 shows that the corrosion behaviour of syringe-formed droplets was similar irrespective of whether the droplet was dried out (a) or not (b). The behaviour of these syringe-formed droplets was similar to the inkjet printed salt area that was subjected to 1 hour initial hydration. However, if the inkjet printed area was not deliquesced prior to exposure, it would sometimes form a continuous droplet (d) or sometimes a discontinuous droplet (e), which can lead to inconsistent results.

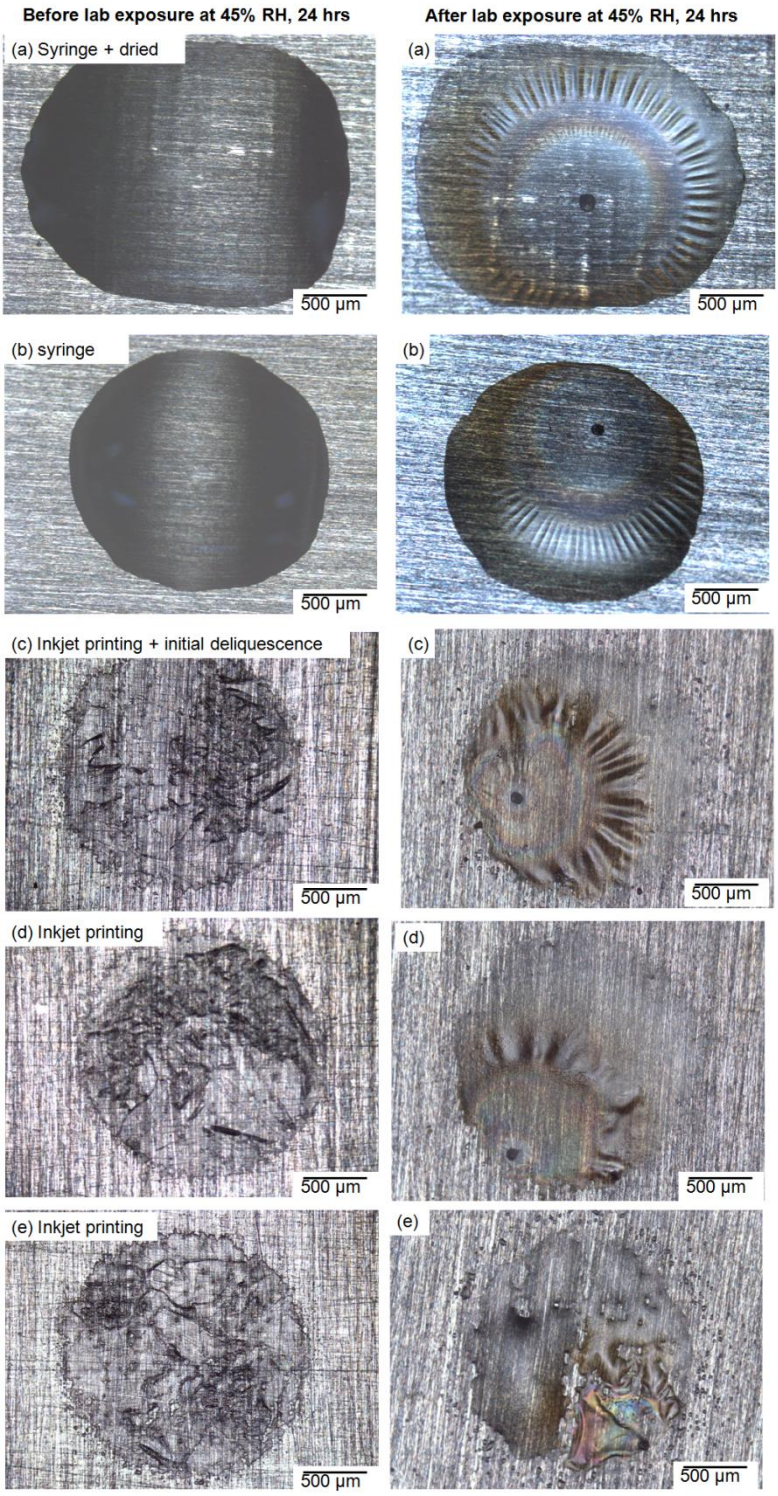

Figure 4-11 Optical images of $MgCl_2$ salt droplets formed by different routes before and after lab exposure at 300 K, 45% RH for 24 hours. (a) 1.6 µl syringe droplet (~2 mm diameter) of 50 mM $MgCl_2$ dried and placed in lab exposure; (b) 1.6 µl syringe droplet (~2 mm diameter) of 50 mM $MgCl_2$ directly placed in lab exposure; (c) 10x 50% colour intensity printed area of 2 mm diameter with initial deliquescence; (d) and (e) 10x 50% colour intensity printed area of 2 mm diameter directly placed in lab exposure.

4.3 Discussion

The results show that salt deposition with an inkjet printer is an effective way to obtain consistent results on the growth of atmospheric corrosion pits. Greater consistency of results is obtained if the salt is initially deliquesced at high humidity, decreasing the risk of formation of discontinuous droplets as shown in Figure 4-11. However, under realistic conditions of exposure, a variable atmospheric corrosion response may result from the presence or absence of initial fluctuations in humidity.

Salt can be deposited in patterns with controlled shapes and sizes, which are easily designed with Microsoft PowerPoint or any similar drawing software that allows printing of patterns with controlled dimensions and colour intensity. Higher salt densities can be obtained by over-printing (providing the pattern is dried after each pass to avoid smearing). Figure 4-7 shows that similar corrosion behaviour is found for patterns with 20% colour intensity overprinted 5 times compared with a single print with 100% colour intensity. The method can also be extended to deposit multiple salts from the different ink cartridges in combinatorial arrays.

A possible reason for the limited secondary spreading and the formation of discontinuous droplets is the relatively poor wetting behaviour of $MgCl_2$ droplets. Tsuru et al. [14] found that NaCl droplets would spread out from the primary wet area and form micro-droplets around the initial primary droplet, while the expansion of the wet area in the $MgCl_2$ droplet was limited. The cathodic reaction takes place predominantly at the edge of the droplet since this is the region for easiest access of oxygen. The cathodic reaction results in the local formation of OH^- ions, and the charge is balanced by metal cations. For NaCl solutions, Na^+ ions remain in solution. However, for $MgCl_2$ solutions, relatively insoluble magnesium hydroxide can form at the edge of the droplet and this can block droplet spreading [14, 83]. Thus in the $MgCl_2$ solution, the secondary spreading should be limited: this is consistent with the observation of little droplet spreading in the present work.

Since $MgCl_2$ droplets do not generally spread significantly beyond the original printed area, the area available for the cathodic reaction will increase with printed area. In Figure 4-5, it is evident that the pit diameter increased with the increasing initial printed deposition area, which is consistent with the theory of cathodic limitation [1, 109]. A larger cathodic area would supply more cathodic current, which will increase the pit growth rate. [1, 111]

Figure 4-10 shows that for the same initial deposition area, the pit diameter increases with an increased amount of salt deposition. Since the area of the droplet is the same as the initial deposition area, changes in pit diameter cannot be directly attributed to changes in the cathode area. For measurements at controlled humidity and controlled droplet area, an increase in the salt deposition density will increase the height of the droplet since the salt concentration in the droplet is controlled by the humidity. The droplet height can have two possible effects: if the oxygen reduction rate is under diffusion control, [18] then a thicker droplet should decrease the rate of the cathodic reaction, leading to smaller pits. However, if ohmic effects dominate, [16, 110] then for a fixed humidity, a higher droplet will lead to a lower approach resistance to the pit, leading to a higher pit current density. In the present work, the pit size is found to increase with salt deposition density (for a fixed cathode size and relative humidity), consistent with ohmic effects. However, it should also be noted that there may also be some effect associated with the initial hydration phase: for a higher salt deposition density and continuous droplet is likely to form more quickly, leading to a greater initial corrosion rate.

4.4 Conclusion

1. Inkjet printing is an effective method for production of salt deposition in patterns, which can be used for atmospheric corrosion measurements.

2. More consistent results are obtained if the salt deposits are fully hydrated at high humidity prior to placing in lower humidity environments; such measurements are consistent with results from droplets formed with a syringe pump.

3. For a given $MgCl_2$ salt deposition density on 304 stainless steel, the pit diameter increases with the original deposition diameter, which is consistent with the idea of cathodic limitation of the pit current.

4. For a constant deposition area, the pit diameter increases with increased salt deposition density: this may be associated with a lower ohmic drop resulting from a higher droplet.

5 Synchrotron micro-tomography studies of atmospheric pitting corrosion of stainless steel

5.1 Introduction

The aim of the present work is to demonstrate the feasibility of applying synchrotron X-ray micro-tomography to visualise the morphology of atmospheric corrosion pits and electrolyte layers, and to quantify the rate of pit growth. Atmospheric pits were visualised in-situ in order to study the time dependence of pit propagation. The work was carried out at I12, the Joint Engineering, Environmental and Processing (JEEP) beamline at Diamond Light Source, United Kingdom.

5.2 Tomographic observation of atmospheric pitting corrosion

Figure 5-1 shows typical horizontal and vertical section views, and a segmented 3D view of a $MgCl_2$ electrolyte layer on a stainless steel pin surface after reconstruction of the tomographic image. Figure 5-1 (a) shows that the corrosion pits are visible at two positions on the surface, both of which are closer to the perimeter of the pin than the centre. The vertical section of Figure 5-1(b) was taken through the larger pit where it can be seen that the pit morphology is shallow. The electrolyte layer is thin and has a 'dome' shape. An inclusion or a defect in the material matrix can also be observed. Since the X-ray transmission through the electrolyte layer, pit and the metal pin are different, shown by a different grey level, the tomographic data can be segmented into different fields. The fields can be segmented and rendered as a 3D tomographic image shown in Figure 5-1(c).

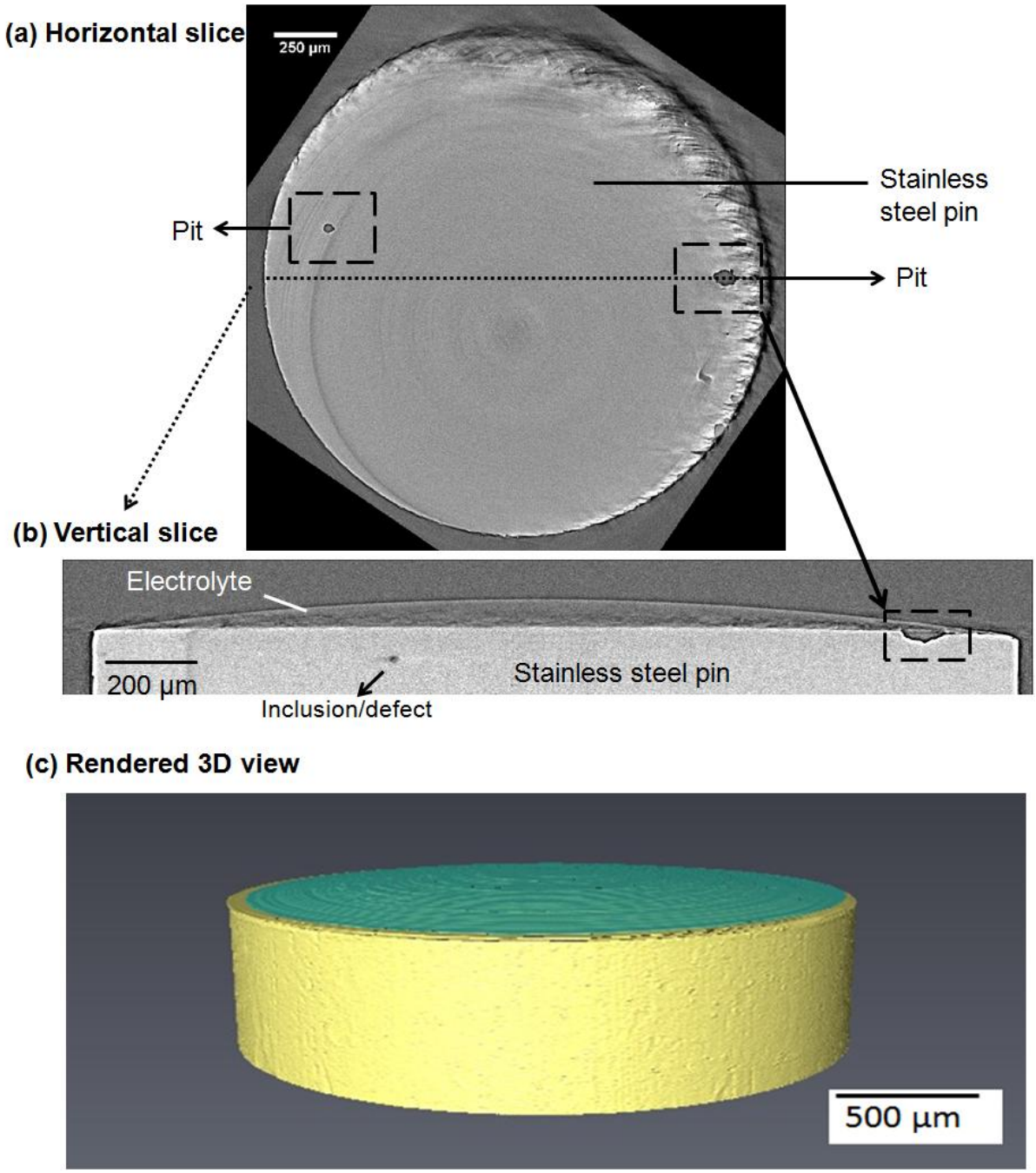

Figure 5-1 A typical (a) horizontal, (b) vertical and (c) rendered 3D views of a stainless steel pin exposed at 21±1°C and 45% RH for 34 hours. The stainless steel pin is covered with $MgCl_2$ solution, and the chloride deposition density is 1000 µg/cm^2. Images are taken after 34 hours following deposition. In (c), the metal is shown in yellow and the electrolyte layer ($MgCl_2$) solution is in green.

5.3 Electrolyte layer

5.3.1 Electrolyte layer data analysis

Typical 3D and 2D views of the electrolyte layer are shown in Figure 5-1. The volume of the electrolyte layer shown in Figure 5-1 was quantified with Avizo software®. The image segmentation process is associated with both threshold and personal judgement. The top of the electrolyte layer, the electrolyte has an elliptical shape, which is segmented via the ellipse selection tool in Avizo software (Figure 5-2). The electrolyte layer close to the top surface of the metal pin is segmented differently, since both of the electrolyte layer and the metal part can be shown in a horizontal view (Figure 5-3). This is probably caused by not placing the metal pin in a completely horizontal position, or the top surface is not totally flat. To segment the electrolyte layer on the same horizontal slice with a proportion of the metal pin as shown in Figure 5-3, the pin horizontal view is first assumed to be fully covered with the electrolyte layer, then a threshold selection tool in Avizo was used to vary the threshold to select the region of the metal part on the pin horizontal view. The electrolyte layer was segmented by deleting the metal part on the pin horizontal view from the fully covered view. Figure 5-4 shows a vertical section of the reconstructed data (left) compared with the same section followed by segmentation of the electrolyte layer with Avizo (right) . It can be seen that the segmentation is relatively well matched with the reconstruction data at the top surface of the electrolyte layer, but is not well matched in the region close to the surface of the metal pin.

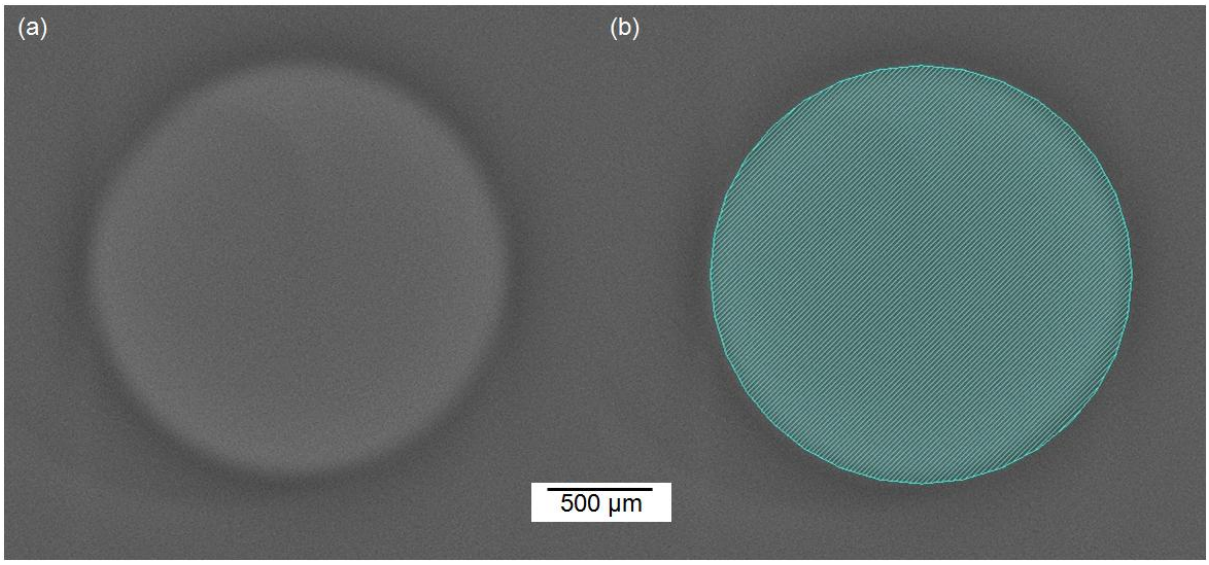

Figure 5-2 A 2D horizontal section of the reconstructed data shown in Figure 5-1, through the upper part of the electrolyte layer (a) compared with the electrolyte segmentation by Avizo (b). The blue shadowed region shows the segmented electrolyte by ellipse tool in Avizo. The stainless steel pin is covered with $MgCl_2$ solution, and the chloride deposition density is 1000 µg/cm^2 , and is exposed at 21±1 °C and 45% RH for 34 hours.

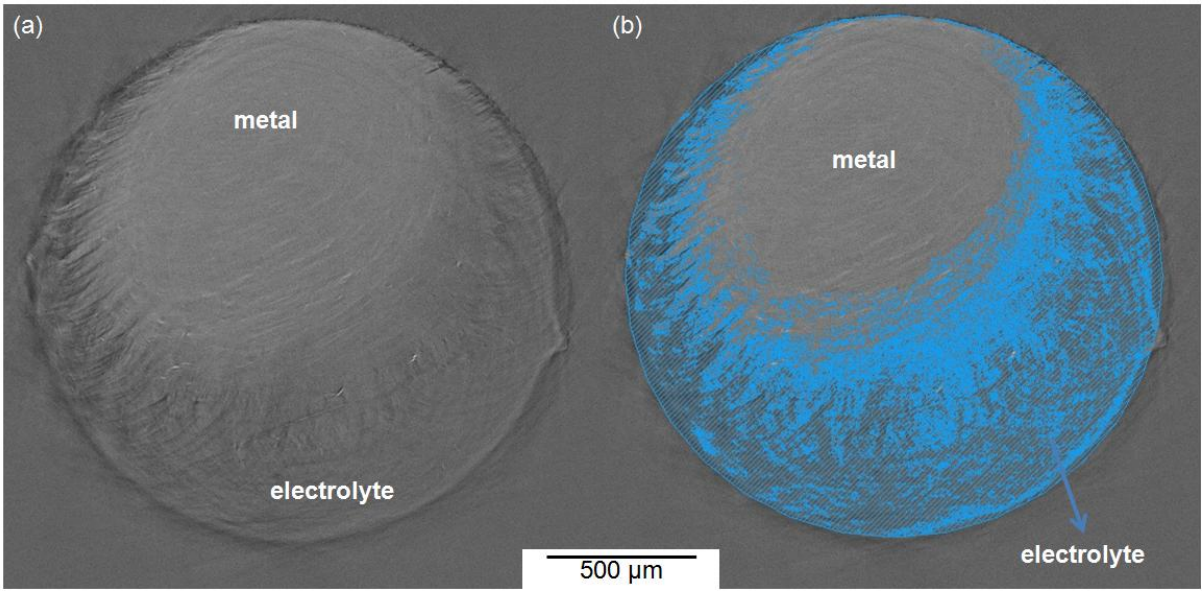

Figure 5-3 A 2D horizontal section of the reconstructed data from Figure 5-1 through the electrolyte layer close to the top surface of the metal pin (a) compares with the electrolyte segmentation by Avizo (b). The blue shadowed region shows the segmented electrolyte in Avizo. The stainless steel pin is covered with $MgCl_2$ solution, and the chloride deposition density is 1000 µg/cm^2 , and is exposed at 21±1 °C and 45% RH for 34 hours.

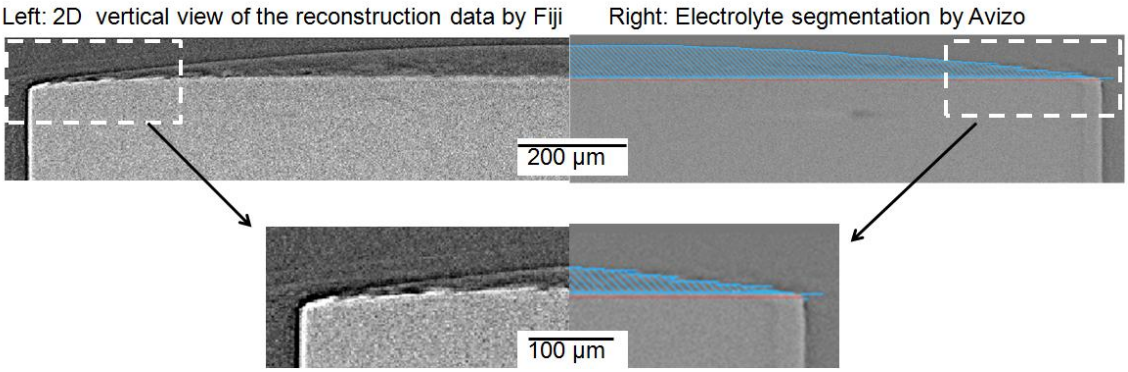

Figure 5-4 The 2D vertical view of the reconstructed data (left) compared with the electrolyte segmentation by Avizo (right). The blue shadowed region is the vertical view of the segmented electrolyte layer.

Two identical samples were prepared with a chloride deposition density of 1000 µg/cm^2 and exposed to 45% RH for 17 hours. This was carried out by depositing a volume of 1.77±0.07 µl of 0.25 M $MgCl_2$ solution (0.5 M chloride solution) by a micropipette and equilibration at 45% RH. Since 45% RH has the same water activity as ~8.4 M $MgCl_2$ [1] and the amount of salt deposition is known, the theoretical volume of the electrolyte layer can be calculated as Equation 5-1, where $C_{original}$ is the original chloride deposition concentration 0.5 M, $V_{original}$ is the original chloride deposition volume 1.77±0.07 µl, $C_{theoretical}$ is the theoretical electrolyte chloride concentration at equilibrium 8.4 M. The theoretical volume of the electrolyte layer is 0.105±0.004 µl.

$$V_{theoretical} = \frac{C_{original} V_{original}}{C_{theoretical}} \qquad \text{Equation 5-1}$$

In order to check the consistency of the segmentation process, the volume of the electrolyte layer on each sample was calculated twice via manual segmentation with Avizo: the results are shown in Table 5-1. The error in the segmentation due to manual judgment is about 3%. It is then possible to cross-check the volumes and hence quantities of electrolyte deposited onto the stainless steel pins via tomography.

Table 5-1 The comparison of the volume of the segmented electrolyte layer with the theoretical volume of 1000 µg/cm^{2}chloride deposition density $MgCl_2$ solution on stainless steel pin exposed at 21±1 °C, 45% RH for 17 hours. The segmented volume has been measured twice for both samples.

Theoretical volume (µl)	Segmented volume Sample 1 (µl)	Segmented volume Sample 2 (µl)
0.105±0.004	0.083	0.105
	0.085	0.104

Table 5-1 shows the segmentation of the electrolyte volume of sample 1 is about ca 20% lower than the theoretical volume, and the segmented volume of the electrolyte of sample 2 is very close to the predicted volume. This discrepancy is possibly due to the deposition process. It is also possibly caused by the small difference of the image contrast between the air and electrolyte: some voxels of electrolyte layer are not included during the data analysis. However for the data in Table 5-1, the electrolyte layers on both samples were segmented twice, and the difference of the segmentation due to manual analysis is about 3%. Thus it is more likely that the difference between the theoretical volume and the segmented volume has arisen due to loss of the electrolyte volume during electrolyte deposition.

5.3.2 Time dependence of electrolyte layer morphology

Figure 5-5 shows the electrolyte layer on the stainless steel pin during a series of measurements over a period of ~80 hours. There is no obvious change in the electrolyte layer morphology. The volume of the electrolyte layer with time dependence is segmented by Avizo, and the result is shown in Table 5-2. The change of the volume of the electrolyte layer is less than 5% with time dependence, which means that the relative humidity control is fairly stable during the experiment.

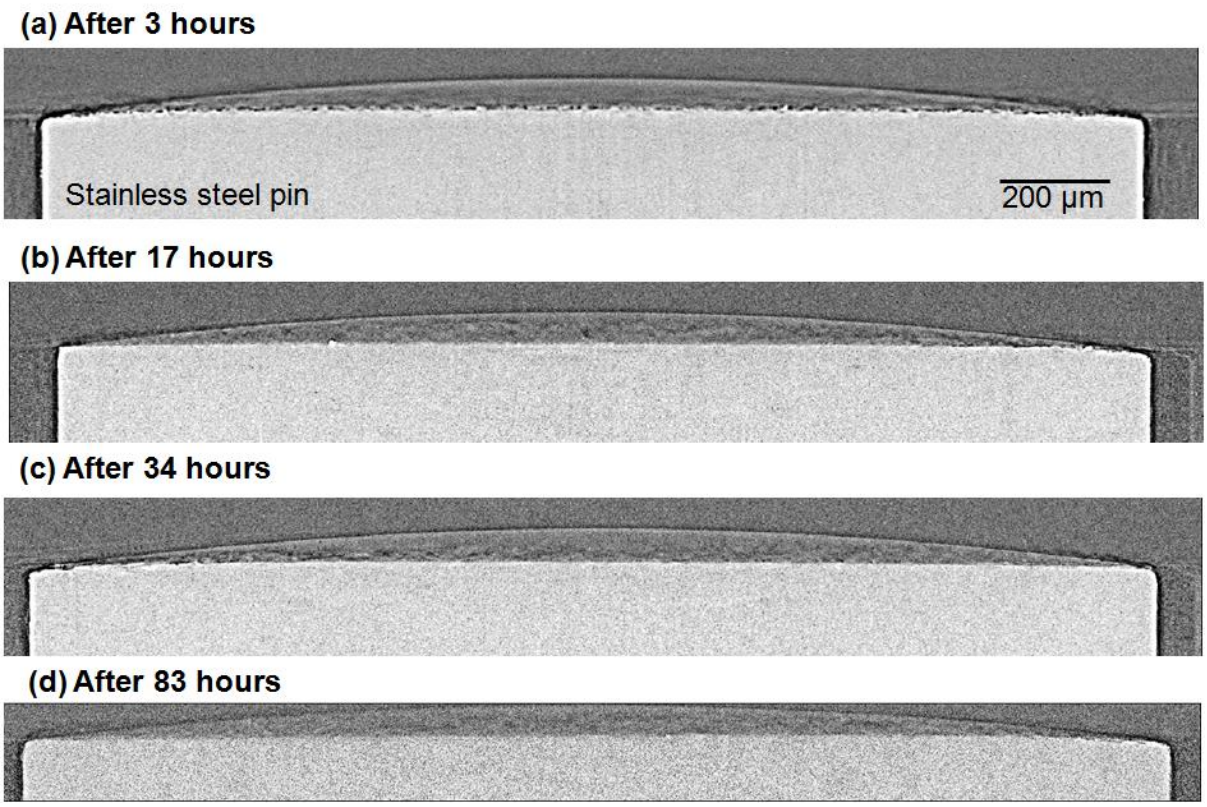

Figure 5-5 Sectional views showing the time dependence of $MgCl_2$ electrolyte after deposition (a) 3 hours (b) 17 hours, (c) 34 hours and (d) 83 hours on a 2 mm stainless steel 304 pin at 21±1 °C and 45% RH. The chloride deposition density is 1000 µg/cm^2.

Table 5-2 Time dependence of electrolyte volume obtained via image segmentation. The electrolyte layers are the same as Table 5-1. The electrolyte layer on both samples after 17 hours following deposition was segmented twice. An error of ±0.002 is based on the repeated segmentation of the two electrolyte layers.

Time (hours)	Segmented volume Sample 1 (µl)	Segmented volume Sample 2 (µl)
3	0.087	0.102
17	0.083±0.002	0.105±0.001
34	0.082	0.099
83	0.081	-

5.3.3 Effect of chloride deposition density on electrolyte layer morphology

The electrolyte layer morphology is affected by the salt deposition density. Figure 5-6 shows vertical sections of electrolyte layers for a range of salt deposition densities.

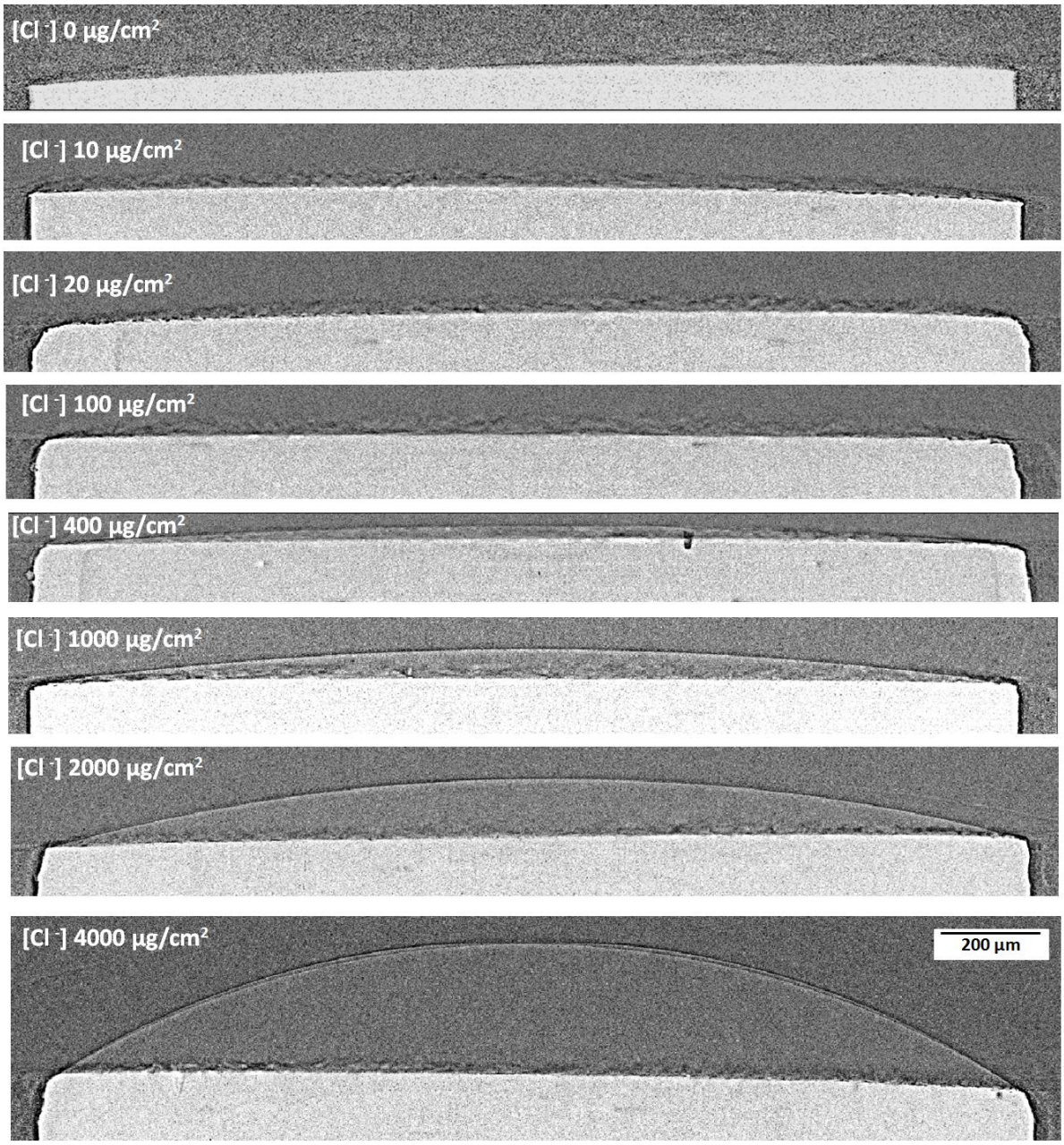

Figure 5-6 Vertical sections of $MgCl_2$ electrolyte layer morphologies as a function of chloride deposition density on stainless steel 304 2 mm pins at 21±1 °C and 45% RH. The deposition density is shown in the figure.

The electrolyte layers for the 0, 10, 20 and 100 μg/cm^2 chloride deposition density samples are difficult to see. For all measurements, the region just above the pin surface has a mottled appearance. This may be due to X-ray scattering from the stainless steel pin surface, which may behave as a rather poor quality X-ray grazing incidence mirror. X-rays may be reflected by the mirror due to a small angle of incidence forming bright and dark regions. As the sample surface was rotating during the experiment, the "mottled" layer may be an irregular scattering effect.

A distinct edge to electrolyte layer can be visualised when the deposition density is 400 μg/cm^2 or above, which makes segmentation feasible. In the current work, two samples were prepared with chloride deposition densities of 400 and 1000 μg/cm^2, and one sample was prepared with chloride deposition densities of 2000 and 4000 μg/cm^2. The segmented volume of the electrolyte layer for these different deposition densities is shown in Table 5-3. The difference between the segmented volume of the electrolyte layer and the predicted volume lies in the range from 1% to 20%.

A comparison between the predicted and measured volume is shown in Figure 5-7. It can be seen that there is a very good correlation. The experimental segmented volume lies in a linear line close to the predicted volume, which suggests the deposition density and relative humidity control is reasonably good. The segmented volume line is slightly lower than the predicted volume line, which is possibly due to the error in the deposition process or some uncertainty of the segmentation process.

Table 5-3 The segmented volume of the electrolyte layer with different chloride deposition density on 2 mm stainless steel pin exposed at 21±1 °C, 45% RH for 24 or 34 hours. The segmented volumes are also compared with the theoretical volume.

Chloride deposition density (μg/cm^2)	Segmented volume (μl)	Theoretical volume (μl)	Error
400	0.039, 0.040	0.042	7%, 5%
1000	0.083, 0.105	0.104	20%, 1%
2000	0.173	0.208	17%
4000	0.393	0.416	6%

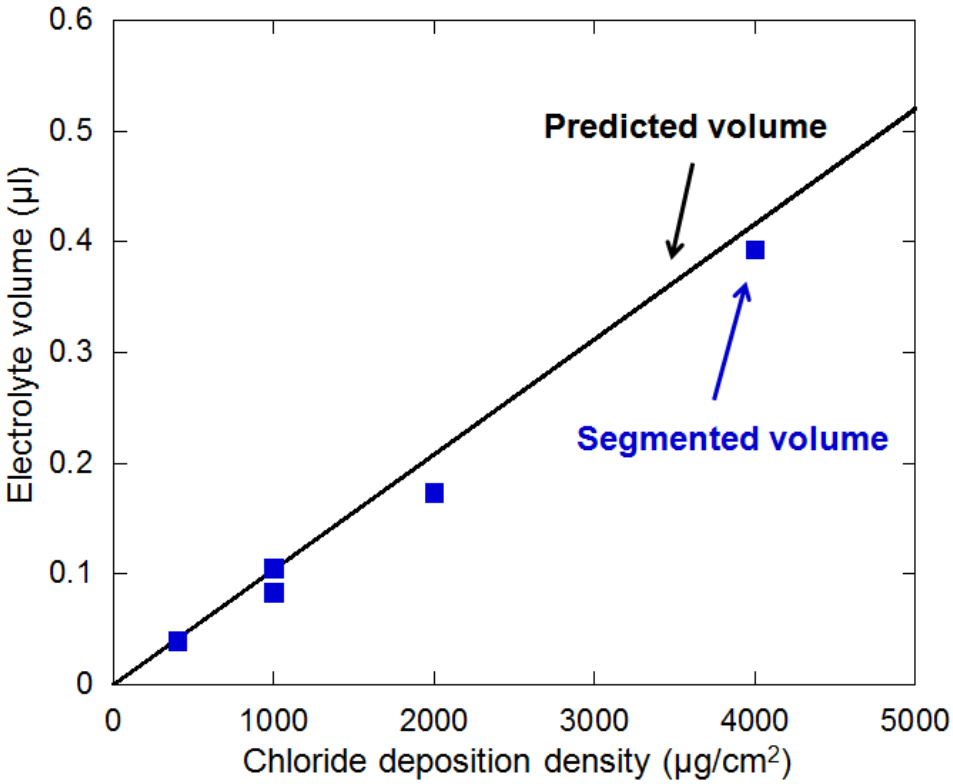

Figure 5-7 The segmented volume and theoretical volume of the electrolyte vs. chloride deposition density.

5.3.4 Formation of micro-droplets and corrosion products on the side of a pin

In the course of an experiment, it is possible that electrolyte can spread from the top surface of the pin to form micro-droplets on the side. The spreading of the electrolyte down the side of the pin might cause localised corrosion and form corrosion products. Micro-droplets and corrosion products on the side of the pins are randomly observed on the samples exposed for 17 hours. A typical example of a vertical section of a micro-droplet and corrosion products is shown in Figure 5-8. Formation of a micro-droplet on the side of a pin can lead the chloride deposition density to be less than the amount of deposition.

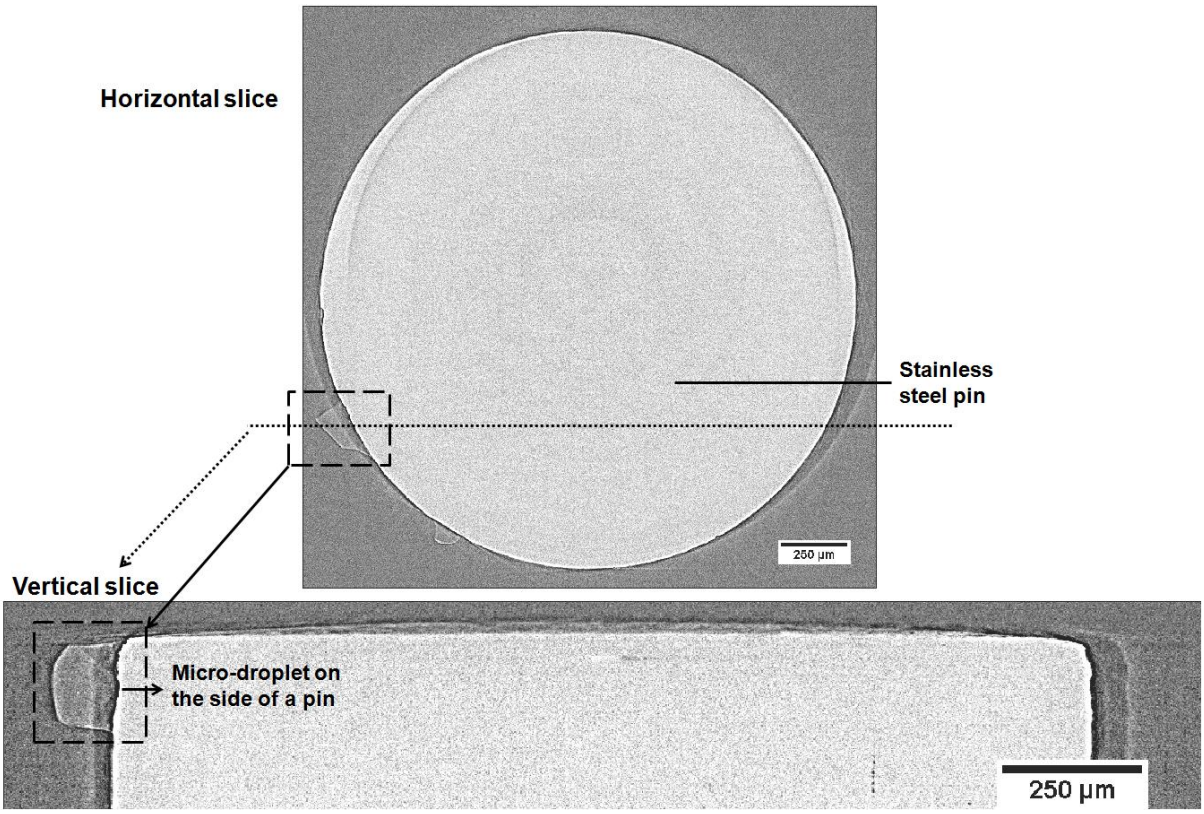

Figure 5-8 A micro-droplet formed on the side of a stainless steel pin at 21±1 °C and 45% RH after 34 hours. The theoretical chloride deposition density on the pin surface was 400 µg/cm^2, but the height of the droplet is less than that seen for a chloride deposition density of 400 µg/cm^2 in Figure 5-6.

5.4 Quantification of atmospheric pitting corrosion of stainless steel

5.4.1 Pitting corrosion data analysis

Segmentation can also be used to quantify the size of pits with the semi-automatic "blow" tool in Avizo: a point is selected in the centre of the pit to determine the grey level that corresponds to the pit interior. The point is then dragged to a location on the edge of the pit. The software then selects the rest of the edge of the pit according to the grey scale at the edge point selected.

Figure 5-9 illustrates how the 'blow' tool is applied to segment the larger pit shown in Figure 5-1. Figure 5-9 (a) shows a horizontal 2D section through a reconstructed image of a pit and Figure 5-9 (b) shows the result (purple shadow area) of semi-automatic segmentation. A 3D

view of the segmented pit is shown in Figure 5-9 (c). The pit top surface is set by comparing the segmented pit mouth area with the pit mouth area measured by SEM and confocal microscopy, and comparing the segmented pit depth profile with the profile measured by confocal microscope. The top surface is selected with the most similar horizontal and vertical view.

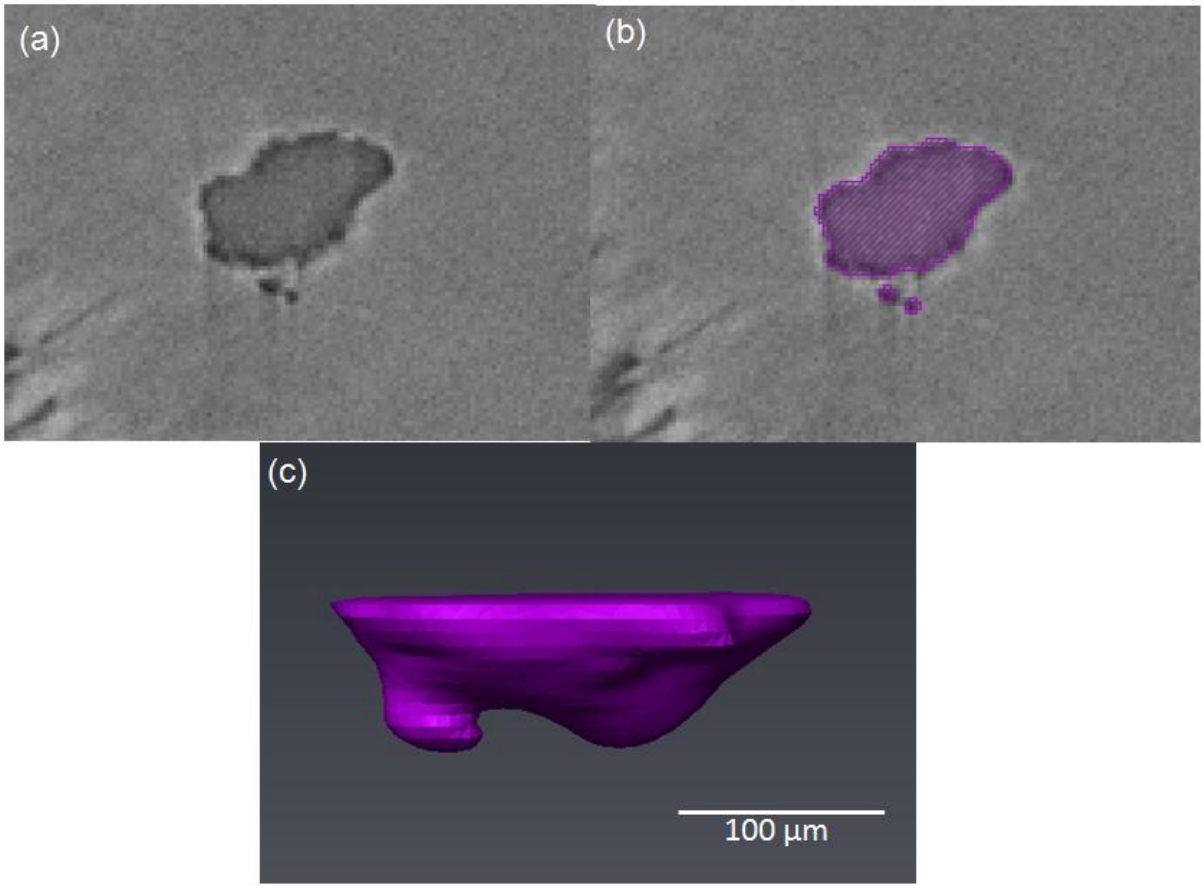

Figure 5-9 The 2D horizontal view of the reconstruction data (a) of the larger pit showing in the horizontal and vertical view in Figure 5-1 compared with the pit segmentation by the blow tool in Avizo (b). The purple shadowed region shows the segmented pit by threshold. (c) is the 3D view of the pit after segmentation. The stainless steel pin is covered with $MgCl_2$ solution, and the chloride deposition is 1000 µg/cm^2. The exposure conditions are 21±1°C and 45% RH for 34 hours.

A primary use of the segmentation process is to provide information of the pit volume. To validate the quantification of the pit diameter, depth and volume derived from X-ray micro-tomography, SEM and confocal microscope techniques have been used to provide independent measurements of the pit mouth area and the pit volume.

One typical pit was selected for comparison. The pit was the same one shown in Figure 5-1. Figure 5-10 shows a comparison of 2D horizonal, 2D vertical and 3D views of this pit by SEM, confocal microscope and X-ray micro-tomography measurements.

Figure 5-10 (b) shows the pit surface horizontal view measured by SEM. The SEM image was used to cross-check the surface features of the pit and compared with the X-ray micro-tomography horizontal view (Figure 5-10 (a)), and determine the top surface of the pit. This is done by comparing the top surface feature and pit mouth area. It can be seen that the pit surface feature in Figure 5-10 (b) is very similar to the feature shown in Figure 5-10 (a). The SEM image of the pit might indicate that there are small active pits grown in the main pit. The small pits grown inside the main pit can be further confirmed in the 3D view by the micro-tomography and confocal microscopy measurement (Figure 5-10 (e) and (f)).

Due to the phase contrast enhancement between the metal pin and the electrolyte, it is difficult to determine the top surface of the pit from the vertical view measured by X-ray micro-tomography. The pit depth profile measured by confocal microscopy can be used to cross-check the top surface of the pit. Figure 5-10 (d) shows the 2D vertical view of the pit, and the plateau of the depth profile is determined as the top surface of the pit. The top surface is finally determined by both comparing the 2D horizontal view measured by SEM (Figure 5-10(b)) and the 2D vertical view measured by confocal microscopy (Figure 5-10(d)).

The confocal microscopy is also used to cross-check the 3D morphology of the pit. Figure 5-10(e) and (f) show the 3D views of the pit measured by X-ray micro-tomography and confocal microscope. Figure 5-10(f) shows that the pit has a shallow and semi-ellipsoid shape and small pits grown in the main pit measured by confocal microscopy, which is consistent with the X-ray micro-tomography measurement shown in Figure 5-10(e).

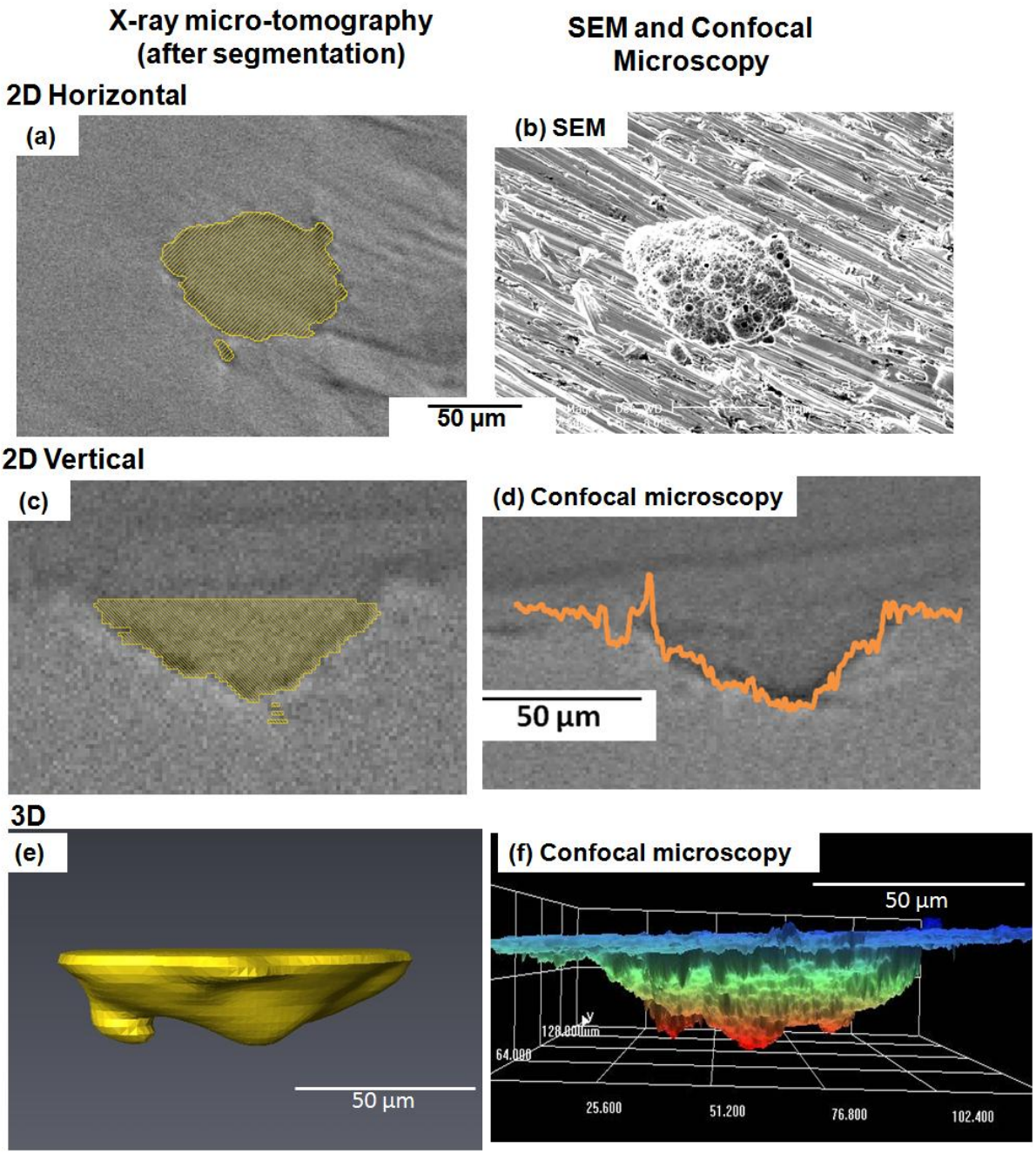

Figure 5-10 The 2D horizontal, vertical and 3D views of the pit shown in Figure 5-1 measured by SEM, confocal microscopy, and X-ray micro-tomography. The pit is on the stainless steel pin covered with $MgCl_2$ solution, and the chloride deposition is 1000 µg/cm^2. The pin has been exposed at 21±1°C and 45% RH for 83 hours.

Table 5-4 compares the results of segmentation for pit mouth area, depth and volume measured by X-ray micro-tomography, SEM and confocal microscopy. The pit mouth area measured by X-ray micro-tomography is similar to the surface area measured by SEM and confocal microscopy, which confirms that the selection of the pit mouth by semi-automatic segmentation is reasonable. The pit depth measured by confocal microscopy is slightly lower than the pit depth measured by X-ray micro-tomography, which is probably due to the limitation of the confocal microscopy caused by the noise of the reflection of the beam. There is a significant difference between the pit volume measured by X-ray micro-tomography compared with that measured by confocal microscopy. Two reasons are possible: firstly, the confocal microscope can only scan from the top of the sample and uses the reflection of the beam to estimate the pit volume, whereas X-rays penetrate through the sample and use projections to reconstruct tomographic data. Any regions of a pit that are underneath overhanging metal will not be detected by confocal microscope. A typical example which might explain the difference of pit volume is shown in Figure 5-11, which shows vertical views of a pit in which there are small pits that propagate under the surface of the main pit. It can be seen that the two small pits were not detected by confocal microscopy, while they can be visualised by X-ray micro-tomography. Secondly, some of the voxels might be included in the pit volume during the segmentation process due to the X-ray scattering at the pit edge. However, it is possible that more voxels are included as the pit volume during the segmentation process of X-ray micro-tomography. It is also possible that the determination of the top surface of the metal affects the pit volume segmentation result.

Table 5-4 The pit mouth area, pit depth and pit volume measured by SEM and confocal microscope compared with the X-ray micro-tomography measurement.

Method	Pit mouth area (μm^2)	Pit depth (μm)	Pit volume (μm^3)
SEM	4450	-	-
Confocal microscopy	4500	28	56000
X-ray micro-tomography	4500	30	71000

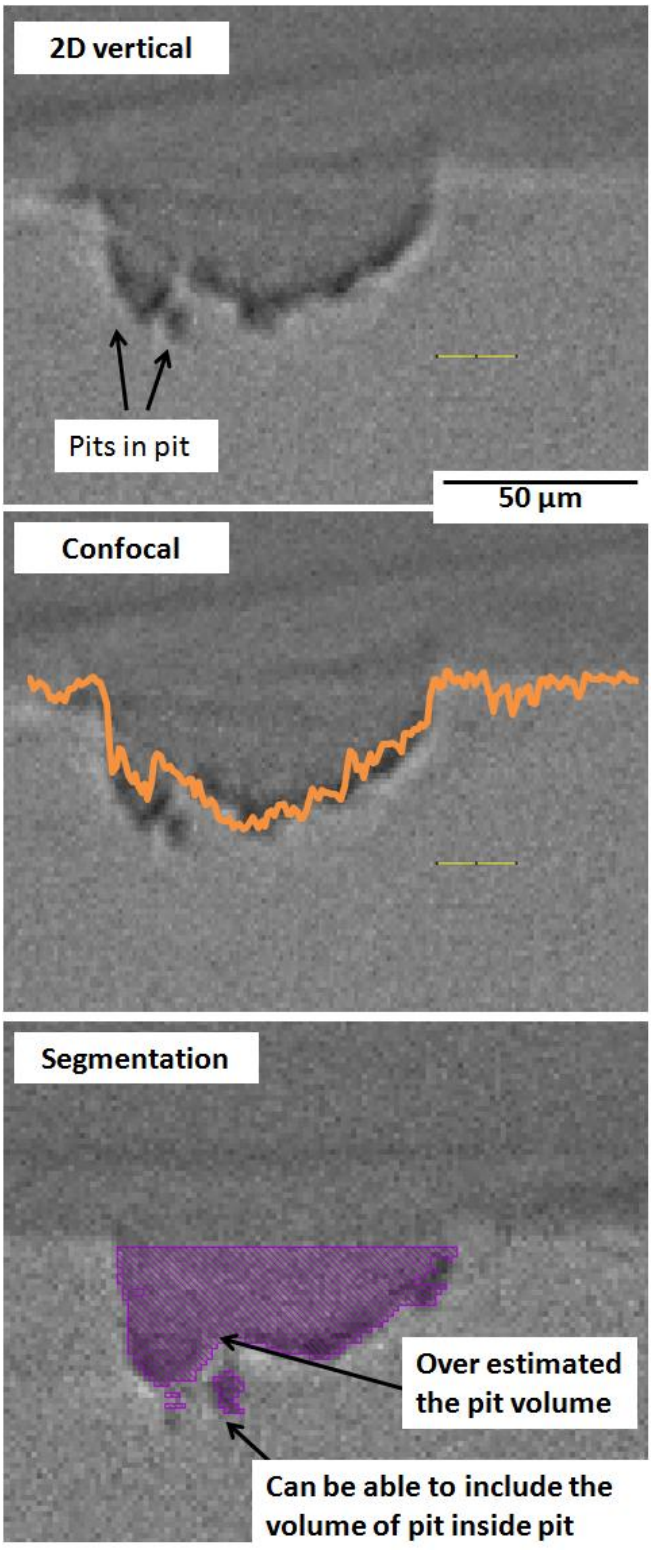

Figure 5-11 The pit depth profile measured by the confocal microscope (orange line), and the segmented pit profile (purple region) of micro-tomography measurement compared with the 2D vertical view of the pit. The pit is on the stainless steel pin covered with $MgCl_2$ solution, and the chloride deposition is 1000 µg/cm^2. The pin has been exposed at 21±1°C and 45% RH for 83 hours.

5.4.2 Dish-shaped pit

Figure 5-12 displays a series of images which illustrate the time dependence of the growth of a dish-shaped pit. This pit morphology is the most common in all experiments. It can be seen that after three hours, a shallow pit is formed but a small hole is present at the bottom of most pits. The pit grows larger after 17 hours, and grows slightly larger after 34 hours, but the increase of volume is not as obvious by eye as the increase which occurs between 3 hours and 17 hours.

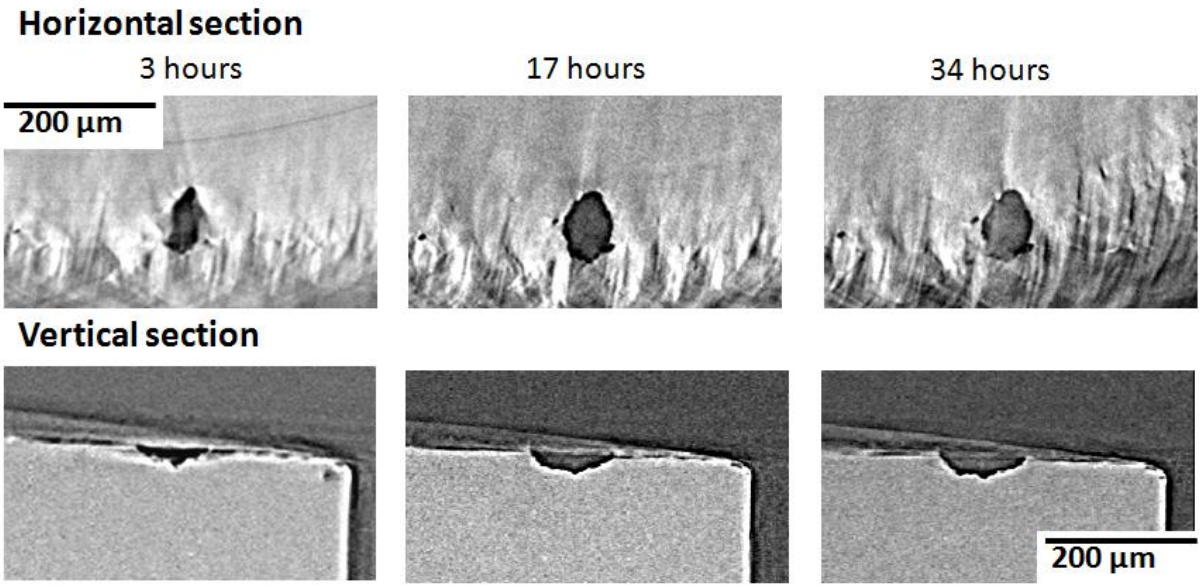

Figure 5-12 Time-dependent sequence of atmospheric pit growth on one stainless steel pin. The pit has a shallow dish shape. The exposure conditions: chloride deposition density 1000 µg/cm^2, 21±1°C and RH 45%.

The dish-shaped pit shown in Figure 5-12 after 34 hours is the same pit that was measured in Figure 5-10 and Table 5-4 in which the segmented pit has been compared with the SEM and confocal microscope measurements in 2D and 3D views. Table 5-5 shows the evolution with time of the pit diameter, depth and volume. The average pit diameter (D) is calculated from the measured pit surface area (S) by Equation 5-2:

$$D = 2\sqrt{(S/\pi)} \qquad \text{Equation 5-2}$$

The pit depth is directly measured and the pit volume is calculated via the segmentation process. The results in Table 5-5 are plotted in Figure 5-13. It can be seen that initially, the pit diameter increases rapidly, but does not increase after 17 hours, while the pit depth has a trend to increase continuously. The pit volume increases fast initially, then increases slowly after 17 hours. This possibly indicates that the pit initially grows horizontally, and then grows vertically.

Table 5-5 The pit diameter, depth and volume increase with the exposure time. The pit diameter is calculated from the pit surface area. The pit is on the stainless steel pin 304 exposed at 21±1°C and 45% RH shown in Figure 5-12. The stainless steel pin is covered with $MgCl_2$ solution, and the chloride deposition is 1000 μg/cm^2.

Exposure time (hours)	Pit diameter (μm)	Pit depth (μm)	Pit volume (μm^3)
3	57.6	21	22000
17	75.2	24	57000
34	75.2	27	66000
83	75.2	30	71000

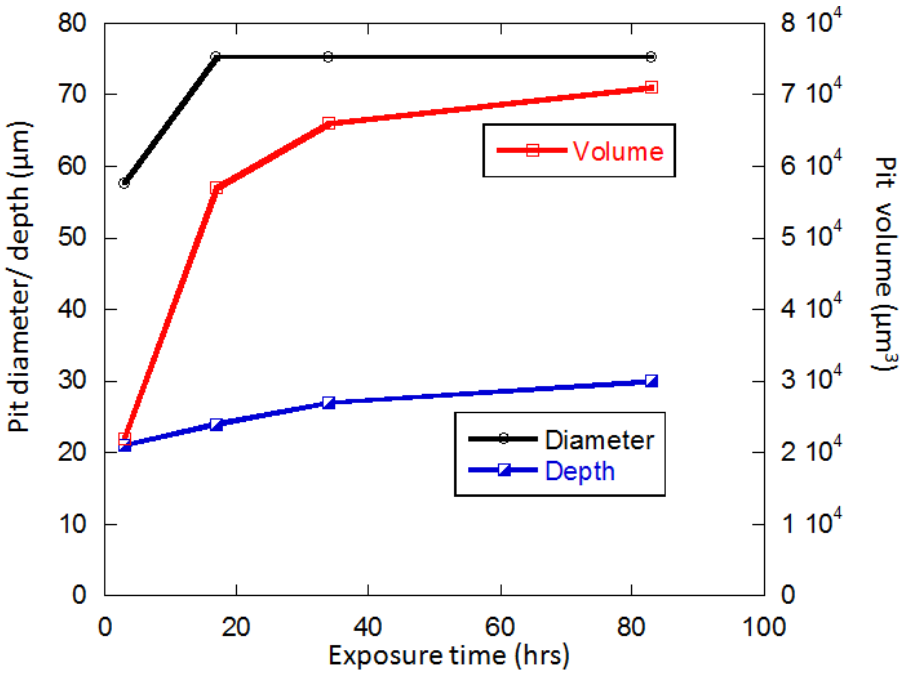

Figure 5-13 Pit diameter, depth and volume vs. the exposure time. The pit diameter is calculated from the pit surface area. The pit is on the stainless steel pin 304 exposed at 21±1°C and 45% RH as shown in Figure 5-12. The stainless steel pin is covered with $MgCl_2$ solution, and the chloride deposition is 1000 µg/cm^2.

5.4.3 Inclusions and defect within the stainless steel

In Figure 5-12, it may be seen that there is a small hole present at the bottom of the pit. The cause of this depression is not known but it is likely to be a legacy of a dissolved inclusion which is a typical site for pit initiation. The inclusions were characterised with EDX for the material used for these micro-tomography experiments, and found to be MnS and mixed oxides of Al_2O_3, SiO_2 and MgO. The SEM image and EDX analysis of the inclusion is shown in Figure 5-14.

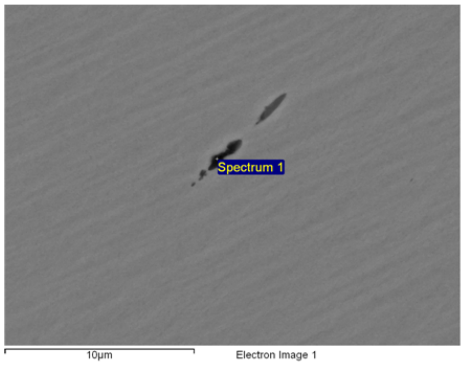

Inclusion composition

Element	Weight%	Atomic%
C K	1.9	5.8
O K	10.4	24.5
Mg K	0.5	0.8
Al K	11.0	15.3
Si K	0.3	0.4
S K	2.3	2.7
Ca K	0.9	0.8
Ti K	0.9	0.7
Cr K	14.7	10.6
Mn K	4.8	3.3
Fe K	47.4	31.9
Ni K	4.9	3.2
Totals	100.00	

Base material composition

Element	Weight%	Atomic%
C K	1.9	8.2
Cr K	19.2	19.1
Fe K	71.2	65.9
Ni K	7.7	6.8
Totals	100.00	

Figure 5-14 A SEM image and the EDX analysis of an inclusion in a polished sample of taken from the batch material used to prepare the stainless steel pins.

5.4.4 A special example of a shallow pit

A special example of the dish-shaped pit is shown in Figure 5-15. Instead of growing in a disk or dish shape, there is a very shallow pit mouth region with a small hole underneath. The pit mouth is poorly distinguished in the 2D vertical section shown in Figure 5-15, because the pit mouth lies as the ‘steered’ region. Thus it is helpful to compare the pit mouth region with the SEM images and pit depth profile measured by confocal microscopy for segmentation. Figure 5-16 shows the 2D and 3D views measured by X-ray confocal microscopy, and measured by SEM and confocal microscopy. In Figure 5-16 (b) and (c), it can be seen that the pit has a wide pit mouth and a small hole in the middle in the SEM and confocal microscope images, which proves that the pit mouth visualised in the horizontal sections by X-ray micro-tomography is valid. The pit depth profile measured by confocal microscope (Figure 5-16 (e)) is not clear to indicate the top surface of the metal, but the 3D view (Figure 5-16(g)) shows that the blue edges appear to be the top surface and there is small hole below the middle of the pit mouth.

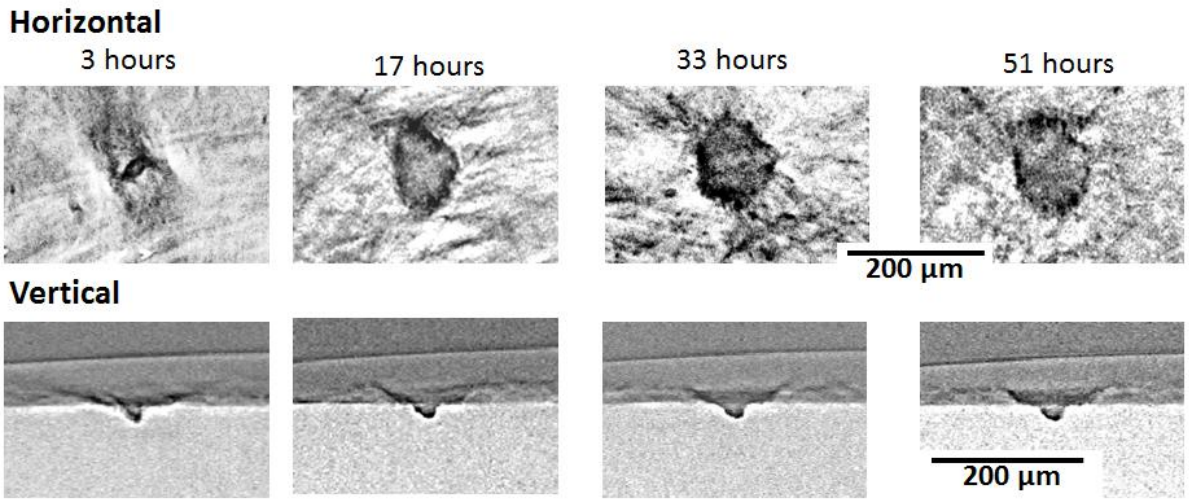

Figure 5-15 Time-dependent sequence of atmospheric pit growth on one stainless steel pin. The exposure condition is chloride deposition density 1000 µg/cm^2, 21±1°C and RH 45%.

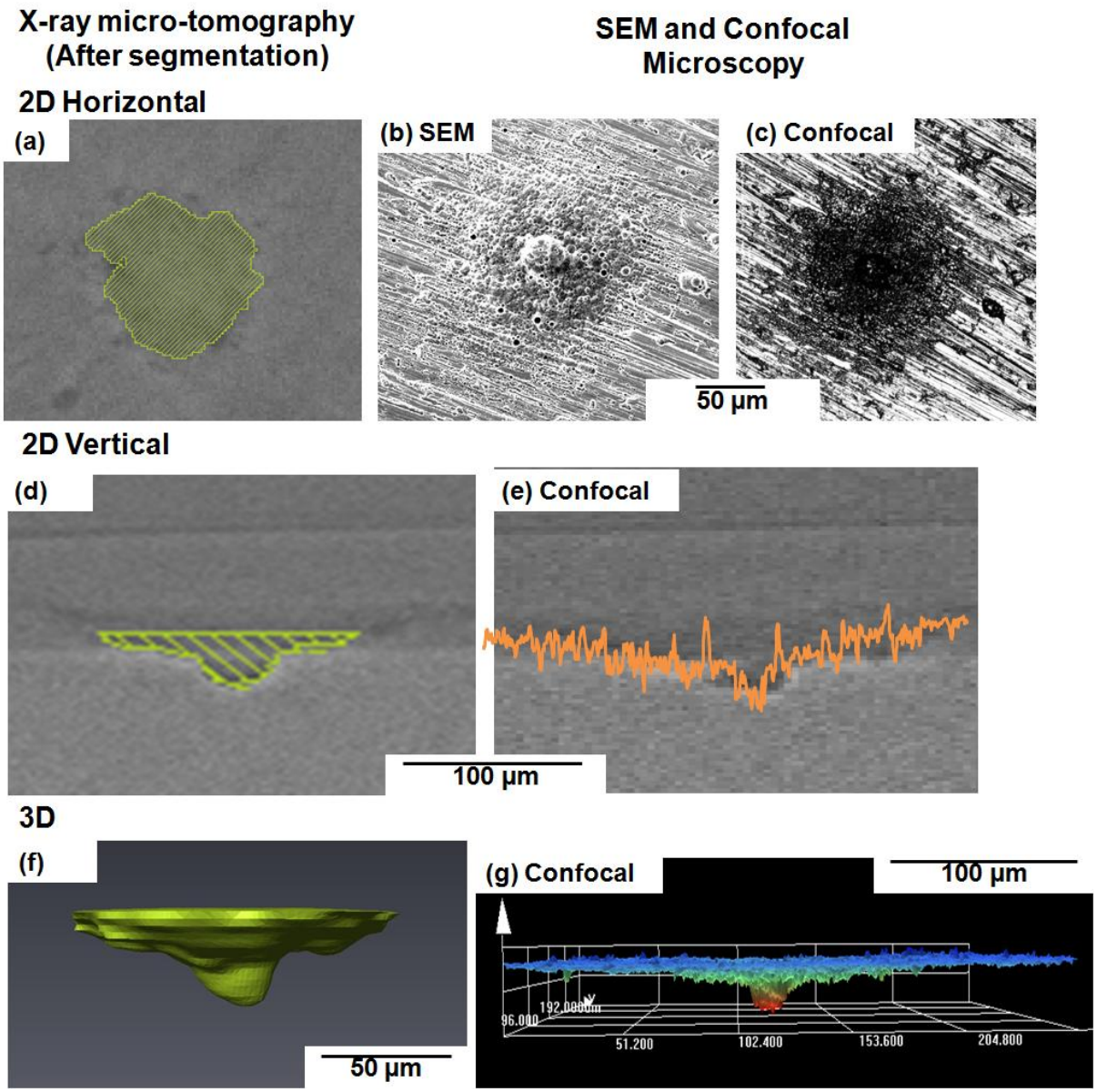

Figure 5-16 The 2D horizontal, vertical and 3D views of the pit shown in Figure 5-15 measured by SEM, confocal microscopy, and X-ray micro-tomography. The pit is on the stainless steel pin covered with $MgCl_2$ solution, and the chloride deposition is 1000 µg/cm^2. The pin has been exposed at 21±1°C and 45% RH for 51 hours.

The pit mouth area, depth and volume derived from X-ray micro-tomography, SEM and confocal microscope measurements were calculated, and the results are shown in Table 5-6. The pit mouth areas measured by confocal microscopy and X-ray micro-tomography are lower than the pit mouth area measured by SEM, although they do not show obvious difference in Figure 5-16. It is possible due to the different segmentation processes of pit mouth areas. Pit mouth areas measured by confocal microscope and micro-tomography are

segmented by controlling threshold to cover the maximum pit mouth, while the area measured by SEM is segmented by selection of pit mouth involves judgment. As before, the pit depth and pit volume measured by confocal microscope are lower than that measured by X-ray micro-tomography, which is probably due to the limitation of the confocal microscopy such as the noise of the reflection of the beam.

Table 5-6 The pit mouth area, pit depth and pit volume measured by SEM and confocal microscope compared with the X-ray micro-tomography measurement.

Method	Pit mouth area (μm^2)	Pit depth (μm)	Pit volume (μm^3)
SEM	10800	-	-
Confocal microscopy	9500	27	53000
X-ray micro-tomography	9700	29	67000

Table 5-7 shows the evolution with time of the pit diameter, depth and volume. The pit diameter and pit volume both grow continuously, but the pit depth does not change significantly during the pit growth. The results in Table 5-7 are plotted in Figure 5-17. It can be seen that the pit volume is very likely to be linear to the square pit diameter which is quite surprising, as for a semi-spherical shape pit the volume should be linear to the cubic pit diameter. This is probably because the pit grows only in the horizontal direction, but does not grow significantly in the vertical direction.

Table 5-7 The pit diameter, depth and volume increase with the exposure time. The pit diameter is calculated from the pit surface area. The pit is on the stainless steel pin 304 exposed at 21±1°C and 45% RH as shown in Figure 5-15. The stainless steel pin is covered with $MgCl_2$ solution, and the chloride deposition is 1000 $\mu g/cm^2$.

Exposure time (hours)	Pit diameter (μm)	Pit depth (μm)	Pit volume (μm^3)
3	27.2	28	7000
17	87.4	29	50000
33	104.0	29	60000
51	111.2	29	69000

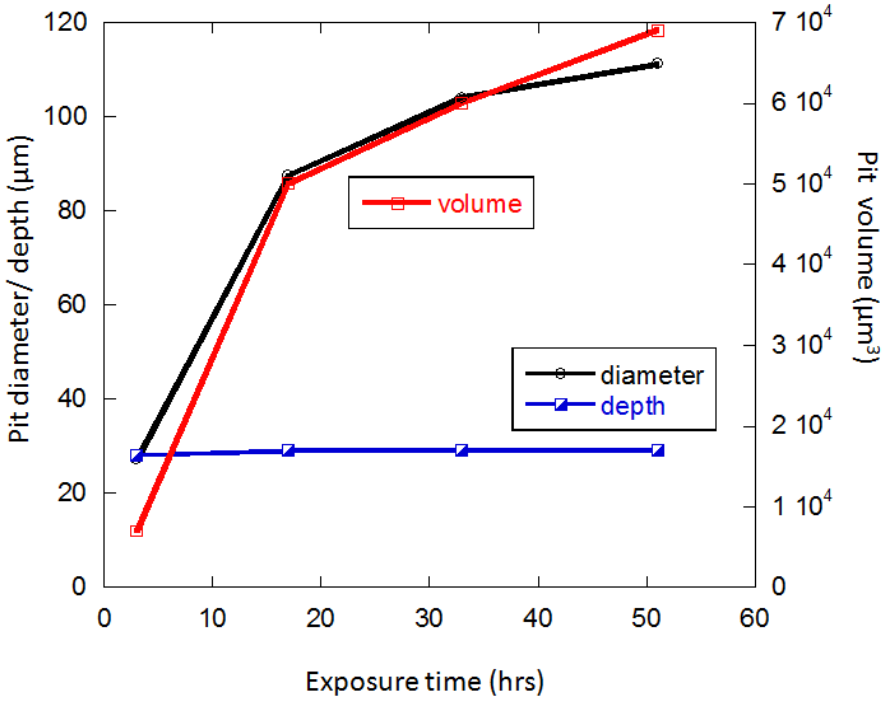

Figure 5-17 Pit diameter, depth and volume vs. the exposure time. The pit diameter is calculated from the pit surface area. The pit is on the stainless steel pin 304 exposed at 21±1°C and 45% RH as shown in Figure 5-15. The stainless steel pin is covered with $MgCl_2$ solution, and the chloride deposition is 1000 µg/cm^2.

5.4.5 Pit growth down a defect

The growth of some of the pits took place along extended defects in the material, which was 2 mm stainless steel rod. Figure 5-18 shows a typical example of this pit and shows the time-dependence of pit growth. After 3 hours, no pit is observed but a pre-existing defect can be seen within the bulk of the metal pin. This defect is likely to be a narrow cavity in the rod resulting from its fabrication, or an inclusion such as MnS, Al_2O_3, SiO_2 and MgO of the type shown in Figure 5-14. After 17 hours, a hemi-spherical pit is formed at the pin surface, which appears to 'drill' down the defect into the material. The shallow hemi-spherical upper part of the pit grows larger and after 33 hours the width of the deep region of the pit has increased. After 51 hours, a deep pit has formed which has a 'neck' part way down. In this situation, X-ray micro-tomography is a much better method to study pit morphology compared with confocal microscopy or SEM since it is unlikely that either confocal microscope or SEM could give information concerning the pit cavity below the 'neck'. The pit growth also indicates that only X-ray micro-tomography can supply the information on in-situ pit growth. SEM and confocal microscopy can only be carried out on ex-situ samples.

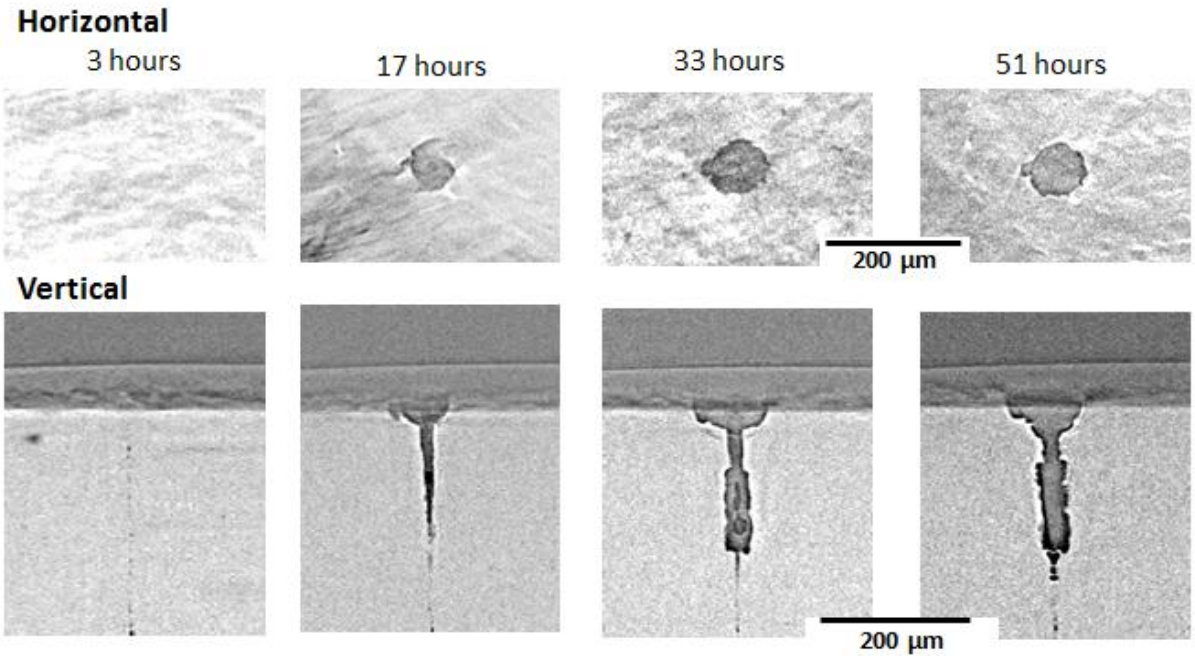

Figure 5-18 Time-dependent sequence of atmospheric pit growth on a 2 mm stainless steel pin under a droplet of $MgCl_2$. The chloride deposition density is 1000 µg/cm^2, the temperature is 21±1°C and the RH is 45%

This assertion is confirmed by the images in Figure 5-19, where the 2D and 3D views of the pit measured with X-ray micro-tomography are compared with the SEM and confocal microscope images. The pit mouth measured with X-ray micro-tomography is well matched with the pit mouth measured with SEM. The SEM image shows that the pit has a fairly circular mouth and is very deep. The vertical views of the pit measured by micro-tomography and confocal microscopy (Figure 5-18 (c) and (d)) confirm that the pit has a hemi-spherical shape at the top and growth in taking place of the bottom of the hemi-sphere. However, it can be seen that the pit depth profile measured by confocal microscopy (Figure 5-18 (d) and (f)) is about 70 µm less than the pit depth measured by X-ray micro-tomography. This is probably due to the limitation of the confocal microscopy method that the confocal beam cannot pass through the cavity below the pit 'neck' and provides root information about the profile below the neck. Another limit of the confocal microscope is the setting of the brightness. A bright beam can be more helpful to study the bottom of a pit but will saturate the detector when it is reflected from the sample top surface. The compromise of the brightness set in confocal microscope means that it cannot be used to detect the bottom of a pit which is more than 200 µm deep.

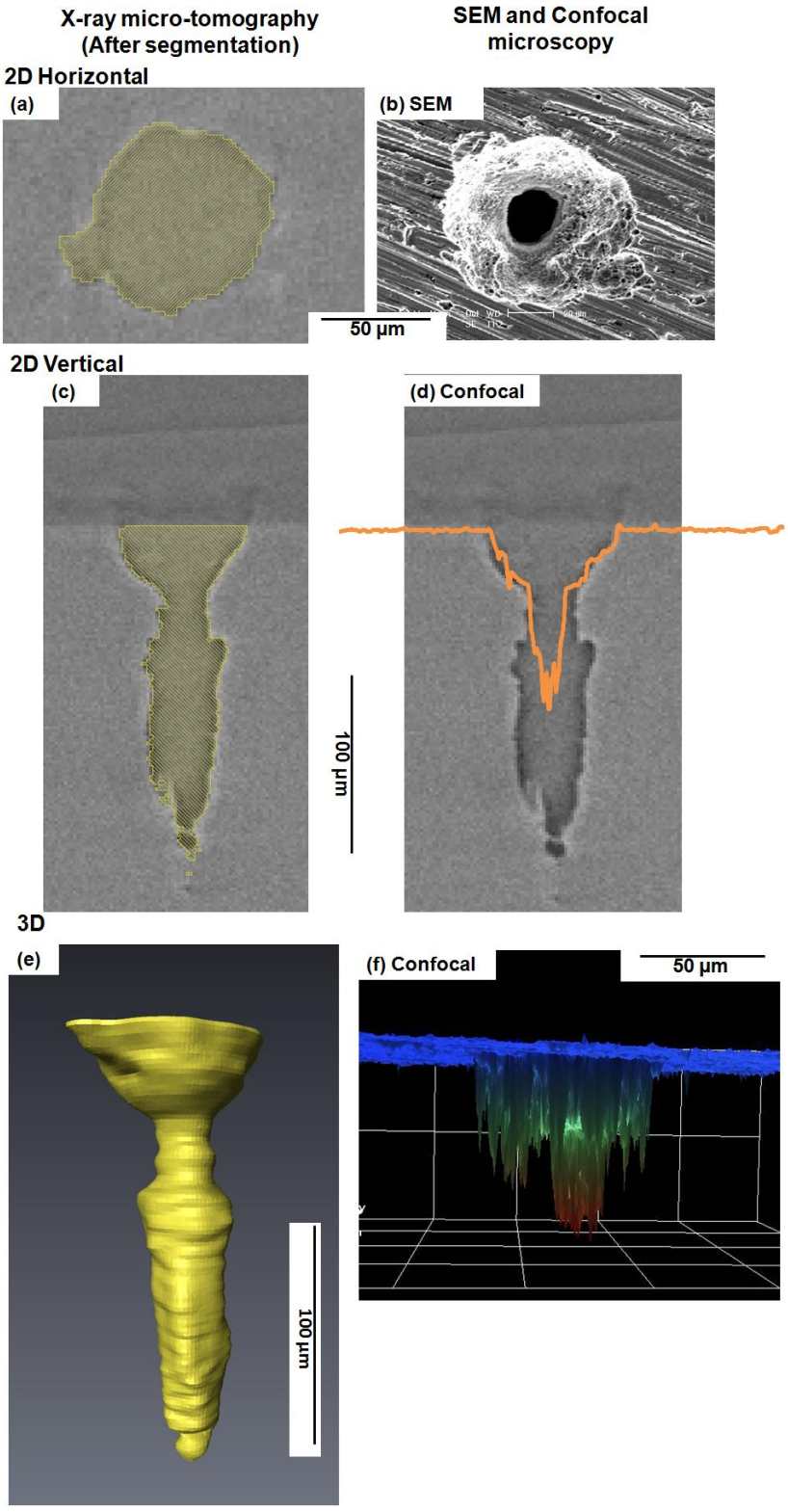

Figure 5-19 The 2D horizontal, vertical and 3D views of the pit shown in Figure 5-18 measured by SEM, confocal microscopy, and X-ray micro-tomography. The pit is on the stainless steel pin covered with $MgCl_2$ solution, and the chloride deposition is 1000 µg/cm^2. The pin has been exposed at 21±1°C and 45% RH for 51 hours.

Table 5-8 shows the pit mouth area, depth and volume derived from X-ray micro-tomography, SEM and confocal microscope measurements. The pit mouth area measured by micro-tomography is consistent with the pit mouth area measured by SEM and confocal microscopy. The pit depth and pit volume measured by confocal microscope as much smaller than that measured by X-ray micro-tomography, which is probably due to the limitation of the confocal microscopy method as discussed above.

Table 5-8 The pit mouth area and pit volume measured by SEM and confocal microscope compared with the segmented pit shown in Figure 5-18.

Method	Pit mouth area (μm^2)	Pit depth (μm)	Pit volume (μm^3)
SEM	5400	-	-
Confocal microscope	5400	160	140000
X-ray microtomography	5400	229	230000

Table 5-9 shows the evolution of the pit diameter, depth and volume. The pit diameter did not increase after 33 hours following deposition. The pit depth increases gradually with time. The pit volume increases significantly between 17 to 33 hours, and increases slowly between 33 to 51 hours. The results shown in Table 5-9 are plotted as Figure 5-20. It can be seen that the pit diameter does not increase after 34 hours exposure, and the pit depth increases approximately linearly with time. However, it should also be noticed that the intercept of time at zero depth is negative, which indicates that there is a pre-existing defect in the material before pit initiation.

Table 5-9 The pit diameter, depth and volume as a function of the exposure time. The pit is on a 304 stainless steel 2 mm diameter pin exposed at 21±1°C and 45% RH as shown in Figure 5-18. The stainless steel pin is covered with $MgCl_2$ solution, and the chloride deposition density is 1000 $\mu g/cm^2$.

Exposure time (hours)	Pit diameter (μm)	Pit depth (μm)	Pit volume (μm^3)
3	-	-	-
17	59.8	192	64000
34	83.4	211	210000
51	83.4	229	230000

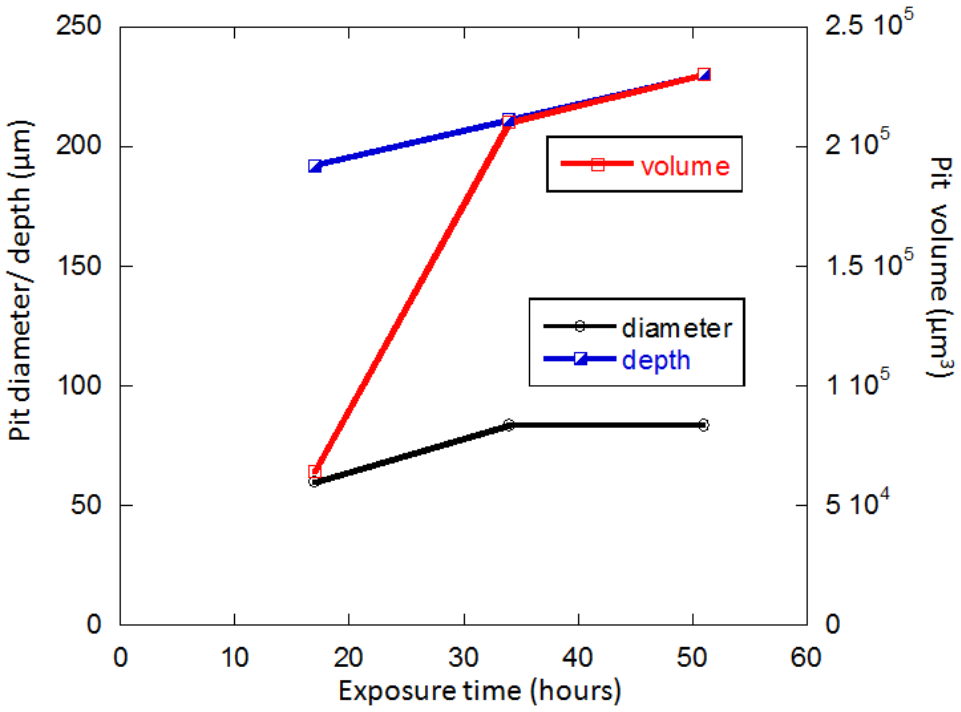

Figure 5-20 The pit diameter, depth and volume as a function of exposure time. The pit is on the stainless steel pin 304 exposed at 21±1°C and 45% RH as shown in Figure 5-18. The stainless steel pin is covered with $MgCl_2$ solution, and the chloride deposition is 1000 µg/cm^2.

5.4.6 Pit growth kinetics

5.4.6.1 Increase in pit depth with time

As described in Section 2.3, in a one dimensional artificial pit, the evolution of pit depth with time is limited by diffusion. Ghahari [136] reported that the depth of two-dimensional pits grown under full immersion conditions is also under diffusion control, but the width of the pit is under ohmic drop control. Since the depth of atmospheric corrosion pits can be measured by micro-tomography, it is feasible to estimate whether the pit growth is under diffusion control. A relationship between the square of pit depth and time can be obtained from Faraday's law of electrolysis as shown in Equation 5-3 and combined with Fick's first law as shown in Equation 5-5. Faraday's law of electrolysis is shown below: it is normally used to verify if the pit depth is under diffusion control.

$$m = \frac{Q}{F}\frac{M}{n} \qquad \text{Equation 5-3}$$

where m is the mass of the substance liberated at an electrode, Q is the transferred charge, F is the Faraday constant (96500 C/mol), n is the transferred charge 2.2, M is the molecular weight. It can be then written as Equation 5-4, where x is the depth of the pit and A is the area.

$$x = \frac{QM}{FnA\rho} \qquad \text{Equation 5-4}$$

Fick's first law is shown as below

$$i = \frac{nFD\Delta C}{x} = \frac{nFD(C_b - C_m)}{x} \qquad \text{Equation 5-5}$$

where i is the current density, D is the diffusion coefficient, and ΔC is the concentration difference between the pit bottom and pit mouth. C_b is the concentration at the pit bottom, C_m is the concentration at the pit mouth. Then a relationship combining Equation 5-4 and Equation 5-5 can be written as Equation 5-6.

$$x^2 = \frac{2MD\Delta C}{\rho} t = \frac{2MD(C_b - C_m)}{\rho} t \qquad \text{Equation 5-6}$$

The molecular weight (M) and the density of the material (ρ) are constant. If pit growth in depth is diffusion-controlled, x^2 should be linear with t, and the intersection of the time should indicate the pit initiation. The slope of the line would be $D(C_b\text{-}C_m)$.

The square of pit depth x^2 vs. time t for the pits shown above is plotted in Figure 5-21. Figure 5-21(a) shows that there is no linear relationship between x^2 and t for either the dish-shaped pit shown in Figure 5-12 or the very shallow pit shown in Figure 5-15. Figure 5-21(b) shows that x^2 changes linearly with t on the pit growth with defects. However, the intercept of time at zero depth is negative, which indicates that a pre-existing defect was present in the material. It should be noted that there are limited data points in Figure 5-21(b) which do not provide compelling evidence that pit growth in depth for defect-initiated pit is under diffusion control.

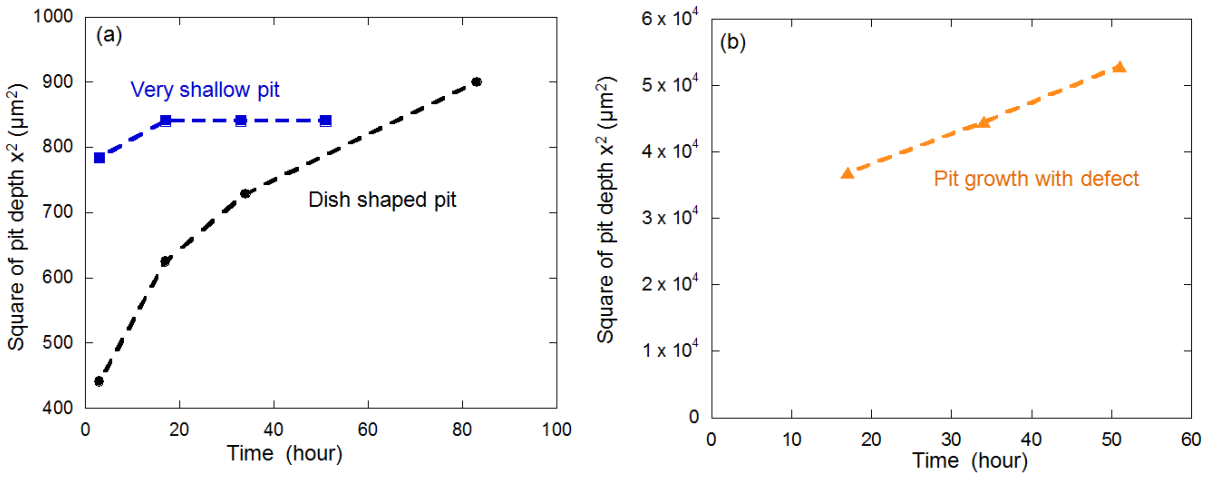

Figure 5-21 The square of pit depth vs. time of (a) dish shaped pit (black) shown in Figure 5-12 and very shallow pit (blue) shown in Figure 5-15, and (b) pit growing with an elongated defect (orange) shown in Figure 5-18. The pits are on 304 stainless steel pins exposed at 21±1°C and 45% RH. The stainless steel pins are covered with $MgCl_2$ solution, and the chloride deposition is 1000 µg/cm^2.

5.4.6.2 Average pit current density

Since the pit volume and the pit surface area can be quantified by X-ray micro-tomography, it is feasible to calculate the evolution of the average current density within the pit. This is calculated by taking the total volume of metal lost between each measurement and the beginning of the experiment, and converting it to charge passed. For each measurement, the total volume of the pit is used, assuming a flat surface at the beginning of the experiment. This charge is then divided by the time to give the average current. In the case of the initial measurement, it is assumed that the pit initiates immediately at the beginning of the experiment; this means that the current density quoted is a minimum value since the pit is likely to have initiated some time after the start of the experiment. The average current density is then calculated from the current by using the surface area of the pit at the end of the time interval. This is the maximum size of the pit during the growth period, so this procedure may introduce an under-estimate of current density. It may also be the case that part of the pit could have repassivated during the time interval, which would also lead to an under-estimate of current density in the active region. For example, Table 5-5 shows that the

dish-shaped pit diameter does not increase significantly in diameter after 17 h, supporting the idea that the edge of the pit may have repassivated.

As described above, the average current density of pit growth can be calculated by Equation 5-7, where i is the average current density, I is the current, A is the pit surface area, Q is the charge passed due to the metal loss, and t is the time at the end of each measurement. The pit surface area (A) was segmented using Avizo software. The charge (Q) is calculated by Equation 5-8, where V is the volume of metal loss which is shown in Table 5-5 and Figure 5-13, ρ is the material's density 7.93 gcm^{-3}, n is the average valence 2.2, F is the Faraday constant 96500 $Cmol^{-1}$, and M_w is the molecular weight 55.8 $gmol^{-1}$.

$$i = \frac{I}{A} = \frac{Q}{tA} \qquad \text{Equation 5-7}$$

$$Q = \frac{\rho V}{nFM_w} \qquad \text{Equation 5-8}$$

Figure 5-22 shows a plot of average current density of pits shown in Figure 5-12, Figure 5-15, and Figure 5-18 as a function of time. It can be seen that from Figure 5-22 that the average current density decreases significantly with time. It is probably affected by a combination of diffusion and *IR* drop. Figure 5-21 shows that there is not a linear relationship between x^2 and t, which would be expected for diffusion control. However, this interpretation relies on the assumption that there is a constant difference in concentration between the pit mouth and pit bottom. It is possible that there is an additional diffusion path along the thin layer of solution outside the pit. In addition, when the pit initiates, the pit depth is relatively shallow and the *IR* drop is relatively small, but as the pit grows deeper, the *IR* drop increases due to the increasing pit depth, which can lead to decreasing current density. Further work is required to confirm the controlling factors in pit depth growth.

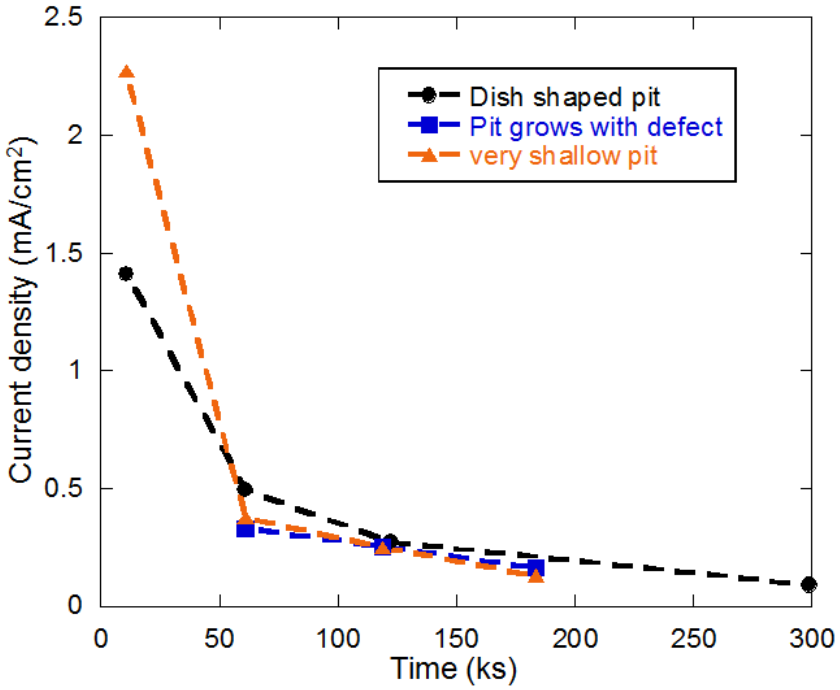

Figure 5-22 Average current density of a pit as a function of time. The dish-shaped pit is shown in Figure 5-10 and Figure 5-12. The very shallow pit is shown in Figure 5-15. The pit grows with defect is shown in Figure 5-18. The pits are on the stainless steel pin 304 exposed at 21±1°C and 45% RH. The stainless steel pins are covered with $MgCl_2$ solution, and the chloride deposition is 1000 µg/cm^2.

5.4.7 Effect of synchrotron X-ray radiation on atmospheric pitting corrosion

According to Nagy and You [137], high flux synchrotron X-rays might lead to production of peroxide, which may increase the corrosion potential, leading to enhanced pit initiation. Figure 5-23 shows the optical images of samples where corrosion developed in the lab and were examined ex situ at the end of the experiment, and two samples which were subjected to several in situ X-ray micro-tomography scans at the synchrotron. All of the samples are deposited with a chloride density of 100 µg/cm^2 and exposed at 45% RH. It can be seen that there are one or two pits on the ex-situ samples, but there are multiple pits on the two in-situ samples.

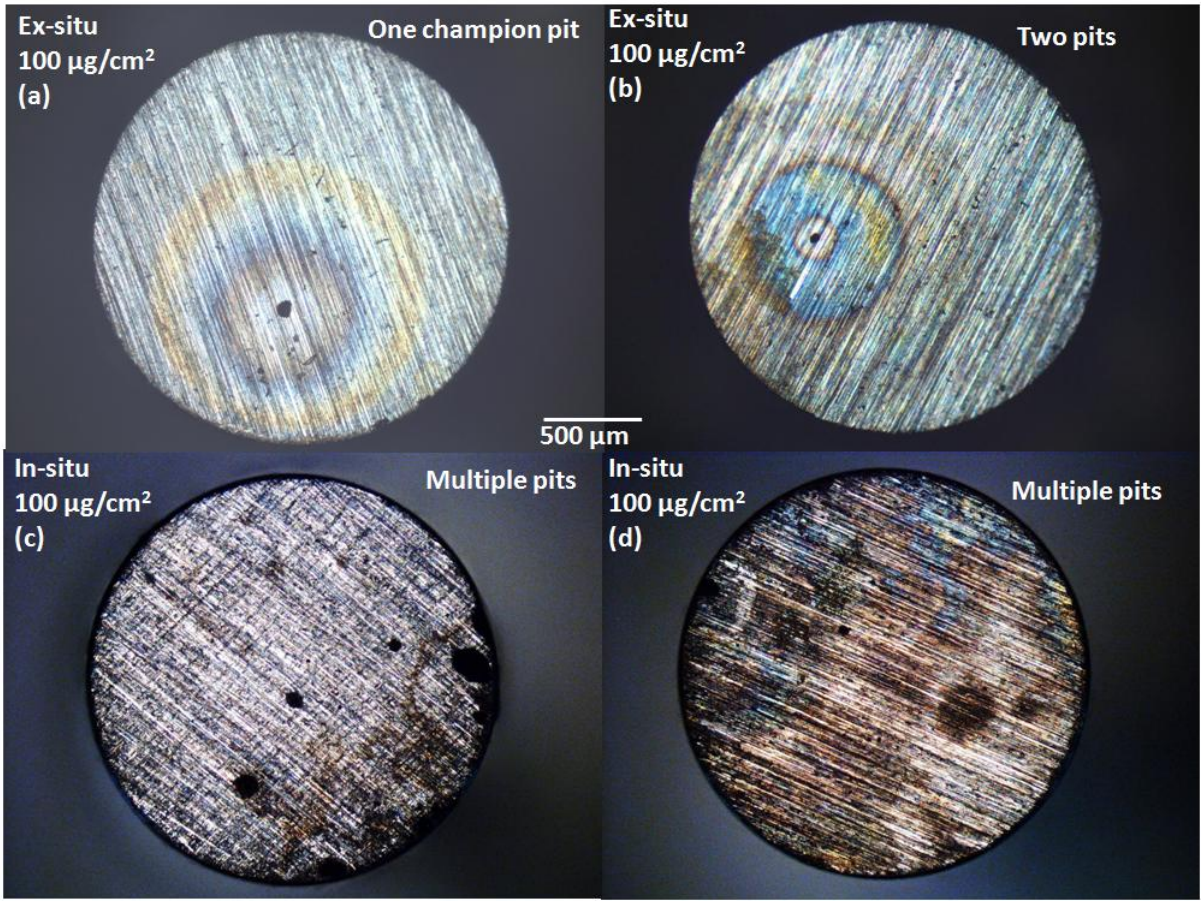

Figure 5-23 Optical images of four stainless steel pins deposited with 100 µg/cm^2 and exposed at 20±1°C, 45% RH. (a) and (b) were exposed in the lab for 24 hours, and (c) and (d) were measured by X-ray tomography with three scans.

The number of pits per sample for ex-situ samples exposed in the lab and in-situ samples measured with synchrotron X-ray micro-tomography is shown in Figure 5-24. It can be seen that there are only one or two pits on most of the ex-situ samples, but there are multiple pits on all the in-situ samples that had been exposed to X-rays for at least three micro-tomography scans. The flux of X-rays (70 keV) is estimated to be about 2 x 10^{12} photons/s. It is therefore very likely that the synchrotron X-ray radiation has affected the atmospheric pitting corrosion process, leading to the formation of more pits.

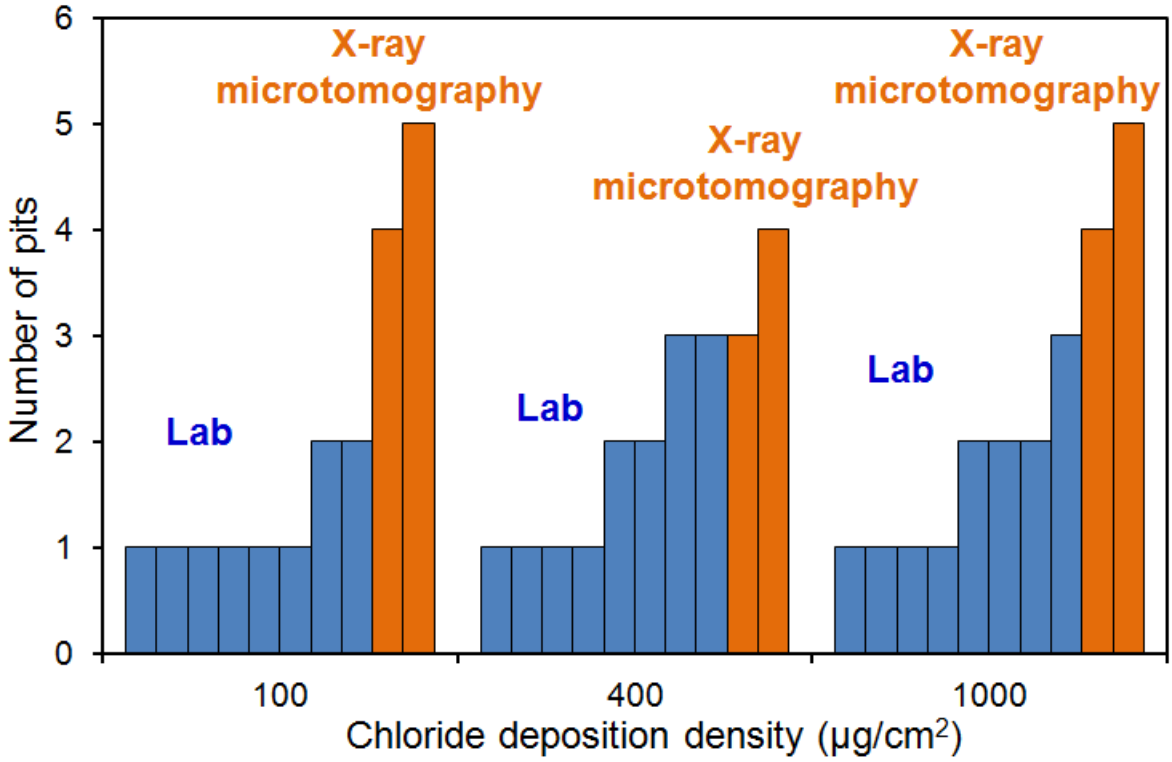

Figure 5-24 The number of pits per sample for samples exposed in the lab without X-ray exposure (blue) and measured with at least three 40-minute X-ray micro-tomography scans (orange) with different chloride deposition densities. The stainless steel pins are exposed at 21±1°C and 45% RH, and are covered with $MgCl_2$ solution, and the chloride deposition is 1000 µg/cm^2.

5.5 Effect of chloride deposition density on atmospheric pitting corrosion

Figure 5-25 shows the number of pits per sample on pairs of stainless steel pins with various chloride deposition densities. It can be seen that for a chloride deposition density of 10 µg/cm^2, there was no pit on one sample, and on the other, there was a possible pit or a defect that was too small to resolve clearly. For a chloride deposition density of 20 µg/cm^2, two small pits formed on each stainless steel pin. The number of pits and the size of pits both increase with the chloride deposition density.

● Pit < 1000 µm³ ● Pit > 10000 µm³

● 1000 < Pit < 10000 µm³

* Defect (probably inclusion) intersects surface – not clear if it is a pit

□ Pit on the side wall of the pin

Chloride deposition density (µg/cm²)	Sample 1	Sample 2
10		*
20	● □	● ●
100	● ● ● ●	● ● ● ● ● ●
400	● ● ● ●	● □ ●
1000	● ● ● ● ●	● ● ● ●
2000	● (without X-ray)	
4000	● ● ● ● ●	

Figure 5-25 The number of pits per sample for samples measured with at least three 40-minute X-ray micro-tomography scans with different chloride deposition densities. The stainless steel pins are exposed at 21±1°C and 45% RH, and are covered with $MgCl_2$ solution, and the chloride deposition is 1000 µg/cm^2.

The volume of the largest pit on each sample was quantified with micro-tomography measurements by Avizo, but this was not verified with confocal microscopy. A plot of pit volume vs. the chloride deposition density is shown in Figure 5-26, which shows that the pit volume increases with the increasing chloride deposition density. Figure 5-27 shows a plot of average pit current density vs. the chloride deposition density. The average pit current density is calculated by taking the total volume of metal lost between each measurement and the beginning of experiment, and converting it to charge passed as described in Section 5.4.6.2. It can be seen that the pit current density does not change by more than a factor of 2 for concentrations of chloride between 10 µg/cm^2 and 1000 µg/cm^2 after the same exposure time following deposition.

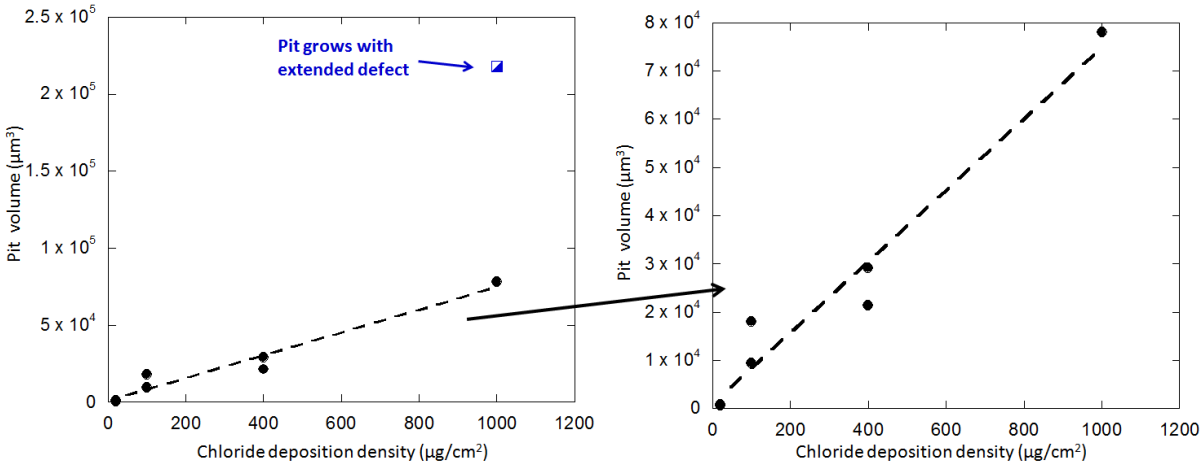

Figure 5-26 Pit volume vs. chloride deposition density. The stainless steel pins are exposed at 21±1°C and 45% RH, and are covered with $MgCl_2$ solution, and the chloride deposition is 1000 µg/cm^2. The dotted line is a linear fit to the data.

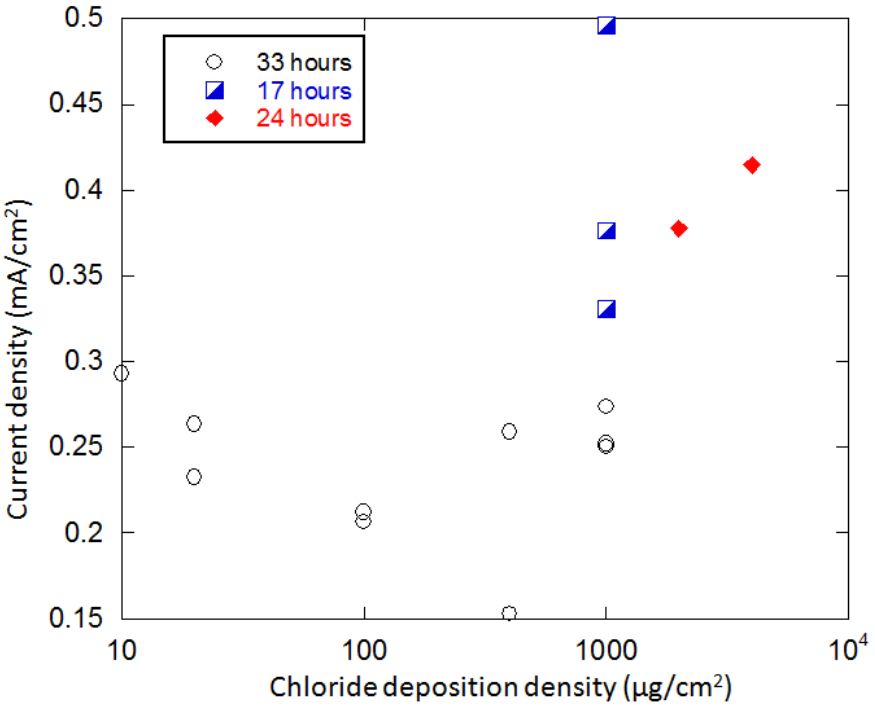

Figure 5-27 The current density of pit vs. chloride deposition density. The average current density is calculated at time intervals from beginning of the experiment following deposition as shown in the figure. The pits are the biggest on each stainless steel pins, and the stainless steel pins are exposed at 21±1°C and 45% RH.

5.6 Discussion

5.6.1 Atmospheric pit morphology

Figure 5-12 shows a shallow dish-shaped pit with a small hole at the bottom, whose morphology is consistent with the findings of Maier and Frankel [18]. The small hole is generally believed to arise from the inclusion, where the pit initiates [1, 138]. Figure 5-15 shows a particularly shallow pit with a small hole at the bottom, which is the only one case found on 12 sample pins measured by the synchrotron micro-tomography method. This particularly shallow pit morphology is different from the typical shallow dish-shaped pit.

The difference of the two morphologies is possibly due to the different process of dissolving MnS inclusions, which has been discussed in Section 2.2.2. MnS is a well-known initiation site for pitting corrosion of stainless steel.

The dish-shaped pit is consistent with the work of Eklund [21], and Castle and Ke [26], who suggested that a sulphur layer can form on the metal surface adjacent to the inclusion whilst

the inclusion dissolves. This S layer can decrease the strength of metal-metal bonds and increase the rate of dissolution [29] for the metal surrounding the inclusion leading dissolution of metal ions from area around the inclusion to form a relatively circular pit mouth area like a dish. The small hole in the middle might be the bottom of the initial inclusion site [1, 18].

The observation of a very shallow pit is consistent with the work of Webb and Alkire [23-25] and Tsutsumi et al. [1]. Webb and Alkire [23-25] carried out a series of electrochemical measurements of dissolving a single sulphide inclusion to study the stainless steel pit initiation process, and suggested that pits preferentially grow from the dissolved inclusion laterally at the metal surface as the pH is relatively low in this region. Tsutsumi et al. [1] observed the pit morphology as a shallow region surrounding a small hole in the middle, and proposed a similar mechanism with Webb and Alkire as described in Section 2.2.2. The very shallow pit is only observed on one of the samples measured by micro-tomography, and has not been observed in lab-based measurements. It is also possible that micro-pits formed the shallow region due to beam damage.

5.6.2 Pit growth along an inclusion

Figure 5-18 shows a deep pit growing along an extended inclusion. This morphology has not been published in literature before because relatively clean materials are more often selected for study and furthermore the sample surface is usually parallel to the rolling direction. The stainless steel pin samples in this study were machined from the cold rolled stainless steel rods, and thus the top surface was perpendicular to the rolling direction, which can increase the possibility of having an extended inclusion in the vertical direction. The pit grew to more than 200 μm deep in 51 hours, indicating that the use of clean steel and the orientation of the metal surface relative to the rolling direction is of importance for industrial use.

5.6.3 Pits-within-pits: active regions

Figure 5-10 shows an SEM image of a shallow dish-shaped pit. It can be seen that there are multiple small pits grown inside the main pit, which has also been shown by the X-ray micro-tomography and confocal microscopy measurement in the vertical section. This is probably due to the partial repassivation of the pit. There might be a limit to the available cathodic current which is dependent on the electrolyte thickness, oxygen concentration and diffusivity. During pit growth, when the anodic current is less than the maximum available

cathodic current, a pit can propagate continuously. However, when the pit grows larger and the anodic current demand exceeds the maximum available cathodic current, some part of the pit has to repassivate and the remaining active parts of the pit continue to dissolve thereby forming the pits inside the main pit. This observation is similar to Maier and Frankel's finding of an 'earing' effect on atmospheric pits [18].

5.6.4 Evolution of pit depth

At high potentials, the growth of one-dimensional pits takes place under diffusion control. [36, 61]. Ghahari et al. [136] also observed that under immersion conditions a 2D pit growth in depth is under diffusion control, and a linear relationship has been observed between the square of pit depth (x^2) and time (t). In the current work as shown in Figure 5-21, there is no obvious linear relationship between x^2 and t, which is possibly due to the limited volume of the electrolyte layer that might supply additional diffusion barrier.

It has been reported that pit growth in depth is under diffusion control in 1D artificial pits [36, 61, 63] and 2D pits [136]. However, these works were carried out in immersed conditions where the metal ion concentration at the pit mouth can be assumed as zero. Equation 5-6 can then be simplified to $x^2 = \frac{2MDC_b}{\rho}t$, C_b is the saturated metal ion concentration, $\frac{2MDC_b}{\rho}$ is a constant. Hence x^2 vs. t is a linear relationship.

Under atmospheric conditions in a real pit, the metal ion concentration at the pit mouth C_m can be affected by the limited volume of the electrolyte layer, and hence $\frac{2MD(C_b - C_m)}{\rho}$ might change with time. The growth of real pits in depth is possibly not under simple diffusion control.

5.6.5 Current density for pit growth

Current densities for pit growth on stainless steel have been reported widely in previous works upon immersed solutions. For example, Frankel et al. measured the current density of a pit on stainless steel 302 in different solutions and reported it in the range of 2 to 4 A/cm^2 [139]. Pistorius and Burstein have measured the current density of a pit in 0.8 M NaCl and 0.2 M HCl solution and found that it is in the range of 2 to 8 A/cm^2 [35].

Maier and Frankel [18] measured the average current density of stainless steel at atmospheric conditions. They used the volume of pits divided by the active area of the pits measured by profilometer, and reported that the current density becomes quite stable at 0.6 mA/cm^2 after $6x10^4$ seconds.

For the current work, Figure 5-22 shows the average current density of pits on stainless steel 304 under $MgCl_2$ electrolyte layer. The average current density decreases with time, and is in the range of 0.2-2.5 mA/cm^2. The current density is much lower than the current densities measured in immersed conditions, but is close to Maier and Frankel's finding as shown in Figure 5-28. However, the current density measured in the present work can decrease to a lower value after longer exposure time. It is possible that there is an under-estimation of the current density as described in Section 5.4.6.2. It is also possible due to the different experimental conditions between the current work and Maier and Frankel's [18]: They carried out lab-based experiment, the samples were covered with about 900 $\mu g/cm^2$ chloride deposition and exposed at 33-34% RH, while the current work was carried out in the presence of intense X-ray radiation covered with 1000 $\mu g/cm^2$ chloride deposition and exposed at 45% RH.

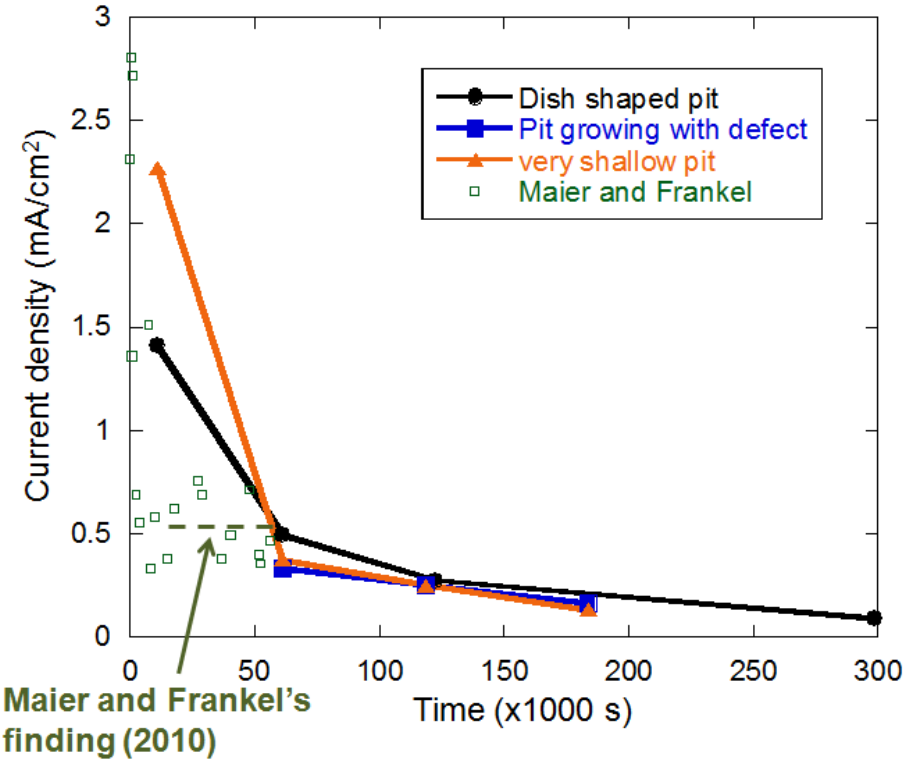

Figure 5-28 Current density of pit growth as a function of time compared with current density reported in Maier and Frankel's work [18]. The pits in the current work are on the stainless steel 304 pins exposed at 21±1°C and 45% RH. The stainless steel pin (2 mm diameter) is covered with $MgCl_2$ solution, and the chloride deposition is 1000 µg/cm^2. Maier and Frankel's work was carried out on stainless steel 304 plates exposed at 33-34% RH. The initial deposition is 0.44 M 2 µl $MgCl_2$ solution, and the chloride deposition density is about 900 µg/cm^2.

5.6.6 Pit stability product

As described in Section 2.2.3 and Section 2.2.4, the notion of the 'pit stability product' has been developed by Galvele [32] and has been further calculated in the immersion solutions with electrochemical control [30, 35, 39]. Pistorius and Burstein have calculated the upper and lower limit of the pit stability product and have found it should be between 0.3 and 0.6 A/m in the immersed condition. Maier and Frankel used the current density as shown in Figure 5-28, assumed the pit depth is about 50 µm, and reported an estimated pit stability product about 3 x 10^{-4} A/m. In the current work, the pit depth is about 30 µm with several hours exposure, the pit stability product can be as low as 6 x 10^{-5} A/m, which is far below the pit stability product calculated in the literature. It might indicate the possibility of pit propagation with a much lower pit stability product under atmospheric conditions. However,

as described in Section 5.4.6.1, it is not clear that the real atmospheric pit growth in depth is under diffusion control. Shallow dish shape of pits are common and so the use of the pit stability product might not be helpful.

5.6.7 Effect of chloride deposition density

Figure 5-26 shows the pit volume vs. chloride deposition density. It can be seen that the pit volume increases with the chloride deposition density, which is consistent with the observation described in Section 4.2.2. As the salt droplet is deposited on the stainless steel pin surfaces, the initial deposition area is the same and the cathode area is the same. For the same controlled temperature and relative humidity exposure environment, the difference of the chloride deposition density can lead to a difference of the electrolyte height, since the electrolyte concentration is controlled by the relative humidity. The difference of the height of the electrolyte layer is illustrated by Figure 5-6.

There are two possible effects which can result from the difference of the height of the electrolyte. For a higher electrolyte layer, the oxygen reduction reaction can decrease as the diffusion length of oxygen in the electrolyte layer increases. This would predict that smaller pits form. On the other hand, for a higher electrolyte layer, the ohmic drop from the electrolyte layer between the pit and the location of the cathodic reaction (edge of pin) can decrease. This predicts that larger pits would form. In the present work, the pit volume increases with the salt deposition density, which is more likely to be consistent with the assumption of the domination of the ohmic drop.

5.6.8 Strengths and weaknesses of X-ray tomography in studying atmospheric corrosion of stainless steel

Synchrotron X-ray micro-tomography has been used to observe in-situ pit growth in stainless steel under atmospheric conditions and in real time. It has shown not only the evolution of pit growth, but also the evolution of the electrolyte layer and the defects within the material. Figure 5-19 and Figure 5-20 show that using X-ray micro-tomography is feasible to observe the pit growth with defects, since the X-ray beam can pass through the cavity below the top hemispherical part of the pit therefore providing information about the bottom of the pit. This is in contrast to other techniques such as SEM, confocal microscopy and profilometer which cannot provide this information. It also can observe the real pits in 3D in-situ and therefore give information about average pit growth kinetics.

However, the time to collect each tomogram is about 40-50 minutes, and there is a risk of beam damage. Nagy and You [137] reported that an intense X-ray beam can affect electrochemical processes. The comparison of the synchrotron X-ray micro-tomography measurements with the lab based measurements shows that beam damage may lead to increasing numbers of pits (Figure 5-25). The multiple pits growth means that cathodically-limited current is shared by the pits, which increases the difficulty of analysing data. In addition, there is a limitation on sample size for micro-tomography measurements.

5.7 Conclusions

- Synchrotron X-ray micro-tomography is well suited to research on atmospheric pitting corrosion of stainless steel. With this method, in-situ pit growth was studied and the electrolyte layer, pits and defects can all be observed with phase contrast enhancement.
- Synchrotron X-ray micro-tomography method can quantify the pit area, depth and volume, and the validation of this technique has been made by comparison with results from SEM and confocal microscopy. Comparison with SEM and confocal microscopy shows that this technique can detect the corrosion cavities which cannot be observed from the top, but care is needed to determine the top surface of the metal.
- The evolution of the electrolyte layer is fairly stable, which indicates the humidity is well controlled. The volume of the electrolyte layer is generally a linear function of the chloride deposition density.
- Most of the corrosion pits have an open mouth and a dish shape and preferentially grow in a lateral direction at first. A small hole in the middle can be observed in the dish-shaped pit, which is possibly the cavity that develops when an inclusion dissolves in the pit initiation process.
- Pits can grow very deeply if there are pre-existing defects within the steel.
- Synchrotron X-ray radiation damage is observed to lead to the growth of multiple pits, which might affect the atmospheric pitting corrosion process.
- The pit volume increases with increased salt deposition density, which may be associated with a lower ohmic drop between the electrolyte layer and the pit.
- The current density of the pit is calculated to be in the range of 0.2 to 2.5 x 10^{-3} A/cm^2, which is far below the current density measured under immersed conditions, but is fairly consistent with Maier and Frankel's finding under atmospheric conditions.

6 Electrochemical kinetics of stainless steel in artificial pits containing concentrated chloride solutions

6.1 Introduction

The aim of this chapter is to determine the dissolution kinetics of stainless steel in relatively concentrated chloride bulk solutions similar to those found under atmospheric corrosion conditions where a lower relative humidity (RH) can correspond to a higher chloride concentration in the bulk solution. For example, 65% RH corresponds to a chloride concentration of ~6 M. The measurements were carried out by using wire 1D artificial pit electrodes as described in Section 3.2.1.

6.2 Electrochemistry of artificial pits

6.2.1 Validation of 1D pit depth and diffusion length

The depth of a wire artificial pit can be determined visually and by integration of the current passed during its growth. The total charge passed during pit growth can be expressed as:

$$Q = \int Idt = \frac{Ax\rho nF}{M_w} \qquad \text{Equation 6-1}$$

$$x = \frac{QM_w}{A\rho nF} \qquad \text{Equation 6-2}$$

where Q is the total charge passed, I is the current, t is time, A is the cross sectional area, x is the pit depth, ρ is the density, n is the average charge on the ions produced during dissolution (2.2 for stainless steel), F is the Faraday constant, and M_w is the molar mass. The pit depth estimated by integration of the current was cross-checked with visual observations. A long working distance microscope coupled to a CCD camera was used in the experiment to measure the depth of the dissolved pit. Figure 6-1 shows the relationship between the depth measured by visual observation and the depth measured by integration of current. The line in Figure 6-1 shows the condition when the pit depth measured by visual observation is consistent with the depth measured by integration of current. It can be seen that the depths measured by visual observation are slightly smaller than those measured by integration of the current, which might be due to cathodic reaction during the early stages of pit growth, or due

to an error of visual observation. The pit depth measured by integration of current is used throughout this chapter.

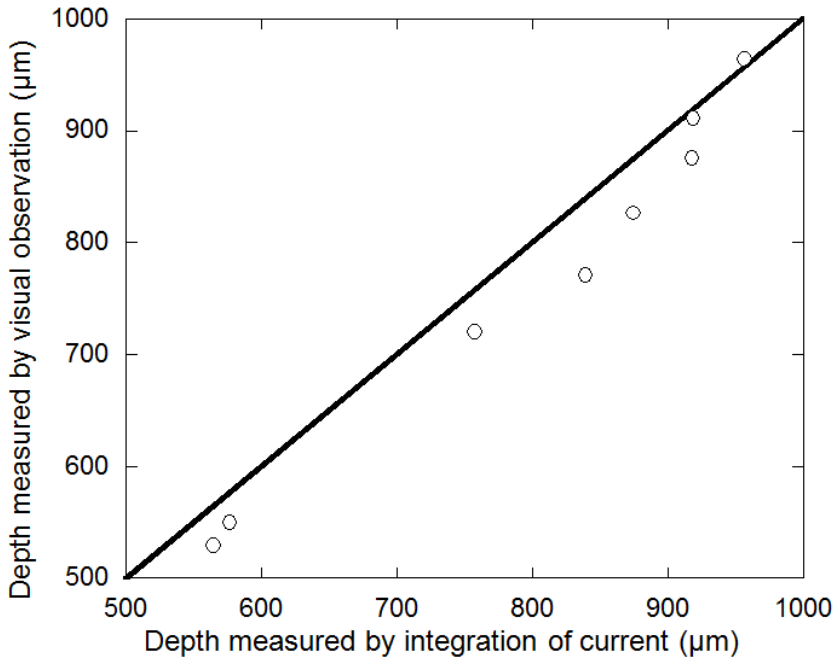

Figure 6-1The relationship between the pit depth measured by visual observations and the depth measured by integration of current of 1D artificial pit of 304 stainless steel 250 µm diameter wire at 20±2 °C.

As described in Section 2.2.6, diffusion of the dissolving metal ions out of a 1D pit is controlled by diffusion away from the pit mouth as well as within the pit. When the pit is deep enough, the diffusion of the metal ions around the pit mouth can be neglected. In order to establish the minimum depth of pit where this is the case, a plot of current density vs. the inverse pit depth is shown in Figure 6-2.

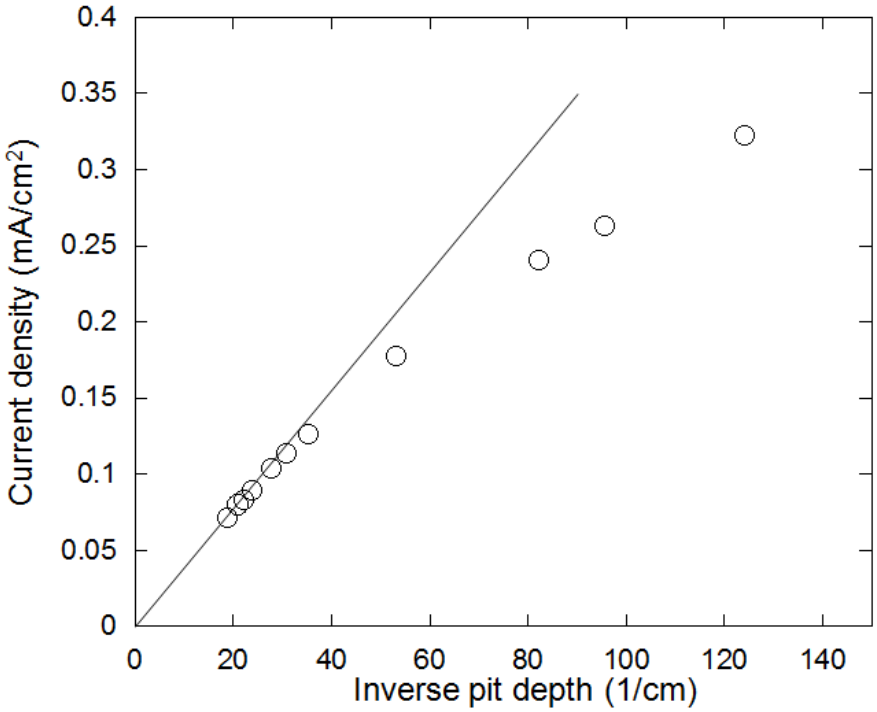

Figure 6-2 A typical example plot of current density vs. inverse pit depth of 1D artificial pit of 304 stainless steel 250 μm diameter wire in 2 M $MgCl_2$ solution at 20±2 °C.

In Figure 6-2, the linear region corresponds to the condition where the pit depth is the valid diffusion length, since the diffusion limited current density (i_{lim}) has a linear relationship with the inverse pit depth ($1/x$) as shown in Equation 2-13.

$$i_{\lim} = \frac{nFD\Delta C}{x} \qquad \text{Equation 2-13}$$

The curved region at higher current density corresponds to a shallow pit depth that can be affected by the external solution [36, 63, 78]. In the present work, all the 1D artificial pits are grown at least 500 μm deep, so that the inverse pit depths are $\leqslant 20$ cm^{-1}.

6.2.2 Effect of a black layer within pits

During growth of 1D artificial pits, black layers in the pit cavity have been observed (Figure 6-3). The composition of the black layer inside the pit is not known. Kawaley [140] found a similar black layer in commercial purity Fe 1D artificial pits but not in high purity Fe, which has lower carbon content, suggesting that it may be a carbon layer. Steinsmo and Isaacs did not make any visual observations in their work on stainless steel artificial pits, but detected a "remnant" salt layer that can influence the dissolution kinetics [78].

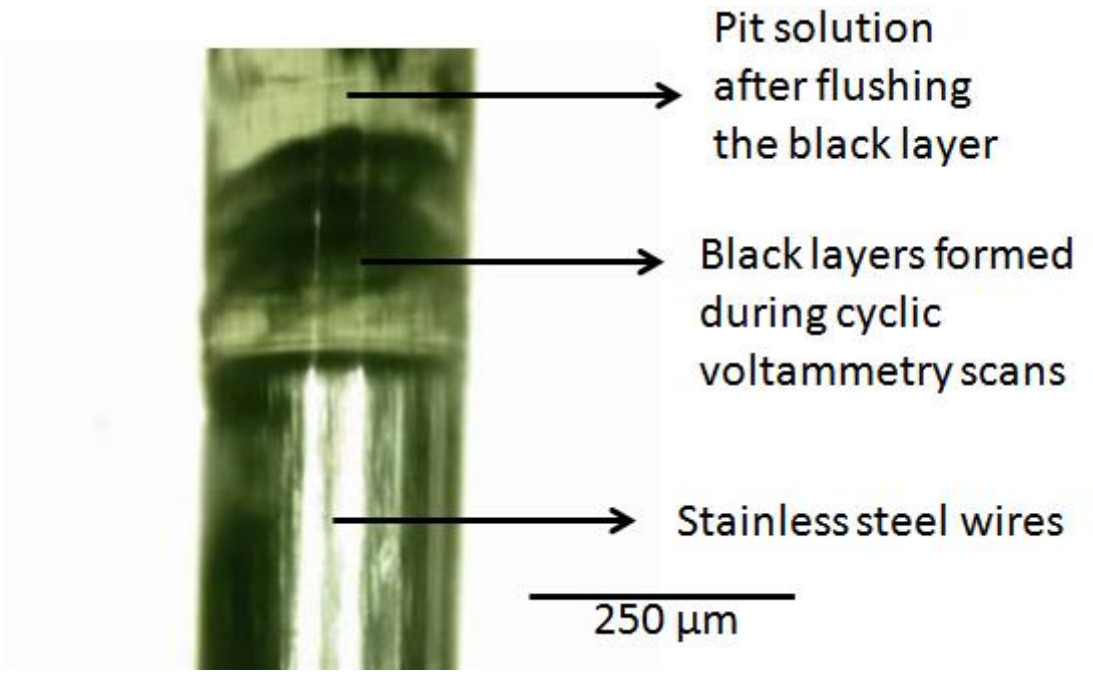

Figure 6-3 An image of a wire artificial pit electrode containing black layers. The pit was grown to a particular depth, flushed with a syringe to remove the black layer, and then cyclic voltammetry was carried out, which led to growth of another black layer in the bottom of the pit.

As the black layer observed in the present work might affect the diffusion of metal ions, an experiment was carried out to determine its effect on the diffusion-limited current density for metal dissolution. The black layer was flushed three times during the experiment with a fine syringe tip, and was observed with an optical microscope. The current density vs. the inverse pit depth has been plotted in Figure 6-4(a). The red dotted line in Figure 6-4(a) was determined by fitting the slope of current density vs. inverse pit depth after flushing the black layers three times. This line can be assumed to be the theoretical diffusion-limited current density without a black layer. Figure 6-4(b) shows the pit stability product (*ix*) vs. time, and Figure 6-4(c) shows an expanded plot for the period before and after the first flushing procedure. The orange dotted line indicates the average value of *ix* before flushing and the red dotted line indicates after flushing the black layers. It can be seen that *ix* was slightly lower when there were black layers in the pit cavity. The current density with the black layer is about 4% lower compared with that without the black layer. The following results in this chapter are measured with the black layer present as it was not possible for it to be consistently removed.

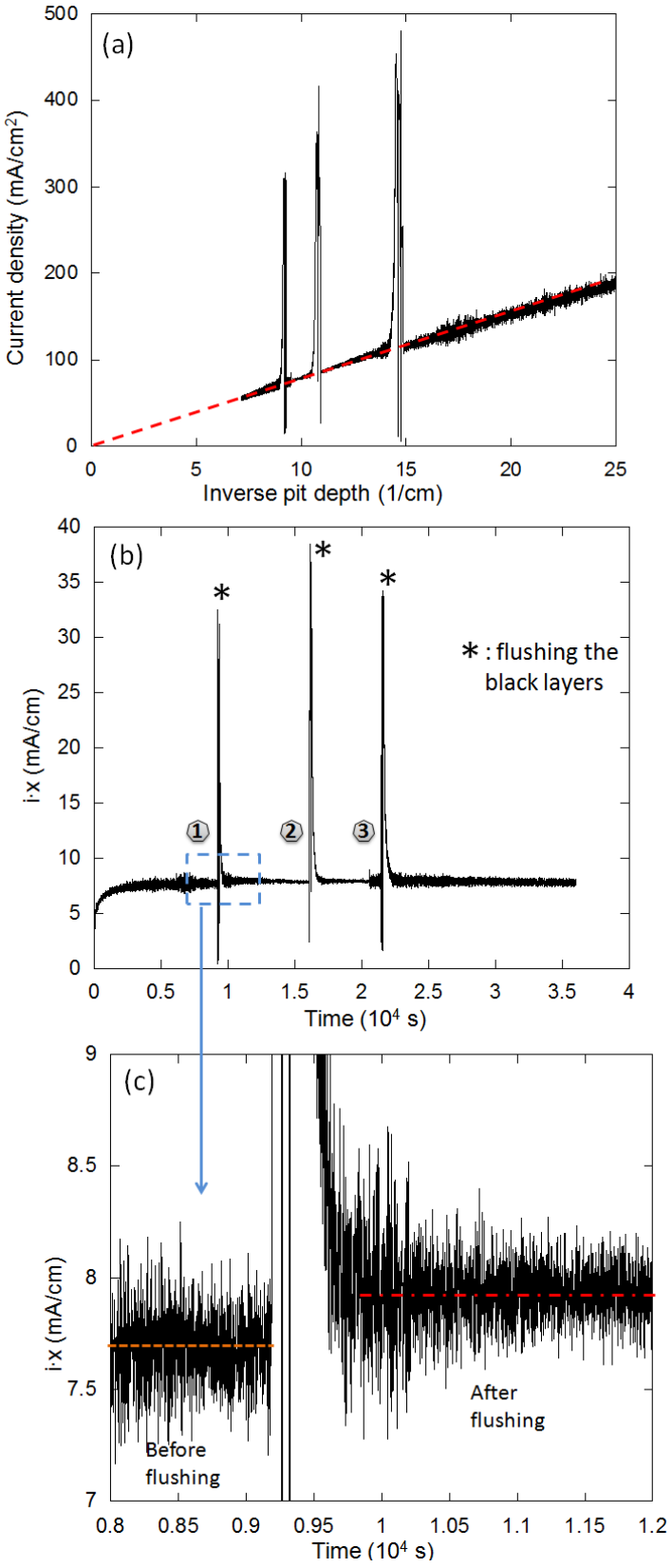

Figure 6-4 (a) Current density vs. the inverse pit depth, (b) pit stability product (i·x) vs. time, and (c) expanded part of (b) for a 304 stainless steel 1D artificial pit. The pit was flushed three times to remove black layers that form in the pit during dissolution.

6.2.3 Diffusion-limited current density during artificial pit growth

As described in Section 2.3, when a relatively high potential is applied to a 1D artificial pit electrode, a salt layer can form due to supersaturation of the solution with metal ions, and the current density is diffusion controlled. As described in Section 2.2.3 and 2.2.4, stable pit growth is associated with a constant pit stability product (*ix*). Figure 6-5(a) shows the current density and Figure 6-5(b) shows the pit stability product (*ix*) as a function of time for a 304 stainless steel 1D artificial pit in $MgCl_2$ solutions of different concentrations grown at the same applied potential 600 mV (vs. SCE). It is clear that the current densities and pit stability product (*ix*) during pit growth in 3 M and 5 M $MgCl_2$ solutions are much lower than the current densities in 0.2 M and 0.5 M $MgCl_2$ solutions. In Figure 6-5, it can be seen that there is noise in the current density, which may be attributed to local passivation and re-activation events taking place beneath the salt layer reported by Newman and Ajjawi [141].

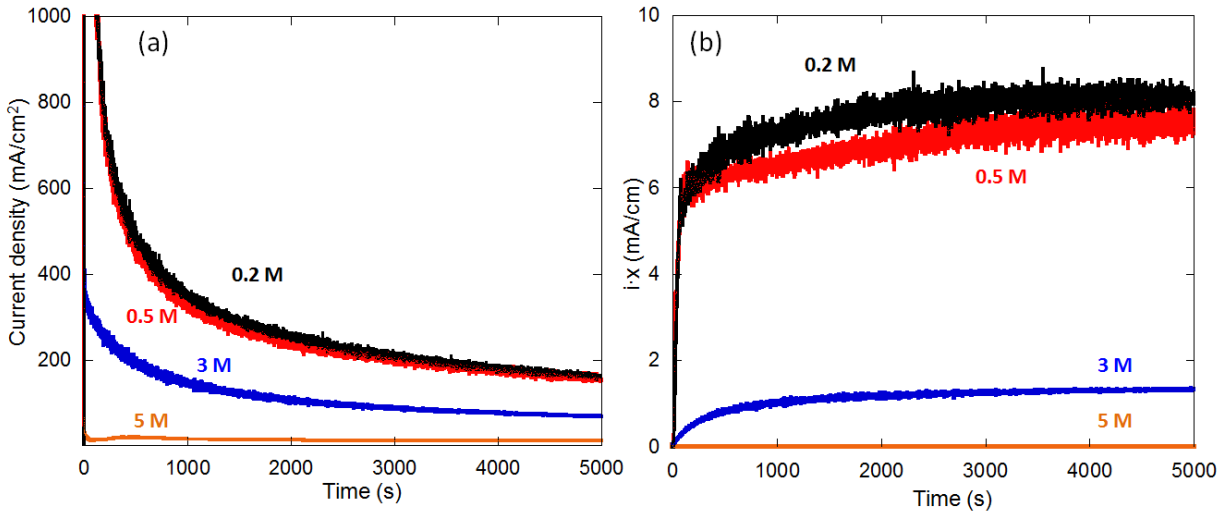

Figure 6-5 (a) Current density and (b) pit stability product (*ix*) in different chloride concentration $MgCl_2$ solutions with time. Experiments were performed on 1D artificial pits in SS304 wire (250 µm diameter) at 600 mV (vs. SCE) at 20±2 °C.

6.2.4 Current-voltage characteristics

Figure 6-6 (a) shows a typical example of the current-voltage characteristics of a 304 stainless steel 1D artificial pit in 0.5 M $MgCl_2$ solution. After growing the wire artificial pit to a depth of 500 µm at 0.6 V (vs. SCE), the potential was swept back until the salt layer was removed. While the salt layer is present, the current density is under diffusion control, and therefore is

independent of the applied potential. Figure 6-6 (b) shows the resistance vs. potential during the potential sweep. The resistance was measured at a fixed high frequency of 100 kHz with a 5 mV amplitude during the corrosion process. It can be seen that the resistance decreases linearly with the decreasing potential, which indicates that the thickness of the salt layer decreases with the decreasing potential.

When the salt layer is completely removed, there is a small increase in the current density, which indicates that the system is no longer under diffusion control. As described in Section 2.3.2, the transition potential (E_T) is defined as the minimum potential at which the current density value is equal to the diffusion-limited current density value, i.e. it is the potential where the transition takes place between a salt-covered and salt-free surface. In the salt layer-free region, the resistance of solution is nearly independent of potential. Then on the forward potential sweep, the current density increases and the metal dissolution rate increases.

When the production rate of metal ions exceeds the diffusion rate, supersaturation of metal ions is produced at the pit interface causing a salt layer to precipitate, which leads to a sudden drop in the current density. The decrease of current density reduces the thickness of the salt layer. As the potential increases further, the current density increases and then is controlled by diffusion. Before the salt layer precipitation, the resistance is nearly independent of potential and has a sudden increase when the salt layer precipitates. The resistance then decreases immediately, as the current density drops and salt layer thins. And then in the diffusion-controlled region, the resistance increases with the increasing potential.

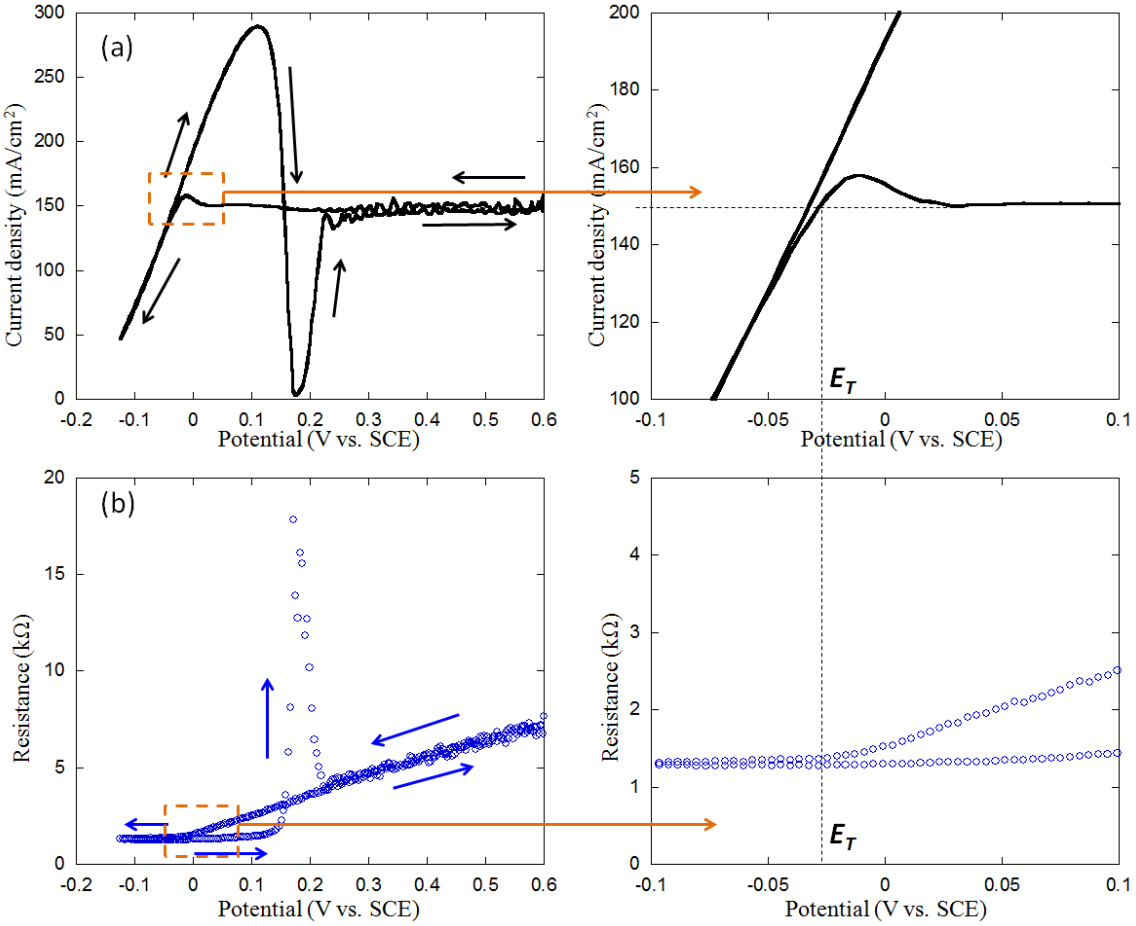

Figure 6-6 (a) A typical current-voltage characteristic and (b) the resistance vs. potential of a 304 stainless steel 1D artificial pit in 0.5 M $MgCl_2$ solution.

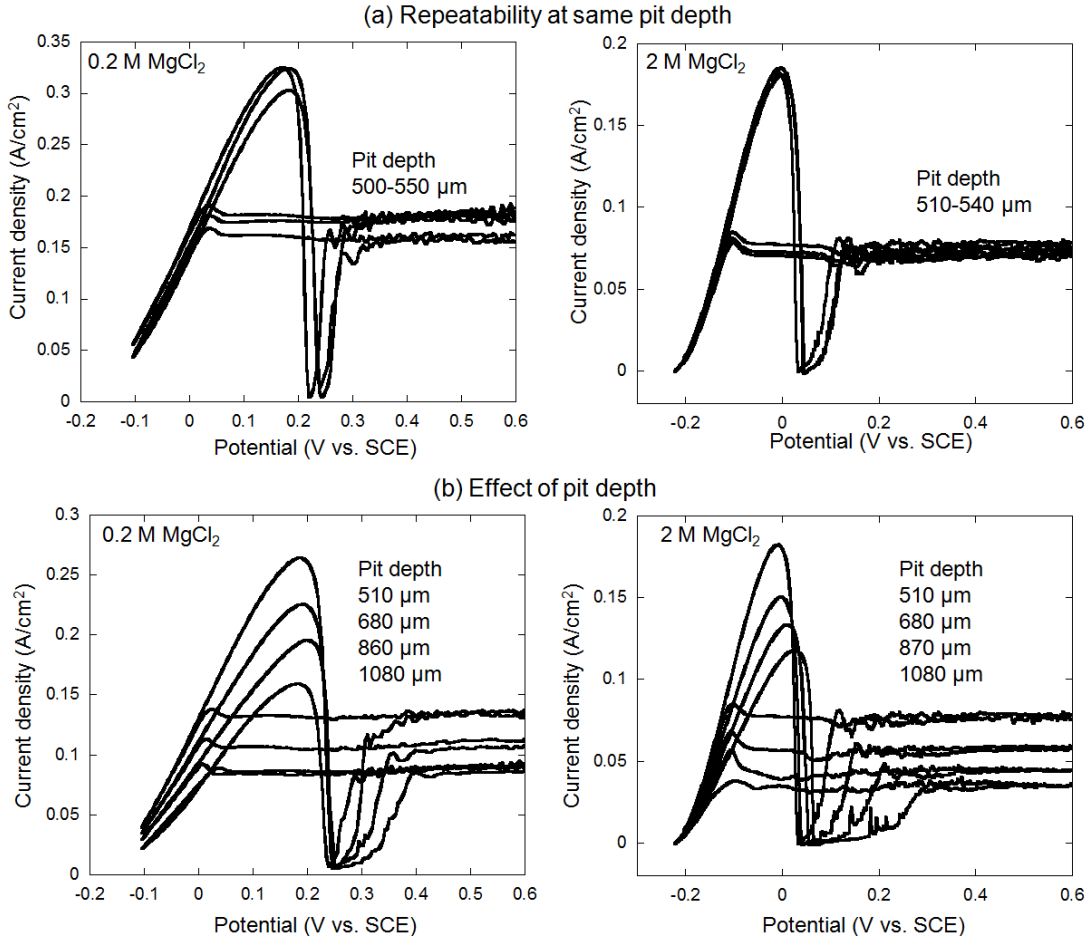

Figure 6-7 (a) The repeatability of the current-voltage characteristics of 304 stainless steel 1D artificial pits at the same pit depth on three different samples and (b) the current-voltage characteristics of stainless steel 1D artificial pits at different pit depths in 0.2 and 2 M $MgCl_2$ solutions at 20±2 °C.

Figure 6-7 (a) shows the repeatability of current-voltage characteristics of three stainless steel artificial pits in 0.2 and 2 M $MgCl_2$ solutions at the same pit depth. Three stainless steel 1D pits were grown to the same depth and it can be seen that the current-voltage characteristics are fairly repeatable. Figure 6-7 (b) shows the current-voltage characteristics at different pit depths. It can be seen that the diffusion-limited current density decreases with increasing pit depth.

Additional cyclic voltammograms for 304 stainless steel 1D artificial pits in various chloride concentration bulk solutions are shown in Figure 6-8. When the pit depth is the same, in lower chloride concentration solutions ($\leqslant$0.5 M $MgCl_2$), the diffusion-limited current density does not change with the bulk chloride concentration (Figure 6-8 (a)). However, in higher chloride

concentration solutions ($\geqslant$ 0.5 M $MgCl_2$ solution), the diffusion-limited current density decreases with increasing bulk chloride concentration (Figure 6-8(b)).

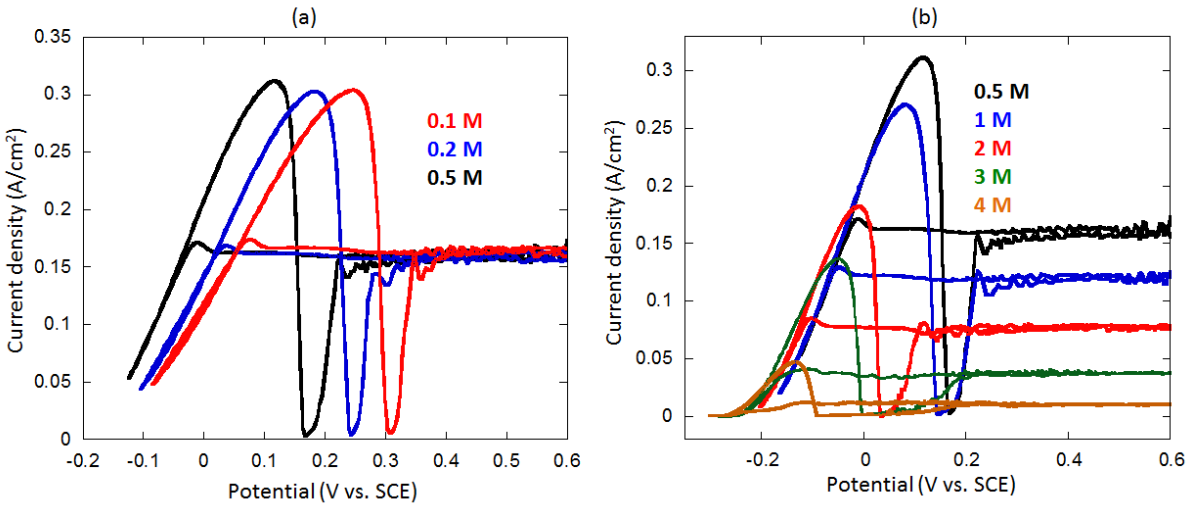

Figure 6-8 Current density vs. potential during potential sweep measurement for 250 µm diameter 304 stainless steel 1D artificial pits (a) in 0.1 M, 0.2 M and 0.5 M $MgCl_2$, and (b) 0.5 M, 1 M, 2 M, 3 M and 4 M $MgCl_2$ at 20±2 °C when the pit depth is about 500 µm.

6.2.5 Critical pit chemistry

As described in Section 2.3.3 and Section 3.4.1, the critical metal ion concentration for passivation for stainless steel 1D artificial pits can be determined by a slow backscanned potential sweep following Ernst and Newman's method [77, 132].

Figure 6-9 shows plots of current density vs. potential in 1 M $MgCl_2$ solution measured by this method for two different pit depths at a potential sweep rate of 0.2 mVs^{-1}. In both plots, the current density first remains in the diffusion-limited current density and then increases slightly before starting to decrease linearly with decreasing potential. The linear change of current density vs. potential corresponds to the *IR* drop controlled region. The starting point of this linear region is defined as the saturated current density (labelled i_{sat}), as it corresponds to the first point in the *IR* drop controlled region after salt layer removal. The value of i_{sat} should equal to i_{lim}. Ernst and Newman [77, 132] defined that the ending point is the current density that corresponds to the critical pit chemistry, as below this current density value in a very slow potential backscan, the diffusion limited current density cannot be instantly regained when scanning rapidly to high potential, which indicates passivation has taken place in the

artificial pit. This current density value is denoted as i^*. In the current work, i^* has not been checked with the above process due to the limitation of the potentiostat.

It can be seen that following the linear part of the current decay, the current density decreases more quickly in Figure 6-9 (a) and decreases more slowly in Figure 6-9 (b). The current decay shown in Figure 6-9 (b) was measured at a deeper pit compared with Figure 6-9 (a). Figure 6-10 shows plots of current density vs. potential for stainless steel artificial pits in solutions of different chloride concentration. It can be seen that when the curve was measured in a deeper pit in lower chloride concentration solutions, or measured in higher chloride concentration solutions, the current density decay curvature is similar to Figure 6-9 (b).

There are three possible reasons for the decay curvature change: crevice formation might take place at the bottom of the pit; a cathodic reaction such as metal plating; or the pit is partially repassivated and the dissolving interface separates into active and passive regions.

The pit was visually observed with an optical microscope to check that it was not creviced. Newman and Isaacs [142] reported that copper could plate out in stainless steel for the anomalous cathodic reaction, but the copper level of the stainless steel wire used in the current work has not been reported. It is also possible that the pit bottom is partially repassivated.

In the present work, when the current change curvature occurs as shown in Figure 6-9(b), the current density to define critical pit chemistry (i^*) is still determined at the end of the linear region, but is labelled differently in the future figures.

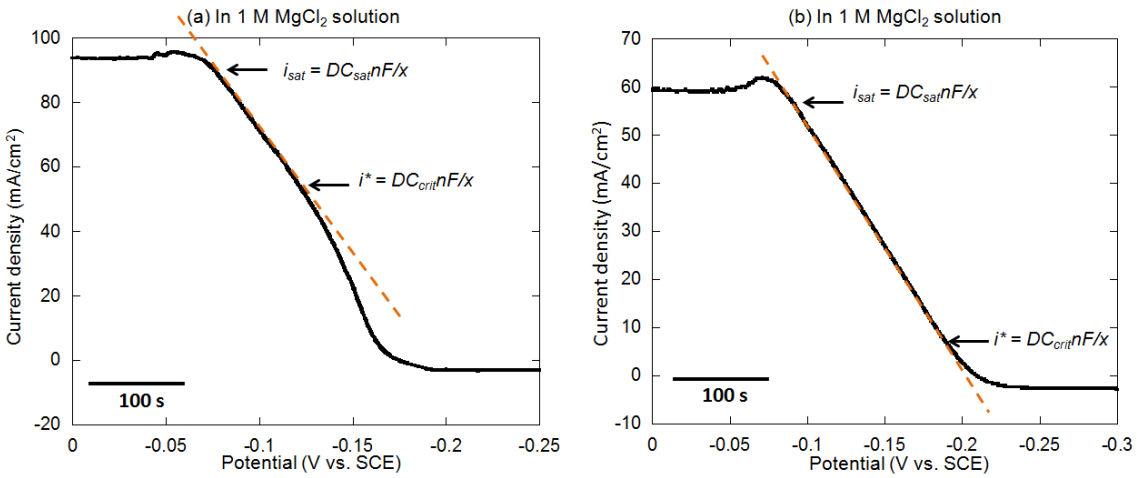

Figure 6-9 Current density vs. potential (time) of 304 stainless steel 1D artificial pits (250 µm wire) in 1 M $MgCl_2$ solution at 20±2 °C with potential sweep at 0.2 mVs^{-1} . The pit depth in (a) is about 700 µm, and the pit depth in (b) is about 1.1 mm.

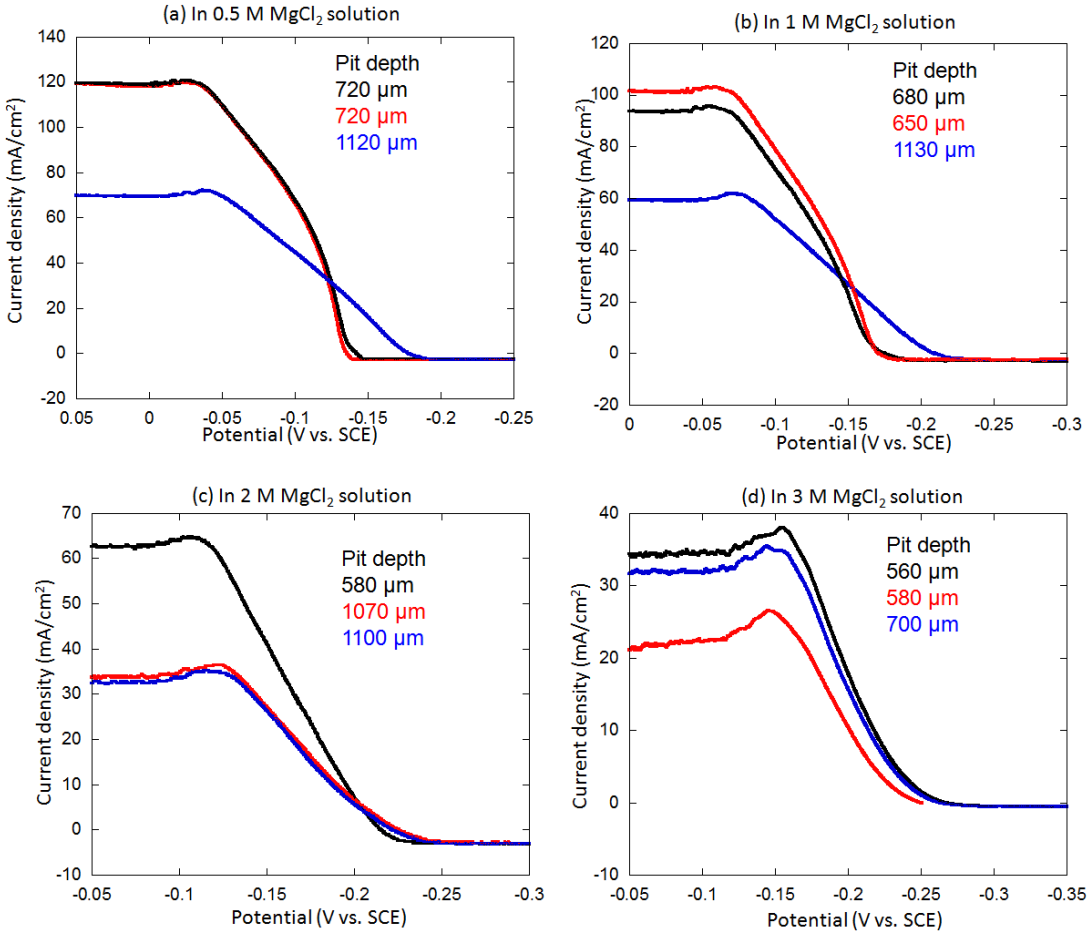

Figure 6-10 Current density vs. potential (time) of 304 stainless steel 1D artificial pits (250 μm wire) in 0.5-3 M $MgCl_2$ solution at 20±2 °C with potential sweep at 0.2 mVs^{-1} . The black, red and blue curves represent three different experiments on 304 stainless steel 1D artificial pits at different depths.

As described in Section 2.2.6, the current density may be expressed as $i = nFD\Delta C/x$, and the metal ion concentration at the pit mouth is approximately zero, so two equations can be expressed as below:

$$DC_{sat} = \frac{i_{\lim} x}{nF} \approx \frac{i_{sat} x}{nF} \qquad \text{Equation 6-3}$$

$$DC_{crit} = \frac{i^* x}{nF} \qquad \text{Equation 6-4}$$

where D is the diffusion coefficient of metal ions, C_{sat} is the saturated metal ion concentration, C_{crit} is the critical metal ion concentration for pit propagation/passivation, i_{lim} is the diffusion-limited current density which equals to i_{sat} the current density at saturated metal ion

concentration, i^* is the current density corresponding to the critical pit chemistry, x is the pit depth, n is the transferred charge and F is the Faraday constant.

Since i_{lim} and i^* can be obtained from Figure 6-10, the values of DC_{sat} and DC_{crit} can be calculated. Figure 6-11 shows the change of DC_{sat} and DC_{crit} with bulk chloride concentration. The hollow blue triangle represents DC_{crit} measured at i^* as shown in Figure 6-9 (a), and the solid blue triangle represents DC_{crit} measured at i^* at the point of special curvature as shown in Figure 6-9 (b).

From 0.01 M to 1 M chloride concentration, there is no significant change in either DC_{sat} or DC_{crit}, whilst above 1 M chloride concentration, both DC_{sat} and DC_{crit} values decrease steeply. If the diffusivity is assumed to be the same, the ratio of the critical pit chemistry to the saturated pit chemistry C_{crit}/C_{sat} can be calculated, and the result is shown as Figure 6-12. From 0.02 to 1 M chloride solution, the C_{crit}/C_{sat} value is about 60-70%, and does not decrease obviously with the increasing chloride concentration. The value of C_{crit}/C_{sat} decreases steeply when the chloride concentration further increases, and can drop to 10-20% in 8 M chloride solution.

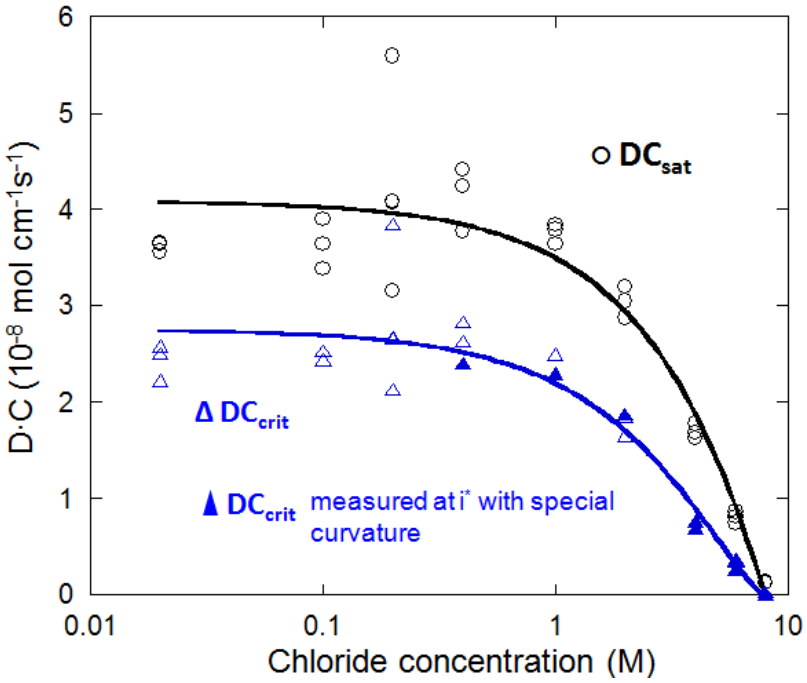

Figure 6-11 Change of DC_{sat} and DC_{crit} with bulk chloride concentration for 304 stainless steel 1D artificial pits in $MgCl_2$ solutions at 20±2 °C. The hollow blue triangle represents DC_{crit} measured at i^* as shown in Figure 6-9 (a), and the solid blue triangle represents DC_{crit} measured at i^* in the special curvature as shown in Figure 6-9 (b).

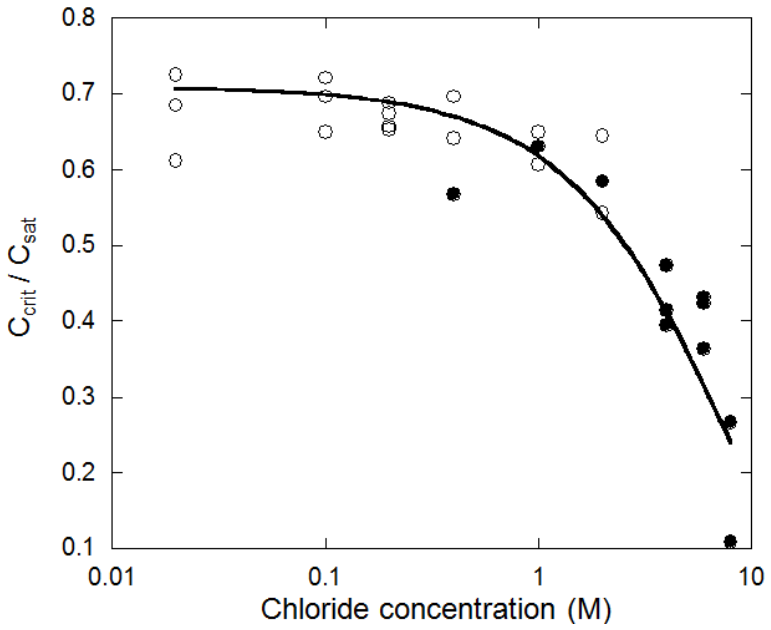

Figure 6-12 C_{crit}/C_{sat} vs. bulk chloride concentration of 304 stainless steel 1D artificial pit in $MgCl_2$ solution at 20±2 °C. The hollow black dot represents C_{crit} measured at i^* as shown in Figure 6-9 (a), and the solid black dot represents C_{crit} measured at i^* in the special curvature as shown in Figure 6-9 (b).

6.2.6 Tafel slope

As described in Section 2.3.4, the dissolution kinetics of pit growth can be expressed as

$$E_{app} = E_{corr} + b_a log\ (i_a/i_{corr}) + IR \qquad \text{Equation 2-14}$$

Then Equation 2-14 can be expressed as below:

$$b_a log(i_a/i_{corr}) = E_{app} - E_{corr} - IR$$

where E_{corr} and i_{corr} are assumed to be constants. The resistance R was measured with an impedance method at a high frequency of 100 kHz with 5 mV amplitude, so it is feasible to plot the current density vs. the *IR*-corrected interfacial potential as shown in Figure 6-13. The region where the current density is independent of the *IR*-corrected potential indicates the region is diffusion-limited. The very low current density data points in Figure 6-13 indicate salt layer formation. It can be seen in the activation/*IR*-controlled region in the blue dashed box that there is a linear relationship between the log of the current density and the *IR*-corrected potential. This linear relationship corresponds to the Tafel slope (b_a). In the present work, b_a is calculated from the activation/*IR* controlled region of the current density value of about 60% to 140% of the diffusion limited current density without salt film as shown in the blue dashed box in Figure 6-13.

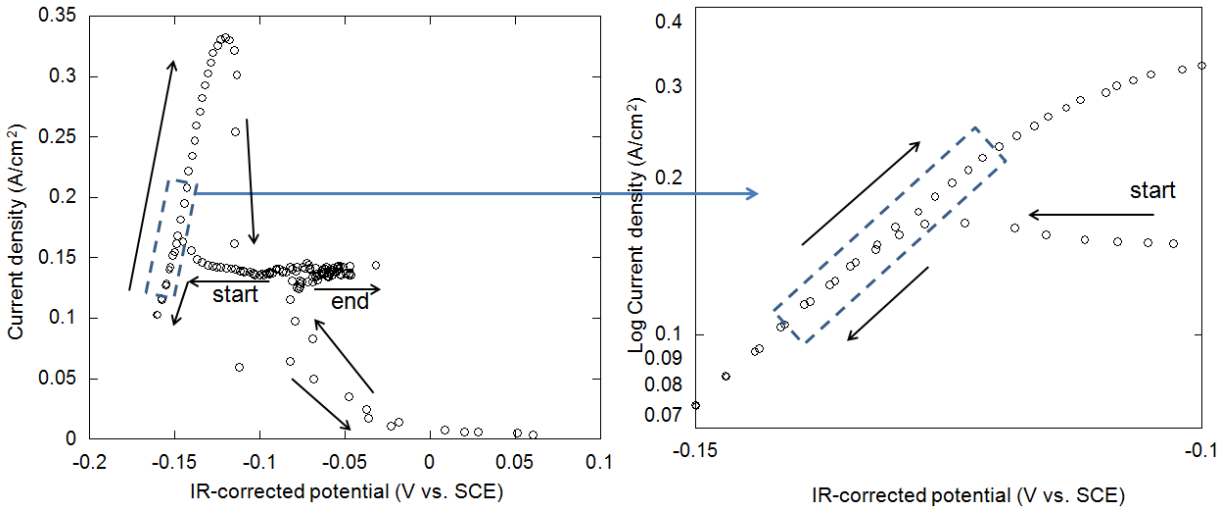

Figure 6-13 Current density vs. *IR*-corrected potential on 304 stainless steel 1D artificial pit in 1 M $MgCl_2$ solution at 20±2 °C. The scan rate of the potential is 10 mV/s. The Tafel slope can be calculated from the potential scan in the activation/IR-controlled region of the log plot as shown in the blue dashed box region.

In this method, the potential sweep rate may affect the Tafel slope calculation, as it can affect the interface chemistry. The solution concentration is initially C_{sat}, but once the current drops below this value, the solution concentration will decrease. If the measurement is sufficiently fast, the change in solution concentration will be small. The fact that the forward sweep and the reverse sweep overlap in this region suggests that this is the case. However, it is important to check the behaviour at different sweep rates. A range of potential sweep rates from 2 mVs^{-1} to 10 mVs^{-1} have been used, and the results of current density vs. *IR*-corrected potential are shown in Figure 6-14. The linear regions of the data are valid for calculation of the anodic Tafel slope. In Figure 6-14, the current density vs. *IR*-corrected potential of the 2 mV/s scan rate is slightly curved in the forward sweep, suggesting that the scan rate might have affected the interfacial chemistry.

The anodic Tafel slopes measured with various potential scan rates are shown in Table 6-1. It can be seen that the scan rate can affect the Tafel slope. The change caused by the scan rate is not great, and the deviation of Tafel slopes is about 20%.

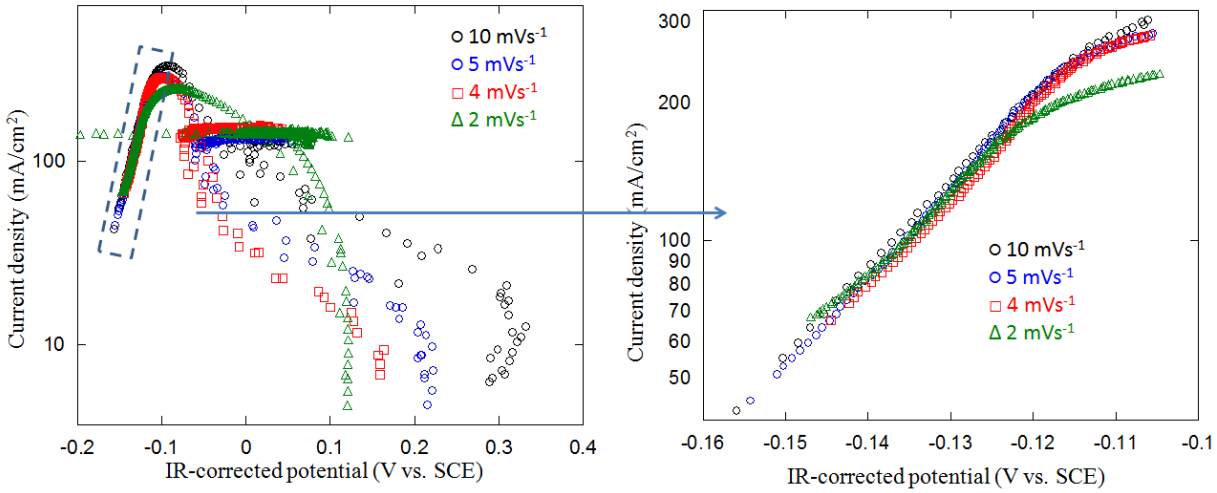

Figure 6-14 Current density vs. *IR*-corrected potential on 304 stainless steel 1D artificial pit in 0.5 M $MgCl_2$ solution at 20±2 °C. The scan rate of the potential is in the range from 2 mV/s to 10 mV/s. The Tafel slope can be calculated in the linear region of the log plot as shown in the dashed box.

Table 6-1 Tafel slope (gradient of *IR*-corrected potential vs. current) calculated from the upwards potential sweep in 0.5 M $MgCl_2$ solution of 304 stainless steel 1D artificial pit at various sweep rates at 18±2 °C. The resistance was measured at 50 kHz and 50 mV amplitude. The Tafel slope was measured three times at different scan rates for the error bar.

Potential scan rate (mVs^{-1})	Tafel slope (mV/decade)
2	51±5
4	52±5
5	53±3
10	56±2

The Tafel slopes in various chloride concentration solutions have been measured in the *IR*-controlled region for both downwards and upwards potential sweeps, and the results are shown in Figure 6-15. There is no obvious change of the Tafel slope when the chloride concentration is different.

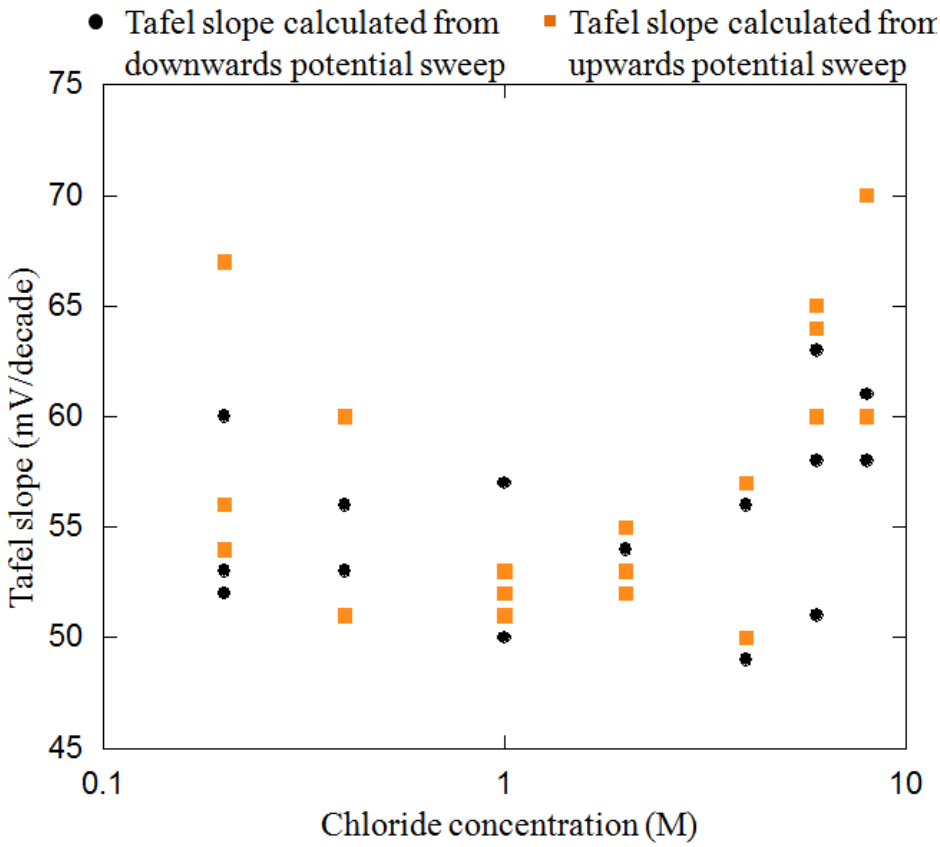

Figure 6-15 Tafel slope as a function of chloride concentration for 304 stainless steel 1D artificial pits in $MgCl_2$ solutions at 20±2 °C. The Tafel slope was calculated from plots of the *IR*-corrected potential vs. current density in downwards potential sweep and upwards potential sweep as shown in Figure 6-8. The resistance was measured at 100 kHz with a 5 mV amplitude throughout the measurements. The potential sweep rate is 6 mVs^{-1} in 0.1 and 0.5 M $MgCl_2$ solution, and is 4 mVs^{-1} in 1 to 4 M $MgCl_2$ solution. Each Tafel slope was measured at least three times for each chloride concentration.

Laycock and Newman have plotted the *IR*-corrected transition potential vs. the log current density to obtain the Tafel slope of stainless steel 302 artificial pits in NaCl solutions [31]. However, they only corrected for the resistance of the external cell, not the pit itself. Since the resistance of the pit can be measured at each point in the present work, the *IR*-corrected transition potential vs. the log diffusion limited current density is shown in Figure 6-16 (a) and are compared with Laycock and Newman's results.

In Figure 6-16 (a), the blue and green data points are the experimental results from the present work calculated with full *IR* correction for 304 stainless steel artificial pits in 0.5 M and 3 M $MgCl_2$ solutions. The slope of the data points is assumed to be the Tafel slope, which

is about 50 mV/decade in the 0.5 M $MgCl_2$ solution and is 48 mV/decade in 3 M $MgCl_2$ solution. It can be seen that the value of the Tafel slopes are significantly lower than Laycock and Newman's results of about 100 mV/decade. The most likely reason for this is that Laycock and Newman considered only the potential drop outside the pit. In the present work, it is possible to separate the cell resistance (R_{cell}) into the pit solution resistance (R_{pit}) and the bulk solution resistance (R_{bulk}) by plotting the cell resistance against various pit depth. The bulk solution resistance is the intercept at zero depth, which was used in the *IR* drop correction in Figure 6-16 (b).

Figure 6-16 (b) shows the transition potential measurements in the present work corrected only with ohmic drop outside the pit vs. log current density. It can be seen that the Tafel slope is 85 mV/decade in 0.5 M $MgCl_2$ solution, which is closer to the values found by Laycock and Newman.

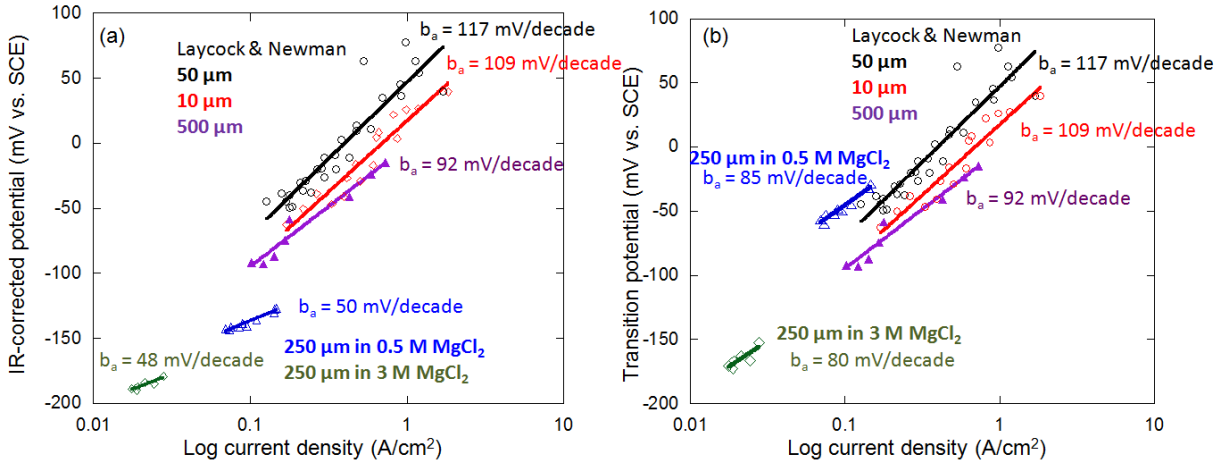

Figure 6-16 *IR*-corrected transition potential vs. log current density for 304 stainless steel 1D wire artificial pits 250 µm diameter in 0.5 M $MgCl_2$ and 3 M $MgCl_2$ at 20±2 °C. The results of Laycock and Newman [31] are shown for comparison: they were measured on 302 stainless steel wire artificial pit electrodes of 10, 50 and 500 µm diameter in 1 M NaCl solution. The transition potential E_T measured by Laycock and Newman was corrected the potential drop outside the pit only. In (a), data from the present work are shown with full *IR* drop correction; in (b), data for the present work are shown with correction of the *IR* drop outside the pit only, for direct comparison with the data of Laycock and Newman [31].

6.3 Pitting and repassivation of stainless steel wires

6.3.1 Pitting potential

The pitting potential was measured from potentiodynamic sweep experiments on abraded 304 stainless steel wire. The potential was scanned from -200 mV or -100 mV vs. OCP to the potential where the current density exceeds 1 $mAcm^{-2}$ as described in Section 3.4.2. Typical pitting potential measurements in $MgCl_2$ solutions are shown in Figure 6-17. In Figure 6-17 (a), where the bulk solution chloride concentration is relatively low, the passive current density is very noisy at higher potentials, which corresponds to the formation of metastable pits. When the bulk solution chloride concentration is relatively high, the typical results of pitting potential measurements are shown in Figure 6-17 (b). The passive current density increases continuously up to an inflexion point, and then increases steeply with the onset of pitting. There is no obvious sign of noisy current that indicates the metastable pit growth.

The value of pitting potential obtained in these experiments is dependent upon the definition of pitting potential which is chosen. For example, if the pitting potential in 0.05 M $MgCl_2$ solution is defined as when the current density exceeds 0.01 mA/cm^2, the pitting potential is in the range of 580 to 610 mV, while if it is defined as the current density exceeds 0.1 mA/cm^2, the difference between the pitting potential measured at 0.01 mA/cm^2 is less than 5 mV. However, if the pitting potential in 5 M $MgCl_2$ solution is defined as the point at which the current density exceeds 0.01 mA/cm^2, the pitting potential is in the range of -300 to -340 mV (vs. SCE), while if it is defined as the current density exceeds 0.1 mA/cm^2, it is about 40 mV lower. In this chapter, the pitting potential is defined to be the potential when the current density exceeds 0.1 mA/cm^2 in the potential scan.

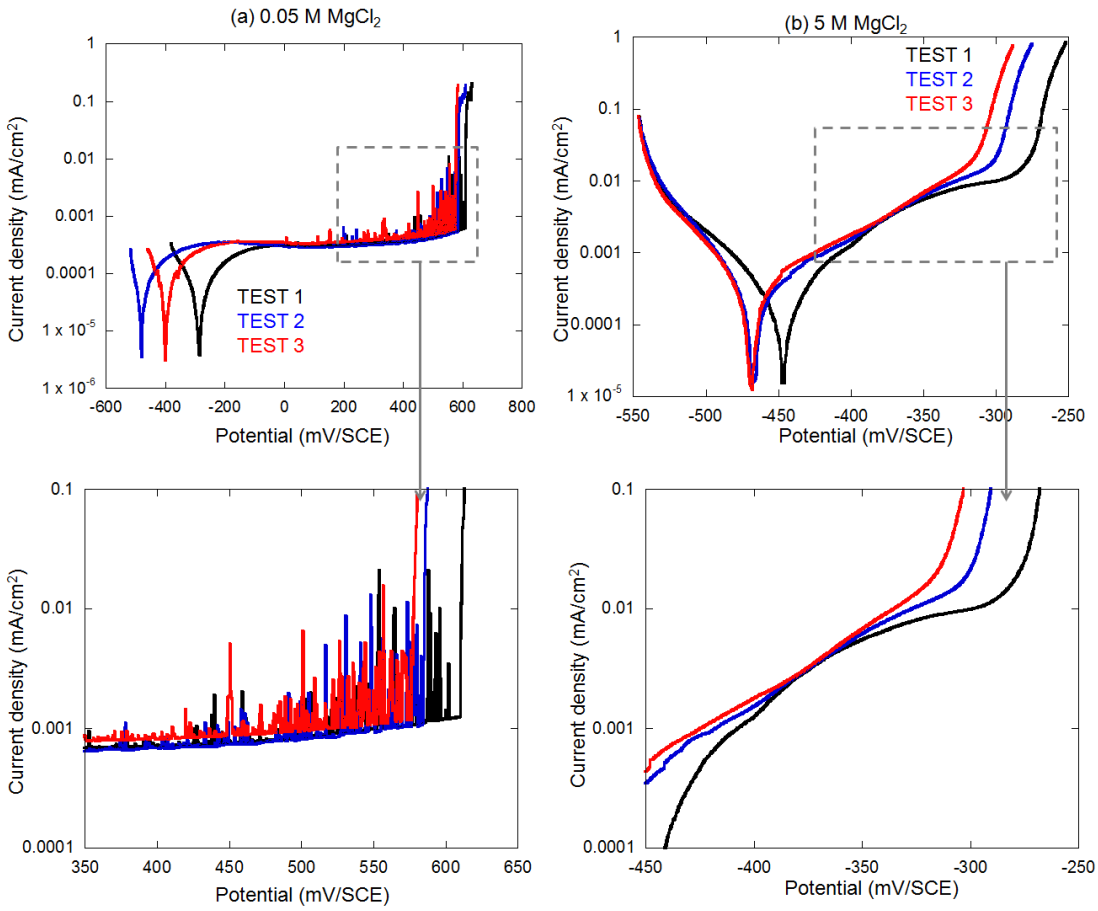

Figure 6-17 Current density vs. potential on 304 stainless steel wire with a 4000 grit surface finish in (a) 0.05 M $MgCl_2$ solution and (b) 5 M $MgCl_2$ solution at 20±2 °C. Each measurement was repeated at least three times.

Figure 6-18 shows the current density vs. potential of the abraded wire electrodes in a range of chloride concentrations. Figure 6-18 (a) shows the measurements in solutions with $MgCl_2$ concentrations of 3 M and below. In all cases the passive current density is similar, and noise associated with metastable pitting is observed at potentials close to the pitting potential. Following breakdown, the increase in current density is very sudden. The pitting potential and onset of metastable pitting decreases with increasing solution concentration.

Figure 6-18 (b) shows the measurements in solutions with $MgCl_2$ concentrations of 3 M and above. The passive current density is significantly higher at 3.2 M compared with 3 M (this experiment was repeated three times to confirm the difference in the range of 100% - 125%). A small amount of metastable pitting was observed at 3.2 M but is not evident at higher concentrations. The passive current density is similar for 3.2, 3.5 and 4 M solutions, but

significantly higher for 5 M. As noted above, for higher solution concentrations, the increase in current at the onset of pitting is less sudden.

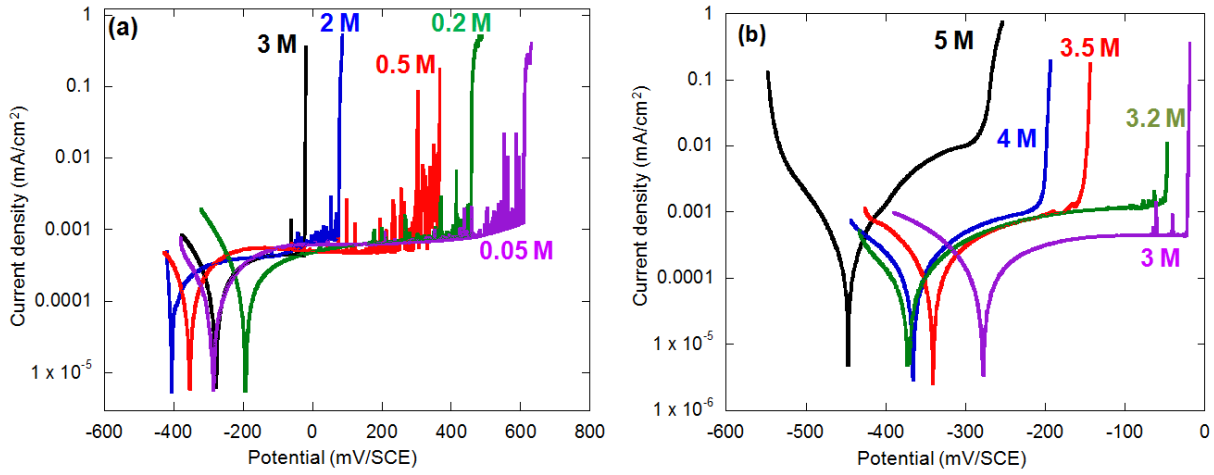

Figure 6-18 Polarisation curves of the current vs. potential of 304 stainless steel wires (250 µm diameter) abraded to 4000 grit by SiC papers in (a) 0.05-3 M $MgCl_2$ solutions and (b) 3-5 M $MgCl_2$ solutions. The potential sweep rate is 0.2 mV/s.

Figure 6-19 shows the SEM images of the pit morphologies observed on 304 stainless steel wires.

Figure 6-19 (a) shows a relatively small pit in 0.1 M $MgCl_2$ solution and (b) a relatively large and open pit in 4 M $MgCl_2$ solution. The pit in the 4 M $MgCl_2$ solution is quite shallow and has lots of corrosion products surrounding it.

Figure 6-19 (c) shows a typical metastable pit observed in 0.1 M $MgCl_2$ solution. Metastable pits have not been observed in high chloride concentration solution, which is consistent with the polarisation curves shown in Figure 6-18.

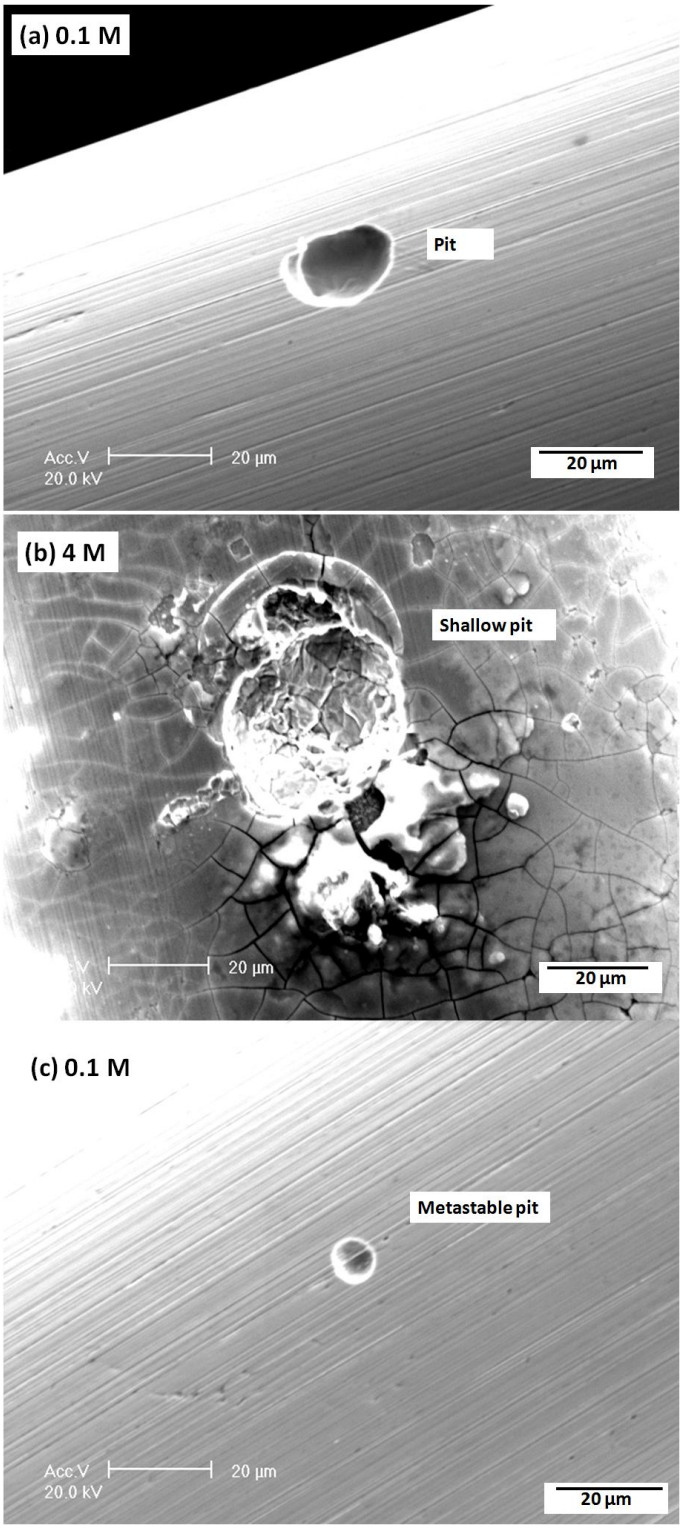

Figure 6-19 The SEM images of pit morphology on 304 stainless steel 4000 grit surface finish in 0.1 M and 4 M $MgCl_2$ solution at 20±2 °C.

The experiments shown in Figure 6-18 were repeated for a surface finish of 120 grit. The relationship between pitting potential and the bulk solution chloride concentration for both surface finishes is shown in Figure 6-20. When the chloride concentration is ⩽2 M, the

dependence of pitting potential upon log chloride concentration is relatively linear. Above 2 M, the pitting potential decreases more steeply with increasing chloride concentration.

The slope of the decrease of pitting potential to log chloride concentration in the relatively linear region with 120 grit surface finish is about 110 mV/decade, and the decrease with 4000 grit surface finish is about 200 mV/decade.

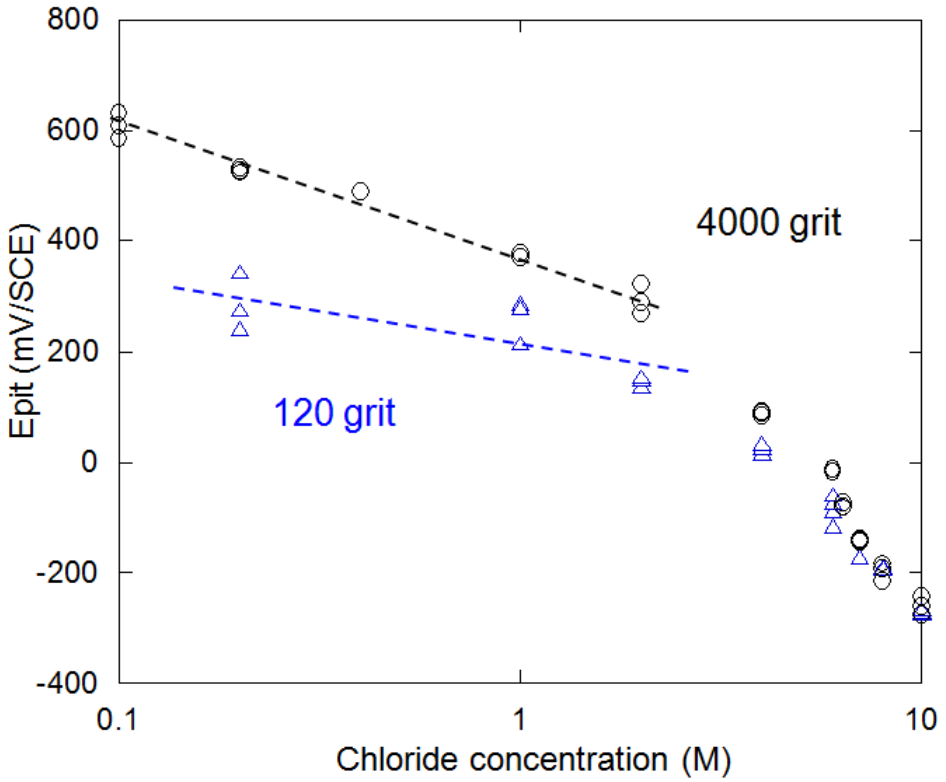

Figure 6-20 Pitting potential vs. chloride concentration on 304 stainless steel with 120 and 4000 grit surface finish wire in $MgCl_2$ solution at 20±2 °C. The pitting potential was defined in the forward potential scan when the current density exceeds 0.1 mA/cm^2.

6.3.2 Repassivation potential

The repassivation potential is measured in different ways in the literature. It can be measured by back sweeping the potential from the pitting potential to the potential at which the current density decreases to 10^{-3} mA·cm^{-2} or 10^{-4} mA·cm^{-2}, or to the potential corresponding to the passive current density. Two typical measurements of repassivation potential are shown in Figure 6-21. It can be seen that the repassivation potential is highly dependent upon the definition. In the current work, the repassivation potential was defined at a current density of 10^{-3} mA·cm^{-1}. The repassivation potential vs. chloride concentration is shown in Figure 6-22.

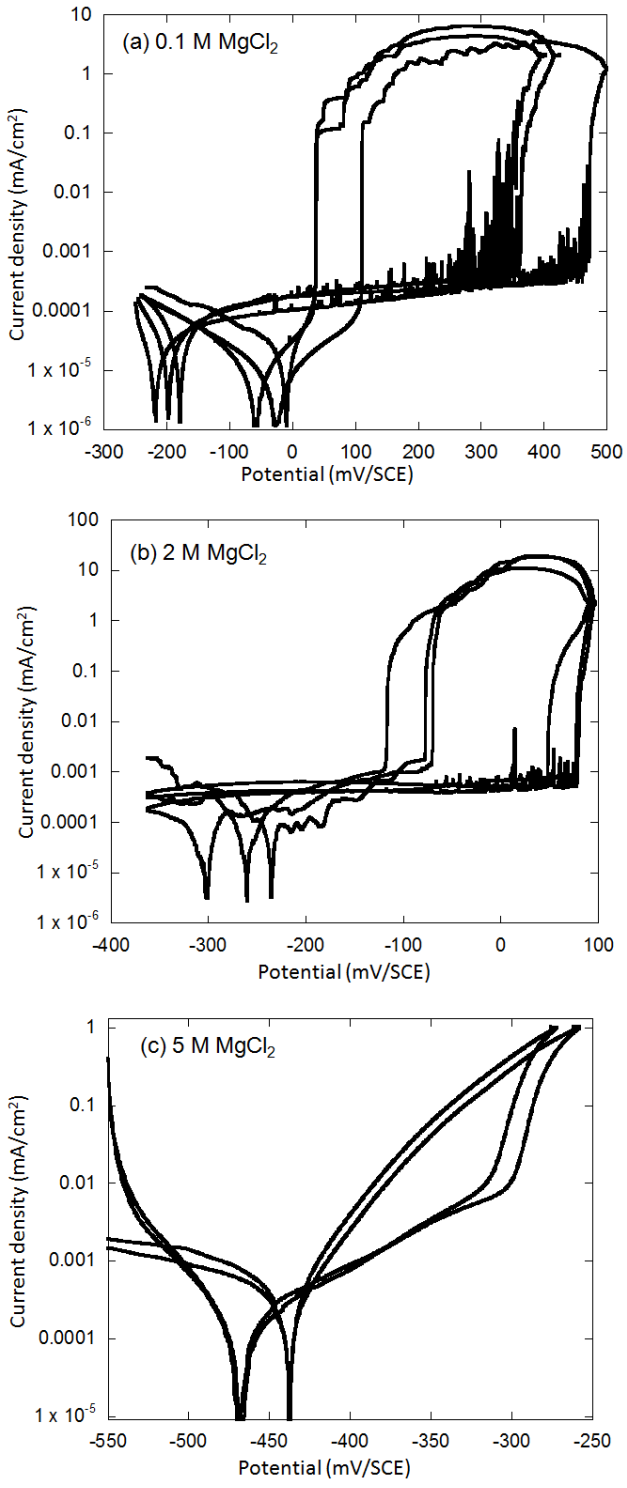

Figure 6-21 Current density vs. potential on 304 stainless steel 4000 grit surface finish wire in 0.1 M, 2 M and 5 M $MgCl_2$ solution at 20±2 °C. The repassivation potential is measured at 10^{-3} mA·cm^{-2}.

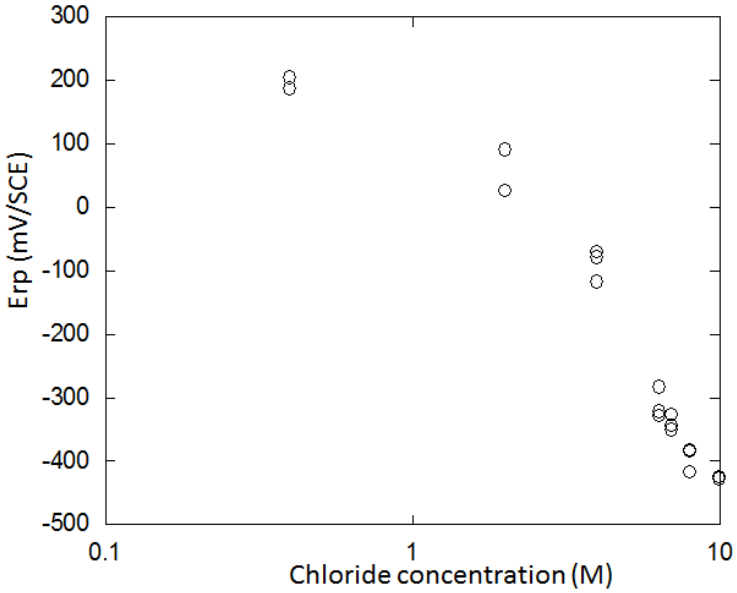

Figure 6-22 Repassivation potential vs. chloride concentration on 304 stainless steel with a 4000 grit surface finish wire in $MgCl_2$ solution at 20±2 °C.

6.4 Discussion

6.4.1 Current-voltage characteristics of artificial pits in stainless steel

Figure 6-8 shows that the diffusion-limited current density decreases with increasing chloride concentration, which indicates that $D\Delta C$ decreases with increasing chloride concentration according to Equation 2-12 $i_{\lim} = \frac{nFD\Delta C}{x}$. The decreasing $D\Delta C$ with increasing chloride concentration can be due to two reasons: the common-ion effect and the decreasing diffusion coefficient. As the bulk chloride concentration increases to $\geqslant$ 1 M, Mg^{2+} ions in the pit cavity cannot be a neglected factor. The common-ion effect can decrease the solubility of dissolving metal ions. This effect is consistent with previous findings by Ernst and Newman [77]. As the viscosity of the $MgCl_2$ solution increases with increasing chloride concentration, the diffusivity of the metal ions would decrease [61], which also can lead the diffusion limited current density to decrease.

6.4.2 Critical pit chemistry of artificial pits in stainless steel

From Figure 6-12, when the chloride concentration is 1 M, C_{crit}/C_{sat} is in the range of 60-70%. This result is consistent with the work of Gaudet et al. [36]. They reported that the critical pit

chemistry required for pit propagation is about 65% of the saturation concentration of metal ions in 304 stainless steel 1D artificial pit in 1 M NaCl solution [36]. From Figure 6-12, it also can be seen that the value of C_{crit}/C_{sat} does not decrease significantly when the chloride concentration is from 0.02 M to 1 M, however it decreases substantially when the chloride concentration increases from 1 M to 8 M. C_{crit} can decrease to 10-20% of C_{sat} in 8 M chloride solution. This is fairly consistent with Ernst and Newman's finding of C_{crit}/C_{sat} decreased to about 10% in 4.5 M $CaCl_2$ solution on stainless steel 316L [77]. The significantly low C_{crit}/C_{sat} in high chloride concentration solution might indicate that less metal ion concentration within the pit is required for pit propagation.

6.4.3 Pit stability product of artificial pits in stainless steel

As described in Section 2.2.3, Galvele has developed a pit stability product *ix* for 1D pit, where *i* is the current density and *x* is the pit depth [32]. Pistorius and Burstein [35] proposed an upper and a lower limit of the pit stability product under immersion conditions. They used another form of the expression of Equation 2-12, $i = \frac{nFD\Delta C}{x}$ to calculate the pit stability product *ix* as a function of $nFD\Delta C$. Since *n* and *F* are constant, *D* is assumed to be a constant 10^{-9} m^2s^{-1}, *ix* only varies with ΔC. Pistorius and Burstein defined the lower limit of *ix* as $nFDC_{crit}$, as C_{crit} is the minimum metal ion concentration to sustain pit propagation. Pistorius and Burstein showed that the pit stability product (*ix*) should be above 0.3 Am^{-1} [35].

Similar to Pistorius and Burstein's approach, it is possible to calculate *ix* in different chloride concentration solutions on 1D artificial pits on stainless steel using the DC_{crit} and DC_{sat} data shown in Figure 6-11. The metal ion concentration of pit for stability of 1D artificial pit is in the range of C_{crit} and C_{sat}. The pit stability product (*ix*) on 1D artificial pits can then be calculated as in the range of $nFDC_{crit}$ and $nFDC_{sat}$, which is in the range of 0.50 Am^{-1} to 0.79 Am^{-1} in 1 M chloride solution, and is in the range of 0.07 Am^{-1} to 0.17 Am^{-1} in 6 M chloride solution. The pit stability product decreases with increasing bulk chloride concentration. This indicates the possibility of pit propagation with significantly lower stability product/ current density in high chloride concentration solutions.

As described in Section 2.4.5, Kelly and his co-workers [109-112, 114] have developed a model to predict the growth of atmospheric corrosion pits in stainless steel. One of the important factors to predict the maximum pit size is the minimum required anodic current (I_{LC})

for pit stability. In Kelly's model, the anodic current demand (I_{LC}) on pit radius (r_{pit}) will be greater than the hemispherical pit stability product (I_{pit}/r_{pit}) for stable pit growth. The value of I_{pit}/r_{pit} is equivalent to the value of $2\pi ix$, where ix is the 1D artificial pit stability product. The value of I_{pit}/r_{pit} are selected as 1 A/m and 3 A/m in Kelly's model as the baseline [110].

However, as described above, the pit stability product ix decreases with increasing chloride concentration. If the value of the pit stability product for a hemispherical pit ' I_{pit}/r_{pit} ' is also assumed to be the value of $2\pi ix$ as Chen and Kelly, I_{pit}/r_{pit} vs. chloride concentration can be shown as below in Figure 6-23 (a).

It can be seen that I_{pit}/r_{pit} decreases significantly with increasing chloride concentration. In lower chloride concentration solutions, the values of I_{pit}/r_{pit} calculated from the current work are higher than the value estimated by Kelly. This means only smaller pits can be supported to be stable (Figure 6-23 (b)). However, in high chloride concentration solutions, the values of I_{pit}/r_{pit} calculated from the current work are lower than the value estimated by Kelly. This means larger pits can be supported to grow stable, and it is possible that there is nearly no limit for pit growth under these conditions. It is clear that the value of measured I/r less than 1 A/m in 6 M and 8 M solutions (which corresponds to ~45%-65% RH), which indicates that the pit size in Kelly's model might be under-estimated under less humid conditions.

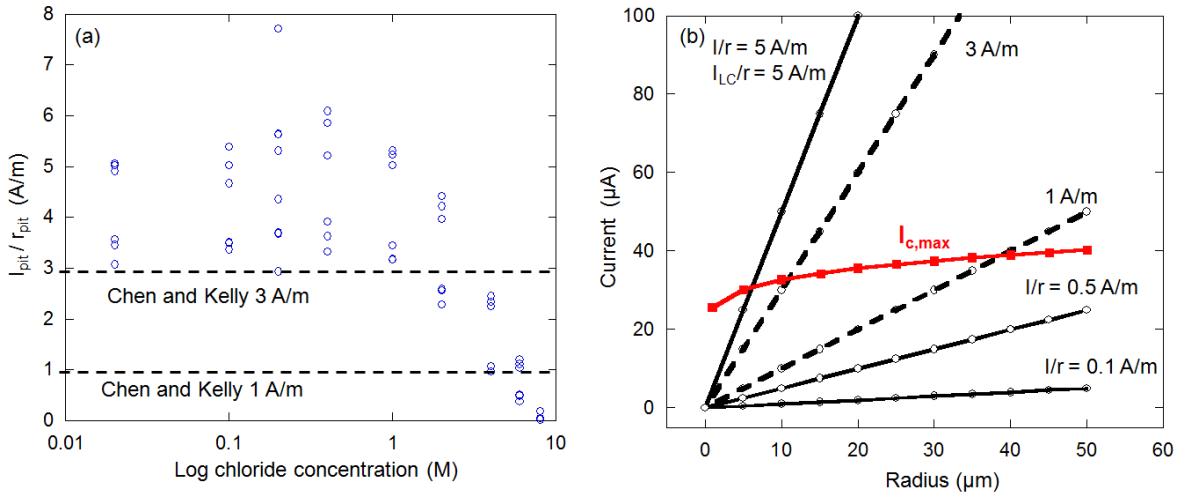

Figure 6-23 (a) Pit stability product I_{pit}/r_{pit} for hemispherical pits vs. log chloride concentration. The black lines are the values of I_{pit}/r_{pit} used by Chen and Kelly, which are the values of $2\pi ix$. The blue data points are the values of $2\pi ix$ measured in the current work, which is in the range of 2π times of $nFDC_{crit}$ and $nFDC_{sat}$. (b) The effect of the radius of the pit on the combination of the anodic current demand and the maximum cathode capacity. The effect of the radius of pit on the anodic current demand I_{LC} is in the range of 0.1 to 5 A/m. The curved points represent the effect of the radius of pit on the maximum cathode capacity, $I_{c,max}$, which is calculated from the model. The RH is 98% and the deposited NaCl density is 100 μg/cm^2. The intersection of the I_{LC} and $I_{c,max}$ curves determines the maximum pit size.

6.4.4 Tafel slope of artificial pits in stainless steel

Figure 6-15 has shown Tafel slopes measured by another method developed in the current work, which is obtained by plotting the current vs. *IR*-corrected potential characteristic by potentiodynamic method in the salt free region, where the interfacial chemistry is probably averaged the concentration in the range of 60% to 140% of saturation. The difference of Tafel slope measured by this method between the Tafel slopes measured by *IR*-corrected transition potential method is not significant. The strength of this method is that Tafel slope can be measured in salt free region and the resistance is measured for *IR*-correction at the same time. However, this method cannot control the current density in a certain range, which can affect the control of interface chemistry. A galvanodynamic method might be used to improve the current density control in future work.

6.4.5 Pitting potential of pits in stainless steel in immersed solutions

From Figure 6-20, it can be seen that there is an approximately linear decrease of pitting potential with log chloride concentration in the range of 0.01-2 M of 304 stainless steel wire with 120 and 4000 grit surface finish. The decrease of pitting potential vs. log chloride concentration with 120 grit surface is about 110 mV/decade, which is close to previous results in literature: Laycock and Newman have measured the decrease of pitting potential from 0.01-1 M on stainless steel 302 wire with 120 grit surface finish is 93 mV/decade [31]. However, the pitting potential measured in the current work decreases more steeply with log chloride concentration when the chloride concentration is higher than 2 M.

It can be seen that the surface finish can affect the pitting potential: the rougher the surface, the lower the pitting potential. It is possible that a coarse surface finish can result in a higher level of deformation of the surface, which may increase the possibility of pit formation. It is also possible that a rougher surface gives deeper "crevices" in the surface that help to stabilise pit growth by providing a diffusion barrier to a metastable pit [143].

Galvele assumed that the decrease of pitting potential with log chloride concentration was due to the change of *IR* drop of the pit, as the chloride concentration in the bulk solution is changed [32], and he suggested an equation of the pitting potential as follows:

$$E_{pit} = A - B\log[Cl^-]$$

where A and B are constant, and B is estimated by $2.3RT/F$, which is 59 mV/decade [32].

Newman [30] has further explained this equation, and Laycock et al. have concluded three assumptions from Newman's work [30] and Galvele's work [32]:

1. The pit solution chemistry at the interface is the same at the pitting potential, even though the bulk solution concentration might vary.

2. The chloride ion is not a reactive ion in the pit solution

3. The bulk solution resistance is negligible compared with the pit solution resistance

Laycock et al. have also analysed the three assumptions and concluded that the third assumption is generally correct unless the bulk solution is relatively dilute. However, the first and second assumptions need further investigation [39].

The second assumption implies that chloride ions are not involved in complexation of metal cations. However, Monir has found spectroscopic evidence for the formation of chromium and iron chloro-complexes close to the dissolving metal in a stainless steel 316 1D artificial pit in 1 M HCl bulk solution [56]. Thus the second assumption is not valid.

In the case of the first assumption, for dilute solutions, it is found that the diffusion-limited current density is independent of bulk chloride concentration, consistent with Equation 2-12. In this equation, ΔC is the difference between the concentration of metal ions at the dissolving interface and the bulk solution. The concentration in the bulk solution is assumed to be zero, and the concentration at the dissolving interface is the saturation concentration, C_{sat}.

Figure 6-8 and Figure 6-11 have shown that for dilute solutions, this value is constant, however, at higher concentrations (above 1 M chloride salt solution), the common-ion effect will cause the saturation concentration to decrease, changing the solution chemistry and therefore invalidating assumption 1. The linear decrease of pitting potential with chloride concentration in the relatively lower chloride concentration solution, which then steeply decreases in the relatively higher concentration solution is also consistent with the simulation of Laycock et al. [39].

In addition, Figure 6-18 and Figure 6-19 have shown that there are no obvious signs of meta-stable pit formation during potential scan in 4 M and 5 M $MgCl_2$ solution, which is consistent with the observed pit morphology: pits have open mouths and probably do not require perforated covers. The pitting potential measured in 4 M and 5 M $MgCl_2$ solution has been found to be in the range of -200 to -350 mV (SCE), which is close to the open circuit potential of stainless steel in chloride solution. This may indicate pitting corrosion can take place at open circuit potential in high chloride concentration solutions, which agrees satisfactorily with Tsutsumi et al.'s observation [1] that pitting can only take place when the chloride concentration exceeds 6 M.

6.4.6 Repassivation potential of pits in stainless steel in immersed solutions

From Figure 6-22, it can be seen that the repassivation potential decreases with the increasing chloride concentration in the bulk solution. This result is consistent with the findings in literature. Yashiro and Tanno [144] assumed the repassivation potential is similar to the pitting potential, which is a linear function of the logarithm of chloride concentration. They have validated the work by measuring the repassivation potential of 304 stainless steel in NaCl solutions ranging from 0.01 to 2 M but at high temperature conditions (150 and 250 °C).

Sridhar and Cragnolino [145] have confirmed that the repassivation potential (E_{rp}) is dependent on chloride concentration, but is less sensitive to chloride concentration than the pitting potential (E_{pit}) by measuring alloy 825 samples at 95 °C. Anderko et al. have developed a simulation model to predict the repassivation potential and found that the E_{rp} has a complex dependence on chloride concentration. From the result of the simulation, E_{rp} decreases with increasing chloride concentration, and decreases more steeply when the chloride concentration is low [146]. The result in Figure 6-22 shows that E_{rp} decreases with the chloride concentration, and decreases steeply in the lower chloride concentration bulk solution, which is consistent with Anderko et al.'s prediction.

As described in Section 2.4.5, another factor of importance in Kelly's model is the maximum cathodic current ($I_{c,max}$). $I_{c,max}$ can be written as a sum of two terms as shown below:

$$\ln I_{c,\max} = \frac{r\pi\kappa(RH,T)\Delta E_{\max}}{I_{c,\max}} \frac{DD[1+m_{salt}(RH,T)MW_{salt}]}{m_{salt}(RH,T)\rho(RH,T)MW_{salt}} + \ln[\frac{\pi e r_a^2 \int_{E_{corr}}^{E_{rp}} (i_c - i_p)dE}{\Delta E_{\max}}]$$

where the second term represents the cathodic kinetics, which are dependent on the overpotential difference between repassivation potential (E_{rp}) and the open circuit potential (E_{corr}).

The values of E_{rp} used in the model are -0.4 V (SCE) for 304 stainless steel, and -0.25 V (SCE) for 316 stainless steel [109, 110, 112, 114], which are based on the simulation of Anderko et al. [146]. However, Anderko et al. indicated that E_{rp} is expected to decrease with increasing chloride concentration, but the chloride concentration assumed by Kelly and co-workers is not clear [109, 110, 112, 114].

From Figure 6-22, it is clear that the value of measured E_{rp} in 8 M chloride solution (which corresponds to ~45% RH) is consistent with the value used in the model. However, the value of E_{rp} measured in the current work is greater than the E_{rp} used in the model when the chloride concentration is lower than 8 M (>45% RH), and the value of measured E_{rp} is slightly lower than the E_{rp} used in the model when the chloride concentration is 10 M (~35% RH).

In the model, if the value of E_{rp} is higher for chloride concentrations lower than 8 M (>45% RH), the second term of maximum cathodic current supply ($\ln(I_{c,max})$) decreases. This means that only smaller pits can grow. However, if the value of E_{rp} is lower (<45% RH), the second term of maximum cathodic current supply ($\ln(I_{c,max})$) increases, so larger pits can

grow. For successful use of the model, it is important that the value of E_{rp} used should be appropriate for the ambient relative humidity.

6.5 Conclusion

- When the chloride concentration of the bulk solution is below 1 M, the diffusion-limited current density is independent of the chloride concentration. The diffusion-limited current density decreases with increasing chloride concentration of the bulk solution. This might be due to the common-ion effect and the decreasing diffusion coefficient with the increasing chloride concentration.
- The percentage of critical pit solution chemistry (C_{crit}/C_{sat}) decreases with increasing chloride concentration, which may indicate that in higher chloride concentration solutions, it might be easier for pits to sustain the critical solution chemistry for propagation.
- Two methods have been used to determine Tafel slopes: plotting the *IR* corrected potential vs. current density in the salt layer-free regime, and plotting the *IR* corrected transition potential vs. current density. The value of the Tafel slope found by the two methods is fairly close.
- The pitting potential decreases with increasing chloride concentration. It decreases linearly with chloride concentration in the relatively lower chloride concentrations, and decreases more steeply in the relatively higher chloride concentration. The repassivation potential also decreases with increasing chloride concentration.
- The electrochemical results of stainless steel 1D artificial pits can supply some hints in the pitting prediction models on the input parameters: For example, the pit stability product and repassivation potential was found to change significantly with increasing chloride concentration, which should be considered when developing an atmospheric pitting corrosion prediction model.

7 Synchrotron X-ray diffraction studies of salt layers in artificial pits containing concentrated chloride solutions

7.1 Introduction

Salt layers may form at the bottom of corrosion pits in stainless steels when the rate of dissolution of the metal leads to production of metal ions at a rate that is greater than they can diffuse away from the metal surface [31, 61, 68, 147]. Under atmospheric conditions, the water activity, and thus solution concentration of the electrolyte layer will equilibrate with the relative humidity. For example, in the case of magnesium chloride solutions, 90% RH corresponds to about 1 M chloride solution (0.5 M $MgCl_2$) and 60% RH corresponds to about 6 M chloride solution (3 M $MgCl_2$) as described in Section 2.4 [1, 16]. The aim of the present work is to explore how the relative humidity (solution concentration) affects the nature of salt layers in stainless steel 304 and 316 artificial pits in 1 M and 6 M chloride concentration solutions by the use of in-situ synchrotron XRD.

7.2 Diffraction patterns from salt layers

Artificial pits were grown in 304 and 316L stainless steel foils in 1 M chloride solution (0.5 M $MgCl_2$). Both pits were grown to a depth of 1.5 to 2 mm under similar conditions (see Section 3.4.3). Diffraction patterns were measured using an X-ray beam 2.5 μm (vertical) by 15 μm (horizontal) in experiments in which a series of measurements were made starting with the beam in the solution, and progressively raising the sample until the beam was incident on the metal. This process was repeated at 5 different locations along the pit surface separated by 100 μm. The five series of diffraction patterns showed similar trends, but were relatively weak, so in order to improve the signal-to-noise ratio, the patterns were summed over the series of measurements where there was diffraction from the salt layer. The intensities were averaged to the strongest peak of $FeCl_2 \cdot 4H_2O$ in the diffraction pattern.

Figure 7-1 shows the normalised diffraction patterns of salt layers at the dissolving surface of stainless steel 304 and 316L in a 1D pit with 1 M chloride bulk solution at 1 V (Ag/AgCl), together with the standard diffraction patterns of $FeCl_2 \cdot 4H_2O$ [148] and $FeCl_2 \cdot 2H_2O$ [149]. It can be seen from Figure 7-1 for stainless steel 304 and 316L in a 1D artificial pit that $FeCl_2 \cdot 4H_2O$ is the main phase in the salt layer. A few peaks of $FeCl_2 \cdot 2H_2O$ are also observed;

these appear to be stronger for 316 L compared with 304. Due to the limited beamtime, each experiment was carried out for one time only.

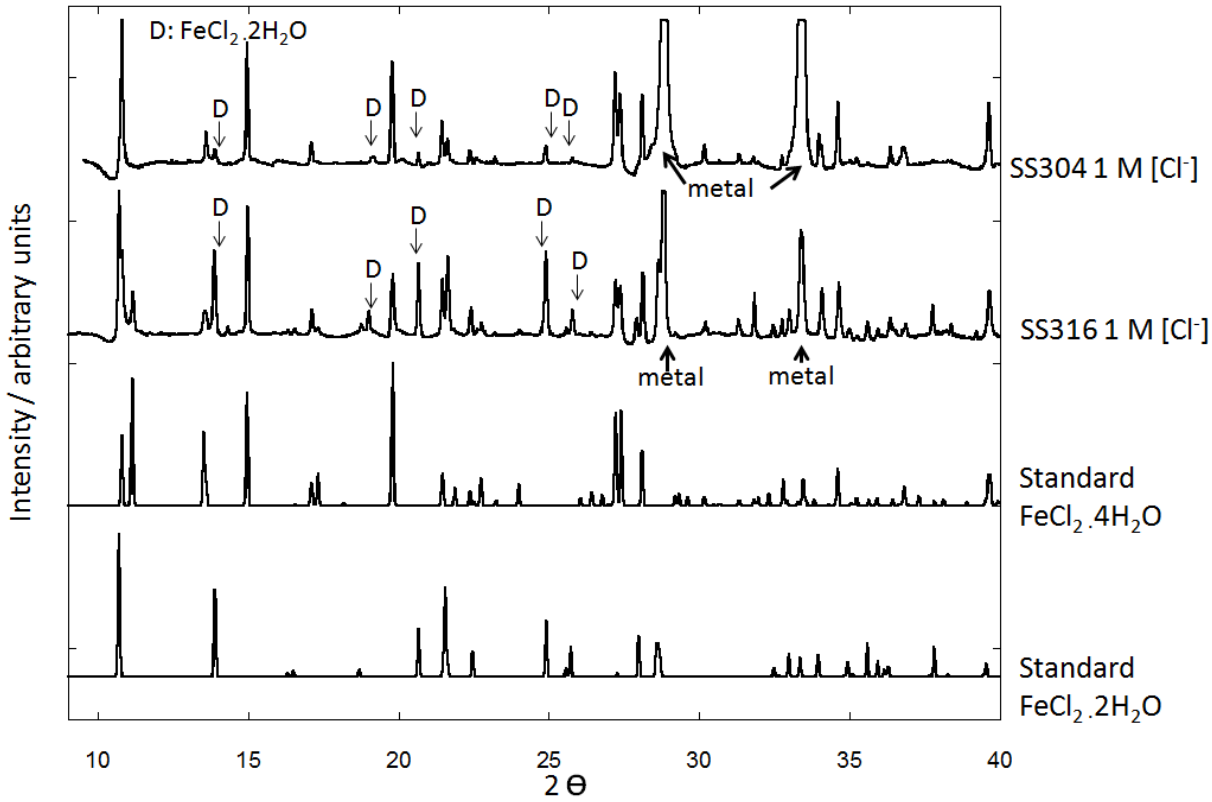

Figure 7-1 X-ray diffraction data from the salt layer on 304 stainless steel 1D pit interface (at 1 V (Ag/AgCl)) in 1 M chloride and 6 M chloride solutions ($MgCl_2$ solutions of 0.5 M and 3 M, respectively) compared with a standard pattern for $FeCl_2 \cdot 4H_2O$. Measurements were made at Diamond Light Source I18 beamline at 12 keV. The data were obtained by summing the diffraction patterns through the salt layer and normalised to the strongest peak of the $FeCl_2 \cdot 4H_2O$ phase in the summed patterns.

7.3 Effect of applied potential on salt layer

The applied potential has a strong effect upon the formation of the $FeCl_2 \cdot 2H_2O$ salt layer. Figure 7-2 shows that the dihydrate phase is found on 1D pit of stainless steel 304 in 1 M chloride solution only when the applied potential is higher than 0.8 V (Ag/AgCl), and is not found when the applied potentials are 0.6 V and 0.4 V (Ag/AgCl). Owing to time constraints, it was not possible to make similar measurements on 316L.

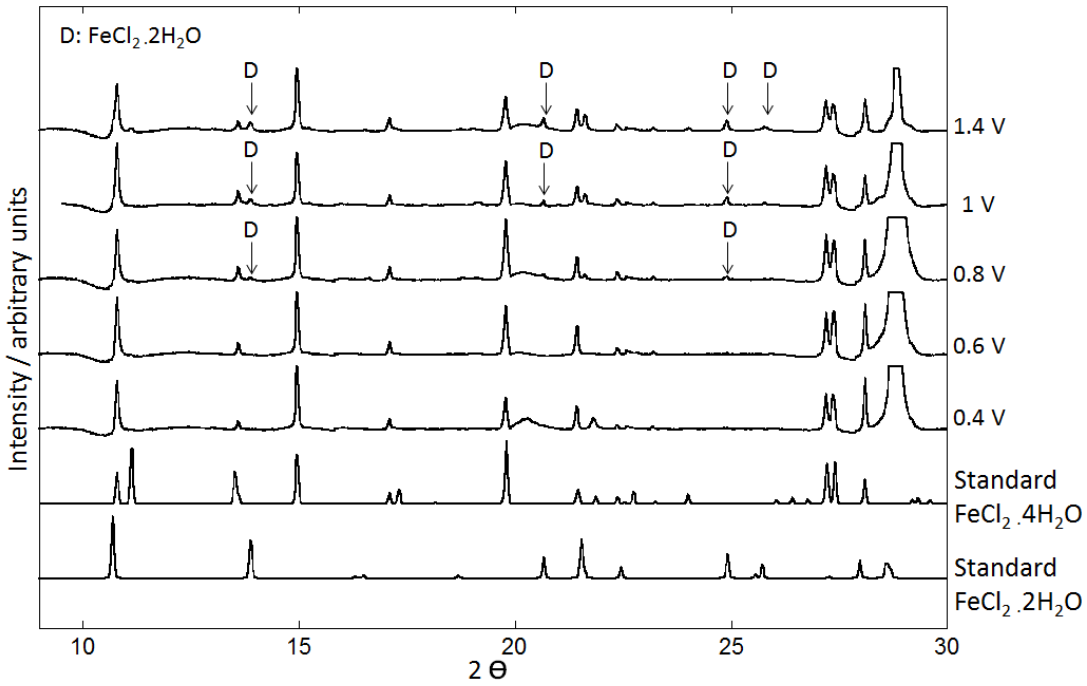

Figure 7-2 Diffraction patterns on stainless steel 304 1D artificial pit at various applied potentials (0.4 V to 1.4 V vs. Ag/AgCl) in 1 M Cl^- solution ($MgCl_2$ solutions of 0.5 M). Measurements were made at Diamond Light Source I18 beamline at 12 keV. The data were obtained by summing the diffraction patterns through the salt layer and normalised to the strongest peak in the $FeCl_2 \cdot 4H_2O$ phase.

7.4 Phase distribution in the salt layer

The salt layer thickness of stainless steel 304 1D artificial pit was determined by counting the number of frames of diffraction patterns in which a different pattern for a crystalline salt was visible. As described in Section 3.7, the sample stage was first placed where the incident X-ray entered the pit solution and was raised in 2 µm increments through the salt layer. For example, in 1 M chloride solution, there were 10±1 diffraction frames in which salt patterns were observed across 5 different horizontal positions of the salt layer, thus the thickness of the salt layer is assumed to be about 20±2 µm. However, there is uncertainty in estimating the salt layer thickness since it involves judgments of where the salt layer begins and ends.

Since the beam size is 2.5 µm (v) x 15 µm (h) and is much smaller than the thickness of the salt layer, it is feasible to characterise the composition of the salt layer as a function of distance from the dissolving metal surface. Figure 7-3 shows the diffraction patterns from a

stainless steel 304 1D artificial pit at various positions relative to the dissolving metal interface at 1 V (Ag/AgCl). It can be seen that the dihydrate phase is found closer to the metal/salt interface, whilst peaks of the main phase $FeCl_2.4H_2O$ are not obviously affected by the position of the X-ray beam relative to the dissolving metal interface.

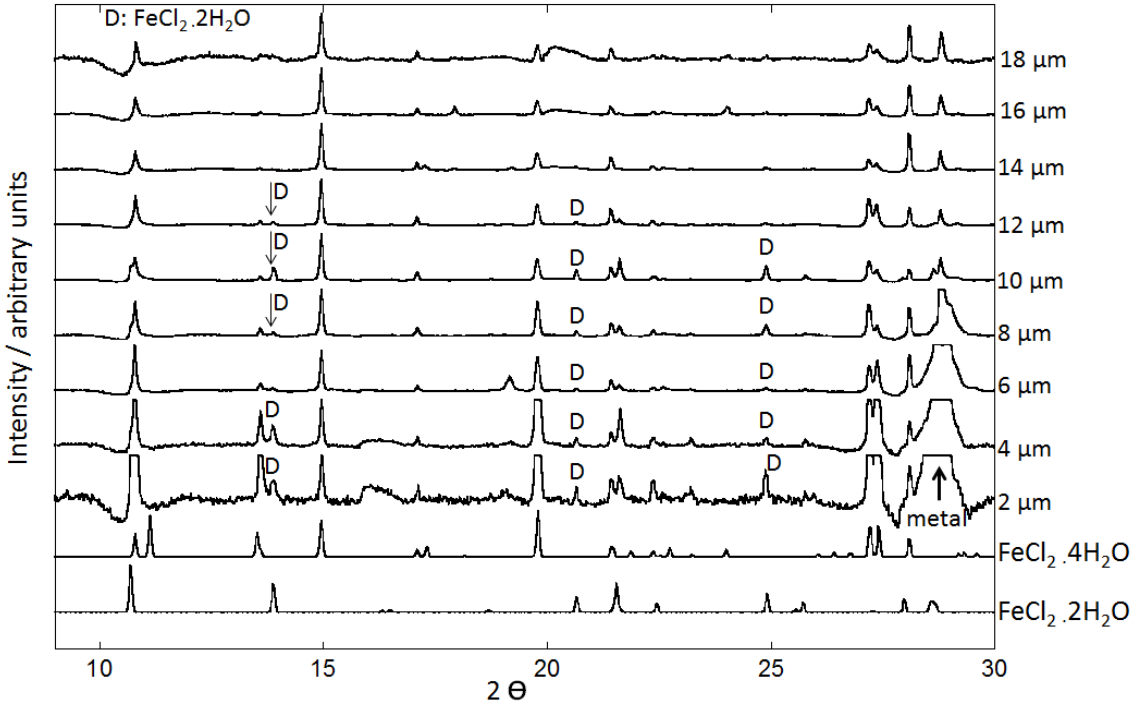

Figure 7-3 Diffraction patterns on stainless steel 304 1D artificial (1 M Cl^-) pit at various positions relative to the dissolving metal interface at 1 V (vs. Ag/AgCl). Measurements were made at Diamond Light Source I18 beamline at 12 keV. The data were obtained by summing the diffraction patterns through the salt layer and normalised to the strongest peak in the $FeCl_2 \cdot 4H_2O$ phase.

7.5 Effect of bulk solution chloride concentration on the salt layer

Figure 7-4 shows single frames from the diffraction data obtained from salt layers in stainless steel 304 and 316L 1D artificial pits in 1 M and 6 M chloride bulk solutions. It can be seen that the diffraction pattern from the 1 M chloride bulk solution is more continuous and less 'spotty' than that obtained from a 6 M bulk chloride solution. This indicates that the crystallites present in 1 M chloride solution are smaller and more numerous than those in the 6 M solution.

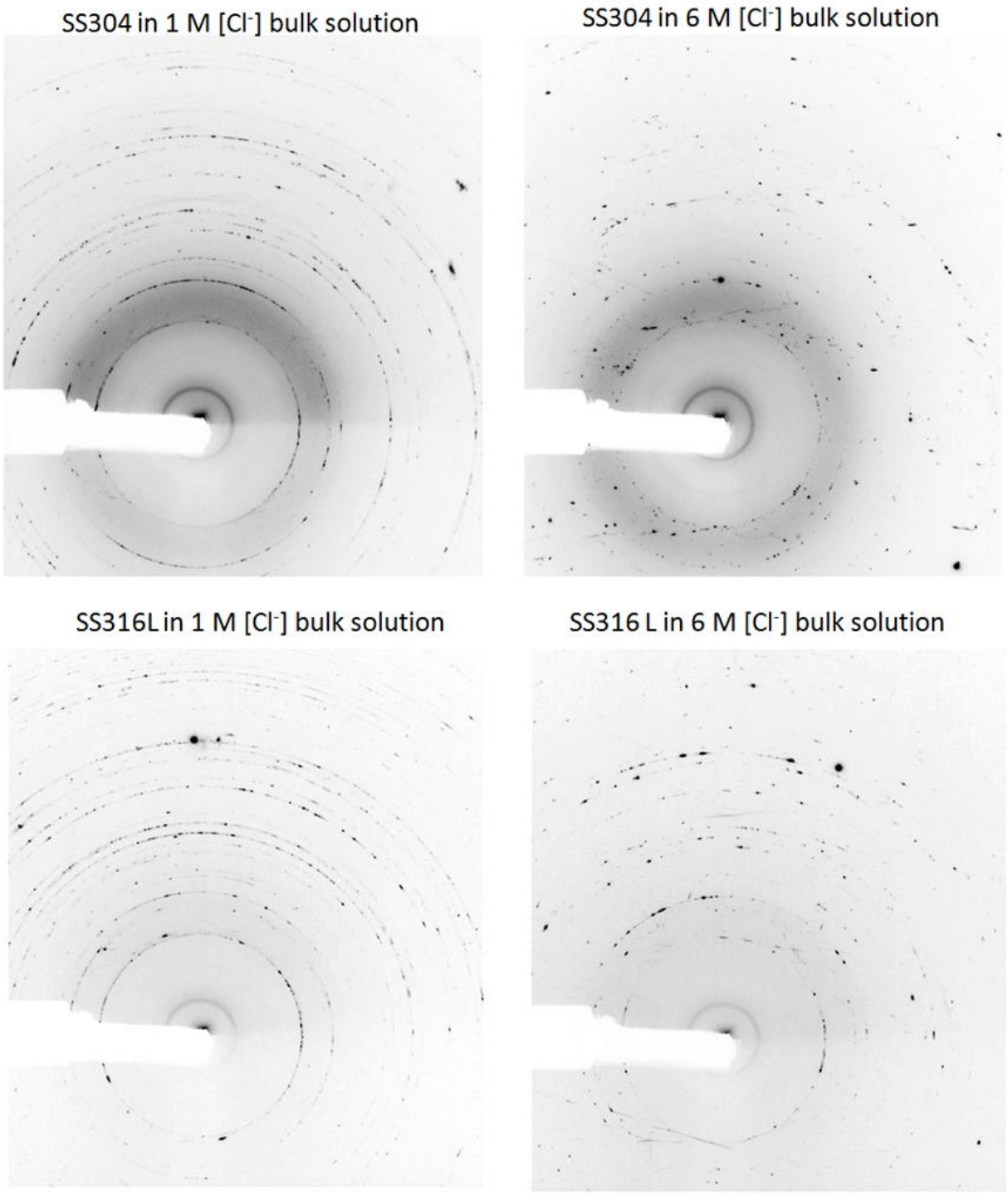

Figure 7-4 Diffraction patterns of salt layers in stainless steel 304 and 316L 1D artificial pits dissolving in 1 M chloride solution (left) and 6 M chloride solution (right) at 1 V (Ag/AgCl) for crystallite morphology. The diffraction pattern of 1 M chloride solution is a single frame pattern 12 µm above the metal/salt interface, and the diffraction pattern of 6 M chloride solution is a single frame pattern 20 µm above the metal/salt interface. The single frame pattern was selected in the middle of the salt layer.

The chloride concentration can also affect the formation of $FeCl_2 \cdot 2H_2O$. Figure 7-5 shows the salt layer diffraction patterns of stainless steel 304 and stainless steel 316L 1D artificial pits in 1 M and 6 M chloride bulk solution. There are more ferrous chloride dihydrate phase peaks in 1 M chloride bulk solution than 6 M chloride solution for both 304 and 316L. Since the diffraction patterns are normalised to the strongest peak of the $FeCl_2 \cdot 4H_2O$ phase, the ratio of $FeCl_2 \cdot 2H_2O$/ $FeCl_2 \cdot 4H_2O$ is higher in 1 M chloride solution than 6 M chloride solution. This possibly indicates that more dehydrated phase salt is formed in 1 M chloride bulk solution than 6 M. This is surprising, since the water activity is lower in the bulk solution of 6 M chloride than in 1 M chloride, hence from a thermodynamic viewpoint it is easier to form $FeCl_2 \cdot 2H_2O$ in a higher chloride concentration solution.

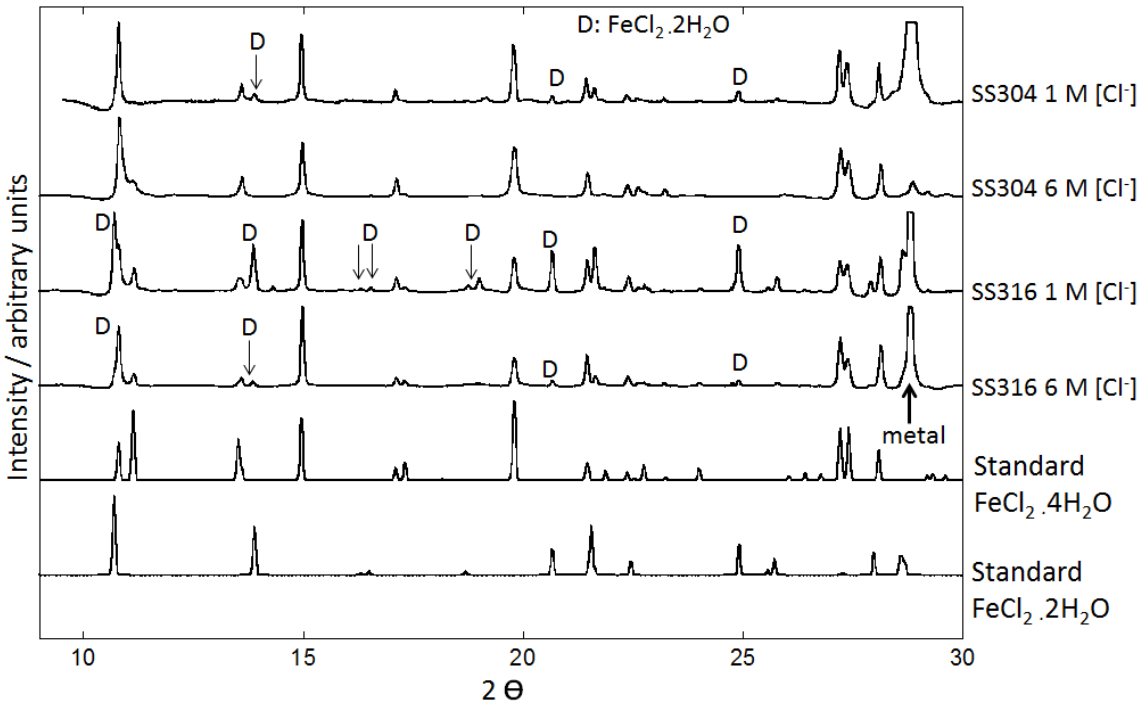

Figure 7-5 Diffraction patterns on 1D pit of stainless steel 304 and 316L at 1 M and 6 M chloride bulk salt solution at 1 V (Ag/AgCl). Measurements were made at Diamond Light Source I18 beamline at 12 keV. The data were obtained by summing the diffraction patterns through the salt layer and normalised to the strongest peak in the $FeCl_2 \cdot 4H_2O$ phase.

Table 7-1 shows the salt layer thickness of stainless steel 304 and 316 L artificial pits in 1 M and 6 M chloride solutions. The salt layer thickness was obtained by counting the number of frames with salt patterns as described in Section 7.4. It can be seen that the salt layer thickness in 6 M solution is much higher than the thickness in 1 M solution.

Table 7-1 Salt layer thickness of stainless steel 304 and 316L artificial pits in 1 M and 6 M chloride solutions. The error is due to five different horizontal positions across the salt layer.

Materials	Solution	Salt layer thickness (μm)
SS304	1 M Cl^-	20±2
SS304	6 M Cl^-	52±8
SS316L	1 M Cl^-	18±2
SS316L	6 M Cl^-	44±4

Figure 7-6 shows the measured diffusion-limited current density of stainless steel 304 and 316L 1D pit in 1 M and 6 M chloride solution during the XRD characterisation. It can be seen that the diffusion-limited current density in 6 M chloride solution is much lower than in 1 M chloride solution.

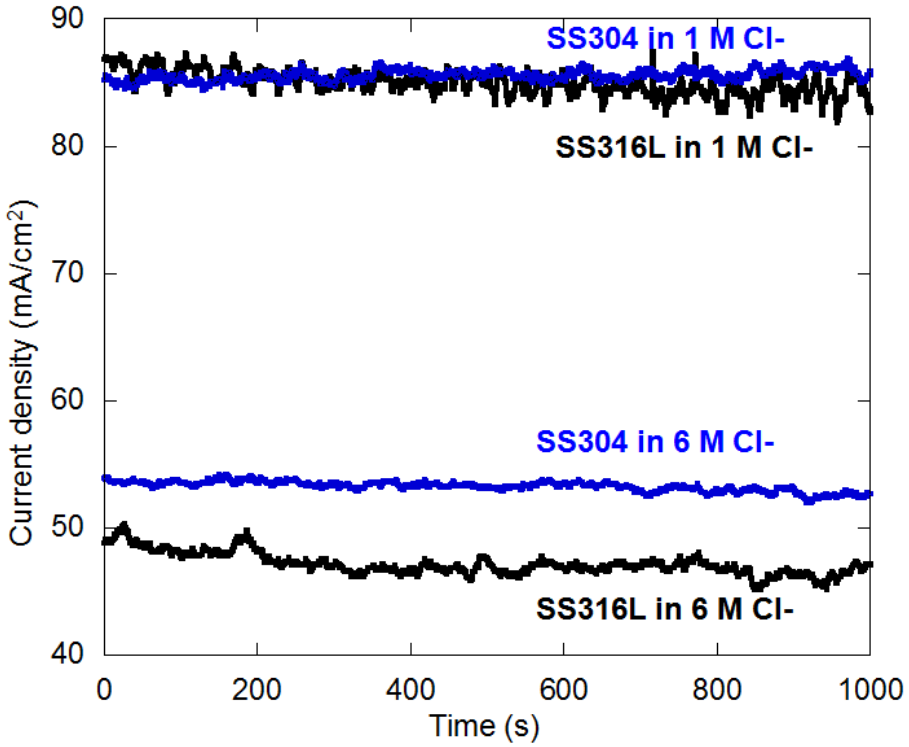

Figure 7-6 The diffusion-limited current density of stainless steel 304 and 316L 1D artificial pit vs. time (arbitrary time) measured during the synchrotron X-ray diffraction characterisation experiment. The current density is measured on the same 1D pit by switching the solution. The pit is grown in 1 M and 6 M chloride solutions at 21±1 °C. The pit depth was 1.5-2 mm.

7.6 Discussion

7.6.1 Salt layer composition

A salt layer is only found in stainless steel artificial pits during metal dissolution, which is a dynamic process. Figure 7-1 shows that the $FeCl_2 \cdot 4H_2O$ and $FeCl_2 \cdot 2H_2O$ salt crystallites are found in stainless steel 304 and 316L 1D artificial pits in 1 M chloride solution, and the tetrahydrate phase is the main phase in the salt layer. Isaacs et al. [52] found iron enrichment in the region of the salt film, Rayment et al. [73] reported the salt film consists of $FeCl_2 \cdot 4H_2O$ on stainless steel 316 1D artificial pits. These results are consistent with previous findings.

7.6.2 Effect of applied potential on the formation of ferrous chloride dihydrate in the salt layer

Figure 7-2 shows that $FeCl_2 \cdot 2H_2O$ is found when the applied potential is 0.8 V (Ag/AgCl) and above, but is not found when the applied potential is 0.6 and 0.4 V (Ag/AgCl). This might be due to the thickness of the salt layer, which is dependent on the applied potential. Novakovski and Sorokina [74], Tester and Isaacs [61] have found that 1D salt-covered pits propagate by diffusion control, and when the applied potential changes (higher than the transition potential forming the salt layer), the salt layer can self-regulate its thickness to adjust the ohmic drop within the pit to maintain the pit dissolution rate at the same value as the diffusion-controlled rate [31, 61, 74, 150]. Thus a higher applied potential will result in a thicker salt layer on the 1D artificial pit.

It is possible that water molecules are more easily transported through a thinner salt layer to form thermodynamically stable $FeCl_2 \cdot 4H_2O$. However, when the applied potential is high, a thicker salt layer forms and the diffusion path for water molecules is longer so that the rate of transport to the inner part of the salt layer will be lower. In the inner part, $FeCl_2 \cdot 2H_2O$ might form because the environment has a low water activity.

7.6.3 Internal structure and thickness of the salt layer

Figure 7-3 shows that the salt layer thickness is about 20 μm thick on stainless steel 304 1D artificial pit in 1 M chloride solution, which is contradictory to other findings in the literature that the salt layer is nanometres thick [65-67]. However, the comparison may not be valid, since the salt layer thickness reported by Beck and Alkire was obtained by consideration of small pits.

It also can be seen from Figure 7-3 that the $FeCl_2 \cdot 2H_2O$ phase is only observed in the salt layer closer to the metal dissolving interface, which indicates the salt layer has a bi-layer structure. The possible explanation is similar to that discussed in Section 7.6.2. It is possible that when the relative position of the salt layer is close to the dissolving metal surface, the diffusion length of the water molecules is relatively longer that the environment might be lack of water for $FeCl_2 \cdot 2H_2O$ formation.

Vetter and Strehblow have studied the salt layer and assumed it is not porous [65]. Beck has found that the salt layer is a high-field conduction layer but has also indicated the salt layer is possibly covered with an outer hydrated layer that water molecules can pass through [67, 151]. Clerc and Landolt have studied the salt layer with AC impedance method and found that the salt layer has a duplex layer where the outer layer is porous and the inner layer is compact [70]. The result of inner salt layer consists of $FeCl_2 \cdot 2H_2O$ and $FeCl_2 \cdot 4H_2O$ phase, and outer layer consists only $FeCl_2 \cdot 4H_2O$ layer is consistent with previous findings.

7.6.4 Effect of chloride concentration on the diffusion-limited current density

It is surprising to find that the dehydrated phase salt is formed more readily in 1 M chloride bulk solution than in 6 M chloride solution, as shown in Figure 7-5. It may be due to the different diffusion-limited current density in the pit, or to different porosity of the salt layer in the two chloride solutions.

Some lab-based experiments have been carried out by using wire artificial pit electrode, and the result is shown in Figure 7-7. Figure 7-7 shows the current-voltage characteristic of the 1D artificial pits in 1 M and 6 M chloride solution. As described in Section 6.2.4, the plateau of current density, independent of potential, means that the system is under diffusion control. The lab based measurements confirm that the diffusion-limited current density of 1D pit in 1 M chloride solution is much higher than it is in 6 M chloride solution. As discussed in Section 6.4.1, common-ion effect reduces the solubility of dissolving metal ions in higher chloride concentration solution.

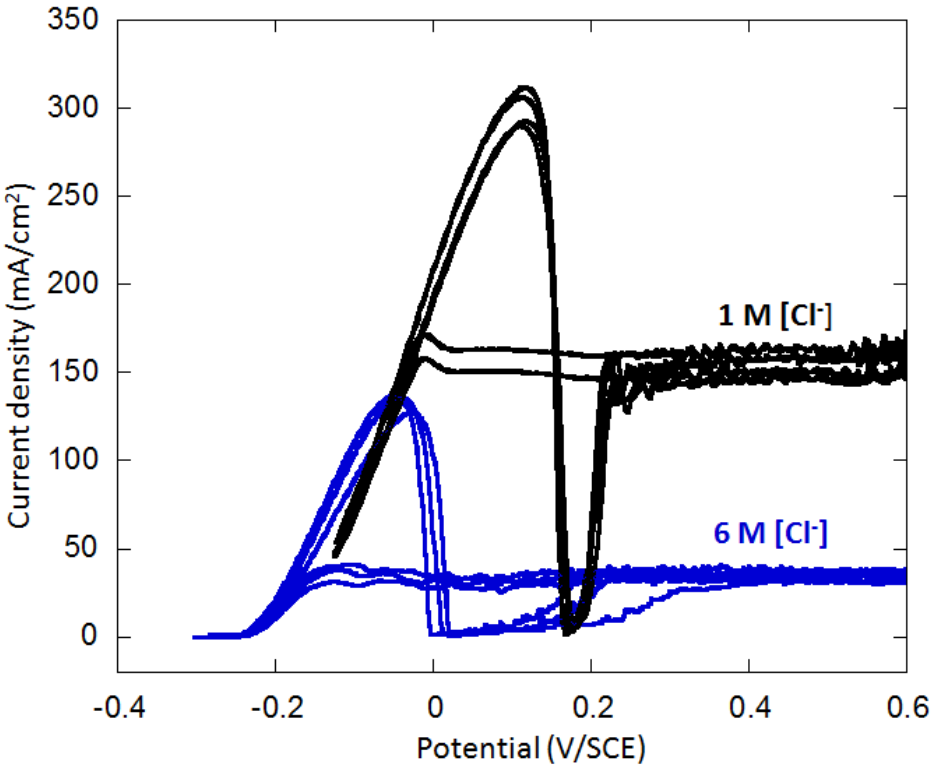

Figure 7-7 Current-voltage characteristics of stainless steel 304 1D pit dissolving in 1 M and 6 M chloride solution on 250 µm diameter pencil electrodes at ~500 µm deep pit at 20±2 °C.

Since the production rate of metal ions within the pit depends on the diffusion-limited current density; a higher diffusion-limited current density means that more metal ions are produced. Each metal ion needs several water molecules to form metal chloride water complexes to be dissolved. Monir has found that the formation of Fe chloro-complexes close to the interface of a 1D artificial pit and the formation of $Fe(H_2O)_6^{2+}$ near the pit mouth by using the synchrotron in-situ spectroscopy method [56]. He has also detected the formation of $Cr(H_2O)_6^{3+}$ and $Ni(H_2O)_6^{2+}$. This indicates that water molecules are consumed in the pit cavity to solvate metal ions during the metal dissolution process. A higher diffusion-limited current density leads to a higher metal ion production rate, which can result in the consumption of more water molecules. The metal dissolving interface in 1 M chloride solution may be more depleted of water to the higher interface current density, which increases the possibility to form $FeCl_2 \cdot 2H_2O$ compared with 6 M chloride solution.

7.6.5 Effect of chloride concentration on the porosity of the salt layer

As discussed above, Clerc and Landolt have suggested that the outer part of the salt layer is porous [70], and Beck has proposed that water molecules can transport through the outer part

of the salt layer. The relatively porosity of the salt layer in 1 M and in 6 M chloride solution may be estimated if two assumptions are made:

1. $FeCl_2 \cdot 4H_2O$ and $FeCl_2 \cdot 2H_2O$ salt crystallites are not conductive and the porosity in the salt layer provides paths for ion condution.

2. The pores of salt layer are uniformly distributed across the salt layer.

Figure 7-8 shows a schematic diagram of the 1D artificial pit with salt layer after making these two assumptions so that a simplified calculation can be carried out.

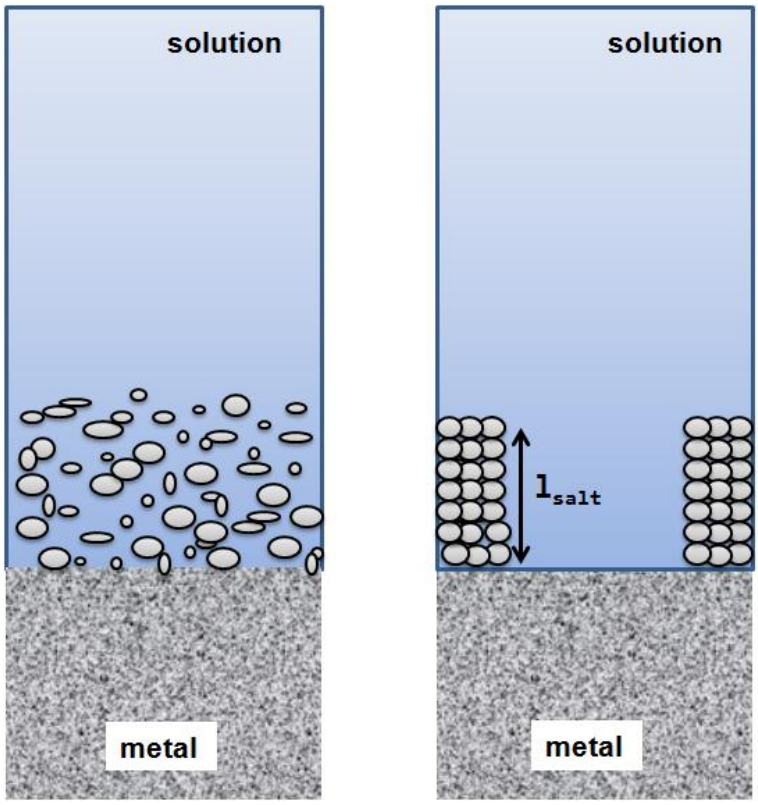

Figure 7-8 A schematic diagram of the assumption to calculate the resistance of pit solution: naturally formed salt layer (left) and the simplified assumption of salt layer formation (right) on stainless steel 1D artificial pit.

From Figure 7-8, when the pit is covered with a salt layer, the total cell resistance (R_{total}) can be divided into two parts, the pit solution resistance in the salt free state (above the salt layer) region $R_{saltfree}$ and the resistance across the salt layer R_{salt} (Equation 7-1):

$$R_{total} = R_{saltfree} + R_{salt} \qquad \text{Equation 7-1}$$

R_{salt} is proportional to the resistivity of the electrolyte within the salt layer ρ, the salt layer thickness l_{salt}, and inversely proportional to A, the cross sectional area of solution in salt layer (Equation 7-2).

$$R_{salt} = \rho \frac{l_{salt}}{A} \qquad \text{Equation 7-2}$$

The cross sectional area of the solution in the salt layer A is the product of the electrode cross-section area $A_{electrode}$, and the porosity of the salt layer η (Equation 7-3).

$$A = \eta A_{electrode} \qquad \text{Equation 7-3}$$

Thus the porosity of the salt layer (η) can be expressed as Equation 7-4.

$$\eta = \frac{A}{A_{electrode}} = \frac{\rho l_{salt}}{R_{salt} A_{electrode}} \qquad \text{Equation 7-4}$$

Since the solution in the salt layer is saturated, resistivity ρ is approximately the same in 1 M and 6 M solutions. The electrode cross-section area $A_{electrode}$ is also the same. The relative porosity in the two solutions is the ratio of the porosity of the salt layer in 6 M solution (η_{6M}) to the porosity of salt layer in 1 M solution (η_{1M}), which then can be expressed as Equation 7-5, where R_{1M} and R_{6M} are the pit solution resistances in 1 M and 6 M chloride solution respectively.

$$\textit{Relative porosity} = \frac{\eta_{6M}}{\eta_{1M}} = \frac{l_{6M} R_{1M}}{l_{1M} R_{6M}} \qquad \text{Equation 7-5}$$

The parameters in Equation 7-5 such as the pit solution resistance in the salt layer region (R_{salt}) and the salt layer thickness can be either directly measured or calculated. The salt layer thickness is counted from the diffraction patterns through solution to metal. The pit solution resistance is measured in-situ during the XRD experiment by the impedance method at a steady high frequency of 50 kHz.

The relative porosity of the salt layer in 6 M chloride solution to 1 M can be then calculated by Equation 7-5 and the data are shown in Table 7-2. The relative porosity of salt layer in 6 M to 1 M chloride solution is approximately 1.5~1.7, which means the salt layer in 6 M chloride

solution might be slightly more porous. Thus it might indicate there are more paths for water molecules to diffuse to the metal dissolving interface in the 6 M chloride bulk solution, forming thermodynamically stable salt $FeCl_2 \cdot 4H_2O$ rather than $FeCl_2 \cdot 2H_2O$.

Table 7-2 Relative porosity of salt layer calculation on 1D pit on stainless steel 304 and 316L.The pit solution resistivity is measured in lab based experiment on stainless steel 304 1D artificial pits.

Materials	Chloride concentration (M)	Cell resistance (kΩ)	Pit solution resistance 'salt-free' (kΩ)	Salt thickness (μm)	Relative porosity η_{6M} / η_{1M}
304	1 M	7.3±0.2	0.8±0.1	20±2	1.5
	6 M	12±3	0.9±0.1	52±8	
316L	1 M	7.1±0.2	0.8±0.1	18±2	1.7
	6 M	10.0±0.5	0.9±0.1	44±4	

7.6.6 Why is more ferrous chloride dihydrate formed in a more dilute solution?

As discussed in Section 7.6.4, the diffusion-limited current density of a 1D stainless steel pit in 6 M chloride solution is much lower than the current density in 1 M chloride solution, which produces metal ions at lower rate at the interface, and thus requires slower transport of water molecules to form metal water complexes, which might be another reason to produce less $FeCl_2 \cdot 2H_2O$.

As discussed in Section 7.6.5, XRD shows that the salt crystallites formed in 1 M chloride solution are relatively fine compared with the crystallites formed in 6 M chloride solution. The relative porosity shown in Table 7-2 indicates that it is probably that the salt layer formed

in 6 M chloride solution is more porous. Water molecules can have more access to diffuse more rapidly to the interface in the 6 M solution forming $FeCl_2 \cdot 4H_2O$ salt rather than $FeCl_2 \cdot 2H_2O$. Thus the lack of formation of $FeCl_2 \cdot 2H_2O$ seems to result from a combination of layer pores and the lower demand for water transport to the interface.

Figure 7-9 shows a schematic diagram of salt layer formation on stainless steel 1D pits in 1 M and 6 M chloride bulk solution based on the discussion in Sections 7.6.4 and 7.6.5.

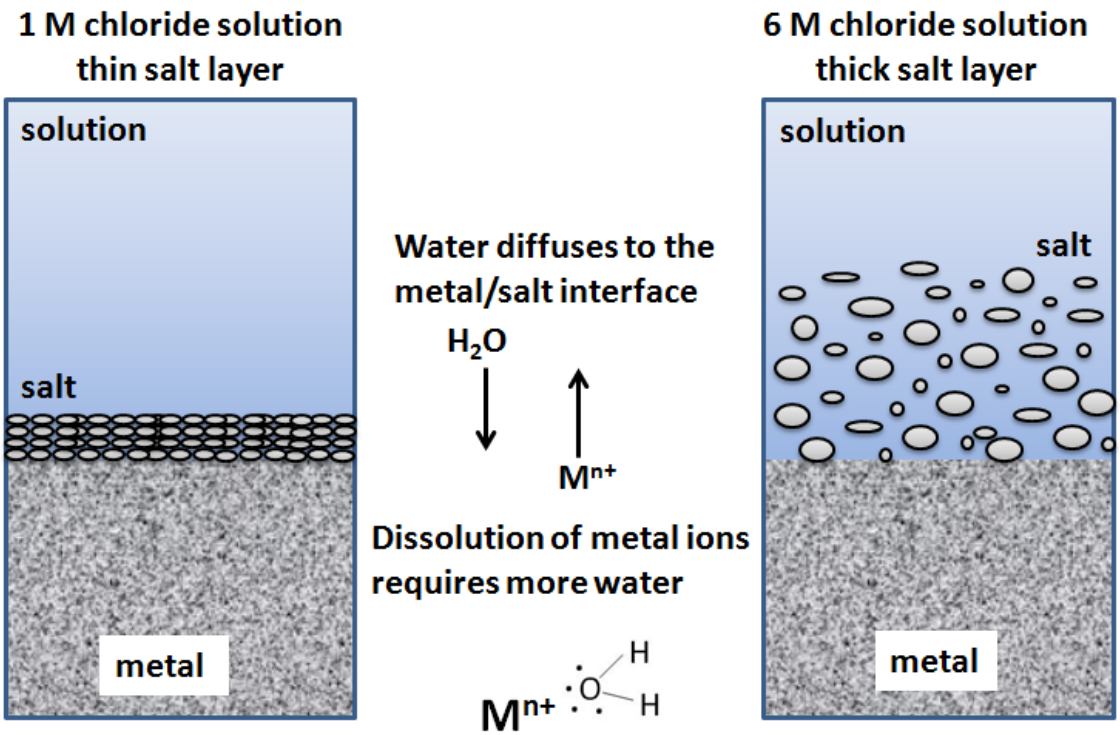

Figure 7-9 A schematic diagram of the assumption of the salt layer formation in 1 M and 6 M chloride bulk solution.

7.7 Conclusions

A salt layer forms at the bottom of a 1D artificial pit of stainless steel in 1 M and 6 M chloride salt solution, and the dominant phase is $FeCl_2.4H_2O$. There is no significant difference of salt layer formation between 316 artificial pits and 304 artificial pits.

With a bulk chloride concentration of 1 M, the salt crystals formed at the 1D pit bottom are smaller than those formed at higher bulk chloride concentration (6 M).

For potentials of $\geqslant$0.8 V (vs. Ag/AgCl) in 1 M chloride bulk solution, a dehydrated phase of iron chloride $FeCl_2 \cdot 2H_2O$ is formed adjacent to the electrode surface.

Surprisingly, at 1 V (Ag/AgCl), the amount of the dehydrated phase is greater in 1 M chloride solution than in 6 M. This may be attributed to two reasons:

- a more porous salt layer is formed in 6 M bulk solution, leading to easier access of water to the dissolving metal surface
- a lower diffusion-limited current density in 6 M chloride bulk solution leading to a lower "demand" for water to solvate the metal ions formed in the dissolution reaction.

These two factors probably lead to a higher water activity adjacent to the dissolving metal surface for a bulk solution of 6 M, favouring formation of the thermodynamically stable salt $FeCl_2 \cdot 4H_2O$.

8 General discussion and Future work

8.1 General discussion

8.1.1 Pit growth under atmospheric conditions

8.1.1.1 Pit morphology

Deposition of electrolytes by inkjet printing has been used to characterise pits grown under realistic atmospheric conditions. Most of the observed pits are shallow and have an open pit mouth. In-situ pit growth in real time has been characterised by synchrotron X-ray micro-tomography. Three pit morphologies were observed, of which the open mouth, dish shaped shallow pit was the most common pit, which agrees with the results of inkjet printing measurements and the work of Maier and Frankel [18].

Pit morphology on abraded wire electrodes has been characterised in high chloride concentration solutions under immersion conditions such as 4 M $MgCl_2$ solution, which corresponds to about 45% RH. Open mouth, shallow pit was observed, which agrees with the micro-tomography work and inkjet printing work.

It should be noted that the pit morphologies of the real atmospheric pits and pits formed under immersion conditions are very different from the morphology of 1D artificial pits. The pit depth of the real pits is less than 50 μm after exposure for a few days, but the pit depth of the artificial pits in the current work can reach more than 1 mm. A deep artificial pit is used to examine the electrochemical behaviour of pits under 1D diffusion conditions in which the diffusion barrier at the entrance to the pit can be neglected. However, the difference in pit morphology may affect the pit growth kinetics as discussed in the section below.

8.1.1.2 Pit growth kinetics

'As described in Section 6.2.4, the steady state growth of an artificial pit with a salt film at the dissolving interface is under diffusion control. The growth in depth of 2D pits has also been shown to be under diffusion control by Ghahari [135]. However, there is no obvious indication in the present work that the growth of real pits in depth is under diffusion control.

This is possibly due to the difference in depth between the artificial pits and real pits. Equation 5-6 shows that under diffusion-controlled conditions, there is a linear relationship

between (pit depth)^2 and the concentration difference between the bottom of the pit and the pit mouth (C_b-C_m).

In 1D pit experiments, pits were grown to a depth where the diffusion length can be regarded as equal to the pit depth and the diffusion barrier at the pit mouth can be neglected and C_m can be assumed to be zero. In 2D pit experiments, pits were grown under immersed conditions [135].In the 1D and 2D pit experiments, C_m can be assumed to be zero. However, under atmospheric conditions, the pit is shallow, but the volume of the electrolyte layer is limited, and the metal concentration of the electrolyte can be quite high especially when corrosion products dissolve. The metal ion concentration at the pit mouth (C_m) might not be a constant during pit growth.

It should also be noted that the atmospheric pit volume increases with increasing chloride deposition density as shown in Chapter 4 and Chapter 5, which may be due to the lower ohmic drop within a thicker electrolyte layer. It is also possible that the growth of real pits is under ohmic drop control, however, further evidence is required to confirm this.

8.1.1.3 Pit stability product

The pit stability product *ix* of 1D artificial pits on stainless steel was found to decrease with increasing chloride concentration. For example, *ix* has been found to be about 0.50-0.79 Am^{-1} in 1 M chloride solution, which agrees with Pistorius and Burstein's finding [35], but can decrease to 0.07-0.17 Am^{-1} in 6 M chloride solution. This indicates the possibility of pit propagation with a significantly lower stability product in high chloride concentration solutions. It probably also explains that stable pits have been observed at relative humidity corresponding to $\geqslant$6 M [1, 80]: at lower RH, a much lower pit stability product is required for pit propagation.

The pit stability product of a real atmospheric pits has been estimated by using the average current density measured by micro-tomography and using an estimated pit depth of 30 μm. The pit stability product of real pit was estimated to be as low as 6 x 10^{-5} Am^{-1}. However, it is not clear that the real atmospheric pit growth in depth is under diffusion control so this estimation of *ix* might not be valid.

8.1.1.4 Pitting potential and repassivation potential

The pitting potential and repassivation potential have been measured on abraded wire electrodes under immersion conditions. Both the pitting potential and the repassivation potential decrease with increasing chloride concentration, which is consistent with Laycock et al.'s assumption [39] and Anderko et al.'s assumption [146]. There are no obvious signs of meta-stable pits formation during potential scans in 4 M and 5 M $MgCl_2$ solution, which is consistent with the morphology of real pits: pits have open mouths and do not have perforated covers. The pitting potential measured in 4 M and 5 M $MgCl_2$ solution has found to be in the range of -200 to -350 mV (SCE), which is close to the open circuit potential of stainless steel in chloride solution. This may indicate that pitting corrosion can take place at open circuit potential in high chloride concentration solutions, which agrees satisfactorily with to Tsutsumi et al.'s work, who found that real pits can only form when the chloride concentration exceeds 6 M [1].

8.1.1.5 Salt layers

Salt layer formation in 1 M and 6 M chloride solutions has been observed by synchrotron XRD on stainless steel 1D artificial pits. This approach is based on the work of Rayment et al. [73]. However, the salt film is characterised in high chloride concentration solution as it is close to real atmospheric conditions. The observation of salt film formation in concentrated chloride solution might indicate the possibility of salt film formation in real pits under atmospheric conditions. Furthermore, $FeCl_2 \cdot 2H_2O$ phase salt has been observed in the present work, which might indicate the corrosion environment can lack water, and the thermodynamics of the dissolving interface might not be stable.

8.1.2 Effect of chloride deposition density on pit growth

Synchrotron X-ray micro-tomography measurements have shown that pit volume increases with increased chloride deposition density, which agrees with the findings of inkjet printing measurements. Increasing pit volume with increasing chloride deposition density might be associated with a lower ohmic drop between the electrolyte layer and the pit. Under a fixed relative humidity, a thicker droplet/electrolyte layer can form in a fixed area if the chloride deposition density is high, which leads to a lower resistance to the pit thus a higher current density for pit growth. The pit growth associated with the ohmic drop is consistent with Chen and Kelly's assumption [110].

8.1.3 Synchrotron X-ray beam damage

Nagy and You [137] have reported that an intense radioactive beam might affect electrochemical processes. In the current work, synchrotron X-ray micro-tomography has been used to observe the in-situ pit growth in stainless steel under atmospheric conditions, however, the time to collect each tomogram is about 40-50 minutes, which may lead to beam damage. The comparison of the synchrotron X-ray micro-tomography measurements with the lab based measurements have shown that the beam damage may lead to increasing numbers of pits.

Synchrotron XRD has been used to characterise the salt layer on stainless steel 1D artificial pits. As discussed above, synchrotron X-ray radiation may lead to beam damage of the sample, which may increase the local temperature that affects corrosion. The energy of the beam and the beam intensity were selected to aquire data of adequate quality while minimising beam damage. Attenuation was always used to reduce the intensity of the beam to mitigate against beam damage.

8.1.4 Recommendation for end users

One of the objectives of this work is to provide a scientific basis for making recommendations for safe conditions for above-ground storage of intermediate level nuclear waste.

The X-ray micro-tomography results are consistent with a lower chloride deposition density limit of 10 to 20 μg/cm^2 for pitting to take place, which is similar to the limit for atmospherically-induced stress corrosion cracking (AISCC) formation between 10 and 25 μg/cm^2 found in the work of Albores-Silva [152]. This supports the suggestion that chloride deposition levels should be limited with the use of filters for safe storage conditions.

A limited range of RH controls has been applied in the atmospheric corrosion experiments, thus the results presented do not provide a sufficiently robust basis for recommendations on the RH for safe storage. However, the electrochemical results in more dilute solutions have shown that repassivation becomes easier as the solution is more dilute, which is equivalent to higher RH. Thus fluctuations in RH to higher values may completely passivate pits, or could passivate the pit mouth but allow the pit bottom to continue to grow, giving deeper and more damaging pits. Thus the effect of cycling RH needs further study.

8.2 Future work

8.2.1 Establishing the mechanism of real pit growth in depth

It has been reported that pit growth in depth is under diffusion control in 1D artificial pits [36, 61], and a recent work carried out by Ghahari [136] reported that under immersion conditions a 2D pit growth in depth is under diffusion control.

In the current work, the increase in depth of corrosion pits with time has been measured with X-ray micro-tomography. For the three pits measured here, the growth rate was not consistent with diffusion-controlled growth assuming a constant solution concentration at the pit mouth. Although further work is needed to confirm this, it is likely that the confined electrolyte in the droplet also provides an additional diffusion barrier, which is not taken into account here.

Measurements could be planned on the same materials with more time interval measurements to validate if real pit growth in depth is under diffusion control by synchrotron X-ray micro-tomography. As well as planning synchrotron radiography measurements on 2D pit under a limited electrolyte layer to check if the kinetics of pit growth in depth has been affected by a limited volume of solution.

8.2.2 Extending to sea salt deposition and solution conditions

In the current work, all the experiments were carried out in $MgCl_2$ solution or under a $MgCl_2$ electrolyte layer. However, in real atmospheric conditions, aerosols consist of a mixture of salt, such as NaCl, $MgCl_2$, and $CaCl_2$ etc [82]. Synchrotron X-ray micro-tomography, XRD and electrochemical methods can be used to study atmospheric pitting corrosion under mixed salt solution electrolyte layer, or in immersed mixed salt solution. However, it is essential to develop the inkjet printing deposition method to deposit mixed salt solutions. The present study has used one cartridge containing $MgCl_2$ solution. For the future work, multiple cartridges could be used containing different salt solutions.

8.2.3 Extending to wet-dry cycling exposure conditions

The present work on synchrotron micro-tomography has focused upon metal pins exposed to constant relative humidity. However, in real atmospheric conditions, wet-dry cycling is more common, which may affect corrosion activities. Hastuty et al. have characterised pitting corrosion of stainless steel 430 in drying process and reported that pitting corrosion would

take place in the chloride concentration range of 6 M to 8 M no matter whether a fast or a slow drying rate was used. Chen et al. [153] investigated to corrosion behaviour of mild steel during wet-dry cycles and reported that meta-stable pits are more common and uniformly distributed in wet cycles rather than in dry cycles.

9 Conclusions

1. Atmospheric pitting corrosion of stainless steel was investigated under salt droplets formed by direct deposition, and those formed by deliquescence of salt circles formed with an inkjet printer. For pits grown under deliquesced salt patterns, it was found that the size of a pit increases with increasing original deposit diameter; this is likely to relate to an increase in the available cathodic area of the droplet. The size of pits also increases with increasing chloride deposition density, which is probably associated with the lower ohmic drop for a thicker droplet/electrolyte layer.

2. In-situ pit growth in real time under atmospheric conditions was investigated by synchrotron X-ray micro-tomography. Most of the pit morphologies were found with an open mouth and a shallow depth, which is consistent with pit morphologies observed in the inkjet printing. However, pits can grow very deep if there are pre-existing defects within the material.

3. The depth of pits under atmospheric conditions has been observed to increase with time, but the growth rate has not been found under diffusion control, which is very likely due to the limited electrolyte volume providing an additional diffusion barrier.

4. The pit stability product of atmospheric corrosion pits is estimated to be about 6×10^{-5} Am^{-1} using in-situ X-ray micro-tomography. This value is far below the pit stability product determined in immersion conditions. However, it is not clear that the depth of atmospheric corrosion pits in depth increases under diffusion control so the pit stability product might not be a relevant parameter.

5. The diffusion-limited current density (i_{lim}), critical pit solution chemistry for pit propagation (C_{crit}/C_{sat}) and pit stability product (ix) on stainless steel 1D artificial pits have been found to decrease with increasing chloride concentration. However, the Tafel slope appears to be independent of chloride concentration.

6. Both the pitting potential and the repassivation potential decrease with increasing chloride concentration. The pitting potential decreases linearly with increasing logarithm of chloride concentration when the chloride concentration is relatively low ($\leqslant$2 M), and decreases more steeply when the chloride concentration is relatively high. The pitting potential measured in high chloride concentration solutions has been found

to be close to the open circuit potential, which indicates that pitting corrosion is likely to take place at open circuit potential under atmospheric conditions corresponding to high chloride concentration solutions.

7. Salt layer formation has been detected in 1D artificial pits in both 1 M and 6 M chloride solutions. The dominant phase is $FeCl_2 \cdot 4H_2O$, but the dehydrated phase of $FeCl_2 \cdot 2H_2O$ is also found. The formation of $FeCl_2 \cdot 2H_2O$ was only observed at relatively higher applied potential ($\geqslant$ 0.8 V vs. SCE), at positions relatively close to the dissolving interface. The amount of $FeCl_2 \cdot 2H_2O$ is greater in 1 M chloride solution than 6 M solution, which is possibly due to a more porous salt layer formation in 6 M solution or due to a lower diffusion-limited current density in 6 M solution.

8. Intense synchrotron X-rays may lead to beam damage that can affect initiation of pits under atmospheric corrosion conditions. Multiple pits were formed after several X-ray micro-tomography scans.

9. The work can be used to provide a basis for recommending safe chloride deposition levels (10-20 $\mu g/cm^3$) to minimise the risk of pitting corrosion, as well as giving an indication of the effect of relative humidity.

10 References

1. Tsutsumi, Y., A. Nishikata, and T. Tsuru, *Pitting corrosion mechanism of type 304 stainless steel under a droplet of chloride solutions.* Corrosion Science, 2007. **49**(3): p. 1394-1407.

2. Ghahari, S.M., D.P. Krouse, N.J. Laycock, T. Rayment, C. Padovani, T. Suter, R. Mokso, F. Marone, M. Stampanoni, M. Monir, and A.J. Davenport, *Pitting corrosion of stainless steel: Measuring and modelling pit propagation in support of damage prediction for radioactive waste containers.* Corrosion Engineering Science and Technology, 2011. **46**(2): p. 205-211.

3. Smart, N.R., C.C. Naish, and A.M. Pritchard. *Corrosion principles for the assessment of stainless steel radioactive waste containers*. Serco report 2006; Available from: http://www.nda.gov.uk/documents/biblio/.

4. NDA. *UK radioactive higher activity wastes storage review*. 2009; Available from: http://www.nda.gov.uk/documents.

5. Frankel, G.S., *Pitting corrosion of metals - a review of the critical factors.* Journal of the Electrochemical Society, 1998. **145**(6): p. 2186-2198.

6. Newman, R.C., *2001 w.R. Whitney award lecture: Understanding the corrosion of stainless steel.* Corrosion, 2001. **57**(12): p. 1030-1041.

7. Frankel, G.S. and N. Sridhar, *Understanding localized corrosion.* Materials Today, 2008. **11**(10): p. 38-44.

8. Trethewey, K.R. and J. Chamberlain, *Corrosion for science and engineering*. 2nd Edition ed. 1995: Longman Scientific & Technical.

9. Sedriks, A.J., *Stainless steel corrosion*. 1979, New York: Wiley.

10. L.L.Shreir, R.A. Jarman, and G.T. Burstein, *Corrosion metal/environment reactions*. 3rd Edition ed. Vol. Volume 1. 1994: Butterworth-Heinemann Ltd.

11. Sharland, S.M., *A review of the theoretical modeling of crevice and pitting corrosion.* Corrosion Science, 1987. **27**(3): p. 289-323.

12. Davenport, A.J., *Second year corrosion lecture notes*. 2008, University of Birmingham: Birmingham.

13. Pourbaix, M., *Significance of protection potential in pitting and intergranular corrosion.* Corrosion, 1970. **26**(10): p. 431-&.

14. Tsuru, T., K.I. Tamiya, and A. Nishikata, *Formation and growth of micro-droplets during the initial stage of atmospheric corrosion.* Electrochimica Acta, 2004. **49**(17-18): p. 2709-2715.

15. Zhang, J., J. Wang, and Y. Wang, *Micro-droplets formation during the deliquescence of salt particles in atmosphere.* Corrosion, 2005. **61**(12): p. 1167-1172.

16. Hastuty, S., A. Nishikata, and T. Tsuru, *Pitting corrosion of type 430 stainless steel under chloride solution droplet.* Corrosion Science, 2010. **52**(6): p. 2035-2043.

17. Schindelholz, E. and R.G. Kelly, *Application of inkjet printing for depositing salt prior to atmospheric corrosion testing.* Electrochemical and Solid State Letters, 2010. **13**(10): p. C29-C31.

18. Maier, B. and G.S. Frankel, *Pitting corrosion of bare stainless steel 304 under chloride solution droplets.* Journal of the Electrochemical Society, 2010. **157**(10): p. C302-C312.

19. Mi, N., M. Ghahari, T. Rayment, and A.J. Davenport, *Use of inkjet printing to deposit magnesium chloride salt patterns for investigation of atmospheric corrosion of 304 stainless steel.* Corrosion Science, 2011. **53**(10): p. 3114-3121.

20. Eklund, G., *Relation between pitting and non-metallic inclusions.* Jernkontorets Annaler, 1971. **155**(9): p. 637-&.

21. Eklund, G.S., *Initiation of pitting at sulfide inclusions in stainless-steel.* Journal of the Electrochemical Society, 1974. **121**(4): p. 467-473.

22. Wranglen, G., *Pitting and sulfide inclusions in steel.* Corrosion Science, 1974. **14**(5): p. 331-349.

23. Webb, E.G. and R.C. Alkire, *Pit initiation at single sulfide inclusions in stainless steel - i. Electrochemical microcell measurements.* Journal of the Electrochemical Society, 2002. **149**(6): p. B272-B279.

24. Webb, E.G. and R.C. Alkire, *Pit initiation at single sulfide inclusions in stainless steel - II. Detection of local pH, sulfide, and thiosulfate.* Journal of the Electrochemical Society, 2002. **149**(6): p. B280-B285.

25. Webb, E.G. and R.C. Alkire, *Pit initiation at single sulfide inclusions in stainless steel - iii. Mathematical model.* Journal of the Electrochemical Society, 2002. **149**(6): p. B286-B295.

26. Castle, J.E. and R. Ke, *Studies by auger-spectroscopy of pit initiation at the site of inclusions in stainless-steel.* Corrosion Science, 1990. **30**(4-5): p. 409-428.

27. Szklarsk.Z, *Influence of sulfide inclusions on pitting corrosion of steels.* Corrosion, 1972. **28**(10): p. 388-&.

28. Ingri, N., Kakolowi.W, L.G. Sillen, and Warnqvis.B, *High-speed computers as a supplement to graphical method .V. Haltafall a general program for calculating composition of equilibrium mixtures.* Talanta, 1967. **14**(11): p. 1261-&.

29. Marcus, P., *The role of alloyed elements and adsorbed impurities in passivation of metal-surfaces.* Journal De Chimie Physique Et De Physico-Chimie Biologique, 1991. **88**(7-8): p. 1697-1711.

30. Newman, R., *Pitting corrosion of metals.* Interface, 2010. **1**: p. 33-38.

31. Laycock, N.J. and R.C. Newman, *Localised dissolution kinetics, salt films and pitting potentials.* Corrosion Science, 1997. **39**(10-11): p. 1771-1790.

32. Galvele, J.R., *Transport processes and mechanism of pitting of metals.* Journal of the Electrochemical Society, 1976. **123**(4): p. 464-474.

33. Pickering, H.W. and R.P. Frankenthal, *Mechanism of localized corrosion of iron and stainless-steel. 1. Electrochemical studies.* Journal of the Electrochemical Society, 1972. **119**(10): p. 1297-&.

34. Frankent.Rp and Pickerin.Hw, *Mechanism of localized corrosion of iron and stainless-steel .2. Morphological studies.* Journal of the Electrochemical Society, 1972. **119**(10): p. 1304-&.

35. Pistorius, P.C. and G.T. Burstein, *Metastable pitting corrosion of stainless-steel and the transition to stability.* Philosophical Transactions of the Royal Society of London Series a-Mathematical Physical and Engineering Sciences, 1992. **341**(1662): p. 531-559.

36. Gaudet, G.T., W.T. Mo, T.A. Hatton, J.W. Tester, J. Tilly, H.S. Isaacs, and R.C. Newman, *Mass-transfer and electrochemical kinetic interactions in localized pitting corrosion.* Aiche Journal, 1986. **32**(6): p. 949-958.

37. Laycock, N.J. and S.P. White, *Computer simulation of single pit propagation in stainless steel under potentiostatic control.* Journal of the Electrochemical Society, 2001. **148**(7): p. B264-B275.

38. Galvele, J.R., *Tafel's law in pitting corrosion and crevice corrosion susceptibility.* Corrosion Science, 2005. **47**(12): p. 3053-3067.

39. Laycock, N.J., D.P. Krouse, S.M. Ghahari, A.J. Davenport, T. Rayment, and C. Padovani, *(invited)localized dissolution kinetics from fast in situ radiography of propagating pits in stainless steel and implications for modeling pitting corrosion over long time-scales.* ECS Transactions, 2012. **41**(25): p. 3-16.

40. Newman, R.C., M.A.A. Ajjawi, H. Ezuber, and S. Turgoose, *An experimental confirmation of the pitting potential model of galvele.* Corrosion Science, 1988. **28**(5): p. 471-477.

41. Frankel, G.S., L. Stockert, F. Hunkeler, and H. Boehni, *Metastable pitting of stainless-steel.* Corrosion, 1987. **43**(7): p. 429-436.

42. Pistorius, P.C. and G.T. Burstein, *Aspects of the effects of electrolyte-composition on the occurrence of metastable pitting on stainless-steel.* Corrosion Science, 1994. **36**(3): p. 525-538.

43. Burstein, G.T., P.C. Pistorius, and S.P. Mattin, *The nucleation and growth of corrosion pits on stainless-steel.* Corrosion Science, 1993. **35**(1-4): p. 57-62.

44. Williams, D.E., J. Stewart, and P.H. Balkwill. *Growth and stability of micropits in stainless steel*. 1992. Pennington NJ: The Electrochemical Society Proceeding Series.

45. Hoar, T.P., *The corrosion of tin in nearly neutral solutions.* Transactions of the Faraday Society, 1937. **33**(2): p. 1152-1166.

46. Mankowski, J. and Z. Szklarskasmialowska, *Studies on accumulation of chloride-ions in pits growing during anodic polarization.* Corrosion Science, 1975. **15**(8): p. 493-501.

47. Wilde, B.E. and E. Williams, *Use of current/voltage curves for study of localized corrosion and passivity breakdown on stainless steels in chloride media.* Electrochimica Acta, 1971. **16**(11): p. 1971-&.

48. Suzuki, T., M. Yamabe, and Y. Kitamura, *Composition of anolyte within pit anode of austenitic stainless-steels in chloride solution.* Corrosion, 1973. **29**(1): p. 18-22.

49. Isaacs, H.S. and R.C. Newman. *Local electrochemistry of pitting corrosion in stainless steel* in *Corrosion Chemistry Within Pits, Crevices and Cracks*. 1987. London HMSO.

50. Hunkeler, F. and H. Bohni. *Corrosion chemistry within pits, crevices and cracks*. in *HMSO*. 1987. London.

51. Ryan, M.P., N.J. Laycock, H.S. Isaacs, and R.C. Newman, *Corrosion pits in thin films of stainless steel.* Journal of the Electrochemical Society, 1999. **146**(1): p. 91-97.

52. Isaacs, H.S., J.H. Cho, M.L. Rivers, and S.R. Sutton, *In-situ X-ray microprobe study of salt layers during anodic-dissolution of stainless-steel in chloride solution.* Journal of the Electrochemical Society, 1995. **142**(4): p. 1111-1118.

53. Sridhar, N. and D.S. Dunn, *Effect of applied potential on changes in solution chemistry inside crevices on type-304L stainless-steel and alloy-825.* Corrosion, 1994. **50**(11): p. 857-872.

54. Brossia, C.S., D.S. Dunn, and N. Sridhar, *The role of metal salt film formation on localized corrosion stabilization,* in *Proceedings of the symposium on critical factors in localized corrosion III - a symposium in honor of the 70th birthday of Jerome Kruger*, R.G. Kelley, et al., Editors. 1999, Electrochemical Society Inc: Pennington. p. 485-499.

55. Davenport, A.J., A.J. Dent, M. Monir, J.A. Hammons, S.M. Ghahari, P.D. Quinn, and T. Rayment, *XANES study of the chemistry of molybdenum in artificial corrosion pits in 316L stainless steel.* Journal of the Electrochemical Society, 2011. **158**(5): p. C111-C117.

56. Monir, M., *XANES study of chemistry of localised corrosion in artificial pits of 316L stainless steel and titanium*, in *School of Metallurgy and Materials*. 2011, University of Birmingham: Birmingham.

57. Ernst, P., N.J. Laycock, M.H. Moayed, and R.C. Newman, *The mechanism of lacy cover formation in pitting.* Corrosion Science, 1997. **39**(6): p. 1133-1136.

58. Tang, Y.C. and A.J. Davenport, *Magnetic field effects on the corrosion of artificial pit electrodes and pits in thin films.* Journal of the Electrochemical Society, 2007. **154**(7): p. C362-C370.

59. Steinsmo, U. and H.S. Isaacs, *The dissolution and repassivation kinetics of Fe-Cr alloys in pit solutions.* Corrosion Science, 1993. **35**(1-4): p. 83-88.

60. Baroux, B., *The kinetics of pit generation on stainless steels.* Corrosion Science, 1988. **28**(10): p. 969-986.

61. Tester, J.W. and H.S. Isaacs, *Diffusional effects in simulated localized corrosion.* Journal of the Electrochemical Society, 1975. **122**(11): p. 1438-1445.

62. Newman, R.C. and H.S. Isaacs, *Diffusion-coupled active dissolution in the localized corrosion of stainless-steels.* Journal of the Electrochemical Society, 1983. **130**(7): p. 1621-1624.

63. Enerhaug, J., U.M. Steinsmo, O. Grong, and L.R. Hellevik, *Dissolution and repassivation kinetics of a 12.3Cr-2.6Mo-6.5Ni super martensitic stainless steel - a comparative study.* Journal of the Electrochemical Society, 2002. **149**(6): p. B256-B264.

64. Hoar, T.P., D.C. Mears, and G.P. Rothwell, *The relationships between anodic passivity brightening and pitting.* Corrosion Science, 1965. **5**: p. 279 to 289.

65. Vetter, K.J. and Strehblow.Hh, *Formation and shape of corrosion pits in localized corrosion on iron theoretical results pertaining to localized corrosion.* Berichte Der Bunsen-Gesellschaft Fur Physikalische Chemie, 1970. **74**(10): p. 1024-&.

66. Isaacs, H.S., *Behavior of resistive layers in localized corrosion of stainless-steel.* Journal of the Electrochemical Society, 1973. **120**(11): p. 1456-1462.

67. Beck, T.R., *Occurrence and properties of anodic salt films in pitting corrosion*, in *NACE*, H. Isaacs, et al., Editors. 1990, Advances in Localized Corrosion: Houston.

68. Beck, T.R. and R.C. Alkire, *Occurrence of salt films during initiation and growth of corrosion pits.* Journal of the Electrochemical Society, 1979. **126**(10): p. 1662-1666.

69. Danielson, M.J., *Transport-properties of salt films on nickel in 0.5N HCl.* Journal of the Electrochemical Society, 1988. **135**(6): p. 1326-1332.

70. Clerc, C. and D. Landolt, *AC impedance study of anodic films on nickel in LiCl.* Electrochimica Acta, 1988. **33**(7): p. 859-871.

71. Grimm, R.D. and D. Landolt, *Salt films formed during mass-transport controlled dissolution of iron-chromium alloys in concentrated chloride media.* Corrosion Science, 1994. **36**(11): p. 1847-1868.

72. Grimm, R.D., A.C. West, and D. Landolt, *AC impedance study of anodically formed salt films on iron in chloride solution.* Journal of the Electrochemical Society, 1992. **139**(6): p. 1622-1629.

73. Rayment, T., A.J. Davenport, A.J. Dent, J.P. Tinnes, R.J.K. Wiltshire, C. Martin, G. Clark, P. Quinn, and J.F.W. Mosselmans, *Characterisation of salt films on dissolving metal surfaces in artificial corrosion pits via in situ synchrotron X-ray diffraction.* Electrochemistry Communications, 2008. **10**(6): p. 855-858.

74. Novakovs.Vm and A.N. Sorokina, *Model study of chloride pitting in 18-8 stainless steel.* Corrosion Science, 1966. **6**(5): p. 227-&.

75. Hakkarainen, T., *Factors determining the dissolution rate in pitting corrosion of stainless steel*, in *Materials Science Forum*, M. Duprat, Editor. 1986, Trans Tech Publications: Swizerland. p. 81-90.

76. Hakkarainen, T. *Anodic behaviour of stainless steel in simulated pit solutions* in *Corrosion Chemistry within Pits, Crevices and Cracks*. 1987. London HMSO.

77. Ernst, P. and R.C. Newman, *Explanation of the effect of high chloride concentration on the critical pitting temperature of stainless steel.* Corrosion Science, 2007. **49**(9): p. 3705-3715.

78. Steinsmo, U. and H.S. Isaacs, *Dissolution and repassivation kinetics of Fe-Cr alloys in pit solutions .1. Effect of the surface salt layer.* Journal of the Electrochemical Society, 1993. **140**(3): p. 643-653.

79. Smart, N.R., C.C. Naish, and A.M. Pritchard, *Corrosion principles for the assessment of stianless steel radioactive waste containers*, S. report, Editor. 2006.

80. Matsumi, M., A. Nishikata, and T. Tsuru. in *Preceedings of the Japan Conference on Material and Environments 46*. 1999. Fukuoka.

81. *Handbook of chemistry and physics*. 75th edition ed, ed. D.R. Lide. 1994: CRC Press.

82. Cole, I.S., W.D. Ganther, D.A. Paterson, G.A. King, S.A. Furman, and D. Lau, *Holistic model for atmospheric corrosion - part 2 - experimental measurement of deposition of marine salts in a number of long range studies.* Corrosion Engineering Science and Technology, 2003. **38**(4): p. 259-266.

83. Neufeld, A.K., I.S. Cole, A.M. Bond, and S.A. Furman, *The initiation mechanism of corrosion of zinc by sodium chloride particle deposition.* Corrosion Science, 2002. **44**(3): p. 555-572.

84. Cole, I.S., D. Lau, and D.A. Paterson, *Holistic model for atmospheric corrosion - part 6 - from wet aerosol to salt deposit.* Corrosion Engineering Science and Technology, 2004. **39**(3): p. 209-218.

85. Turnbull, A., K. Mingard, J.D. Lord, B. Roebuck, D.R. Tice, K.J. Mottershead, N.D. Fairweather, and A.K. Bradbury, *Sensitivity of stress corrosion cracking of stainless steel to surface machining and grinding procedure.* Corrosion Science, 2011. **53**(10): p. 3398-3415.

86. Hinds, G., L. Wickstrom, K. Mingard, and A. Turnbull, *Impact of surface condition on sulphide stress corrosion cracking of 316L stainless steel.* Corrosion Science, 2013. **71**: p. 43-52.

87. Chen, Z.Y., S. Zakipour, D. Persson, and C. Leygraf, *Effect of sodium chloride particles on the atmospheric corrosion of pure copper.* Corrosion, 2004. **60**(5): p. 479-491.

88. Chen, Z.Y., D. Persson, F. Samie, S. Zakipour, and C. Leygraf, *Effect of carbon dioxide on sodium chloride-induced atmospheric corrosion of copper.* Journal of the Electrochemical Society, 2005. **152**(12): p. B502-B511.

89. Zhang, J.B., J. Wang, and Y.H. Wang, *Electrochemical investigations of micro-droplets formed on metals during the deliquescence of salt particles in atmosphere.* Electrochemistry Communications, 2005. **7**(4): p. 443-448.

90. Li, S.X. and L.H. Hihara, *Atmospheric corrosion initiation on steel from predeposited NaCl salt particles in high humidity atmospheres.* Corrosion Engineering Science and Technology, 2010. **45**(1): p. 49-56.

91. Lobnig, R., J.D. Sinclair, M. Unger, and M. Stratmann, *Mechanism of atmospheric corrosion of copper in the presence of ammonium sulfate particles - effect of surface particle concentration.* Journal of the Electrochemical Society, 2003. **150**(6): p. A835-A849.

92. Dubuisson, E., P. Lavie, F. Dalard, J.P. Caire, and S. Szunerits, *Study of the atmospheric corrosion of galvanised steel in a micrometric electrolytic droplet.* Electrochemistry Communications, 2006. **8**(6): p. 911-915.

93. Dubuisson, E., P. Lavie, F. Dalard, J.P. Caire, and S. Szunerits, *Corrosion of galvanised steel under an electrolytic drop.* Corrosion Science, 2007. **49**(2): p. 910-919.

94. Calvert, P., *Inkjet printing for materials and devices.* Chemistry of Materials, 2001. **13**(10): p. 3299-3305.

95. Sirringhaus, H. and T. Shimoda, *Inkjet printing of functional materials.* Mrs Bulletin, 2003. **28**(11): p. 802-803.

96. de Gans, B.J., P.C. Duineveld, and U.S. Schubert, *Inkjet printing of polymers: State of the art and future developments.* Advanced Materials, 2004. **16**(3): p. 203-213.

97. Tekin, E., B.J. de Gans, and U.S. Schubert, *Ink-jet printing of polymers - from single dots to thin film libraries.* Journal of Materials Chemistry, 2004. **14**(17): p. 2627-2632.

98. Croucher, M.D. and M.L. Hair, *Design criteria and future-directions in inkjet ink technology.* Industrial & Engineering Chemistry Research, 1989. **28**(11): p. 1712-1718.

99. Chung, J.W., S.W. Ko, N.R. Bieri, C.P. Grigoropoulos, and D. Poulikakos, *Conductor microstructures by laser curing of printed gold nanoparticle ink.* Applied Physics Letters, 2004. **84**(5): p. 801-803.

100. Lee, H.H., K.S. Chou, and K.C. Huang, *Inkjet printing of nanosized silver colloids.* Nanotechnology, 2005. **16**(10): p. 2436-2441.

101. Nishikata, A., Y. Ichihara, and T. Tsuru, *Electrochemical impedance spectroscopy of metals covered with a thin electrolyte layer.* Electrochimica Acta, 1996. **41**(7-8): p. 1057-1062.

102. Nishikata, A., Y. Ichihara, Y. Hayashi, and T. Tsuru, *Influence of electrolyte layer thickness and pH on the initial stage of the atmospheric corrosion of iron.* Journal of the Electrochemical Society, 1997. **144**(4): p. 1244-1252.

103. Cruz, R.P.V., A. Nishikata, and T. Tsuru, *AC impedance monitoring of pitting corrosion of stainless steel under a wet-dry cyclic condition in chloride-containing environment.* Corrosion Science, 1996. **38**(8): p. 1397-1406.

104. Cruz, R.P.V., A. Nishikata, and T. Tsuru, *Pitting corrosion mechanism of stainless steels under wet-dry exposure in chloride-containing environments.* Corrosion Science, 1998. **40**(1): p. 125-139.

105. Frankel, G.S., M. Stratmann, M. Rohwerder, A. Michalik, B. Maier, J. Dora, and M. Wicinski, *Potential control under thin aqueous layers using a kelvin probe.* Corrosion Science, 2007. **49**(4): p. 2021-2036.

106. Stratmann, M. and H. Streckel, *On the atmospheric corrosion of metals which are covered with thin electrolyte layers .1. Verification of the experimental-technique.* Corrosion Science, 1990. **30**(6-7): p. 681-696.

107. Stratmann, M. and H. Streckel, *On the atmospheric corrosion of metals which are covered with thin electrolyte layers .2. Experimental results.* Corrosion Science, 1990. **30**(6-7): p. 697-714.

108. Tsutsumi, Y., A. Nishikata, and T. Tsuru, *Monitoring of rusting of stainless steels in marine atmospheres using electrochemical impedance technique.* Journal of the Electrochemical Society, 2006. **153**(7): p. B278-B282.

109. Chen, Z.Y. and R.G. Kelly, *An analytical modeling method for calculating the maximum cathode current deliverable by a circular cathode under atmospheric exposure*, in *Simulation of electrochemical processes II*, V.G. DeGiorgi, C.A. Brebbia, and R.A. Adey, Editors. 2007, Wit Press/Computational Mechanics Publications: Southampton. p. 33-41.

110. Chen, Z.Y. and R.G. Kelly, *Computational modeling of bounding conditions for pit size on stainless steel in atmospheric environments.* Journal of the Electrochemical Society, 2010. **157**(2): p. C69-C78.

111. Cui, F.S., F.J. Presuel-Moreno, and R.G. Kelly, *Computational modeling of cathodic limitations on localized corrosion of wetted SS 316L at room temperature.* Corrosion Science, 2005. **47**(12): p. 2987-3005.

112. Shedd, M.E. and R.G. Kelly, *The modeling and measurement of boundary conditions for pit size on stainless steels under atmospheric exposure conditions.* ECS Transactions, 2012. **41**(25): p. 31-37.

113. Williams, D.E., J. Stewart, and P.H. Balkwill, *The nucleation, growth and stability of micropits in stainless-steel.* Corrosion Science, 1994. **36**(7): p. 1213-1235.

114. Chen, Z.Y., F. Cui, and R.G. Kelly, *Calculations of the cathodic current delivery capacity and stability of crevice corrosion under atmospheric environments.* Journal of the Electrochemical Society, 2008. **155**(7): p. C360-C368.

115. DiamondLightSource. *About diamond - how do synchrotron work*. 2013; Available from: www.diamond.ac.uk/Home/About/Synchrotrons/Machine.html.

116. ESRF. *Principle structure of synchrotron*. 2013; Available from: www.esrf.eu/about/synchrotron-science/synchrotron.

117. Willmott, P. An introduction to synchrotron radiation techniques and applications. 2011: John Wiley & Sons Ltd.

118. Ghahari, S.M., A.J. Davenport, T. Rayment, T. Suter, J.P. Tinnes, C. Padovani, J.A. Hammons, M. Stampanoni, F. Marone, and R. Mokso, *In situ synchrotron X-ray micro-tomography study of pitting corrosion in stainless steel.* Corrosion Science, 2011. **53**(9): p. 2684-2687.

119. Connolly, B.J., D.A. Horner, S.J. Fox, A.J. Davenport, C. Padovani, S. Zhou, A. Turnbull, M. Preuss, N.P. Stevens, T.J. Marrow, J.Y. Buffiere, E. Boller, A. Groso, and M. Stampanoni, *X-ray microtomography studies of localised corrosion and transitions to stress corrosion cracking.* Materials Science and Technology, 2006. **22**(9): p. 1076-1085.

120. Davenport, A.J., C. Padovani, B.J. Connolly, N.P.C. Stevens, T.A.W. Beale, A. Groso, and M. Stampanoni, *Synchrotron X-ray microtomography study of the role of Y in corrosion of magnesium alloy WE43.* Electrochemical and Solid State Letters, 2007. **10**(2): p. C5-C8.

121. Knight, S.P., M. Salagaras, A.M. Wythe, F. De Carlo, A.J. Davenport, and A.R. Trueman, *In situ X-ray tomography of intergranular corrosion of 2024 and 7050 aluminium alloys.* Corrosion Science, 2010. **52**(12): p. 3855-3860.

122. DiamondLightSource. *Artistic images - 3D model of the machine*. Available from: http://www.diamond.ac.uk/Home/Media/images.html.

123. Stock, S.R., *X-ray microtomography of materials.* International Materials Reviews, 1999. **44**(4): p. 141-164.

124. Salvo, L., P. Cloetens, E. Maire, S. Zabler, J.J. Blandin, J.Y. Buffiere, W. Ludwig, E. Boller, D. Bellet, and C. Josserond, *X-ray micro-tomography an attractive characterisation technique in materials science.* Nuclear Instruments & Methods in Physics Research Section B-Beam Interactions with Materials and Atoms, 2003. **200**: p. 273-286.

125. Stock, S.R., *Recent advances in X-ray microtomography applied to materials.* International Materials Reviews, 2008. **53**(3): p. 129-181.

126. Banhart, J., *Andvanced tomographic methods in materials research and engineering*. 2008: Oxford University Press.

127. Marrow, T.J., L. Babout, A.P. Jivkov, P. Wood, D. Engelberg, N. Stevens, P.J. Withers, and R.C. Newman, *Three dimensional observations and modelling of intergranular stress corrosion cracking in austenitic stainless steel.* Journal of Nuclear Materials, 2006. **352**(1-3): p. 62-74.

128. Eckermann, F., T. Suter, P.J. Uggowitzer, A. Afseth, A.J. Davenport, B.J. Connolly, M.H. Larsen, F. De Carlo, and P. Schmutz, *In situ monitoring of corrosion processes within the bulk of AlMgSi alloys using X-ray microtomography.* Corrosion Science, 2008. **50**(12): p. 3455-3466.

129. Eckermann, F., T. Suter, P.J. Uggowitzer, A. Afseth, M. Stampanoni, F. Marone, and P. Schmutz, *In situ microtomographically monitored and electrochemically controlled corrosion initiation and propagation in AlMgSi alloy AA6016.* Journal of the Electrochemical Society, 2009. **156**(1): p. C1-C7.

130. Ko, M., N.J. Laycock, B. Ingham, and D.E. Williams, *In situ synchrotron X-ray diffraction studies of CO2 corrosion of carbon steel with scale inhibitors ATMPA and PEI at 80 degrees C.* Corrosion, 2012. **68**(12): p. 1085-1093.

131. Dowsett, M., A. Adriaens, C. Martin, and L. Bouchenoire, *The use of synchrotron X-rays to observe copper corrosion in real time.* Analytical Chemistry, 2012. **84**(11): p. 4866-4872.

132. Ernst, P. and R.C. Newman, *Pit growth studies in stainless steel foils. II. Effect of temperature, chloride concentration and sulphate addition.* Corrosion Science, 2002. **44**(5): p. 943-954.

133. Prosek, T., A. Iversen, C. Taxen, and D. Thierry, *Low-temperature stress corrosion cracking of stainless steels in the atmosphere in the presence of chloride deposits.* Corrosion, 2009. **65**(2): p. 105-117.

134. Neufeld, A.K., I.S. Cole, A. Bond, and S.A. Furman, *The initiation mechanism of corrosion of zinc by sodium chloride particle deposition* Corrosion Science, 2002. **44**(6): p. 1391-1391.

135. Chen, Z.Y., D. Persson, A. Nazarov, S. Zakipour, D. Thierry, and C. Leygraf, *In situ studies of the effect of CO2 on the initial NaCl-induced atmospheric corrosion of copper.* Journal of the Electrochemical Society, 2005. **152**(9): p. B342-B351.

136. Ghahari, M., *In situ synchrotron X-ray characterisation and modelling of pitting corrosion of stainless steel*, in *School of Metallurgy and Materials*. 2012, University of Birmingham: Birmingham.

137. Nagy, Z. and H. You, *Applications of surface X-ray scattering to electrochemistry problems.* Electrochimica Acta, 2002. **47**(19): p. 3037-3055.

138. Hastuty, S., Y. Tsutsumi, A. Nishikata, and T. Tsuru, *Pitting corrosion of type 430 stainless steel in the process of drying of chloride solution layer.* Isij International, 2012. **52**(5): p. 863-867.

139. Frankel, G.S., L. Stockert, F. Hunkeler, and H. Bohni, *Metastable pitting of stainless steel.* Corrosion 1987. **43**: p. 429-436.

140. Kawaley, G., *Localised corrosion of iron in food products*, in *Department of Metallurgy and Materials*. 2008, University of Birmingham.

141. Newman, R.C. and M.A.A. Ajjawi, *A microelectrode study of the nitrate effect on pitting of stainless-steels.* Corrosion Science, 1986. **26**(12): p. 1057-1063.

142. Newman, R.C. and H. Isaacs. *Dissolution and passivation kinetics of Fe-Cr-Ni alloys during localized corrosion*. in *Passivity of Metals and Semiconductors*. 1983. Amsterdam.

143. Burstein, G.T. and P.C. Pistorius, *Surface-roughness and the metastable pitting of stainless-steel in chloride solutions.* Corrosion, 1995. **51**(5): p. 380-385.

144. Yashiro, H. and K. Tanno, *The effect of electrolyte-composition on the pitting and repassivation behavior of AISI 304 stainless-steel at high-temperature.* Corrosion Science, 1990. **31**: p. 485-490.

145. Sridhar, N. and G.A. Cragnolino, *Applicability of repassivation potential for long-term prediction of localized corrosion of alloy-825 and type-316L stainless-steel.* Corrosion, 1993. **49**(11): p. 885-894.

146. Anderko, A., N. Sridhar, and D.S. Dunn, *A general model for the repassivation potential as a function of multiple aqueous solution species.* Corrosion Science, 2004. **46**(7): p. 1583-1612.

147. Boehni, H. and F. Hunkeler. *Growth kinetics and stability of localised corrsion processes*. in *Advances in Localized Corrosion*. 1990. Houston: NACE.

148. Verbist, J.J., T.F. Koetzle, M.S. Lehmann, and W.C. Hamilton, *Neutron-diffraction study of iron(II) chloride tetrahydrate, FeCl2.4H2O.* Journal of Chemical Physics, 1972. **56**(7): p. 3257-&.

149. Morosin, B. and E.J. Graeber, *Crystal structures of manganese (2) and iron(2) chloride dihydrate.* Journal of Chemical Physics, 1965. **42**(3): p. 898-&.

150. Isaacs, H.S. and G. Kissel, *Surface preparation and pit propagation in stainless-steels.* Journal of the Electrochemical Society, 1972. **119**(12): p. 1628-&.

151. Beck, T.R., *Electrical conductivities of some metal salt films under anodic conditions.* Chemical Engineering Communications, 1985. **38**(3-6): p. 393-400.

152. Albores-Silva, O.E., E.A. Charles, and C. Padovani, *Effect of chloride deposition on stress corrosion cracking of 316L stainless steel used for intermediate level radioactive waste containers.* Corrosion Engineering Science and Technology, 2011. **46**(2): p. 124-128.

153. Chen, A.N., F.H. Cao, X.N. Liao, W.J. Liu, L.Y. Zheng, J.Q. Zhang, and C.A. Cao, *Study of pitting corrosion on mild steel during wet-dry cycles by electrochemical noise analysis based on chaos theory.* Corrosion Science, 2013. **66**: p. 183-195.